Variational cluster approximation at finite temperatures

Von der Fakultät Mathematik und Physik der Universität Stuttgart
zur Erlangung der Würde eines Doktors der Naturwissenschaften
(Dr. rer. nat.) genehmigte Abhandlung

Vorgelegt von
Jan Lotze
aus Stuttgart

Hauptberichter: **Prof. Dr. Maria Daghofer**
Mitberichter: **Prof. Dr. Walter Metzner**
Prüfungsvorsitzender: **Prof. Dr. Sebastian Loth**

Tag der mündlichen Prüfung: 13.05.2022

Universität Stuttgart

FMQ

Institut für Funktionelle Materie und Quantentechnologien
der Universität Stuttgart
2022

“How can I be remembered?”
he said.
“Be difficult to forget”,
the Oracle said.
“How? Do I create art?
Be famous? Be powerful?”

“Be kind.”

– James Miller

To my mother, Ruth Lotze,
who passed away before seeing
the completion of this thesis.

Abstract

Being able to describe thermodynamics and dynamics of ordered systems at finite temperature allows capturing the signatures of different phases as well as thermal transitions between them. Systems of strongly correlated electrons residing in multiple orbitals where spin-orbit coupling is of significance can exhibit a multitude of exotic phases. Modelling these systems and capturing their properties for the entire temperature range is a non-trivial task. In this thesis, the implementation details of several cluster solvers used for the variational cluster approximation (VCA) at finite temperature are described, since this method is capable of modelling the systems mentioned before while incorporating local quantum fluctuations. The most reliable, sufficiently benchmarked and best performing solver among them is then used to investigate the magnetic and orbital properties of Sr_2IrO_4 and Ca_2RuO_4 described by three-band Hubbard models, as well as the Kondo lattice model at half-filling.

Starting at zero temperature, three cluster solvers and four representations of the Green's function are presented which are employed within VCA. Each of the representations has its area of application depending on the solver used.

The Lanczos algorithm constructs iteratively an invariant subspace of the Hamiltonian in which it has tridiagonal shape. Computing the eigenvalues and eigenvectors allows constructing the spectral representation of the Green's function. Inversion of the tridiagonal matrix yields the continued fraction representation of the Green's function. Hence it can be obtained without having to diagonalise the tridiagonal Hamiltonian in the Lanczos basis. It can thus be used in combination with a matrix-product state (MPS) solver which is here the main motivation of considering it.

Using the Band Lanczos algorithm allows resolving degenerate or clustered eigenvalues. Constructing a joint Krylov subspace of all excited states occuring in the electron/hole part of the Green's function makes it possible to separate weights from poles leading to the Q-matrix representation of the Green's function. In the context of VCA, this gives the advantage of performing the contour integration analytically.

Computing the Green's function as expansion of Chebyshev polynomials requires only the evaluation of a recursion relation. Since no basis is constructed, orthogonality does not have to be enforced. Furthermore no diagonalisations have to be performed. It thus provides an alternative representation of the Green's function to be employed with a MPS solver which avoids difficulties occuring for the continued fraction representation.

Following the case of zero temperature, finite temperature versions of the full diagonalisation, exact diagonalisation (Band) Lanczos and Chebyshev solver are presented. For the latter two types of solvers, traces with exact eigenvectors, with random vectors and a combination of both are discussed. Several details relevant for reducing the computation time, the entropy and specific heat as new observables, realising different reference systems and obtaining expectation values in the grand canonical ensemble are given.

Applying purely exact eigenvectors is straightforward but approximate in case of exact diagonalisation where only the dominant selection of states is incorporated. Employing only random vectors leads to the finite temperature Lanczos method (FTLM), where a trace over the complete basis is approximated via an average of random vectors. Increasing the system size or employing more random vectors improve this approximation. Expressions and error estimates used numerically are explicitely given. An improvement at low temperature by splitting the trace into a part with exact and random trace vectors is described. References to another FTLM implementation using a split trace and a typicality-based solver employing random phase vectors are given.

Employing MPSs makes it possible to consider larger systems but also requires more time to handle them. Among the representations of the Green's function given, the continued fraction and Chebyshev representations are argued to be the most promising for being constructed using MPS. A proof of principle for a MPS solver is given using the continued fraction representation. Issues arising due to loss of orthogonality are predicted to be overcome with the Chebyshev representation.

To test the implemented solvers, the one-band Hubbard model is considered. Analytical results on one-dimensional one and two site clusters serve to verify the implementation employing full diagonalisation. The basic implementation of FTLM-based solvers is verified by comparing their results on one-dimensional two and four site clusters with those of full diagonalisation. For all practical purposes considered during testing, the FTLM-based solvers give reliable results only at high temperatures as compared to the interesting temperature range where the antiferromagnetic (AFM) to paramagnetic (PM) phase transition occurs. Using traces with exact and random vectors makes it possible to reach lower temperatures. Comparing the results obtained using these split traces with literature confirm their implementation. Employing solely exact trace vectors turns out to be the most expedient option. The agreement between results of an exact diagonalisation solver with those of a Chebyshev solver, both using exact trace vectors, verify the implementation of the Chebyshev solver.

After the validity of the solvers is sufficiently attested, the full and exact diagonalisation solvers employing only exact trace vectors are used to investigate the PM to AFM phase transition in Sr_2IrO_4 which is accompanied by the opening of an insulating gap. While this transition results at low temperature in a spin-orbit coupling enabled Mott insulator, a topic of current interest is the influence of the magnetic order on the gap opening. Namely whether the gap opens due to electronic correlations with magnetic order as side effect (Mott-type insulator) or due to the magnetic order itself (Slater-type insulator). Since both mechanisms are not mutually exclusive, determining the origin of the transition is a delicate endeavour. Another, more academic question concerns the importance of nonlocal quantum fluctuations to capture the spectral features of magnetic fluctuations and how a lack of these fluctuations affects the Néel temperature.

The compound is modeled as a three-band Hubbard model with five electrons. Concerning the magnetic order at low temperature, its signatures in the spectrum and the responsible orbital are identified. Within VCA, a local self-energy omitting nonlocal quantum fluctuations turns out to be sufficient to qualitatively reproduce the spectra of the magnetically ordered systems. Yet such a treatment overestimates the magnetic orders stability and misses spectral features in the unoccupied states. In order to contribute to the discussion, whether the Mott- or Slater-type insulating mechanism dominates in Sr_2IrO_4, VCA does not allow for a definite conclusion and a cluster-dynamical-impurity approximation (CDIA) study should be attempted where the metallic phase can be parametrised explicitely. Since CDIA amounts to VCA where the hybridisation with added bath sites is optimised, the VCA results presented provide a starting point for the CDIA computations.

In contrast to the previous compound, in Ca_2RuO_4 the AFM to PM and insulator to metal transitions are separated by a significant temperature range. However the question addressed here is, if there occurs an additional phase transition in between from an orbitally ordered to a disordered phase. Recent experimental evidence discards the option of real order, but leaves open the possibility of complex phase relations in the $(\mathrm{yz}, \mathrm{xz})$-subspace. From a more general perspective, this investigation is a follow up of a VCA study at zero temperature which addressed the question whether Ca_2RuO_4 or a similar material with different spin-orbit coupling and crystal field splitting is better described as an excitonic or a spin-one magnet.

The compound is modeled as a three-band Hubbard model with four electrons. Using VCA, spin-orbit coupling is found to destabilize the magnetic order. However it seemingly does not affect the Néel temperature which is most likely a finite-size effect. With increasing temperature, the capability of spin-orbit coupling to mix different orbitals becomes less effective. Combined with signatures of orbital fluctuations and the absence of real orbital order, this suggests fluctuations in the phase between the orbital components, which is no longer fixed by spin-orbit coupling as the origin of these orbital fluctuations.

Motivated by a VCA study at zero temperature and a FTLM study at finite temperature, the half-filled Kondo lattice model is investigated with finite temperature VCA. Considering the AFM magnetisation, the AFM and PM specific heat as well as the on-site spin-spin correlator allows constructing a phase diagram. The characteristic temperatures lead to three phases: an AFM, a PM of Kondo singlets and a thermal PM. Looking at the density of states and the spectral function provides information on the fate of the Kondo singlets with increasing temperature as well as their signatures compared to the thermal PM.

Inhaltsangabe

Anhand der Beschreibung der Thermodynamik und Dynamik geordneter Systeme bei endlicher Temperatur können die Signaturen verschiedener Phasen sowie Übergänge zwischen denselben erfasst werden. Systeme stark korrelierter Elektronen welche sich in mehreren Orbitalen befinden und bei denen Spin-Bahn Kopplung von Bedeutung ist, können exotische Phasen aufweisen. Die Modellierung solcher Systeme und Bestimmung ihrer Eigenschaften über den gesamten Temperaturbereich stellt eine nicht-triviale Aufgabe dar. In dieser Arbeit wird die Implementation mehrerer Cluster-Solver für die Variationelle Cluster Approximation (VCA) bei endlichen Temperaturen beschrieben, da diese Methode in der Lage ist die genannten Systeme zu modellieren und zudem lokale Quantenfluktuationen berücksichtigt. Der verlässlichste, hinreichend getestetste und performanteste Solver wird anschließend dazu verwendet den Magnetismus und die Orbitalphysik von Sr_2IrO_4 und Ca_2RuO_4, beschrieben durch Drei-Band Hubbard Modelle, sowie das halb-gefüllte Kondo Gittermodell zu untersuchen.

Beginnend beim absoluten Temperaturnullpunkt werden drei Cluster-Solver und vier Darstellungen der Greenschen Funktion präsentiert, welche in VCA Anwendung finden. Jede der Darstellungen besitzt Vorteile, je nachdem welcher Solver verwendet wird.

Der Lanczos Algorithmus konstruiert iterativ einen invarianten Unterraum des Hamiltonoperators in welchem dieser die Form einer Tridiagonalmatrix annimmt. Indem die Eigenwerte und Eigenvektoren bestimmt werden, lässt sich die Spektraldarstellung der Greenschen Funktion konstruieren. Inversion der Tridiagonalmatrix ergibt die Kettenbruchdarstellung der Greenschen Funktion. Diese Darstellung setzt also keine Diagonalisierung des Hamiltonoperators voraus und kann daher in Kombination mit einem Solver welcher Matrix-Produkt Zustände (MPSs) nutzt verwendet werden.

Mit dem Band Lanczos Algorithmus können entartete oder geclusterte Eigenwerte aufgelöst werden. Indem mit allen angeregten Zuständen welche im Elektronen-/Lochteil der Greenschen Funktion auftauchen ein gemeinsamer Krylov Unterraum konstruiert wird, können die Gewichte von den Polen getrennt werden, was zur Q-Matrixdarstellung der Greenschen Funktion führt. Sie erlaubt es die auftretende Konturintegration analytisch zu berechnen.

Um die Greensche Funktion in Chebyshev-Polynomen zu entwickeln muss nur eine Rekursionsformel ausgewertet werden. Da hierbei keine Basis konstruiert wird, muss keine Orthogonalität zwischen Vektoren zugesichert werden. Außerdem muss der Hamiltonoperator nicht diagonalisiert werden. Die Chebyshev-Darstellung kann daher ebenfalls in Kombination mit einem Solver, welcher MPSs nutzt, verwendet werden.

Für endliche Temperaturen werden volle Diagonalisierungs-, exakte Diagonalisierungs- und Chebyshev-Solver vorgestellt. Bei den beiden letzten Arten von Solvern werden Spuren mit exakten Eigenvektoren, Zufallsvektoren und einer Kombination aus beidem diskutiert. Diverse Details zur Reduktion der Laufzeit, neuen Observablen, der Realisierung verschiedener Referenzsysteme und zur Bestimmung von Erwartungswerten im großkanonischen Ensemble werden genannt.

Am Naheliegendsten ist die Verwendung exakter Eigenvektoren, welche im Fall exakter Diagonalisierung aber die Näherung beinhaltet nur eine Auswahl an dominante Zuständen zu berücksichtigen. Werden nur Zufallsvektoren verwendet, so handelt es sich um die Hochtemperatur-Lanczos Methode (FTLM), bei welcher die Spur über eine vollständige Basis durch einen Mittelwert über Zufallsvektoren angenähert wird. Die Näherung kann verbessert werden, indem das untersuchte System vergrößert oder mehr Zufallsvektoren hinzugenommen werden. In der Numerik genutzte Ausdrücke und Fehlerabschätzungen werden explizit angegeben. Eine Aufteilung der Spur in einen Anteil exakter Eigenvektoren und Zufallsvektoren, welche die Ergebnisse bei niedrigen Temperaturen verbessert, wird beschrieben. Verweise auf eine weitere FTLM Implementation mit aufgeteilter Spur und einen typicality-basierten Solver, welcher komplexe, zufällige Phasenvektoren verwendet, werden angegeben.

Die Verwendung von MPSs erlaubt es größere Systeme zu betrachten, was allerdings auch mehr Rechenzeit in Anspruch nimmt. Es wird argumentiert, dass unter den verschiedenen Darstellungen der Greenschen Funktion die Kettenbruch- und Chebyshev-Darstellung am vielversprechendsten sind um sie mit einem Solver welcher MPSs verwendet zu konstruieren. Ein Machbarkeitsbeweis für einen Cluster-Solver welcher MPSs nutzt wird mit der Kettenbruchdarstellung gegeben. Komplikationen welche aufgrund des Verlusts der Orthogonalität auftreten, sollten mit der Chebyshev-Darstellung überwunden werden können.

Das Ein-Band Hubbard Modell dient als Testmodell für die implementierten Solver. Analytische Ergebnisse auf eindimensionalen Clustern mit einem und zwei Plätzen dienen dazu die volle Diagonalisierung als Solver zu verifizieren. Die grundlegende Implementation der FTLM-basierten Solver wird durch Vergleich mit Ergebnissen welche über volle Diagonalisierung für eindimensionale Cluster mit zwei und vier Plätzen erhalten wird, verifiziert. Für alle untersuchten Fälle ergeben die FTLM-basierten Solver allerdings nur bei hohen Temperaturen abseits des interessanten Temperaturbereichs in welchem der Phasenübergang vom Antiferromagneten (AFM) zum Paramagneten (PM) liegt zuverlässige Ergebnisse. Indem sowohl exakte als auch Zufallsvektoren verwendet werden, können tiefere Temperaturen erreicht werden. Ein Vergleich der Ergebnisse, welche mit aufgeteilter Spur erhalten werden, mit der Literatur bestätigt die Implementation. Allerdings ist die reine Verwendung von exakten Spurvektoren am zielführendsten. Für den Fall exakter Spurvektoren wird der Chebyshev-Solver durch Vergleich mit Ergebnissen die mittels exakter Diagonalisierung erhalten werden bestätigt.

Nachdem die Funktionsweise aller Solver hinreichend bestätigt ist, werden die Solver für volle und exakte Diagonalisierung ausschließlich mit exakten Spurvektoren genutzt. Zunächst wird der Übergang vom PM zum AFM in Sr_2IrO_4 untersucht, welcher von der Öffnung einer isolierenden Bandlücke begleitet ist. Dieser Übergang mündet bei niedriger Temperatur in einem durch Spin-Bahn Kopplung induzierten Mott Isolator. Von aktuellem Interesse ist allerdings der Einfluss der magnetischen Ordnung auf die Öffnung der Bandlücke: öffnet sich die Bandlücke aufgrund der elektronischen Korrelationen mit der magnetischen Ordnung als Nebeneffekt (Mott Isolator) oder aufgrund der magnetischen Ordnung selbst (Slater Isolator)? Da sich beide Mechanismen nicht gegenseitig ausschließen handelt es sich bei der Bestimmung des Ursprungs vom Übergang um eine delikate Angelegenheit. Eine weitere, eher akademische Frage betrifft die Bedeutung nicht-lokaler Quantenfluktuationen für Signaturen magnetischer Fluktuationen in der Spektralfunktion sowie für die Néel Temperatur.

Die Verbindung wird als Drei-Band Hubbard Modell mit fünf Elektronen modelliert. Die magnetischen Signaturen im Spektrum und die Orbitale welche das magnetische Moment zur Verfügung stellen, werden identifiziert. Mit VCA genügt eine lokale Selbstenergie, welche nicht-lokale Quantenfluktuationen vernachlässigt, um qualitativ die Spektren magnetisch geordneter Systeme zu reproduzieren. Allerdings wird dabei die Stabilität der magnetischen Ordnung überschätzt und Signaturen in den unbesetzten Zuständen fehlen. Um zur Diskussion beizutragen, ob in Sr_2IrO_4 der Mott- oder Slater-artige Mechanismus dominiert welcher das System isolierend macht, reicht VCA nicht aus um eine eindeutige Schlussfolgerungen zu ziehen und eine Untersuchung mittels der Clustervariante der Dynamischen Störstellen Approximation (CDIA) sollte angestrebt werden innerhalb welcher die metallische Phase parametrisiert werden kann. Da CDIA eine Variante von VCA ist, bei welcher die Hybridisierung mit Badplätzen optimiert wird, stellen die präsentierten VCA Ergebnisse einen sinnvollen Startpunkt für CDIA Rechnungen dar.

Im Gegensatz zur vorherigen Verbindung liegen die Übergänge vom AFM zum PM und vom Isolator zum Metall in Ca_2RuO_4 bei signifikant unterschiedlichen Temperaturen. Hier stellt sich die Frage, ob ein weiterer Übergang von einer orbital-geordneten zu einer ungeordneten Phase stattfindet. Aktuelle experimentelle Erkenntnisse verwerfen eine reelle Ordnung, lassen aber eine komplexen Phasenbeziehung im (yz, xz)-Unterraum zu. Von einem allgemeineren Standpunkt aus betrachtet handelt es sich um die Folgeuntersuchung einer VCA Studie beim absoluten Temperaturnullpunkt. In dieser wurde der Frage nachgegangen, ob Ca_2RuO_4 oder eine ähnliche Verbindung mit unterschiedlicher Spin-Bahn Kopplung und Kristallfeldaufspaltung besser als exzitonischer oder Spin-eins Magnet beschrieben wird.

Die Verbindung wird als Drei-Band Hubbard Modell mit vier Elektronen modelliert. Die mit VCA erhaltenen Ergebnisse implizieren, dass Spin-Bahn Kopplung die magnetische Ordnung destabilisiert. Scheinbar betrifft dies nicht die Néel Temperatur, wobei es sich vermutlich um einen finite-size Effekt handelt. Mit zunehmender Temperatur nimmt die Wirkung von Spin-Bahn Kopplung, unterschiedliche Orbitale zu koppeln, ab. In Kombination mit Signaturen von Orbitalfluktuationen und der Abwesenheit reeller Orbitalordnung suggeriert dies Phasenfluktuationen zwischen den verschiedenen Orbitalkomponenten, welche nicht mehr durch Spin-Bahn Kopplung fixiert sind und als Ursprung der Orbitalfluktuationen angesehen werden können.

Motiviert durch eine VCA Studie beim absoluten Temperaturnullpunkt und einer FTLM Studie bei endlicher Temperatur wird das Kondo Gittermodell bei halber Füllung mit VCA bei endlicher Temperatur untersucht. Anhand der AFM Magnetisierung, der AFM und PM spezifischen Wärmekapazität sowie des lokalen Spin-Spin Korrelators kann ein Phasendiagramm konstruiert werden. Die charakteristischen Temperaturen führen zu drei Phasen: ein AFM, ein PM aus Kondo Singuletts und ein thermischer PM. Die Zustandsdichte und Spektralfunktion erlauben Rückschlüsse auf das Schicksal der Kondo Singuletts mit steigender Temperatur und ihre Signaturen in Abgrenzung zum thermischen PM.

Contents

Abstract/Inhaltsangabe **iii**

1. Introduction **1**
1.1. Motivation . . . 1
1.2. Structure . . . 2

2. Fundamentals **4**
2.1. Mathematical prerequisites . . . 4
2.1.1. Second quantisation . . . 4
2.1.2. Quantum statistics . . . 7
2.1.3. Green's functions . . . 8
2.1.4. Diagrammatic perturbation theory . . . 13
2.1.5. Self-energy . . . 16
2.1.6. Connection between Ω and G . . . 18
2.1.7. Generalisation of the Luttinger-Ward functional . . . 21
2.2. Method . . . 22
2.2.1. Self-energy-functional theory (SFT) . . . 22
2.2.2. Cluster perturbation theory (CPT) . . . 24
2.2.3. Variational cluster approximation (VCA) . . . 27
2.3. Cluster solvers at zero temperature . . . 28
2.3.1. Lanczos algorithm . . . 28
2.3.2. Continued fraction representation . . . 31
2.3.3. Band Lanczos algorithm . . . 32
2.3.4. Chebyshev expansion . . . 35
2.3.5. Brute-force numerical integration . . . 41
2.3.6. Q-matrix representation & Semi-analytical treatment . . . 43
2.4. Cluster solvers at finite temperature . . . 45
2.4.1. FD and ED . . . 45
2.4.2. Finite temperature Lanczos method (FTLM) . . . 49
2.4.3. Chebyshev expansion . . . 53
2.4.4. High-frequency expansion . . . 53
2.4.5. Entropy . . . 55
2.4.6. Cluster-dynamical-impurity approximation (CDIA) . . . 58
2.4.7. Setting the filling . . . 59

3. Matrix-product state solver for VCA **60**

4. One-band Hubbard model: Testing ground 62
- 4.1. FD, ED and FTLM . . . 62
  - 4.1.1. Hubbard atom . . . 62
  - 4.1.2. Two site Hubbard cluster . . . 66
  - 4.1.3. Four site Hubbard cluster . . . 68
  - 4.1.4. Comparison to solvers in literature . . . 74
- 4.2. Chebyshev expansion . . . 81
- 4.3. Conclusion . . . 82

5. Three-band Hubbard model: Physical application 83
- 5.1. d^5 configuration: Sr_2IrO_4 . . . 83
  - 5.1.1. Hamiltonian, basis and orders . . . 85
  - 5.1.2. 2×1 site cluster . . . 88
  - 5.1.3. 1 site cluster . . . 92
  - 5.1.4. 2×1 site cluster with local self-energy . . . 93
  - 5.1.5. 2×2 site cluster . . . 95
  - 5.1.6. Néel temperature . . . 98
  - 5.1.7. Conclusion and Outlook . . . 99
- 5.2. d^4 configuration: Ca_2RuO_4 . . . 101
  - 5.2.1. Hamiltonian, observables and orders . . . 102
  - 5.2.2. Zero tetragonal CF splitting . . . 104
  - 5.2.3. Dominant tetragonal CF splitting . . . 111
  - 5.2.4. Realistic tetragonal CF splitting . . . 113
  - 5.2.5. 1 site cluster . . . 120
  - 5.2.6. Conclusion and Outlook . . . 123

6. Kondo lattice model 125
- 6.1. Hamiltonian, observables and orders . . . 128
- 6.2. Comparisons at zero temperature . . . 129
- 6.3. Finite temperature . . . 131
- 6.4. Doped paramagnet . . . 137
- 6.5. Conclusion and Outlook . . . 137

7. Conclusion and Outlook 139

A. Mixed ensemble 142

B. High- and low-temperature limits 143

C. Finite temperature expectation values 145

D. Parallelisation 147
- D.1. Improved IO . . . 147
- D.2. Debatable implementation choices . . . 148

Zusammenfassung 150

Acknowledgements 153

Bibliography 158

List of Abbreviations

Methods and Models

CDIA	Cluster-dynamical-impurity approximation
CDMFT	Cluster dynamical mean-field theory
CPT	Cluster perturbation theory
DFT	Density functional theory
DIA	Dynamical impurity approximation
DMFT	Dynamical mean-field theory
ED	Exact diagonalisation
FD	Full diagonalisation
KLM	Kondo lattice model
KPM	Kernel polynomial method
KS	Kondo singlet
QMC	Quantum Monte Carlo
RKKY	Ruderman, Kittel, Kasuya and Yosida
SFT	Self-energy functional theory
VCA	Variational cluster approximation

Parameters and Observables

CF	Crystal field
DOS	Density of states
SOC	Spin-orbit coupling

Phases

AFM	Antiferromagnet
CAFM	Cubic harmonics antiferromagnetic
CFM	Cubic harmonics ferromagnetic
KAFM	Kramers antiferromagnetic
KFM	Kramers ferromagnetic
PM	Paramagnet

Text

i.e.	that means (latin: id est)
s.t.	such that
w.r.t.	with respect to

1 Introduction

1.1 Motivation

At zero temperature, the ground state determines the static properties of a system and only excitations give information on other energy levels, provided these can be reached within the excitation process. In real experiments, zero temperature is never reached and depending on the system investigated, further states matter. Upon increasing the temperature, more states become significant and can thus change the character of the system.

Strongly correlated electron systems with several active orbitals are specified by their spin, orbital and charge degrees of freedom. Different energy scales freezing these degrees of freedom in place and stabilising various types of order determine the temperatures, where the degrees of freedom are activated and orders are destroyed. At low temperature, an antiferromagnetic groundstate may dominate, whose magnetic moment is provided by only one orbital and whose charge is fixed. Raising the temperature may introduce non-magnetic states of similar orbital structure which transforms the system into a paramagnet but keeps some degree of orbital polarisation. At even higher temperatures, other orbitals can become significant and allow for charge fluctuations. Once the temperature bridges a previously insulating gap, metallic behaviour can emerge.

In summary, temperature provides an experimentally well accessible turning knob which allows dialing through the various energy scales present in a system. As a measure of energy fluctuations, the specific heat permits detection of phase transitions as divergencies and can provide hints at the presence of spin, orbital or charge excitations. Deducing the entropy from the measured specific heat at low temperature can give information on the degree of freedom, since it amounts to the degeneracy of the states at zero temperature. Since real materials have in addition the lattice as degree of freedom, features visible in theoretical models of strongly correlated electron systems may be hidden in real measurements.

In this thesis, the implementation details of several cluster solvers used for the variational cluster approximation (VCA) at finite temperature are described. The most reliable, sufficiently benchmarked and best performing solver among them is then used to investigate the magnetic and orbital properties of Sr_2IrO_4 and Ca_2RuO_4 described by three-band Hubbard models, as well as the Kondo model at half-filling.

A simple numerical experiment is performed for each system investigated: The magnetically ordered system at low temperature is heated up, until the magnetisation vanishes at the transition temperature. Besides the transition temperature where the order parameter vanishes, observing this evolution permits detecting features of the magnetic order in the specific heat, the density of states or the spectral function. Combined with sweeping an interaction parameter, the competition of thermal and nonlocal quantum fluctuations determine the location of phase boundaries. An example for this occurs in the Kondo lattice model, where the transition temperature from a paramagnet of local Kondo singlets to the thermal paramagnet changes depending on the singlet stability. Or in case of Ca_2RuO_4, where the capability of spin-orbit coupling to mix different orbitals visible in the spectral function depletes with increasing temperature.

Allowing for temporal fluctuations, the transition from an insulating to a metallic phase could be considered. This way, the question whether Sr_2IrO_4 is more of a correlation- or magnetism-driven insulator could be addressed.

Besides merely describing systems at finite temperature via VCA, using finite temperature also extends the capabilities of the method itself. Since the VCA is a cluster meanfield type of method, it is more or less restricted to make statements about orders specifically investigated. In this context, the specific heat allows detection of prominent fluctuations without having to enforce an order. The presence of the respective degrees of freedom in the model is sufficient. This way, a peak in the specific heat can indicate orbital fluctuations, while an orbital order as possible origin does not have to be formulated, as is found for Ca_2RuO_4.

In summary, investigating systems at finite temperatures with VCA provides benefits for both, the scope of the description as well as the capabilities of the method. While the method provides access to thermodynamic and dynamic observables of the systems at finite temperature, finite temperature provides the method with a way to quantify precursors of order.

1 2 Structure

This thesis contains five main chapters besides the introduction.

In chapter 2, the mathematical prerequisites for the VCA are presented. After recapitulating the basics of second quantisation and quantum statistics, the properties of Green's functions in many-body physics are discussed. Subsequently, the main steps in diagrammatic perturbation theory to obtain the Green's function and the grand potential are sketched. Introducing afterwards the self-energy and the connection between grand potential and Green's function refines this sketch. Thereby also the fundamental relation of self-energy functional theory is obtained, which can be seen from another perspective as the definition of the Luttinger-Ward functional. However to be of use, this functional is condensed to its basic properties and generalised afterwards.

Next, the fundamentals of the method employed are discussed. After the self-energy functional theory is presented as framework to construct cluster-approximations, the determination of quantities required in the VCA as one branch of approximations is shown. This comprises the relations of cluster perturbation theory (CPT) on the analytical side. Using the insights from all previous chapters, the algorithm followed in the VCA is given.

Following this overview, the background of the implemented cluster solvers is described. First, zero temperature solvers are considered since they provide the basis for their finite temperature counterparts. These comprise full diagonalisation, Lanczos and Band-Lanczos exact diagonalisation as well as a solver employing the recursion relations of Chebyshev polynomials. Their output can be used to construct one of four representations of the Green's function, the spectral, continued fraction, Q-matrix and Chebyshev representation.

At finite temperature, the full diagonalisation solver uses the trace of eigenvectors, while in case of exact diagonalisation and for the Chebyshev solver the trace can be approximated by random vectors. In the latter case, a combination of exact and random trace vectors can be used to improve the results at low temperature. Hence different combinations of the Lanczos and Band-Lanczos solver as well as the Chebyshev solver using either exact or random trace vectors or a combination of both are presented.

Some technical details on how to improve the performance by using a high-frequency expansion, the computation of the entropy within VCA, the reference system of the cluster-dynamical-impurity approximation and the realisation of different fillings are described.

As a first application, a cluster solver employing matrix-product states is used in chapter 3 to construct the continued fraction representation for one-dimensional Hubbard clusters of different size at zero temperature. This merely serves as a proof of principle.

Afterwards in chapter 4, the different finite temperature cluster solvers are tested and compared using the one-band Hubbard model.

Then, the thermodynamic and dynamic properties of Sr_2IrO_4 and Ca_2RuO_4 are determined by applying finite temperature VCA to three-band Hubbard models in chapter 5. Finally, the half-filled Kondo lattice model is considered in chapter 6.

2 Fundamentals

The method employed in this thesis is based on an expression for the static grand potential in terms of the dynamic Matsubara function. In order to motivate its shape, some basics are reviewed and the derivation is sketched. The presentation follows the one given in the authors master thesis [Lot17]. Afterwards, several solvers implemented and used at zero and finite temperature are presented. Some technical details to improve performance, the entropy as newly accessible observable and the inclusion of bath sites are discussed. Further details on post-processing and interpreting the data are contained in appendix A.

2 1 Mathematical prerequisites

2 1 1 Second quantisation

Within second quantisation, the permutation properties of physical many-body wavefunctions are transferred to construction operators with corresponding (anti-)commutation relations. The advantage of the formalism over wavefunction based approaches is the clarity and simplicity of expressions. The presentation follows [Nol14].

Consider an N-particle system described by a Hamiltonian H. Then the Hilbert space $\mathscr{H}_N$ of the system is given by the direct product of all single-particle Hilbert spaces $\left\{\mathscr{H}_1^{(i)}\right\}_{i=1\ldots N}$,

$$\mathscr{H}_N = \bigotimes_{i=1}^{N} \mathscr{H}_1^{(i)}. \tag{2.1}$$

Each single-particle Hilbert space is spanned by an orthonormal basis of states $\{|\varphi_\alpha\rangle\}$ with α being a multi-index comprising the quantum numbers characterising the basis state. For simplicity it is assumed that the basis is denumerable. The case of continuous α can be inferred from [Nol14]. Therefore, the basis states are:

- orthogonal: $\langle\varphi_\alpha|\varphi_\beta\rangle = \delta_{\alpha\beta}$,
- complete: $\sum\limits_\alpha |\varphi_\alpha\rangle\langle\varphi_\alpha| = \mathbb{1}_{\mathscr{H}_1}$.

Representations often used for the single-particle states are the real- and reciprocal-space representations. N-particle states are denoted by

$$\left|\varphi_{\alpha_1}^{(1)}\varphi_{\alpha_2}^{(2)}\ldots\varphi_{\alpha_N}^{(N)}\right\rangle = \left|\varphi_{\alpha_1}^{(1)}\right\rangle\left|\varphi_{\alpha_2}^{(2)}\right\rangle\ldots\left|\varphi_{\alpha_N}^{(N)}\right\rangle = \bigotimes_{i=1}^{N}\left|\varphi_{\alpha_i}^{(i)}\right\rangle. \tag{2.2}$$

As mentioned in the outline, the physical many-body states have certain permutation properties and form only a subset of all available states in $\mathscr{H}_N$. For systems in a physical state, measurable quantities $\langle A\rangle$ may not differ if two identical particles i, j switch their single-particle states $|\varphi_{\alpha_i}\rangle$, $|\varphi_{\alpha_j}\rangle$, meaning

$$\left\langle\ldots\varphi_{\alpha_i}^{(i)}\ldots\varphi_{\alpha_j}^{(j)}\ldots\middle|A\middle|\ldots\varphi_{\alpha_i}^{(i)}\ldots\varphi_{\alpha_j}^{(j)}\ldots\right\rangle \overset{!}{=} \left\langle\ldots\varphi_{\alpha_i}^{(j)}\ldots\varphi_{\alpha_j}^{(i)}\ldots\middle|A\middle|\ldots\varphi_{\alpha_i}^{(j)}\ldots\varphi_{\alpha_j}^{(i)}\ldots\right\rangle. \tag{2.3}$$

This demand is formalised by introducing a permutation operator $\mathcal{P}$, which consists of p transpositions $\{T_i\}_{i=1\dots p}$ and acts as

$$\mathcal{P}\left|\varphi^{(1)}_{\alpha_1}\varphi^{(2)}_{\alpha_2}\dots\varphi^{(N)}_{\alpha_N}\right\rangle = \left|\varphi^{(i_1)}_{\alpha_1}\varphi^{(i_2)}_{\alpha_2}\dots\varphi^{(i_N)}_{\alpha_N}\right\rangle \tag{2.4}$$

onto a many-body state, where $\{i_1, i_2, \dots, i_N\}$ is a permutation of $\{1, 2, \dots, N\}$. One finds that $\mathcal{P}$

- is Hermitian in the subspace of physical many-body states: $\mathcal{P}^\dagger = \mathcal{P}$,
- commutes in the subspace of physical many-body states with physical observables: $[A, \mathcal{P}]_- = 0$,
- has the physical many-body states as eigenstates with eigenvalues $\lambda = (\pm 1)^p$.

By means of the spin-statistics theorem, physical many-body states which are odd/even under the exchange of two identical particles describe systems of half-integer/integer spin particles and are called fermions/bosons. Identifying fermions/bosons by the signature $\varepsilon = \mp 1$, the N-particle Hilbert-space of physical many-body states is denoted as $\mathscr{H}^{(\varepsilon)}_N$. The full Hilbert-spaces of arbitrary particle number are the direct product of all N-particle Hilbert-spaces,

$$\mathscr{H}^{(\varepsilon)} = \bigotimes_{N=0}^{\infty} \mathscr{H}^{(\varepsilon)}_N \subset \mathscr{H} = \bigotimes_{N=0}^{\infty} \mathscr{H}_N. \tag{2.5}$$

In order to construct the physical many-body states explicitely, an anti-symmetrisation/a symmetrisation operator $S_\varepsilon = c_\varepsilon \sum_{\mathcal{P}} \varepsilon^p \mathcal{P}$ is defined, where the constant c_ε is a normalisation factor. It converts many-body states into physical many-body states

$$S_\varepsilon \left|\varphi^{(1)}_{\alpha_1}\varphi^{(2)}_{\alpha_2}\dots\varphi^{(N)}_{\alpha_N}\right\rangle = \left|\varphi_{\alpha_1}\varphi_{\alpha_2}\dots\varphi_{\alpha_N}\right\rangle^{(\varepsilon)}. \tag{2.6}$$

Since the (anti-)symmetrisation operator constructs physical many-body states from arbitrary (physical or unphysical) many-body states, the order of the single-particle states within the arbitrary many-body state is unimportant. The normalisation factor merely compensates for overcounting of single-particle states and therefore depends only on the occupation of these states. Hence what matters is the occupation number n_{α_i} of each single-particle state $|\varphi_{\alpha_i}\rangle$. Therefore a more economical notation

$$\left|N; n_{\alpha_1} n_{\alpha_2} \dots n_{\alpha_N}\right\rangle^{(\varepsilon)} = \left|\varphi_{\alpha_1}\varphi_{\alpha_2}\dots\varphi_{\alpha_N}\right\rangle^{(\varepsilon)} = S_\varepsilon\Bigg(\underbrace{\left|\varphi^{(1)}_{\alpha_1}\right\rangle\left|\varphi^{(2)}_{\alpha_1}\right\rangle\dots}_{n_{\alpha_1}} \quad \underbrace{\left|\varphi^{(p)}_{\alpha_i}\right\rangle\left|\varphi^{(p+1)}_{\alpha_i}\right\rangle\dots}_{n_{\alpha_i}}\Bigg) \tag{2.7}$$

with $N = \sum_i n_{\alpha_i}$ as the total number of particles is used. Demanding normalised states, the constant is

$$c_\varepsilon = \frac{1}{\sqrt{N!}} \cdot \frac{1}{\sqrt{\prod_i (n_{\alpha_i}!)}}, \tag{2.8}$$

where $n_{\alpha_i} \in \{0, 1\}$ for fermions and $n_{\alpha_i} \in \mathbb{N}_0$ for bosons. For the physical many-body states again a basis exists, whose states are:

- orthogonal: $^{(\varepsilon)}\!\left\langle N; n_{\alpha_1} n_{\alpha_2} \dots n_{\alpha_N} \middle| N'; n'_{\alpha_1} n'_{\alpha_2} \dots n'_{\alpha_N}\right\rangle^{(\varepsilon)} = \delta_{NN'} \prod_i \delta_{n_{\alpha_i} n'_{\alpha_i}}$,
- complete: $\sum_{n_{\alpha_1}} \sum_{n_{\alpha_2}} \dots \left|N; n_{\alpha_1} n_{\alpha_2} \dots\right\rangle^{(\varepsilon)\,(\varepsilon)}\!\left\langle N; n_{\alpha_1} n_{\alpha_2} \dots\right| = \mathbb{1}_{\mathscr{H}^{(\varepsilon)}}$.

Coming to the aforementioned operators, the creation operator $c^\dagger_{\alpha_i}$ adding a particle in state $|\varphi_{\alpha_i}\rangle$ is defined by its action onto a physical many-body state

$$\begin{aligned} c^\dagger_{\alpha_i}\left|N; n_{\alpha_1} n_{\alpha_2} \dots n_{\alpha_i} \dots\right\rangle^{(\varepsilon)} &= c^\dagger_{\alpha_i}\left|\varphi_{\alpha_1}\varphi_{\alpha_2}\dots\varphi_{\alpha_N}\right\rangle^{(\varepsilon)} \\ &\equiv \sqrt{n_{\alpha_i}+1}\left|\varphi_{\alpha_i}\varphi_{\alpha_1}\varphi_{\alpha_2}\dots\varphi_{\alpha_N}\right\rangle^{(\varepsilon)} \\ &= \varepsilon^{N_{\alpha_i}}\sqrt{n_{\alpha_i}+1}\left|N+1; n_{\alpha_1} n_{\alpha_2}\dots(n_{\alpha_i}+1)\dots\right\rangle^{(\varepsilon)}, \end{aligned} \tag{2.9}$$

with $N_{\alpha_i} = \sum_{j=1}^{i-1} n_{\alpha_j}$. Its adjoint operator denoted as annihilation operator c_{α_i} removing a particle in state $|\varphi_{\alpha_i}\rangle$ is defined as

$$c_{\alpha_i}\left|N; n_{\alpha_1} n_{\alpha_2} \dots n_{\alpha_i} \dots\right\rangle^{(\varepsilon)} \equiv \varepsilon^{N_{\alpha_i}}\sqrt{n_{\alpha_i}}\left|N-1; n_{\alpha_1} n_{\alpha_2}\dots(n_{\alpha_i}-1)\dots\right\rangle^{(\varepsilon)}. \tag{2.10}$$

In the following, creation and annihilation operator are jointly denoted as construction operators. Combining the action of both operators onto an arbitrary physical many-body state gives the (anti-) commutation relations

$$\left[c_\alpha, c^\dagger_\beta\right]_{-\varepsilon} = \delta_{\alpha\beta}, \tag{2.11}$$

$$\left[c_\alpha, c_\beta\right]_{-\varepsilon} = 0, \tag{2.12}$$

$$\left[c^\dagger_\alpha, c^\dagger_\beta\right]_{-\varepsilon} = 0. \tag{2.13}$$

Employing the basis of physical many-body states allows rewriting physical observables A consisting of a one- and two-body part as

$$\begin{aligned} A &= \sum_{i=1}^{N} A_1^{(i)} + \frac{1}{2}\sum_{i,j}^{i\neq j} A_2^{(i,j)} \\ &= \sum_{\alpha,\beta}\langle\varphi_\alpha|A_1\left|\varphi_\beta\right\rangle c^\dagger_\alpha c_\beta + \frac{1}{2}\sum_{\substack{\alpha,\beta,\\ \gamma,\delta}}\left\langle\varphi^{(1)}_\alpha\varphi^{(2)}_\beta\right|A_2\left|\varphi^{(1)}_\delta\varphi^{(2)}_\gamma\right\rangle c^\dagger_\alpha c^\dagger_\beta c_\gamma c_\delta. \end{aligned} \tag{2.14}$$

A generic, fermionic Hamiltonian with one- and two-body interactions takes the shape

$$H = \sum_{\alpha,\beta} t_{\alpha\beta} c^\dagger_\alpha c_\beta + \frac{1}{2}\sum_{\substack{\alpha,\beta,\\ \gamma,\delta}} v(\alpha\beta\delta\gamma) c^\dagger_\alpha c^\dagger_\beta c_\gamma c_\delta, \tag{2.15}$$

where $t_{\alpha\beta}$ incorporates the kinetic and potential energy of an electron in an external potential as well as $v(\alpha\beta\delta\gamma)$ contains the Coulomb-interaction

- $t_{\alpha\beta} = \left\langle\varphi_\alpha\right|\left(\frac{p^2}{2m} + V(\boldsymbol{r})\right)\left|\varphi_\beta\right\rangle$,
- $v(\alpha\beta\delta\gamma) = \frac{e^2}{4\pi\varepsilon_0}\left\langle\varphi^{(1)}_\alpha\varphi^{(2)}_\beta\right|\frac{1}{|\boldsymbol{r}^{(1)}-\boldsymbol{r}^{(2)}|}\left|\varphi^{(1)}_\delta\varphi^{(2)}_\gamma\right\rangle$.

Besides construction operators, the occupation number operator

$$n_\alpha = c^\dagger_\alpha c_\alpha \tag{2.16}$$

as well as the particle number operator

$$N = \sum_\alpha n_\alpha \tag{2.17}$$

frequently arise when employing second quantisation. Advantages of treating states and observables on the same footing are clearer and easily reducible expressions whose meaning can be inferred from the context of the calculations.

2.1.2 Quantum statistics

Quantum statistics covers the quantum mechanical description of many-particle systems with focus on their thermodynamic properties. The presentation follows [Sch06].

Since operators in second quantisation act on states by increasing/reducing the particle number, here only the grand canonical ensemble specified by the chemical potential μ, volume V and temperature T as independent state-variables is discussed. The density operator as quantum version of the classical probability density is

$$\varrho = \exp\left[-\beta(H-\mu N)\right]/\Xi \equiv \exp\left[-\beta\mathcal{H}\right]/\Xi, \tag{2.18}$$

where $\beta = 1/k_\mathrm{B}T$ is proportional to the inverse temperature and $\mathcal{H} = H - \mu N$. In analogy to the classical partition function, the quantum version is given by the trace

$$\Xi = \mathrm{tr}(\exp\left[-\beta\mathcal{H}\right]) \tag{2.19}$$

leading to the grand potential

$$\Omega = -\frac{1}{\beta}\ln(\Xi). \tag{2.20}$$

Dependent state-variables emerge from the first law of thermodynamics (including the presence of an external magnetic field B)

$$\mathrm{d}\Omega = -S\,\mathrm{d}T - p\,\mathrm{d}V - \langle N\rangle\,\mathrm{d}\mu - M\,\mathrm{d}B, \tag{2.21}$$

giving:

- entropy: $S = -\left(\frac{\partial\Omega}{\partial T}\right)_{\mu,V,B}$,
- pressure: $p = -\left(\frac{\partial\Omega}{\partial V}\right)_{\mu,T,B}$,
- particle number: $\langle N\rangle = -\left(\frac{\partial\Omega}{\partial\mu}\right)_{V,T,B}$,
- magnetic moment: $M = -\left(\frac{\partial\Omega}{\partial B}\right)_{\mu,V,T}$.

Expectation values of observables $\mathcal{O}$ can be obtained from the density operator ϱ via

$$\langle\mathcal{O}\rangle = \mathrm{tr}(\varrho\mathcal{O}), \tag{2.22}$$

which yields for instance the internal energy $U = \langle H\rangle$ or the free energy $F = \Omega + \mu\langle N\rangle$. Response properties may be found from their thermodynamic expressions:

- specific heat: $C_V = T\left(\frac{\partial S}{\partial T}\right)_V$,
- isothermal compressibility: $\kappa_T = \frac{V}{\langle N\rangle^2}\left(\frac{\partial\langle N\rangle}{\partial\mu}\right)_{T,V}$,
- magnetic susceptibility: $\chi = \frac{\mu_0}{V}\left(\frac{\partial M}{\partial B}\right)_{\mu,V,T}$.

2.1.3 Green's functions

Green's functions are known from mathematics as solutions to inhomogeneous differential equations with linear differential operator, delta-function as inhomogeneity and homogeneous boundary conditions. These defining properties imply the occurence of Green's functions in the linear response regime. The Green's function spectral (Lehmann) representation is connected to the spectral function, which contains information on the elementary excitations in the system described by the differential operator. The presentation follows [OPV16; Nol14; BF16].

Consider an inhomogeneous differential equation for a function $f(x)$,

$$\mathrm{D} f(x) = g(x), \tag{2.23}$$

where D is a linear differential operator, $g(x)$ the inhomogeneity and homogeneous boundary conditions $f(x=L)=0$ or $f'(x=L)=0$ are imposed. Then a solution to this differential equation is

$$f(x) = \int \mathrm{d}x' \, G\left(x,x'\right) g\left(x'\right), \tag{2.24}$$

with the Green's function $G(x,x')$ satisfying the inhomogeneous differential equation

$$\mathrm{D}\, G\left(x,x'\right) = \delta\left(x-x'\right), \tag{2.25}$$

where $\delta(x-x')$ is the delta-function. Interpreting $g(x)$ as 'input' and $f(x)$ as 'output', $G(x,x')$ takes the role of the response function in linear response theory. Focussing on time-dependent quantum mechanical problems, the inhomogeneous differential equation follows from reordering the Schrödinger equation into

$$\left[\mathrm{i}\frac{\partial}{\partial t} - H_0(\boldsymbol{r})\right]\Psi_0(\boldsymbol{r},t) = 0, \tag{2.26}$$

$$\left[\mathrm{i}\frac{\partial}{\partial t} - H(\boldsymbol{r})\right]\Psi(\boldsymbol{r},t) = 0, \tag{2.27}$$

where the Hamiltonian is split into a free and a perturbative part $H(\boldsymbol{r}) = H_0(\boldsymbol{r}) + H_1(\boldsymbol{r})$. Here and in the following, $\hbar = 1$ is chosen. Introducing the free and full Green's functions G_0, G satisfying the respective inhomogeneous differential equations

$$\left[\mathrm{i}\frac{\partial}{\partial t} - H_0(\boldsymbol{r})\right]G_0(\boldsymbol{r},t) = \delta\left(\boldsymbol{r}-\boldsymbol{r}'\right)\delta\left(t-t'\right), \tag{2.28}$$

$$\left[\mathrm{i}\frac{\partial}{\partial t} - H(\boldsymbol{r})\right]G(\boldsymbol{r},t) = \delta\left(\boldsymbol{r}-\boldsymbol{r}'\right)\delta\left(t-t'\right) \tag{2.29}$$

makes it possible to give several recursive solutions for the wavefunction

$$\Psi(\boldsymbol{r},t) = \Psi_0(\boldsymbol{r},t) + \int \mathrm{d}\boldsymbol{r}' \int \mathrm{d}t' \, G_0\left(\boldsymbol{r},\boldsymbol{r}';t,t'\right) H_1\left(\boldsymbol{r}'\right)\Psi\left(\boldsymbol{r}',t'\right), \tag{2.30}$$

$$\Psi(\boldsymbol{r},t) = \Psi_0(\boldsymbol{r},t) + \int \mathrm{d}\boldsymbol{r}' \int \mathrm{d}t' \, G\left(\boldsymbol{r},\boldsymbol{r}';t,t'\right) H_1\left(\boldsymbol{r}'\right)\Psi_0\left(\boldsymbol{r}',t'\right). \tag{2.31}$$

Considering the integrals in equations (2.30)–(2.31) as the action of an operator onto Ψ, Ψ_0, one can simplify the notation to

$$\Psi = \Psi_0 + G_0 H_1 \Psi, \tag{2.32}$$

$$\Psi = \Psi_0 + G H_1 \Psi_0. \tag{2.33}$$

Solving equation (2.32) by iteratively inserting the wavefunction Ψ on the right-hand side, one finds by comparison with equation (2.33) a Dyson equation for the Green's functions

$$G = G_0 + G_0 H_1 G. \tag{2.34}$$

The solution of the partial differential equation (2.29), yields

$$G\left(\boldsymbol{r}, \boldsymbol{r}'; t, t'\right) = -\mathrm{i}\Theta\left(t - t'\right)\left\langle \boldsymbol{r} \left| \exp\left[-\mathrm{i}H\left(t - t'\right)\right] \right| \boldsymbol{r}' \right\rangle, \tag{2.35}$$

which makes it possible to identify the Green's function as a propagator

$$\Psi(\boldsymbol{r}, t) = \int \mathrm{d}\boldsymbol{r}' \int \mathrm{d}t'\, G\left(\boldsymbol{r}, \boldsymbol{r}'; t, t'\right) \Psi\left(\boldsymbol{r}', t'\right). \tag{2.36}$$

In the many-body case, various more or less useful versions of the Green's function exist. The retarded, advanced and causal Green's functions G^{ret}_{AB}, G^{av}_{AB}, G^{c}_{AB} are

$$G^{\mathrm{ret}}_{AB}\left(t, t'\right) \equiv \langle\!\langle A(t); B(t') \rangle\!\rangle^{\mathrm{ret}} = -\mathrm{i}\Theta\left(t - t'\right)\left\langle \left[A(t), B(t')\right]_{-\varepsilon} \right\rangle, \tag{2.37}$$

$$G^{\mathrm{av}}_{AB}\left(t, t'\right) \equiv \langle\!\langle A(t); B(t') \rangle\!\rangle^{\mathrm{av}} = +\mathrm{i}\Theta\left(t' - t\right)\left\langle \left[A(t), B(t')\right]_{-\varepsilon} \right\rangle, \tag{2.38}$$

$$G^{\mathrm{c}}_{AB}\left(t, t'\right) \equiv \langle\!\langle A(t); B(t') \rangle\!\rangle^{\mathrm{c}} = -\mathrm{i}\left\langle \mathrm{T}_{\varepsilon}\left[A(t) B(t')\right] \right\rangle, \tag{2.39}$$

where the operators are given in their Heisenberg representation

$$A(t) = \exp(\mathrm{i}\mathcal{H}t) A \exp(-\mathrm{i}\mathcal{H}t) \tag{2.40}$$

and $[\cdot,\cdot]_{-\varepsilon}$ as well as $\mathrm{T}_{\varepsilon}(\ldots)$ are the:

- (anti-)commutator: $[A(t), B(t')]_{-\varepsilon} = A(t)B(t') - \varepsilon B(t')A(t)$,
- Wick time-ordering operator:
  $\mathrm{T}_{\varepsilon}[A(t)B(t')] = \Theta(t - t')A(t)B(t') + \varepsilon\Theta(t' - t)B(t')A(t)$.

All these Green's functions satisfy the same equation of motion

$$\mathrm{i}\frac{\partial}{\partial t} \langle\!\langle A(t); B(t') \rangle\!\rangle^{\alpha} = \delta\left(t - t'\right)\left\langle \left[A(t), B(t')\right]_{-\varepsilon} \right\rangle + \langle\!\langle [A, \mathcal{H}]_{-}(t); B(t') \rangle\!\rangle^{\alpha}, \tag{2.41}$$

but differ in their boundary conditions:

- $\langle\!\langle A(t); B(t') \rangle\!\rangle^{\mathrm{ret}} = 0$ for $t < t'$
- $\langle\!\langle A(t); B(t') \rangle\!\rangle^{\mathrm{av}} = 0$ for $t > t'$
- $\langle\!\langle A(t); B(t') \rangle\!\rangle^{\mathrm{c}} = \begin{cases} -\mathrm{i}\,\langle A(t - t')B(0) \rangle, & \text{for } t > t' \\ -\mathrm{i}\,\varepsilon\,\langle B(0)A(t - t') \rangle, & \text{for } t < t'. \end{cases}$

The equation of motion's shape gives its solutions the name 'Green's functions'. One way to determine the Green's functions is to solve the hierarchy of differential equations introduced by the higher Green's function $\langle\langle [A,\mathcal{H}]_-(t);B(t')\rangle\rangle^\alpha$ on the right-hand side of equation (2.41). As the boundary condition for the causal Green's function is rather complicated, its use in such a procedure is questionable. Its existence is justified, since the free single-particle causal Green's function at zero temperature $\langle\langle\, c_\alpha(t);c^\dagger_\beta(t')\,\rangle\rangle^{\mathrm{c}}$ happens to be the propagator in zero temperature diagrammatic perturbation theory.

For diagrammatic perturbation theory at finite temperature, the Matsubara function

$$G^{\mathrm{M}}_{AB}(\tau,\tau')\equiv\langle\langle A(\tau);B(\tau')\rangle\rangle^{\mathrm{M}}=-\left\langle \mathrm{T}_\tau\left[A(\tau)B(\tau')\right]\right\rangle \tag{2.42}$$

takes the role of the causal Green's function. Therein, the operators are written in the modified Heisenberg representation

$$A(\tau)=\exp(\mathcal{H}\tau)A\exp(-\mathcal{H}\tau)\,, \tag{2.43}$$

with the 'imaginary time' τ following from a Wick rotation as $t \rightarrow \tau=-\mathrm{i}\,t$ and T_τ as the:

- time-ordering operator:
$$\mathrm{T}_\tau\left[A(\tau)B(\tau')\right]=\Theta(\tau-\tau')A(\tau)B(\tau')+\varepsilon^p\Theta(\tau'-\tau)B(\tau')A(\tau),$$

where p denotes the number of transpositions required to reorder the construction operators in the second term such that they match the order of the first term. Concerning the modified Heisenberg representation, it is important to mention that the actions of propagating an operator in time and taking the adjoint of this operator do not commute

$$\left[\exp(\mathcal{H}\tau)A\exp(-\mathcal{H}\tau)\right]^\dagger=A(\tau)^\dagger\neq A^\dagger(\tau)=\left[\exp(\mathcal{H}\tau)A^\dagger\exp(-\mathcal{H}\tau)\right]. \tag{2.44}$$

In analogy to the regular Heisenberg representation, there exists an equation of motion for operators,

$$-\frac{\partial}{\partial\tau}A(\tau)=[A(\tau),\mathcal{H}]_- \tag{2.45}$$

called Bloch equation. Among the Matsubara functions for arbitrary operators $A(\tau)$, $B(\tau')$, the single-particle Matsubara function with $A(\tau)=c_\alpha(\tau)$ and $B(\tau')=c^\dagger_\beta(\tau')$,

$$G^{\mathrm{M}}_{\alpha\beta}(\tau,\tau')\equiv-\left\langle \mathrm{T}_\tau\left(c_\alpha(\tau)c^\dagger_\beta(\tau')\right)\right\rangle \text{ for } \tau\in\mathbb{R},-\beta<\tau<\beta=\frac{1}{k_{\mathrm{B}}T}, \tag{2.46}$$

is of major importance, since its non-interacting form turns out to be the propagator in diagrammatic perturbation theory at finite temperature. It is:

- in general discontinuous at $\tau=0$: $G^{\mathrm{M}}_{\alpha\beta}(0^+)-G^{\mathrm{M}}_{\alpha\beta}(0^-)=-\delta_{\alpha\beta}$,
- homogeneous for a Hamiltonian which is not explicitely time-dependent: $G^{\mathrm{M}}_{\alpha\beta}(\tau,\tau')=G^{\mathrm{M}}_{\alpha\beta}(\tau-\tau')$,
- periodic with period 2β: $G^{\mathrm{M}}_{\alpha\beta}(\tau+n\beta)=\varepsilon G^{\mathrm{M}}_{\alpha\beta}(\tau+(n-1)\beta)$ for $n\in\mathbb{Z}$, $\beta>\tau+n\beta>0$.

The last property allows expanding the Matsubara function as a Fourier series

$$G^{\mathrm{M}}_{\alpha\beta}(\tau)=\frac{1}{\beta}\sum_{n=-\infty}^{\infty}\exp(-\mathrm{i}\,E_n\tau)\,G^{\mathrm{M}}_{\alpha\beta}(E_n), \tag{2.47}$$

$$G^{\mathrm{M}}_{\alpha\beta}(E_n)=\int_{[0,\beta]}\mathrm{d}\,\tau\,G^{\mathrm{M}}_{\alpha\beta}(\tau)\exp(\mathrm{i}\,E_n\tau)\,, \tag{2.48}$$

where the Matsubara energies E_n are divided into:

- fermionic Matsubara energies: $E_n = (2n+1)\frac{\pi}{\beta}$,
- bosonic Matsubara energies: $E_n = 2n\frac{\pi}{\beta}$,

since other terms drop out due to the signature ε.

A useful expression for the Green's function is its energy representation in the basis of eigenstates of the Hamiltonian called 'spectral (Lehmann) representation'. For the retarded and advanced Green's function, as well as for the Matsubara function this coincides with the Hilbert transform of the spectral function. The spectral function is connected to the elementary excitations of the system described by the Hamiltonian. This connection can be motivated by considering several probing methods, such as:

- Photoemission spectroscopy: $Z = c_\alpha$,
- Inverse Photoemission spectroscopy: $Z = c_\alpha^\dagger$,
- Auger electron spectroscopy: $Z = c_\alpha c_\beta$,
- Appearance-potential spectroscopy: $Z = c_\alpha^\dagger c_\beta^\dagger$,

where Z is the transition operator describing the action of the process onto the system. In photoemission spectroscopy, the system looses one electron which is excited by an incident photon, whereas for inverse photoemission spectroscopy, an electron is added to the system giving rise to a photon. Auger electron spectroscopy and its complement, appearance-potential spectroscopy, add or remove two electrons. In order to determine the intensity spectrum measured within an experiment, it is considered as histogram of the probability for the process described by Z to happen:

- probability for a state $|\varepsilon_m\rangle$ to be occupied: $\exp(-\beta\varepsilon_m)/\Xi$
- probability for the process $|\varepsilon_m\rangle \xrightarrow{Z} |\varepsilon_n\rangle$ to occur: $|\langle\varepsilon_n|Z|\varepsilon_m\rangle|^2$
- restriction on the transferred energy: $E \overset{!}{=} \varepsilon_n - \varepsilon_m$

↪ intensity: $I_Z(E) = \Xi^{-1}\sum_{m,n}\exp(-\beta\varepsilon_m)|\langle\varepsilon_n|Z|\varepsilon_m\rangle|^2\delta[E-(\varepsilon_n-\varepsilon_m)]$

This expression of the intensity implies

$$I_Z(E) = \exp(\beta E) I_{Z^\dagger}(-E) \tag{2.49}$$

for the connection between a spectroscopic method and its complement. A quantity containing information on both spectra is the spectral function

$$S^{\pm}_{ZZ^\dagger}(E) \equiv I_{Z^\dagger}(E) \pm I_Z(-E), \tag{2.50}$$

whose connection to the Green's functions is revealed as its Fourier transform amounts to

$$S^{\pm}_{ZZ^\dagger}(t) = \frac{1}{2\pi}\left\langle\left[Z(t), Z^\dagger(0)\right]_\pm\right\rangle. \tag{2.51}$$

Performing a Wick rotation links the spectral function to the Matsubara function. In practice, the connection in energy-space is more useful. It emerges by considering the trace in the expectation value to run over the eigenstates of the Hamiltonian and via Fourier transformation from time to energy. Considering only fermions by employing the notation $S_{AB} = S^+_{AB}$ and

$$\begin{aligned} S^+_{AB} &= \Xi^{-1}\sum_{m,n}\exp(-\beta\varepsilon_m)\langle\varepsilon_m|A|\varepsilon_n\rangle\langle\varepsilon_n|B|\varepsilon_m\rangle\,\delta[E-(\varepsilon_n-\varepsilon_m)] \\ &+ \Xi^{-1}\sum_{m,n}\exp(-\beta\varepsilon_m)\langle\varepsilon_m|B|\varepsilon_n\rangle\langle\varepsilon_n|A|\varepsilon_m\rangle\,\delta[-E-(\varepsilon_n-\varepsilon_m)], \end{aligned} \tag{2.52}$$

the retarded and advanced Green's function are

$$G_{AB}^{\mathrm{ret,av}}(E) = \int_{\mathbb{R}} \mathrm{d}E' \, \frac{S_{AB}(E')}{E - E' \pm \mathrm{i}\,0^+}, \tag{2.53}$$

which allows determining the spectral function via

$$S_{AB}(E) = \mp \frac{1}{\pi} \operatorname{Im}[G_{AB}^{\mathrm{ret,av}}(E)] \text{ if } S_{AB}(E) \in \mathbb{R}, \tag{2.54}$$

using the Dirac identity

$$\frac{1}{x \pm \mathrm{i}\,0^+} = P\frac{1}{x} \mp \mathrm{i}\,\pi\delta(x), \tag{2.55}$$

where P denotes the principal value. This identity is nothing but the representation of the delta-function by a Cauchy-Lorentz distribution of vanishing width. The requirement of a real spectral function is fulfilled for the single-particle Green's functions with $A = c_\alpha$, $B = c_\beta^\dagger$. For the relation including the Matsubara function, the argument of the retarded and advanced Green's function lifted to the upper or lower complex plane has to be replaced by $\mathrm{i}\,E_n$ giving

$$G_{AB}^{\mathrm{M}}(E_n) = \int_{\mathbb{R}} \mathrm{d}E' \, \frac{S_{AB}(E')}{\mathrm{i}\,E_n - E'}. \tag{2.56}$$

Retarded and advanced Green's function are therefore extensions of the Matsubara function to the real axis. A more frequently used expression summarising retarded and advanced Green's as well as Matsubara function is

$$G_{AB}(z) = \sum_{m,n} \frac{\exp(-\beta\varepsilon_m)}{\Xi} \left[\frac{\langle \varepsilon_m | A | \varepsilon_n \rangle \langle \varepsilon_n | B | \varepsilon_m \rangle}{z - (\varepsilon_n - \varepsilon_m)} \right] + \sum_{m,n} \frac{\exp(-\beta\varepsilon_m)}{\Xi} \left[\frac{\langle \varepsilon_m | B | \varepsilon_n \rangle \langle \varepsilon_n | A | \varepsilon_m \rangle}{z + (\varepsilon_n - \varepsilon_m)} \right] \tag{2.57}$$

with z as placeholder for $E \pm \mathrm{i}\,0^+$ and $\mathrm{i}\,E_n$.

Additionally, correlation functions and expectation values can be expressed in terms of suitable spectral functions. For fermions, the spectral theorem states this connection as

$$\left\langle B\left(t'\right) A\left(t\right) \right\rangle = \int_{\mathbb{R}} \mathrm{d}E \, \frac{S_{AB}(E)}{\exp(\beta E) + 1} \exp\left[-\mathrm{i}\,E\left(t - t'\right)\right], \tag{2.58}$$

which occurs when the trace in the expectation value is chosen to run over the eigenstates of the Hamiltonian. Recognising the Fermi distribution

$$f(E) = \frac{1}{\exp(\beta E) + 1} \tag{2.59}$$

allows defining the spin-resolved quasiparticle density of states (DOS) through the single-particle spectral function via

$$\langle n_\sigma \rangle = \sum_\alpha f(E) S_{\alpha\alpha}(E) \tag{2.60}$$

as

$$\rho_\sigma = \sum_\alpha S_{\alpha\alpha}(E). \tag{2.61}$$

To obtain expectation values via the single-particle Matsubara function introduced in equation (2.46), it can be evaluated as

$$G_{\alpha\beta}^{\mathrm{M}}\left(0, 0^+\right) = \langle c_\beta^\dagger c_\alpha \rangle = \frac{1}{\beta} \sum_{n=-\infty}^{\infty} \exp\left(\mathrm{i}\,E_n 0^+\right) G_{\alpha\beta}^{\mathrm{M}}(E_n) \tag{2.62}$$

by using the Fourier series from equation (2.47).

2.1.4 Diagrammatic perturbation theory

Diagrammatic perturbation theory provides an approach to describe interacting many-body systems. The interaction part is considered as perturbation of the free system. Bearing this decomposition in mind, the equation of motion of the corresponding time-evolution operator can be solved iteratively. Exploiting the perturbative character of the interaction, the time-evolution operator is expanded in powers of the interaction. Simplifying the expressions using Wick's theorem paves the way for representing mathematical expressions with diagrams. These diagrams serve as mnemonic giving an overview of how to simplify expressions. The presentation follows [Pot98; Nol14].

Just along the line, where the generic Hamiltonian in equation (2.15) is split into one- and two-body parts, the free system H_0 is given by the one-body terms, whereas the two-body terms form the interaction part V

$$H_0 = \sum_{\alpha,\beta} t_{\alpha\beta} c^\dagger_\alpha c_\beta, \tag{2.63}$$

$$V = \frac{1}{2} \sum_{\substack{\alpha,\beta,\\ \gamma,\delta}} v(\alpha\beta\delta\gamma) c^\dagger_\alpha c^\dagger_\beta c_\gamma c_\delta. \tag{2.64}$$

Besides the modified Heisenberg representation introduced in section 2.1.3, there exists a modified interaction representation $A_\mathrm{I}(\tau) = \exp(\mathcal{H}_0\tau) A \exp(-\mathcal{H}_0\tau)$, where $\mathcal{H}_0$ is the Hamiltonian of the free system including the chemical potential term. This new representation is a manifestation of the Hamiltonians' decomposition and becomes necessary, since the interaction makes the Bloch equation (2.45) difficult to solve. Expressing an operator given in the Heisenberg representation by the operator in the interaction representation as

$$A(\tau) = S(0,\tau) A_\mathrm{I}(\tau) S(\tau,0), \tag{2.65}$$

defines the S-matrix

$$S\left(\tau,\tau'\right) = \exp[\mathcal{H}_0\tau] \exp\left[-\mathcal{H}\left(\tau-\tau'\right)\right] \exp\left[\mathcal{H}_0\tau'\right]. \tag{2.66}$$

In order to determine the S-matrix, the left-hand side of its Bloch equation is evaluated giving a first-order differential equation

$$-\frac{\partial}{\partial\tau} S\left(\tau,\tau'\right) = V_\mathrm{I}\left(\tau\right) S\left(\tau,\tau'\right). \tag{2.67}$$

Integrating this equation of motion with the boundary condition $S(\tau,\tau) = \mathbb{1}$ yields a recursive equation for the S-matrix, which is solved by iteratively inserting the S-matrix on the right-hand side thus leading to the von-Neumann series

$$S\left(\tau,\tau'\right) = \mathbb{1} + \sum_{n=1}^{\infty} (-1)^n \int_{[\tau',\tau]} \mathrm{d}\tau_1 \int_{[\tau',\tau_1]} \mathrm{d}\tau_2 \cdots \int_{[\tau',\tau_{n-1}]} \mathrm{d}\tau_n\, V_\mathrm{I}(\tau_1) V_\mathrm{I}(\tau_2) \ldots V_\mathrm{I}(\tau_n). \tag{2.68}$$

Since the operators in the integrand of equation (2.68) are ordered in time, the time-ordering operator T_τ is added as identity which acts on all time-dependent perturbations keeping them time-ordered. With T_τ in front, the perturbations $\{V_\mathrm{I}(\tau_i)\}_{i=1,\dots,n}$ can thus be considered commutative which makes it possible to fix the order of the operators while renaming the integration-variables. One can show by induction, that the volume of an n-cube can be expressed by the sum over all permutations of times of the successive integrations along each time axis with the first running from τ' to τ and the rest having as upper boundary the respectively previous integration variable

$$\int\limits_{[\tau',\tau]}\mathrm{d}\,\tau_1\int\limits_{[\tau',\tau]}\mathrm{d}\,\tau_2\cdots\int\limits_{[\tau',\tau]}\mathrm{d}\,\tau_n\,(\cdot)=\sum_{\pi\in S_n}\int\limits_{[\tau',\tau]}\mathrm{d}\,\tau_{\pi(1)}\int\limits_{[\tau',\tau_{\pi(1)}]}\mathrm{d}\,\tau_{\pi(2)}\cdots\int\limits_{[\tau',\tau_{\pi(n-1)}]}\mathrm{d}\,\tau_{\pi(n)}\,(\cdot), \tag{2.69}$$

where $(\cdot)$ represents the time-ordered integrand and $\pi(i)$ is the index of the previously i-th time obtained by permuting the indices $\{1,2,\dots,n\}$. Combined with the series expansion of the exponential function, this relation implies that the S-matrix can formally be written as a time-ordered exponential

$$S\left(\tau,\tau'\right)=\mathrm{T}_\tau\exp\left[-\int\limits_{[\tau',\tau]}\mathrm{d}\,\tau''\,V_\mathrm{I}(\tau'')\right]. \tag{2.70}$$

From now on, all operators are given in the interaction representation and the index ‘I’ is omitted. Various quantities can be rewritten in terms of the S-matrix, such as the:

- partition function: $\Xi=\Xi_0\,\langle S(\beta,0)\rangle^{(0)}$,
- single-particle Matsubara function: $G_{\alpha\beta}=-\frac{\Xi_0}{\Xi}\left\langle\mathrm{T}_\tau\left(S(\beta,0)c_\alpha(\tau)c^\dagger_\beta(0)\right)\right\rangle^{(0)}$,
- grand potential: $\Omega-\Omega_0=-\frac{1}{\beta}\ln\left(\frac{\Xi}{\Xi_0}\right)$,

where Ξ_0 is the partition function and $\langle\cdot\rangle^{(0)}$ the expectation value of the free system $\mathcal{H}_0$.

The formal expression of the S-matrix may appear elegant, but the exponential denotes in practice merely the series expansion. By expanding the series, the preliminary task becomes clear: calculating free expectation values of strings of time-ordered construction operators in their interaction representation. This is achieved by Wick’s theorem, which reduces the full expectation value to combinations of free single-particle Matsubara functions, where the expectation value in equation (2.46) is replaced by the free expectation value. Just as reminder, the free single-particle Matsubara function $G^{(0)}_{\alpha\beta}$ is obtained from its definition (2.46) by evaluating the free expectation values with the free Hamiltonian represented in the basis of Bloch states having a diagonal contribution from the one-body term. A proof of the theorem can be performed by via the equation of motion [SL13], by considering a generating functional [Col15] or by induction [Nol14]. In summary, applying Wick’s theorem allows expressing the partition function, the full single-particle Matsubara function or the grand potential in terms of the known free single-particle Matsubara function. The remaining task is to evaluate these contributions.

Although Wick's theorem demonstrates how interacting quantities can be determined, the actual calculations are lengthy, merely because the corresponding mathematical expressions are long. In order to reduce work and the number of contributions, the occuring terms can be represented by diagrams. A short summary of their main elements and the simplifications follows:

- Main elements of the diagrams are **particle lines** and **vertices** shown in figure 2.1. Particle lines are denoted by a solid line with an arrow. As it represents the free single-particle Matsubara function $G^{(0)}_{\alpha\beta}(\tau_{\text{an}},\tau_{\text{cr}})$, the arrow points from the annihilation operator time τ_{an} to the creation operator time τ_{cr}. Vertices incorporate the two-body interaction and are given by a dashed vertical line, where due to the type of interaction, two particle lines must enter and two must leave. The number of vertices n denotes the order of the diagram. At equal construction operator times, the creation operator times are considered to be slightly larger than the annihilation operator times $\tau_{\text{cr}} = \tau_{\text{an}} + 0^+$.

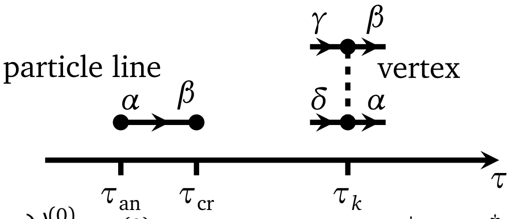

$$-\left\langle \mathrm{T}_\tau\left(c_\alpha(\tau_{\text{an}})c^\dagger_\beta(\tau_{\text{cr}})\right)\right\rangle^{(0)} = G^{(0)}_{\alpha\beta}(\tau_{\text{an}},\tau_{\text{cr}}) \qquad v(\alpha\beta\delta\gamma)c^\dagger_\alpha(\tau_k)c^\dagger_\beta(\tau_k)c_\gamma(\tau_k)c_\delta(\tau_k)$$

2.1 – Main elements of the diagrams.

- **Loop rule:** Each loop (see figure 2.2a) occuring in the diagrams contributes a factor ε.
- **Connected diagrams:** Consider as 'main branch' (see figure 2.2b) the connection of both external lines via particle lines. Within the numerator of the full single-particle Matsubara function all diagram parts disconnected from the main branch sum up to $\langle S(\beta,0)\rangle^{(0)}$.
- **Topologically equivalent diagrams:** Diagrams of n-th order, where 'upper' and 'lower' part of one vertex are interchanged belong to a class of 2^n diagrams giving the same contribution. In addition, n-th order diagrams which differ by a permutation of vertices belong to a class of $n!$ diagrams giving the same contribution. This is visualised in figure 2.2c.

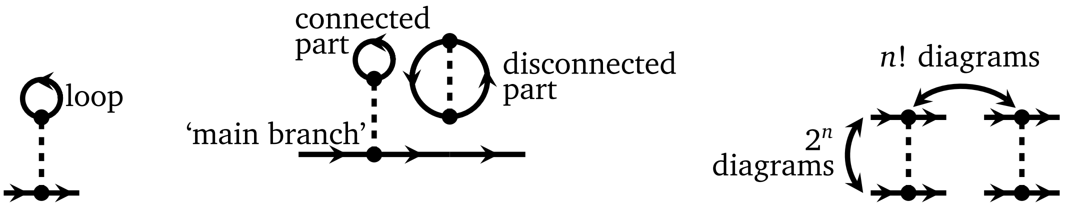

(a) Loop. (b) Connections. (c) Permutations.

2.2 – Illustration of 'loops' in diagrams, connected and disconnected diagram parts as well as the 'main branch' of a diagram. Furthermore the permutations of 'upper' and 'lower' part of vertices as well as of whole vertices are shown.

- **Linked-cluster theorem:** All diagrams contributing to the partition function can be obtained by combining all pairwise different, connected diagrams called linked clusters in all possible ways to construct connected or disconnected diagrams of pairwise different structure. Two diagrams are of different structure, if they differ in the order of the vertices in their connected parts as illustrated in figure 2.3. Since diagrams consisting of k equivalent linked clusters would give additional contributions besides their product due to overcounting, they have to be weightened by a factor $1/k!$. Reordering these terms gives

  $$\langle S(\beta,0)\rangle^{(0)} = \exp\left[\langle S(\beta,0)\rangle^{(0)}_{\text{con}} - 1\right], \tag{2.71}$$

  where con means that only connected diagrams are summed.

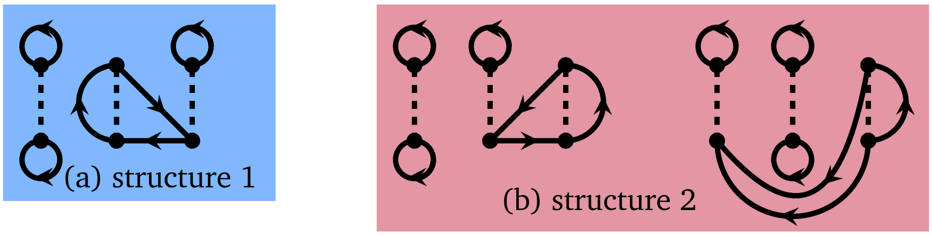

(a) structure 1

(b) structure 2

2.3 – Illustration of similar diagrams with different structure. The structures are distinguished by the order of the vertices in connected parts of the diagram.

Summarising these insights yields rules to construct the diagrams contributing to the partition function, the single-particle Matsubara function or the grand potential including a specific order of the interaction. Moreover, the mathematical expressions corresponding to the various diagrams can be written down directly. To compute these contributions, further strategies such as the Feynman parametrisation [PS95] exist. Diverging contributions become tractable by reordering the expressions in generic ways to isolate the divergencies (regularisation) and omitting the divering parts (renormalisation). Additional informations on the diagram rules in solid state theory can be found in [Pot98; Nol14; BF16; Col15].

2 1 5 Self-energy

Perturbation theory is based on the assumption that the perturbation is small and higher order terms can be neglected. As this might not be the case, partial sums such as the full single-particle Matsubara function or the self-energy of the infinitely large perturbation series have to be considered. Combining multiple partial sums and expressing each in terms of the others makes it possible to solve the problem self-consistently. The presentation follows [Pot98; LW60; Nol14].

The basis of approaching the many-body problem perturbatively is the assumption that the interaction is small which allows neglecting higher order terms. From the phenomenological point of view, the interaction is not always small and one is left with the infinite series of the exponential function to be summed up. A way to tackle this issue is to introduce partial sums of diagrams.

One example for such a partial sum is the self-energy. Self-energy insertions are diagrams which have two open connections, one to an in- and one to an outgoing particle line. They can be classified further by calling them proper/improper if they cannot/can be made to fall into two parts by cutting a single particle line. Examples for proper and improper diagrams are given in the figures 2.4. All improper self-energy insertions can be constructed by connecting two or more proper self-energy insertions by particle lines. Therefore only proper self-energy insertions are required and their sum is called self-energy $\boldsymbol{\Sigma}$.

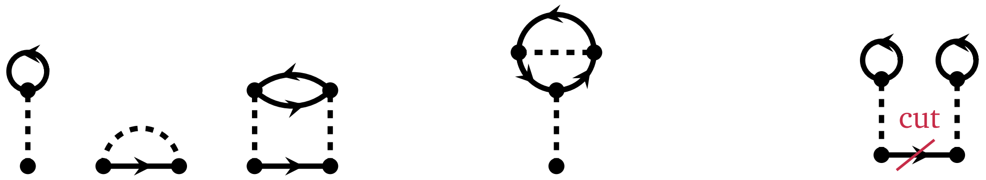

(a) Proper, skeletons.

(b) Proper, no skeleton.

(c) Improper.

2.4 – Examples for 'proper' and 'improper' diagrams, which cannot/can be made to fall into two parts by cutting a single particle line. The other tag refers to 'skeleton' diagrams, which are proper self-energy insertions, containing themselves no further self-energy insertions.

Apart from the zeroth order diagram, a diagram of the full single-particle Matsubara function can be constructed by combining the particle line of a free propagator, a proper self-energy diagram and some other diagram of the full single-particle Matsubara function. Summation over all proper self-energy insertions yields the Dyson equation

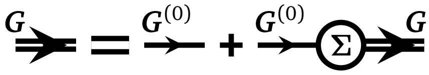

$$G_{\alpha\beta}(E_n) = G^{(0)}_{\alpha\beta}(E_n) + \sum_{\gamma,\delta} G^{(0)}_{\alpha\gamma}(E_n)\Sigma_{\gamma\delta}(E_n)G_{\delta\beta}(E_n), \tag{2.72}$$

where $\boldsymbol{\Sigma}$ denotes the self-energy insertions. This equation can formally be solved by making use of the von Neumann series and gives

$$\boldsymbol{G}(E_n) = \left[\boldsymbol{G}^{(0)}(E_n)^{-1} - \boldsymbol{\Sigma}(E_n)\right]^{-1}. \tag{2.73}$$

Using this result and the von Neumann series makes it possible to determine the sum of all proper and improper self-energy insertions $\boldsymbol{\Sigma}'$ as

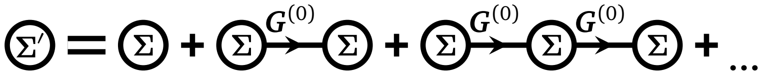

$$\begin{aligned}\boldsymbol{\Sigma}'(E_n) &= \boldsymbol{\Sigma}(E_n) + \boldsymbol{\Sigma}(E_n)\boldsymbol{G}^{(0)}(E_n)\boldsymbol{\Sigma}(E_n) + \boldsymbol{\Sigma}(E_n)\boldsymbol{G}^{(0)}(E_n)\boldsymbol{\Sigma}(E_n)\boldsymbol{G}^{(0)}(E_n)\boldsymbol{\Sigma}(E_n) + \ldots \\ &= \boldsymbol{\Sigma}(E_n)\boldsymbol{G}(E_n)\boldsymbol{G}^{(0)}(E_n)^{-1}.\end{aligned} \tag{2.74}$$

Conversely, one can now try to express the self-energy in terms of the full propagator. This is achieved by introducing skeleton diagrams, which are proper self-energy insertions containing themselves no further self-energy insertions. The missing self-energy insertions are introduced by replacing the free propagator in the skeleton diagrams by the full propagator. These diagrams are called dressed skeletons and their sum gives the self-energy. Examples for skeleton diagrams can be found in the figures 2.4, whereas examples for dressed skeleton diagrams are given in the figures 2.5.

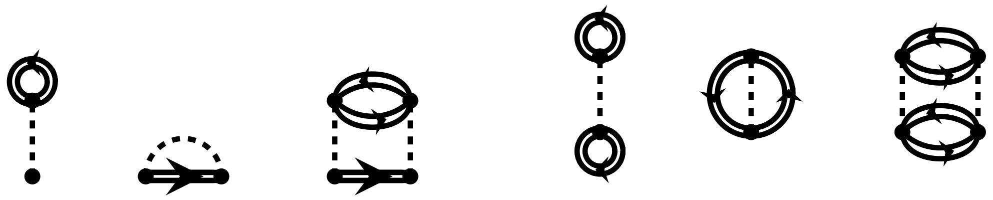

(a) Self-energy. (b) Grand potential.

2.5 – Examples for dressed skeleton diagrams of the self-energy and the grand potential.

Combining the Dyson equation and the equation for the self-energy defines a set of equations which can be solved self-consistently. Starting from an initial self-energy, one can solve the Dyson equation for the full propagator. Calculating then the new self-energy closes the cycle. Going on until the self-energy remains the same within such an iteration results in the full propagator and the self-energy.

2 1 6 Connection between Ω and G

◈ *Connecting the static grand potential Ω and the dynamic Matsubara function $\mathbf{G}$ based on their diagrammatic expressions opens the door to a whole range of thermodynamically consistent 'conserving approximations' [BK61; Bay62]. Besides finding distinct analytic approximations within diagrammatic perturbation theory, it also provides the basis for self-energy-functional theory [Pot12], a framework to construct cluster-approximations suited for numerical investigations to be introduced in section 2.2.1. The presentation follows [LW60].* ◈

Since determining the self-energy is reduced to finding the dressed skeleton diagrams, the question is now whether this reduction is also possible for the grand potential. It is possible, but not in the same way as it is achieved for the self-energy. Merely replacing all free by full propagators within the skeleton diagrams of the grand potential would lead to an overcounting of diagrams, since the reduction of closed, linked diagrams to skeletons is not unique as shown in figure 2.6a. This problem does not occur for the self-energy, since the vertices connected to external lines are singled out as shown in figure 2.6b.

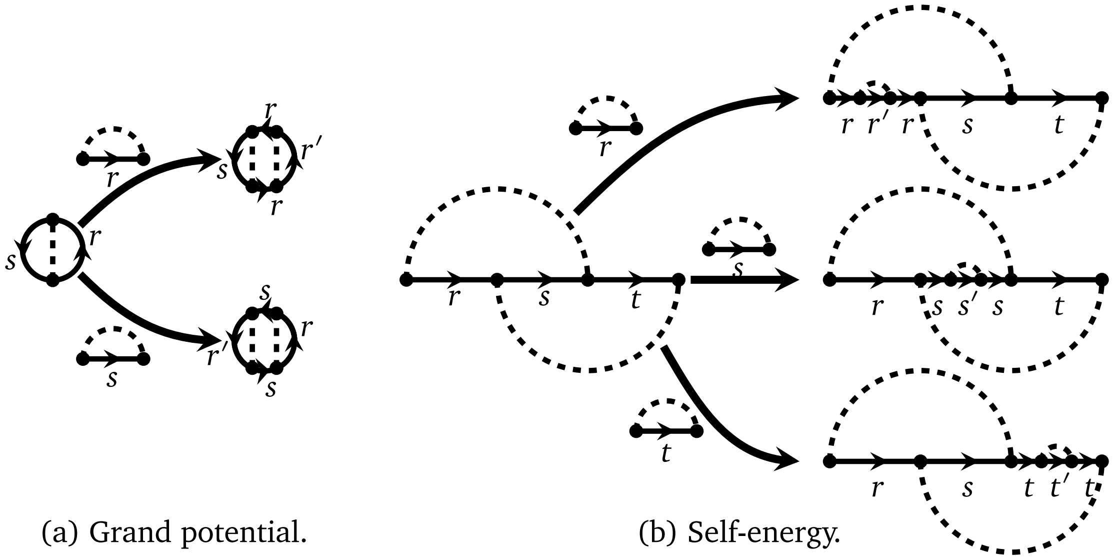

(a) Grand potential. (b) Self-energy.

2.6 – Illustration, how skeleton diagrams would include several diagrams contributing to the grand potential multiple times, whereas they can be used to construct the self-energy.

The idea is now not to reduce the diagrams of the grand potential to skeletons, but to decompose them into proper or improper self-energy insertions. Breaking one free propagator in a diagram of the grand potential yields a proper or improper self-energy insertion as shown in figure 2.7. Fixing the broken link by adding a free propagator gives back the diagram of the grand potential.

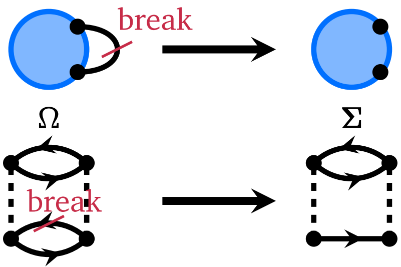

2.7 – Schematic illustration and explicit example, how breaking one single particle line transforms a diagram contributing to the grand potential into a self-energy diagram.

Doing this for all $2n$ free propagators of an n-th order diagram of the grand potential gives $2n$ times the same diagram. Hence, the expression for an n-th order diagram of the grand potential is

$$\Omega^n = \frac{1}{2n}\frac{1}{\beta}\sum_{\ell}\sum_{\alpha,\gamma} G^{(0)}_{\alpha\gamma}(E_\ell)\Sigma'^{n}_{\gamma\alpha}(E_\ell), \tag{2.75}$$

where the factor $1/2n$ compensates for the overcounting and $\Sigma'^{n}_{\beta\gamma}$ denotes the total self-energy part of n-th order containing proper and improper diagrams. In comparison with previous partial sums, here the overcounting correction complicates the summation over diagrams of all order to the whole grand potential. To get rid of this factor, a coupling constant λ in the interaction is introduced. This adds to each n-th order self-energy a factor λ^n. Integrating over λ removes the overcounting factor and gives

$$\Omega^n(\lambda) = \frac{1}{2\beta}\sum_{\ell}\sum_{\alpha,\gamma} G^{(0)}_{\alpha\gamma}(E_\ell)\int\limits_{[0,\lambda]}\frac{\mathrm{d}\lambda'}{\lambda'}\,\Sigma'^{n}_{\gamma\alpha}\left(E_\ell,\lambda'\right). \tag{2.76}$$

The whole grand potential follows as

$$\Omega(\lambda) = \Omega_0 + \sum_{n}\Omega^n = \Omega_0 + \frac{1}{2\beta}\sum_{\ell}\sum_{\alpha,\gamma} G^{(0)}_{\alpha\gamma}(E_\ell)\int\limits_{[0,\lambda]}\frac{\mathrm{d}\lambda'}{\lambda'}\,\Sigma'_{\gamma\alpha}\left(E_\ell,\lambda'\right), \tag{2.77}$$

where $\Sigma'_{\gamma\alpha}$ is the sum of all proper and improper self-energy insertions. Making use of equation (2.74) and rewriting the integral equation as a differential equation, the grand potential can be obtained by solving

$$\lambda\frac{\mathrm{d}\Omega}{\mathrm{d}\lambda} = \frac{1}{2\beta}\sum_{\ell}\sum_{\alpha,\gamma}\Sigma_{\alpha\gamma}(E_\ell)G_{\gamma\alpha}(E_\ell,\lambda) \tag{2.78}$$

with initial condition $\Omega(\lambda=0)=\Omega_0$. In order to obtain the grand potential, Luttinger and Ward [LW60] proposed the expression

$$Y = \left\{-\frac{1}{\beta}\sum_{\ell}\exp(\mathrm{i}E_\ell 0^+)\left(\sum_{\alpha}\ln\left[-G^{-1}(E_\ell)\right]_{\alpha\alpha} + \sum_{\alpha,\gamma}G_{\alpha\gamma}(E_\ell)\Sigma_{\gamma\alpha}(E_\ell)\right)\right\} + Y', \tag{2.79}$$

where Y' is the contribution from summing all closed, linked skeleton diagrams with the free propagator replaced by the full one. By showing that Y solves the differential equation (2.78) with the correct initial condition, the connection between grand potential Ω and propagator Σ is established.

Thus one searches

$$\lambda \frac{\mathrm{d}Y}{\mathrm{d}\lambda} = \lambda \cdot \left[\frac{\delta Y}{\delta \Sigma_{\alpha\gamma}(E_\ell)} \frac{\partial \Sigma_{\gamma\alpha}(E_\ell)}{\partial \lambda} + \frac{\partial Y}{\partial \lambda} \right], \tag{2.80}$$

where $\delta Y / \delta \boldsymbol{\Sigma}$ denotes the functional derivative of Y w.r.t. Σ, since the indices denoting the components of $\boldsymbol{\Sigma}$ are infinitely many. To show that $\delta Y / \delta \boldsymbol{\Sigma}$ vanishes, Y' is formulated similar to the n-th order diagram of the grand potential: Consider a ν-th order diagram of Y'. Breaking any of the 2ν full propagators yields a diagram contributing to the self-energy. Fixing the broken link by a full propagator gives again the diagram of Y'. Doing this with every full propagator of the diagram, gives 2ν times the same diagram. Summing over all ν-th order diagrams yields

$$Y' = \frac{1}{\beta} \sum_{\nu} \sum_{\ell} \sum_{\alpha,\gamma} \frac{1}{2\nu} G_{\alpha\gamma}(E_\ell) \Sigma^{\nu''}_{\gamma\alpha}(E_\ell). \tag{2.81}$$

Taking the functional derivative w.r.t. the self-energy $\boldsymbol{\Sigma}$ is possible by employing that $\boldsymbol{\Sigma}^{\nu''}$ depends on the whole self-energy only via $2\nu - 1$ full propagators and by using the Dyson equation

$$\begin{aligned} \frac{\delta Y}{\delta \Sigma_{\alpha\gamma}(E_\ell)} &= \frac{\delta \{\cdot\}}{\delta \Sigma_{\alpha\gamma}(E_\ell)} + \frac{\delta Y'}{\delta \Sigma_{\alpha\gamma}(E_\ell)} \\ &= -\frac{1}{\beta} \sum_{\alpha,\gamma,\ell} G^2_{\alpha\gamma}(E_\ell) \Sigma_{\gamma\alpha}(E_\ell) + \frac{1}{\beta} \sum_{\alpha,\gamma,\ell} G^2_{\alpha\gamma}(E_\ell) \Sigma_{\gamma\alpha}(E_\ell) \\ &= \boldsymbol{0}, \end{aligned} \tag{2.82}$$

where $\{\cdot\}$ refers to the curly bracket in equation (2.79). Hence with the partial derivative $\partial Y / \partial \lambda$ only vertices of $\boldsymbol{\Sigma}^{\nu''}$ in Y' contribute. Writing $\boldsymbol{\Sigma}^{\nu''} = \lambda^\nu \boldsymbol{\Sigma}''$ and performing the summation over all ν to the whole self-energy $\boldsymbol{\Sigma}$ gives the differential equation

$$\lambda \frac{\mathrm{d}Y}{\mathrm{d}\lambda} = \frac{1}{2\beta} \sum_{\ell} \sum_{\alpha,\gamma} G_{\alpha\gamma}(E_\ell) \Sigma_{\gamma\alpha}(E_\ell) = \lambda \frac{\mathrm{d}\Omega}{\mathrm{d}\lambda}. \tag{2.83}$$

In order to verify the initial condition, the addends in the sum over energies at zero interaction $\lambda = 0$,

$$Y(\lambda = 0) = -\frac{1}{\beta} \sum_{\alpha} \sum_{\ell} \exp\left(\mathrm{i} E_\ell 0^+\right) \ln\left[-G^{(0)}(E_\ell)^{-1}\right]_{\alpha\alpha} \tag{2.84}$$

is rewritten as residue of a function with poles at E_ℓ. Deforming the corresponding contour and performing an integration by parts yields

$$Y(\lambda = 0) = -\frac{1}{\beta} \ln[\exp(-\beta(E_\ell - \mu) + 1] = \Omega_0. \tag{2.85}$$

By that the expression

$$\Omega = -\frac{1}{\beta} \sum_{\ell} \exp(\mathrm{i} E_\ell 0^+) \left\{ \sum_{\alpha} \ln\left[-G^{-1}(E_\ell)\right]_{\alpha\alpha} + \sum_{\alpha,\gamma} G_{\alpha\gamma}(E_\ell) \Sigma_{\gamma\alpha}(E_\ell) \right\} + \Phi \tag{2.86}$$

$$\equiv -\operatorname{Tr}\left[\ln\left(-\boldsymbol{G}^{-1}\right)\right] - \operatorname{Tr}[\boldsymbol{G}\boldsymbol{\Sigma}] + \Phi \tag{2.87}$$

for the grand potential is established, where Φ denotes the Luttinger-Ward functional Y' and $\mathrm{Tr}[\boldsymbol{A}]$ abbreviates $\beta^{-1}\sum_\ell\sum_\alpha \exp(\mathrm{i}\,E_\ell 0^+)A_{\alpha\alpha}$. Although this is the main result, the stationarity of the grand potential w.r.t. the variation of the self-energy

$$\frac{\delta\Omega}{\delta\boldsymbol{\Sigma}} = 0 \tag{2.88}$$

is essential for the self-energy-functional theory and is mentioned here for future reference.

2.1.7 Generalisation of the Luttinger-Ward functional

The perturbative expression for the grand potential relies on the convergence of the skeleton diagram series for the Luttinger-Ward functional. To derive the expression for the grand potential non-perturbatively, the Luttinger-Ward functional has to be generalised. The presentation follows [Pot12].

The validity of the diagrammatic expression for the grand potential relies on the convergence of the skeleton diagram series for the Luttinger-Ward functional. Nevertheless, the diagrammatic definition of Φ depending on the actual system can be condensed to a list of defining properties and thereby generalised to a functional operating on a space of systems:

- $\check{\Phi}_{\boldsymbol{U}}[\boldsymbol{G}]$ is a functional.
- The domain of $\check{\Phi}_{\boldsymbol{U}}$ is the ‘space of Green’s functions $\boldsymbol{G}$’.
- Evaluating the Luttinger-Ward functional at the physical Green’s function $\boldsymbol{G}_{\boldsymbol{t},\boldsymbol{U}}$ of a system with Hamiltonian $H = H(\boldsymbol{t},\boldsymbol{U})$ relates it to the grand potential of the system via
$$\Omega_{\boldsymbol{t},\boldsymbol{U}} = -\mathrm{Tr}\left[\ln\left(-\boldsymbol{G}_{\boldsymbol{t},\boldsymbol{U}}^{-1}\right)\right] - \mathrm{Tr}\left[\boldsymbol{G}_{\boldsymbol{t},\boldsymbol{U}}\boldsymbol{\Sigma}_{\boldsymbol{t},\boldsymbol{U}}\right] + \check{\Phi}[\boldsymbol{G}_{\boldsymbol{t},\boldsymbol{U}}]. \tag{2.89}$$
- The functional derivative of $\check{\Phi}$ w.r.t. its argument is again a functional of the Green’s function
$$\frac{\delta\check{\Phi}_{\boldsymbol{U}}[\boldsymbol{G}]}{\delta\boldsymbol{G}} = \check{\boldsymbol{\Sigma}}_{\boldsymbol{U}}[\boldsymbol{G}]. \tag{2.90}$$
  As the diagrammatic expression shows, the evaluation of $\check{\boldsymbol{\Sigma}}_{\boldsymbol{U}}$ at the physical Green’s function yields the physical self-energy
$$\check{\boldsymbol{\Sigma}}_{\boldsymbol{U}}[G_{\boldsymbol{t},\boldsymbol{U}}] = \boldsymbol{\Sigma}_{\boldsymbol{t},\boldsymbol{U}}. \tag{2.91}$$
- The Luttinger-Ward functional is universal in the sense, that it is fully determined by the interaction parameters $\boldsymbol{U}$.
- Non-interacting limit: $\check{\Phi}_{\boldsymbol{U}}[\boldsymbol{G}] = 0$ for $\boldsymbol{U} = \boldsymbol{0}$.

A way of deriving the expression of the grand potential non-perturbatively starts from the path integral expression of the grand canonical partition function Ξ as given in [Pot12]. Therein, the physical action $A_{\boldsymbol{t},\boldsymbol{U}}$ is generalised to a universal ($\boldsymbol{U}$-dependent) functional $\check{A}_{\boldsymbol{U}}\left[\boldsymbol{G}_0^{-1}\right]$ with the inverse free Green’s function $\boldsymbol{G}_0^{-1}$ as argument. Inserting the physical free Green’s function $\boldsymbol{G}_{\boldsymbol{t},\boldsymbol{0}}$ gives again the physical action $A_{\boldsymbol{t},\boldsymbol{U}}$. This translates to a generalisation of the grand canonical partition function $\check{\Xi}_{\boldsymbol{U}}\left[\boldsymbol{G}_0^{-1}\right]$ and the grand potential $\check{\Omega}_{\boldsymbol{U}}\left[\boldsymbol{G}_0^{-1}\right]$ to functionals giving at the physical free Green’s function the physical quantities $\Xi_{\boldsymbol{t},\boldsymbol{U}}$ and $\Omega_{\boldsymbol{t},\boldsymbol{U}}$. The functional derivative

$$\frac{\delta\check{\Omega}_{\boldsymbol{U}}\left[\boldsymbol{G}_0^{-1}\right]}{\delta\boldsymbol{G}_0^{-1}} \equiv -\beta^{-1}\check{\mathcal{G}}_{\boldsymbol{U}}\left[\boldsymbol{G}_0^{-1}\right] \tag{2.92}$$

defines a new universal functional $\check{\boldsymbol{\mathcal{G}}}_U\left[\boldsymbol{G}_0^{-1}\right]$ which gives at the physical free Green's function the physical full Green's function $\boldsymbol{G}_{t,U}$. Setting up the equation

$$\check{\boldsymbol{\mathcal{G}}}_U\left[\boldsymbol{G}^{-1}+\Sigma\right]=\boldsymbol{G} \tag{2.93}$$

defines as solution the functional $\check{\Sigma}[\boldsymbol{G}]$. From the Dyson equation it becomes clear, that evaluated at the physical full Green's function, this functional gives the physical self-energy $\boldsymbol{\Sigma}_{t,U}$. Combining all these functionals leads to a functional satisfying the properties of the Luttinger-Ward functional

$$\check{\Phi}_U[\boldsymbol{G}]=\check{\Omega}_U\left[\boldsymbol{G}^{-1}+\check{\Sigma}_U[\boldsymbol{G}]\right]-\mathrm{Tr}\ln(\boldsymbol{G})+\mathrm{Tr}\left(\boldsymbol{G}\check{\Sigma}_U[\boldsymbol{G}]\right). \tag{2.94}$$

2 2 Method

2 2 1 Self-energy-functional theory (SFT)

◈*Self-energy-functional theory provides a framework to construct cluster-approximations of lattice models in solid state theory. The method is thermodynamically consistent, since it is based on the expression* (2.86) *for the grand potential and its variational property* (2.88). *The presentation follows [Pot12].*◈

Within self-energy-functional theory (SFT), the functional $\check{\Sigma}_U[\boldsymbol{G}]$ is assumed to be locally invertible when the system is not at a critical point or a phase transition. This makes it possible to form yet another universal functional, the Legendre transform of the Luttinger-Ward functional

$$\check{F}_U[\Sigma]=\check{\Phi}_U\left[\check{\boldsymbol{G}}_U[\Sigma]\right]-\mathrm{Tr}\left(\check{\boldsymbol{G}}_U[\Sigma]\Sigma\right). \tag{2.95}$$

By defining the self-energy functional as

$$\check{\Omega}_{t,U}[\boldsymbol{\Sigma}]=\mathrm{Tr}\left\{\ln\left(\frac{1}{\boldsymbol{G}_{t,0}^{-1}-\boldsymbol{\Sigma}}\right)\right\}+\check{\boldsymbol{F}}_U[\Sigma], \tag{2.96}$$

one obtains a quantity,

- which gives at the physical self-energy $\boldsymbol{\Sigma}_{t,U}$ the physical grand potential $\Omega_{t,U}$.
- whose functional derivative w.r.t. $\boldsymbol{\Sigma}$ being stationary is equivalent to a Dyson-like equation

$$\frac{\delta\check{\Omega}_{t,U}[\Sigma]}{\delta\Sigma}=\boldsymbol{0}\Leftrightarrow\check{\boldsymbol{G}}_U[\Sigma]=\frac{1}{\boldsymbol{G}_{t,0}^{-1}-\boldsymbol{\Sigma}}. \tag{2.97}$$

The physical self-energy can therefore be determined by searching for the stationary point of the self-energy functional. Having the physical self-energy, the grand potential and the propagator can be calculated which give access to dynamic and thermodynamic quantities.

In practice, expression (2.96) for the self-energy functional has to be approximated to be of use. There are three types of approximation schemes which allow to determine the physical self-energy:

- **Type I**: The Euler equation $\delta\check{\Omega}/\delta\boldsymbol{\Sigma} = 0$ is explicitely derived, but simplified to determine the physical self energy. This may lead to thermodynamic inconsistencies.
- **Type II**: The functional $\check{\Omega}$ is modified s.t. the Euler equation can be solved. Here, the thermodynamic potential is consistent with the self-energy, but it is difficult to find such approximations.
- **Type III**: The functional $\check{\Omega}$ is only considered on a restricted domain of self-energies, where the Euler equation can be solved. By that, the functional form is kept and the approximation is controlled by the extent of the domain.

In SFT, a specific version of type III approximation is employed, where the self-energy is considered to be parametrised by the parameters of one-body operators. Main motive for this is the absence of a closed form for the Luttinger-Ward functional $\check{\Phi}_U$ and the idea to remove it from the agenda. To eliminate $\check{\Phi}_U$, the self-energy functional $\check{\Omega}'_U$ of a ‘reference system’ with a Hamiltonian having the same interaction part as the original system, but different one-body operators is considered. Taking the difference of both self-energy functionals gives

$$\check{\Omega}_U[\boldsymbol{\Sigma}] - \check{\Omega}'_U[\boldsymbol{\Sigma}] = -\operatorname{Tr}\ln\left(-\boldsymbol{G}_0^{-1} + \boldsymbol{\Sigma}\right) + \operatorname{Tr}\ln\left(-\boldsymbol{G}_0'^{-1} + \boldsymbol{\Sigma}\right), \tag{2.98}$$

where the occurence of $\check{\Phi}_U$ is replaced by quantities of a reference system, whose dependence on the self-energy is yet unspecified. Evaluating the whole expression at the self-energy of the reference system $\boldsymbol{\Sigma}'$, the unknown quantities are determined

$$\check{\Omega}[\boldsymbol{\Sigma}'] - \Omega' = -\operatorname{Tr}\ln\left(-\boldsymbol{G}_0^{-1} + \boldsymbol{\Sigma}'\right) + \operatorname{Tr}\ln\left(-\boldsymbol{G}'^{-1}\right), \tag{2.99}$$

where Ω' is the grand potential and $\boldsymbol{G}'$ the full Green’s function of the reference system. Choosing an at least numerically tractable reference system allows evaluation of the self-energy functional. There are two possible types of reference systems:

- Decompose the original lattice system into isolated clusters with on-site interaction.

↪ Variational cluster approximation (VCA)

- Start from a physical site and add bath sites to it, which possess bath energies (meaning chemical potentials) and are connected to the physical site via hybridisation (meaning hopping terms).

↪ Dynamical impurity approximation (DIA).

In the limit of infinitely many bath sites, the DIA becomes the variational version of the dynamical mean-field theory (DMFT) which by itself performs the optimisation in an iterative fashion. Combining both ways of constructing the reference system by adding bath sites to a cluster leads to the variational version of the cluster dynamical mean-field theory (CDMFT).

Since the only requirement for the reference system consists in having the same interaction part as the original system, the Hamiltonian of the reference system can in principle be extended by arbitrary one-body terms. Each parameter of a one-body term can in turn be used to parametrise the self-energy. The number of variational parameters should be restricted to physically meaningful ones, since finding the stationary point in the space spanned by these parameters becomes harder with increasing dimension of the space. Examples for terms already present in the Hamiltonian are the on-cluster hoppings and the chemical potential. A physically motivated additional term would be a staggered magnetic field coupled to the electron spins

$$H = h' \cdot \sum_i z_i (n_{i\uparrow} - n_{i\downarrow}), \tag{2.100}$$

where $z_i = \pm 1$ transforms the systen into a bipartite one. The magnetic field h' is no physical field, but a fictitious one similar to the internal fields occuring in mean-field theory and therefore denoted as 'Weiss field'. Its value is determined by the stationarity condition of the self-energy functional. If the system would incorporate a physically applied magnetic field, the Weiss field would depend on it, since it modifies the stationarity condition. Physical and fictitious field differ in general and the Weiss field may be larger or smaller than the physical one. A spontaneously symmetry broken state is found, if the self-energy functional is stationary at vanishing physical, but finite Weiss field.

2 2 2 Cluster perturbation theory (CPT)

In cluster perturbation theory (CPT), the self-energy of a lattice system is approximated by that of a system composed of clusters in the limit of weak inter-cluster hoppings. It provides the basic equation to determine the reference system's Green's function needed in VCA and allows computing well resolved spectral functions. The presentation follows [Pot14; Sén12].

Just as the connection between grand potential and propagator have been introduced diagrammatically, this is the path to motivate cluster perturbation theory (CPT). Considering a system composed of clusters, the generic Hamiltonian (2.15) is split into three parts illustrated in figure 2.8:

- On-cluster hoppings $H_0(\boldsymbol{t})$,
- Inter-cluster hoppings $H_0(\boldsymbol{V})$,
- On-cluster interactions H_1,

where $\boldsymbol{t}$ denotes the on- and $\boldsymbol{V}$ the inter-cluster hopping matrix $t_{\alpha\beta}$ and $V_{\alpha\beta}$.

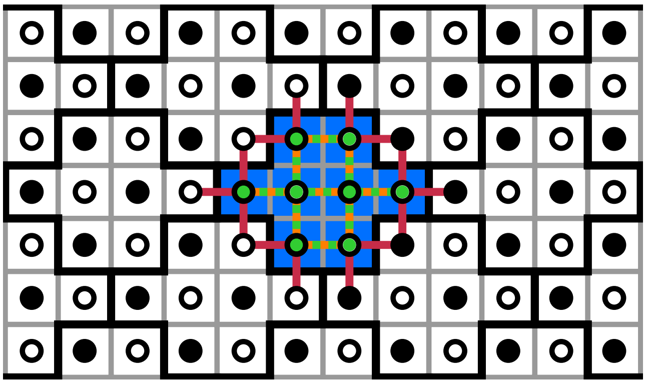

2.8 – Illustration of the on-cluster hoppings $H_0(\boldsymbol{t})$, inter-cluster hoppings $H_0(\boldsymbol{V})$ and on-cluster interactions H_1. The bipartite character of the lattice supported by the cluster is highlighted by filled and empty circles.

Similar to the treatment of the on-site interaction H_1, the inter-cluster hopping is also considered as perturbation. Following the procedure of section 2.1.4 with the perturbation being the sum of interaction and inter-cluster hoppings, Wick's theorem decomposes the strings of construction operators into products of free single-particle Matsubara functions. Since terms within the inter-cluster hopping consist of one creation and one annihilation operator, the corresponding symbol Ⓥ connects to one entering and one leaving particle line. In addition to the diagrams, where only the interaction acts as perturbation, additional diagrams appear, where single particle lines are replaced by an alternating sequence of particle lines and inter-cluster hoppings. Sharing the property of being connected to two lines, all diagrams including either the inter-cluster hoppings or the self-energy, as well as propagators can be constructed alike by a Dyson-like equation. The main question is in which sequence the propagators are dressed by the perturbations. Since the self-energy contains free propagators, but the inter-cluster hopping does not, the free propagators should first be dressed by the inter-cluster hoppings and afterwards by the self-energy

1) $\boldsymbol{G}^{(0)} = \boldsymbol{G}'^{(0)} + \boldsymbol{G}'^{(0)} \boldsymbol{V} \boldsymbol{G}^{(0)}$,
2) $\boldsymbol{G} = \boldsymbol{G}^{(0)} + \boldsymbol{G}^{(0)} \boldsymbol{\Sigma} \boldsymbol{G}$,

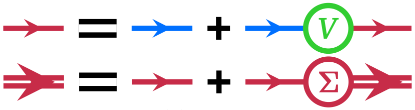

where $\boldsymbol{G}'^{(0)}$ is the free cluster propagator, $\boldsymbol{G}^{(0)}$ is the full free propagator, $\boldsymbol{\Sigma}$ is the full self-energy and $\boldsymbol{G}$ the full propagator. By inverting this sequence, the contributions of inter-cluster hoppings to the self-energy are neglected, which leaves effectively only the cluster self-energy $\boldsymbol{\Sigma}'$

1) $\boldsymbol{G}' = \boldsymbol{G}'^{(0)} + \boldsymbol{G}'^{(0)} \boldsymbol{\Sigma}' \boldsymbol{G}'$,
2) $\boldsymbol{G}_{\mathrm{CPT}} = \boldsymbol{G}' + \boldsymbol{G}' \boldsymbol{V} \boldsymbol{G}_{\mathrm{CPT}}$,

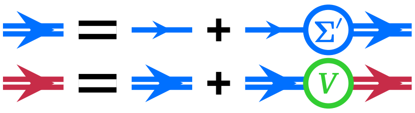

with $\boldsymbol{G}'^{(0)}$ as free cluster propagator, $\boldsymbol{G}'$ as full cluster propagator and $\boldsymbol{G}_{\mathrm{CPT}}$ as CPT propagator. This approximation to the full Green's function is the basic equation of CPT. Another way to obtain this relation is via strong-coupling perturbation theory described in reference [PST00] based on the path integral approach. Knowing the cluster Green's function and the inter-cluster hopping, one can compute the Green's function of a system of decoupled clusters as it is required for the VCA.

Besides determining the Green's function of a cluster system in real space, its shape in reciprocal space is of major importance for the spectral function motivated in section 2.1.3. Due to the artificial superlattice introduced by dividing the lattice into clusters, the Green's function is only periodic w.r.t. translations in the superlattice, but not w.r.t. arbitrary translations commensurate with the whole lattice. An example for this would be two sites on different clusters, which are connected by a vector of the whole lattice, but not by one of the superlattice. The full dependence on all reciprocal lattice vectors is obtained by periodisation of the Green's function. Thereby, the Green's function is regularly Fourier transformed w.r.t. the superlattice vectors. Within the Fourier transformation w.r.t. vectors connecting sites of (the same or different) clusters, the 'off-diagonal terms' are discarded, i.e. the (in general) different reciprocal lattice vectors are replaced by the same vector. From a pragmatic point of view, this is justified, since the quasiparticle DOS and the spectral function as quantities of interest are independent from the off-diagonal terms. In a nutshell, each site of a cluster is assigned the same reciprocal lattice vector and only sites on different clusters have different reciprocal lattice vectors.

Here, coordinates of sites relative to the cluster origin are denoted $\boldsymbol{R}$ and locations of clusters are $\tilde{\boldsymbol{r}}$ giving the absolute coordinate of sites on the lattice $\boldsymbol{r} = \tilde{\boldsymbol{r}} + \boldsymbol{R}$. The respective reciprocal lattice vectors are $\boldsymbol{K}$, $\tilde{\boldsymbol{k}}$ and $\boldsymbol{k} = \boldsymbol{K} + \tilde{\boldsymbol{k}}$. For a lattice of N_{cl} clusters of ℓ sites each, the resulting $\boldsymbol{k}$-dependent Green's function reads

$$\boldsymbol{G}(E, \boldsymbol{k}) = \frac{1}{L} \sum_{\boldsymbol{R},\boldsymbol{R}'} \exp[-\mathrm{i}\boldsymbol{k}(\boldsymbol{R} - \boldsymbol{R}')] \boldsymbol{G}_{\boldsymbol{R}\boldsymbol{R}'}(E, \tilde{\boldsymbol{k}}), \tag{2.101}$$

with $L = N_{\mathrm{cl}} \cdot \ell$ being the total number of lattice sites and $\tilde{\boldsymbol{k}}$ the reciprocal lattice vector occuring in $\boldsymbol{V}(\tilde{\boldsymbol{k}})$ constructed directly in reciprocal space giving $\boldsymbol{k} = \tilde{\boldsymbol{k}} + \boldsymbol{K}$. In practice, the replacement $\tilde{\boldsymbol{k}} \to \boldsymbol{k}$ is used, where the available $\boldsymbol{k} \in \{2\pi \boldsymbol{n}/N_{\mathrm{cl}} | n_i = 0, \ldots, N_{\mathrm{cl}}^{(i)} - 1\}$ are parametrised by the number of clusters. One argument for this replacement is, that since $\boldsymbol{G}_{\boldsymbol{R}\boldsymbol{R}'}(E, \tilde{\boldsymbol{k}})$ is $\tilde{\boldsymbol{k}}$-periodic, choosing a finer $\boldsymbol{k}$-grid would yield no additional information. Another argument is, that since each site on the same cluster has the same phase, it amounts to a constant offset which can be set to zero without changing the Green's function.

Since the magnetic orders considered in this thesis transform the lattice into a bipartite one, the clusters building it up have to be selected accordingly. For later reference, the two-dimensional clusters employed in this thesis are depicted in figure 2.9 with the corresponding superlattice vectors specified in a table next to them. The lattice vectors of one-dimensional clusters with n sites in one and the two-site cluster in two dimensions are provided in the table as well.

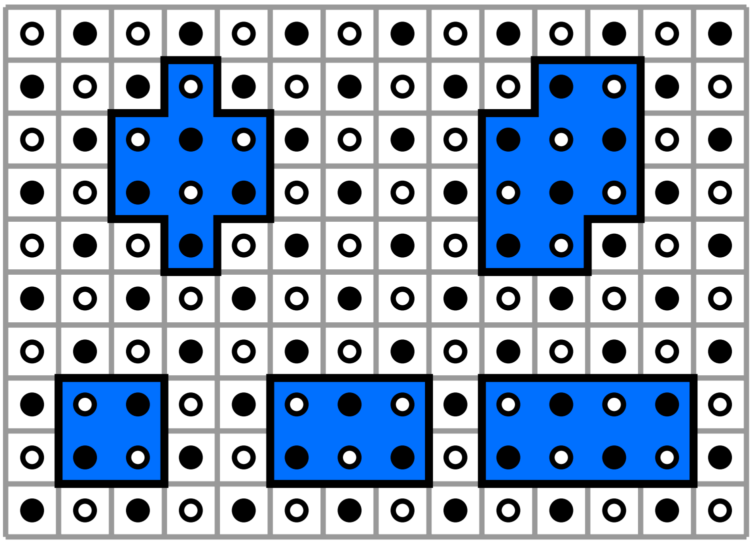

cluster	lattice vectors
$n \times 1$	n
2×1	$(2,0)$, $(1,-1)$
2×2	$(2,0)$, $(0,2)$
3×2	$(3,1)$, $(3,-1)$
4×2	$(4,0)$, $(0,2)$
$\sqrt{8} \times \sqrt{8}$	$(2,2)$, $(2,-2)$
$\sqrt{10} \times \sqrt{10}$	$(3,1)$, $(-1,3)$

2.9 – Two-dimensional clusters employed in this thesis and corresponding superlattice vectors. The bipartite character of the lattice supported by the cluster is highlighted by filled and empty circles.

2 2 3 Variational cluster approximation (VCA)

Representing one of the two branches of possible approximation schemes within the SFT, the Variational cluster approximation (VCA) can be perceived as variational extension of the CPT, where the self-energy functional is optimised w.r.t. the coefficients of one-body operators. The presentation follows [Pot12; Sén08].

Since now all properties required for the VCA have been discussed, the algorithm to follow is shown in figure 2.10. Numerical details on how to obtain the cluster grand potential and cluster Green's function are discussed in section 2.3 for zero and 2.4 for finite temperature.

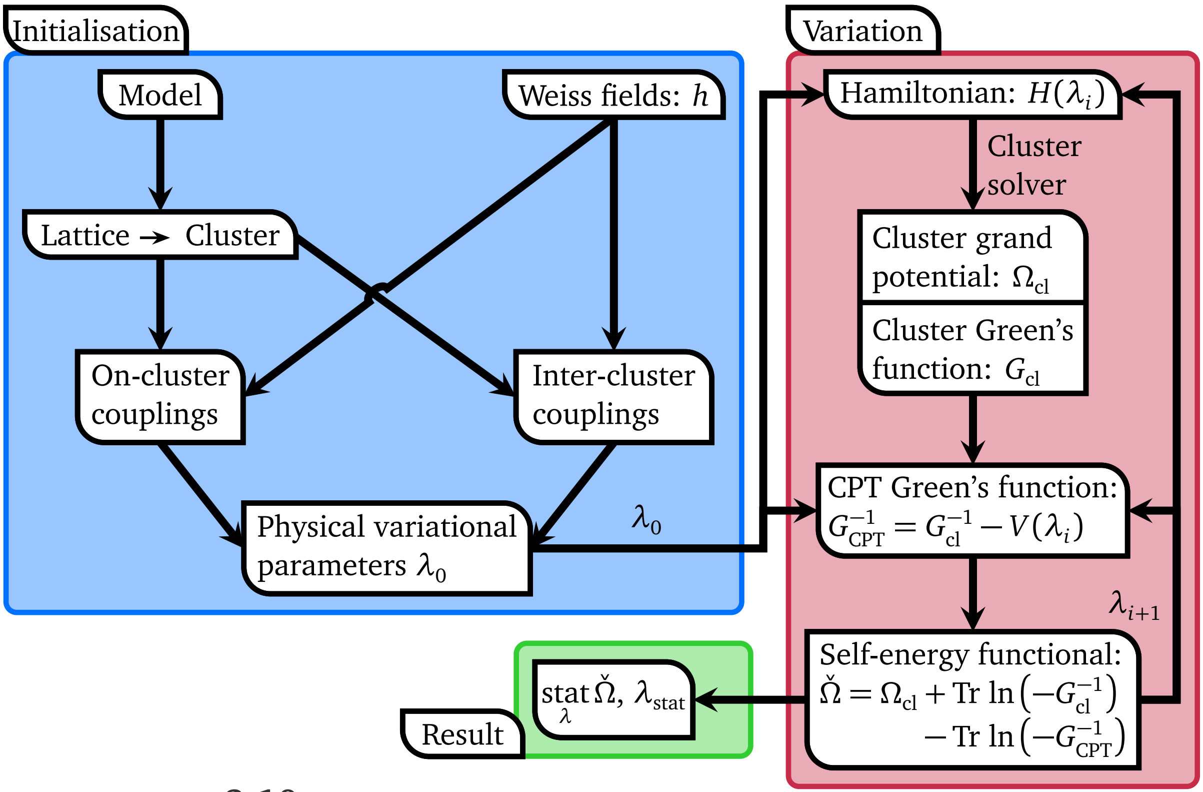
Initialisation
Model
Weiss fields: h
Lattice → Cluster
On-cluster couplings
Inter-cluster couplings
Physical variational parameters λ_0
λ_0
Variation
Hamiltonian: $H(\lambda_i)$
Cluster solver
Cluster grand potential: Ω_{cl}
Cluster Green's function: G_{cl}
CPT Green's function: $G_{\mathrm{CPT}}^{-1} = G_{\mathrm{cl}}^{-1} - V(\lambda_i)$
λ_{i+1}
Self-energy functional: $\check{\Omega} = \Omega_{\mathrm{cl}} + \mathrm{Tr}\ln\left(-G_{\mathrm{cl}}^{-1}\right) - \mathrm{Tr}\ln\left(-G_{\mathrm{CPT}}^{-1}\right)$
$\operatorname{stat}_{\lambda} \check{\Omega},\ \lambda_{\mathrm{stat}}$
Result

2.10 – Algorithm of the VCA. A description is given in the text.

Starting point is a model defined by a Hamiltonian and a lattice of given geometry. By decomposing the lattice into clusters, the couplings inside the Hamiltonian are divided into on- and inter-cluster couplings. On-cluster couplings connect sites of the same cluster, whereas inter-cluster couplings link sites of different clusters. As described in the end of section 2.2.1, additional Weiss fields h followed by operators of on- or inter-cluster type are introduced to extend the Hamiltonian. After the set of variational parameters λ_0 is fixed, the initialisation is complete. Its result is a modified Hamiltonian $H(\lambda_0)$ depending on the variational parameters.

In order to find the variational parameters λ_{stat} making the self-energy functional $\check{\Omega}$ stationary, the quantities occuring in its definition have to be determined. Employing the cluster solver gives the cluster grand potential Ω_{cl} and the cluster Green's function G_{cl} as described in section 2.3 for zero and 2.4 for finite temperature. The cluster Green's function G_{cl} and the analytically known inter-cluster couplings V yield the CPT Green's function G_{CPT} introduced in section 2.2.2. Combining the cluster grand potential, the cluster Green's function and the CPT Green's function to the self-energy functional $\check{\Omega}[\Sigma(\lambda_i)]$ completes the construction of the function $\check{\Omega}(\lambda_i)$ to be made stationary. Minimisation of $\check{\Omega}(\lambda_i)$, maximisation as minimisation of $-\check{\Omega}(\lambda_i)$ or searching the saddlepoint of $\check{\Omega}(\lambda_i)$ by minimising the function's derivative gives the variational parameters characterising the physical system.

2 3 Cluster solvers at zero temperature

Three cluster solvers and four representations of the Green's function employed within the zero temperature VCA are presented. Depending on the solver, only specific representations can be used.

2 3 1 Lanczos algorithm

The Lanczos algorithm constructs iteratively an invariant subspace of the Hamiltonian in which it has tridiagonal shape. Computing the eigenvalues and eigenvectors allows construction of the spectral representation of the Green's function. Inversion of the tridiagonal matrix yields the continued fraction representation of the Green's function to be discussed in section 2.3.2. The presentation follows [Aic04] and is adapted from [Lot17].

Consider the problem of finding the ground state energy of a system determined by a given Hamiltonian with discrete spectrum. A naive way of determining it, would be to choose a suitable basis, rewrite the operator as matrix, diagonalise this matrix and obtain the ground state energy as the lowest eigenvalue among the diagonal elements. Depending on the basis, the matrix is more or less densely filled, but its size increases exponentially with system size. Full diagonalisation (FD) therefore is limited to small systems.

The main restriction, in form of the size of the $N \times N$ Hamiltonian matrix $\boldsymbol{H}$, can be overcome by employing invariant subspaces $\mathscr{K}$ of size $M < N$. These spaces are spanned by vectors $\{|\varphi_i\rangle\}_{i=1,\ldots,M}$ of N components, where the application of the Hamiltonian matrix leads to a linear combination of themselves

$$|\chi\rangle \in \mathscr{K} \Rightarrow \boldsymbol{H}\,|\chi\rangle \in \mathscr{K}\ \forall\ |\chi\rangle \in \mathscr{K}. \tag{2.102}$$

Applying $\boldsymbol{H}$ to an $N \times M$ matrix $\boldsymbol{K}$, whose columns consist of the vectors $|\varphi_i\rangle$ merely produces a new $N \times M$ matrix $\boldsymbol{K}'$ whose columns are linear combinations of the $|\varphi_i\rangle$. From the perspective of a vector to which $\boldsymbol{K}'$ may be applied, the same resulting vector can be obtained by using $\boldsymbol{K}'' = \boldsymbol{K}\,\boldsymbol{H}_M$, where $\boldsymbol{H}_M$ is an $M \times M$ matrix

$$\boldsymbol{H}\,\boldsymbol{K} = \boldsymbol{K}\,\boldsymbol{H}_M. \tag{2.103}$$

Establishing these connections makes it possible to determine the eigenvalues E and eigenvectors $|\Psi\rangle$ of $\boldsymbol{H}$ via the eigenvalues E and eigenvectors $\boldsymbol{K}\,|\Psi\rangle$ of $\boldsymbol{H}_M$

$$\boldsymbol{H}_M\,|\Psi\rangle = E\,|\Psi\rangle \tag{2.104}$$

$$\hookrightarrow \boldsymbol{H}\,[\boldsymbol{K}\,|\Psi\rangle] = E\,[\boldsymbol{K}\,|\Psi\rangle]. \tag{2.105}$$

In this manner, the cost of finding a subset of eigenvalues and eigenvectors of the Hamiltonian matrix is reduced by employing an invariant subspace and the smaller matrix $\boldsymbol{H}_M$.

Within the Lanczos algorithm, the Krylov subspace of the Hamiltonian H being

$$\mathcal{K}_M = \operatorname{linspan}\left\{|x_0\rangle, H\,|x_0\rangle, H^2\,|x_0\rangle, \ldots, H^{M-1}\,|x_0\rangle\right\}, M < N, \tag{2.106}$$

where $|x_0\rangle$ is a normalised random vector, is constructed. Decomposing the initial vector $|x_0\rangle$ into eigenstates of H shows, that $\mathcal{K}_M$ forms an approximately invariant subspace of H.

This is due to the ground state dominating for large M within

$$\begin{aligned} H^M \left|x_0\right\rangle &= H^M \sum_{k=0}^{N} c_k \left|\Psi_k\right\rangle = \sum_{k=0}^{N} c_k E_k^M \left|\Psi_k\right\rangle \\ &= E_0^M \left[c_0 \left|\Psi_0\right\rangle + \sum_{k=1}^{N} c_k \left(\frac{E_k}{E_0}\right)^M \left|\Psi_k\right\rangle \right] \propto \left|\Psi_0\right\rangle , \end{aligned} \tag{2.107}$$

since its energy E_0 is according to amount the largest eigenvalue of H. Coming now to the recursive procedure of the ground state Lanczos algorithm valid at $T = 0$, the initial state $\left|x_0\right\rangle$ is discussed first. Since only an approximately invariant subspace is considered, $\left|x_0\right\rangle$ has to have a finite overlap with the ground state. Without any information on the ground state, a normalised random vector in the canonical basis $\{\boldsymbol{e}_1, \boldsymbol{e}_2, \ldots, \boldsymbol{e}_N\} \in \mathbb{R}^N$ as initial state is sufficient. Having some information on the ground state, the initial state should be written in the basis spanning the subspace characterised by the respective quantum numbers with random coefficients.

Within the Lanczos algorithm, the orthonormal basis of $\mathcal{K}_M$ is constructed by iteratively orthogonalising the vectors spanning the Krylov subspace (2.106) and normalising them afterwards. Starting from $\left|x_0\right\rangle$, the vector emerging from $H\left|x_0\right\rangle$ orthogonal to the initial state is

$$\left|\widetilde{x}_1\right\rangle = H\left|x_0\right\rangle - \alpha_0 \left|x_0\right\rangle , \tag{2.108}$$

where $\alpha_0 = \langle x_0|H|x_0\rangle$. Normalisation gives the Krylov subspace's second basis vector $\left|x_1\right\rangle = \left|\widetilde{x}_1\right\rangle / \|\left|\widetilde{x}_1\right\rangle\|$. For all further states, the strategy can be summarised as iteration rule:

- Construct an orthogonal basis vector: $\left|\widetilde{x}_{n+1}\right\rangle = H\left|x_n\right\rangle - \alpha_n \left|x_n\right\rangle - \beta_n \left|x_{n-1}\right\rangle$
  with:
  - $\alpha_n = \langle x_n|H|x_n\rangle$,
  - $\beta_n = \langle x_{n-1}|H|x_n\rangle = \|\left|\widetilde{x}_n\right\rangle\|$.
- Normalise the basis vector: $\left|x_{n+1}\right\rangle = \dfrac{\left|\widetilde{x}_{n+1}\right\rangle}{\|\left|\widetilde{x}_{n+1}\right\rangle\|}$.

In the following, the vectors forming this Krylov subspace's basis $\{\left|x_i\right\rangle\}_{i=0,\ldots,M-1}$ are called Lanczos vectors. Expressed in terms of the Lanczos vectors, the Hamiltonian matrix is real, symmetric and tridiagonal

$$\langle x_i|H|x_j\rangle = \begin{pmatrix} \alpha_0 & \beta_0 & 0 & \cdots & 0 \\ \beta_0 & \alpha_1 & \beta_1 & 0 & \vdots \\ 0 & \beta_1 & \alpha_2 & \beta_2 & 0 \\ \vdots & 0 & \beta_2 & \ddots & \beta_{M-1} \\ 0 & \cdots & 0 & \beta_{M-1} & \alpha_{M-1} \end{pmatrix} . \tag{2.109}$$

Its eigenvalues $\{\xi_i\}_{i=0,\ldots,M-1}$ converge for large M to the Hamiltonian's eigenvalues within the Krylov subspace $\{E_i\}_{i=0,\ldots,M-1}$. The eigenstates of the Hamiltonian $\{\left|\Psi_i\right\rangle\}_{i=0,\ldots,M-1}$ are obtained by applying the matrix $\boldsymbol{K}$, whose columns consist of the Lanczos vectors, to the eigenvectors $\{\left|\chi_i\right\rangle\}_{i=0,\ldots,M-1}$ of $\langle x_i|H|x_j\rangle$,

$$\left|\Psi_i\right\rangle = \boldsymbol{K}\left|\chi_i\right\rangle . \tag{2.110}$$

In contrast to FD, methods constructing the Hamiltonian only partially and diagonalising it are denoted exact diagonalisation (ED). One problem of Lanczos ED are ‘orthogonality leaks’. This term refers to the loss of orthogonality between the Lanczos vectors due to numerical errors after a sufficient number of iterations. A way to tackle this problem is to reorthogonalise the new Lanczos vectors w.r.t. the old ones every N_{orth} steps.

If one is interested only in the lowest lying eigenvalues as is the case here, one checks every N_{diag} steps by diagonalising the tridiagonal Hamiltonian matrix, whether the ground state is converged and terminates, if this is the case. However it can also happen, that the Lanczos algorithm constructs the whole basis of an invariant subspace, s.t. further iterations do not offer any new information. Hence the norm of the new Lanczos vector should be monitored and the procedure terminated once the norm becomes too small.

Employing the ground state $|\Psi_0\rangle$, expectation values at $T = 0$ can be calculated. The grand potential of a cluster Ω_{cl} at $T = 0$—as required in the zero temperature VCA—is formed by the ground state energy and the particle number

$$\Omega = \varepsilon_0 - \mu \langle \Psi_0 | \hat{N} | \Psi_0 \rangle \,. \tag{2.111}$$

In practice, the chemical potential is included within the Hamiltonian s.t. the grand potential at $T = 0$ is equal to the ground state energy.

In addition to the grand potential, the VCA requires the Green’s function of the cluster. Consider the spectral representation of the single-particle retarded Green’s function

$$G^{\text{ret}}_{\alpha\beta}(E) = \sum_n \left[\frac{\left\langle \Psi_0 \middle| c_\alpha \middle| \Psi^+_n \right\rangle \left\langle \Psi^+_n \middle| c^\dagger_\beta \middle| \Psi_0 \right\rangle}{E - E^+_n + \mathrm{i}0^+} \right] + \sum_m \left[\frac{\left\langle \Psi_0 \middle| c^\dagger_\beta \middle| \Psi^-_m \right\rangle \left\langle \Psi^-_m \middle| c_\alpha \middle| \Psi_0 \right\rangle}{E + E^-_m + \mathrm{i}0^+} \right] \,, \tag{2.112}$$

where $E^\pm_n = \varepsilon^\pm_n - \varepsilon_0$ is the energy difference between the nth excited state $|\Psi^\pm_n\rangle$ with $N \pm 1$ electrons and the ground state $|\Psi_0\rangle$ with N electrons. The Green’s function is characterised by its electron weights $Q^{(\text{e})}_{\alpha n} = \langle \Psi_0 | c_\alpha | \Psi^+_n \rangle$, hole weights $Q^{(\text{h})}_{\beta n} = \langle \Psi_0 | c^\dagger_\beta | \Psi^-_n \rangle$ and poles $E^\pm_n$. In order to obtain these quantities, the ground state $|\Psi_0\rangle$ and its energy ε_0 are approximately determined within a first Lanczos run. From the ground state expressed in the canonical or some specific basis, the states

- $|\Psi^+_\alpha\rangle = c^\dagger_\alpha \, |\Psi_0\rangle$,
- $|\Psi^-_\alpha\rangle = c_\alpha \, |\Psi_0\rangle$,
- $|\Psi^+_\beta\rangle = c^\dagger_\beta \, |\Psi_0\rangle$,
- $|\Psi^-_\beta\rangle = c_\beta \, |\Psi_0\rangle$

are obtained by applying the creation or annihilation operator, i.e. changing the occupation of one of the basis states specified by the indices α, β. Afterwards, the states $|\Psi^+_\beta\rangle$ and $|\Psi^-_\alpha\rangle$ are used as initial states of two additional Lanczos runs to approximately construct two eigenbases $\{|y^+_n\rangle\}_{n=0,\dots,M-1}$ and $\{|y^-_m\rangle\}_{m=0,\dots,M-1}$ of the Hamiltonian to give the poles E^+_n, E^-_m and weights $Q^{(\text{e})}_{\alpha n} Q^{(\text{e})\dagger}_{\beta n}$, $Q^{(\text{h})}_{\beta m} Q^{(\text{h})\dagger}_{\alpha m}$. To reduce the numerical effort, the weights are constructed using matrix elements obtained during the Lanczos runs. They can be inferred by expressing the approximate eigenstates as linear combination of the Lanczos vectors

$$|\Psi^\pm_n\rangle = \sum_i |y^\pm_i\rangle \, \langle y^\pm_i | \Psi^\pm_n \rangle \,. \tag{2.113}$$

Exploiting the orthogonality of the Lanczos vectors $\langle y_i^{\pm}|y_j^{\pm}\rangle = \delta_{ij}$ and that the initial Lanczos vector $|y_0^+\rangle$ is the normalised excited state $|\Psi_\beta^+\rangle\,/\|\,|\Psi_\beta^+\rangle\,\|$, the electron weights become

$$Q_{\alpha n}^{(\mathrm{e})} Q_{\beta n}^{(\mathrm{e})\dagger} = \left[\sum_i \langle \Psi_\alpha^+|y_i^+\rangle\,\langle y_i^+|\Psi_n^+\rangle\right] \cdot \langle \Psi_n^+|y_0^+\rangle \cdot \|\,|\Psi_\beta^+\rangle\,\|, \tag{2.114}$$

requiring only two types of matrix elements to be determined within the Lanczos run. The first type $\langle \Psi_\alpha^+|y_i^+\rangle$ contains the overlap of any initial Lanczos vector $\left\{|y_0^+\rangle = |\Psi_\alpha^+\rangle\,/\|\,|\Psi_\alpha^+\rangle\,\|\right\}_\alpha$ of any Lanczos run with the ith Lanczos vector $|y_i^+\rangle$ of a specific run β. For the second type $\langle y_i^+|\Psi_n^+\rangle$, the matrix elements contain the coefficients of the Hamiltonians eigenstates expressed by Lanczos vectors. In contrast, the norms of any initial vector $\|\,|\Psi_\beta^+\rangle\,\|$ can be determined in advance of all Lanczos runs. For the hole part with the initial Lanczos vector $|y_0^-\rangle = |\Psi_\alpha^-\rangle\,/\|\,|\Psi_\alpha^-\rangle\,\|$, the respective weights are

$$Q_{\beta m}^{(\mathrm{h})} Q_{\alpha m}^{(\mathrm{h})\dagger} = \left[\sum_i \langle \Psi_\beta^-|y_i^-\rangle\,\langle y_i^-|\Psi_m^-\rangle\right] \cdot \langle \Psi_m^-|y_0^-\rangle \cdot \|\,|\Psi_\alpha^-\rangle\,\|. \tag{2.115}$$

Note that the two Lanczos runs have to be performed for all combinations of indices α, β. Using this procedure in combination with the cluster Hamiltonian yields the cluster Green's function.

2 3 2 Continued fraction representation

The continued fraction representation of the Green's function can be obtained without having to diagonalise the tridiagonal Hamiltonian in the Lanczos basis. It can thus be used in combination with a matrix-product state solver which will be discussed in section 3. The presentation follows [Sén08].

In case the cluster solver does not allow to diagonalise the tridiagonal Hamiltonian to obtain the Green's function, the spectral representation cannot be constructed since the eigenenergies are not available. The continued fraction representation only requires the tridiagonal structure of the Hamiltonian and circumvents diagonalising the Hamiltonian in the sector of excitated states.

Starting from the spectral representation of the retarded single-particle Green's function in equation (2.112), one obtains by removing the identity within the excited subspace

$$G_{AB}^{\mathrm{ret}}(z) = G_{AB}^+(z) - G_{BA}^-(z) \tag{2.116}$$

with the complex energy $z = E + \mathrm{i}\,\eta$, $\eta > 0$, the operators $A = c_\alpha$ $B = c_\beta^\dagger$ as well as the short-hand notation

$$G_{AB}^{\pm}(z) = \langle \Psi_0|A[\pm z - (H - \varepsilon_0)]^{-1}B|\Psi_0\rangle\,. \tag{2.117}$$

Exploiting the three-band structure of the Hamiltonian matrix obtained after evaluating the Lanczos algorithm given in equation (2.109), one can compute the diagonal part of the resolvent by means of Cramer's rule [Dag94] as a continued fraction

$$G_{c_\alpha, c_\alpha^\dagger}^+(z) = \cfrac{\beta_0^2}{+z - \alpha_0 + \varepsilon_0 - \cfrac{\beta_1^2}{+z-\alpha_1+\varepsilon_0-\cfrac{\beta_2}{+z-\alpha_2+\varepsilon_0-\ldots}}}, \tag{2.118}$$

$$-G_{c_\alpha^\dagger, c_\alpha}^-(z) = \cfrac{\beta_0^2}{-z - \alpha_0 + \varepsilon_0 - \cfrac{\beta_1^2}{-z-\alpha_1+\varepsilon_0-\cfrac{\beta_2}{-z-\alpha_2+\varepsilon_0-\ldots}}}, \tag{2.119}$$

where $\{\alpha_i\}_{i=0,\dots,M-1}$ and $\{\beta_i\}_{i=0,\dots,M-1}$ are the entries of the Hamiltonian within the excited state sectors.

In practice, the maximal number of Lanczos iterations determines the cut off. To obtain the off-diagonal entries of the Green's function with $\alpha \neq \beta$, one considers linear combinations [Sén08], which is sufficient in case $G^+_{c_\alpha, c_\beta^\dagger}(z) = G^+_{c_\beta, c_\alpha^\dagger}(z)$ holds

$$G^+_{c_\alpha, c_\beta^\dagger}(z) = \frac{1}{2}\left[G^+_{c_\alpha + c_\beta, c_\alpha^\dagger + c_\beta^\dagger}(z) - G^+_{c_\alpha, c_\alpha^\dagger}(z) - G^+_{c_\beta, c_\beta^\dagger}(z) \right], \tag{2.120}$$

$$G^-_{c_\beta^\dagger, c_\alpha}(z) = \frac{1}{2}\left[G^-_{c_\alpha^\dagger + c_\beta^\dagger, c_\alpha + c_\beta}(z) - G^-_{c_\alpha^\dagger, c_\alpha}(z) - G^-_{c_\beta^\dagger, c_\beta}(z) \right]. \tag{2.121}$$

In general, only $G^+_{c_\alpha, c_\beta^\dagger}(z) = G^+_{c_\beta, c_\alpha^\dagger}(z^*)^*$ is valid, s.t. one needs to consider complex combinations of two annihilation and creation operators respectively. Considering the spectral representation (2.112), the weights occuring therein can be complex. When evaluating the Lanczos algorithm with a real valued starting vector, the Hamiltonian determines whether the Lanczos vectors are real valued as well. Complex couplings, such as spin-orbit coupling, can lead to complex Lanczos vectors, which may imply a complex ground and/or complex excited states entering the weights. For the one-band Hubbard model without complex couplings, the case presented above is sufficient. The details in case complex combinations become necessary are shown in appendix C of [SSY18] and remain to be implemented.

2 3 3 Band Lanczos algorithm

◈*The Band Lanczos algorithm allows resolving degenerate or clustered eigenvalues. Constructing a joint Krylov subspace of all excited states occuring in the electron/hole part of the Green's function makes it possible to separate weights from poles leading to the Q-matrix representation of the Green's function to be introduced in section 2.3.6. In the context of VCA, this enables performing the contour integration analytically. The presentation follows [Fre00; Ali+99].*◈

A major drawback of the approach described in section 2.3.1 is that for the computation of the Green's function, every initial vector $\left\{ |y_0^\pm\rangle = |\Psi_\alpha^\pm\rangle / \| \, |\Psi_\alpha^\pm\rangle \, \| \right\}_\alpha$ generates its own Krylov subspace. Hence in general, the poles and eigenstates are different for each initial vector, thus blurring the distinction between poles and weights by requiring the Green's function to be evaluated at explicite energies E for further computations. The ability to treat poles and weights separately can be regained by using all initial vectors $\{|\Psi_\alpha^\pm\rangle\}$ to construct one Krylov subspace with one joint set of eigenstates and corresponding poles. This is achieved using the Band Lanczos algorithm [Fre00]. Furthermore, degenerate or clustered eigenvalues can be resolved using the Band Lanczos algorithm which becomes important at finite temperature.

Starting from the set of initial random vectors $\{|\mathscr{C}_0\rangle, \dots, |\mathscr{C}_{B-1}\rangle\} = \{|\mathscr{C}_\alpha\rangle\}_{\alpha=0,\dots,B-1}$, a basis of the Krylov subspace is constructed. After the first vector $|\mathscr{C}_0\rangle$ is normalised and accepted as Lanczos vector $|x_0\rangle$, a new 'candidate' vector $|\mathscr{C}_B\rangle = H\,|x_0\rangle$ is created. The new set of candidates $\{|\mathscr{C}_\alpha\rangle\}_{\alpha=1,\dots,B}$ is then orthogonalised w.r.t. the newly accepted Lanczos vector $|x_0\rangle$. For the following $B-1$ initial candidates, $\{|\mathscr{C}_\alpha\rangle\}_{\alpha=1,\dots,B-1}$, the same is done: they are normalised and accepted as Lanczos vector or, as candidates, orthogonalised w.r.t. the newly accepted Lanczos vector. However the newly created candidate $|\mathscr{C}_{i+B}\rangle = H\,|x_{i>0}\rangle$ is in addition orthogonalised w.r.t. all previously accepted Lanczos vectors. After all B initial vectors are handled this way, one ends up with a list of $2B+1$ vectors

$$[\,|x_0\rangle, \dots, |x_{B-1}\rangle, |\mathscr{C}_B\rangle, \dots, |\mathscr{C}_{2B}\rangle, |\cdot\rangle\,], \tag{2.122}$$

of B Lanczos vectors, B candidates and one empty entry. This empty entry $|\cdot\rangle$ serves as space for the candidate of the next iteration $H\,|x_B\rangle$, which is generated from $|\mathscr{C}_B\rangle$ being the 'current' candidate of the $(B+1)$th iteration. In the following iterations, the oldest Lanczos vector is removed from the list (2.122) and the newly accepted Lanczos vector is added. The new candidate is always orthogonalised w.r.t. the B Lanczos vectors in the list (2.122), while the old candidates are only orthogonalised w.r.t. the newest Lanczos vector. One way to imagine the procedure is to shift the list (2.122) by one element to the left while adding one at the right, giving

$$[|x_1\rangle\,,\ldots,|x_B\rangle\,,|\mathscr{C}_{B+1}\rangle\,,\ldots,|\mathscr{C}_{2B+1}\rangle\,,|\cdot\rangle]. \tag{2.123}$$

There is an additional difference compared to the regular Lanczos algorithm: When the norm of a vector becomes (approximately) zero, the procedure does not need to terminate. Since each initial random vector may sweep its own invariant subspace, a zero norm means only, that this specific Lanczos vector does not yield any further information and should not be included in further iterations. This means, that the bandwidth $2B+1$ and the list size are reduced by two, since no new Lanczos vector implies no new candidate, giving

$$[|x_1\rangle\,,\ldots,|x_{B-1}\rangle\,,|\mathscr{C}_{B}\rangle\,,\ldots,|\mathscr{C}_{2B-1}\rangle\,,|\cdot\rangle]. \tag{2.124}$$

Only once B vectors have been removed from the list (2.122) leaving the list empty, all available information has been obtained. Once one removes a vector from the list (2.122), one has to make sure, that the Lanczos vectors remain out of the exhausted invariant subspace. For that purpose, the vector $|x_i\rangle$ generating the removed candidate $|\mathscr{C}_{i+B}\rangle = H\,|x_i\rangle$ is kept and all further new candidates are orthogonalised w.r.t. $|x_i\rangle$. Removal of these vectors and orthogonalisation w.r.t. the generating vector is called 'deflation'. This leads to the following schematic shape of the Hamiltonian matrix:

$$\langle x_i|H|x_j\rangle =$$

$$\begin{pmatrix}
\colorbox{cyan}{H_{11}} & H_{12} & H_{13} & H_{14} & H_{15} & H_{16} & 0\cdots\cdots & & & & & & \\
\colorbox{red}{H_{21}} & \colorbox{cyan}{H_{22}} & H_{23} & H_{24} & H_{25} & H_{26} & H_{27} & 0\cdots\cdots & & & & & \\
\colorbox{red}{H_{31}} & \colorbox{red}{H_{32}} & \colorbox{cyan}{H_{33}} & H_{34} & H_{35} & H_{36} & H_{37} & \colorbox{orange}{H_{38}} & \colorbox{orange}{H_{39}} & \colorbox{orange}{$H_{3,10}$} & \colorbox{orange}{$H_{3,11}$} & \colorbox{orange}{$H_{3,12}$} & \colorbox{orange}{$H_{3,13}$} \\
\colorbox{red}{H_{41}} & \colorbox{red}{H_{42}} & \colorbox{red}{H_{43}} & \colorbox{cyan}{H_{44}} & H_{45} & H_{46} & H_{47} & H_{48} & 0\cdots\cdots & & & & \\
\colorbox{red}{H_{51}} & \colorbox{red}{H_{52}} & \colorbox{red}{H_{53}} & \colorbox{red}{H_{54}} & \colorbox{cyan}{H_{55}} & H_{56} & H_{57} & H_{58} & H_{59} & 0\cdots\cdots & & & \\
\colorbox{green}{H_{61}} & \colorbox{red}{H_{62}} & \colorbox{red}{H_{63}} & \colorbox{red}{H_{64}} & \colorbox{red}{H_{65}} & \colorbox{cyan}{H_{66}} & H_{67} & H_{68} & H_{69} & H_{6,10} & 0\cdots\cdots & & \\
0 & \colorbox{green}{H_{72}} & \colorbox{red}{H_{73}} & \colorbox{red}{H_{74}} & \colorbox{red}{H_{75}} & \colorbox{red}{H_{76}} & \colorbox{cyan}{H_{77}} & H_{78} & H_{79} & H_{7,10} & \colorbox{orange}{$H_{7,11}$} & \colorbox{orange}{$H_{7,12}$} & \colorbox{orange}{$H_{7,13}$} \\
\vdots & 0 & H_{83} & \colorbox{green}{H_{84}} & \colorbox{red}{H_{85}} & \colorbox{red}{H_{86}} & \colorbox{red}{H_{87}} & \colorbox{cyan}{H_{88}} & H_{89} & H_{8,10} & H_{8,11} & 0\cdots\cdots & \\
 & \vdots & H_{93} & 0 & \colorbox{green}{H_{95}} & \colorbox{red}{H_{96}} & \colorbox{red}{H_{97}} & \colorbox{red}{H_{98}} & \colorbox{cyan}{H_{99}} & H_{9,10} & H_{9,11} & H_{9,12} & 0 \\
 & & H_{10,3} & \vdots & 0 & \colorbox{green}{$H_{10,6}$} & \colorbox{red}{$H_{10,7}$} & \colorbox{red}{$H_{10,8}$} & \colorbox{red}{$H_{10,9}$} & \colorbox{cyan}{$H_{10,10}$} & H_{10,11} & H_{10,12} & \colorbox{orange}{$H_{10,13}$} \\
 & & H_{11,3} & & \vdots & 0 & H_{11,7} & \colorbox{green}{$H_{11,8}$} & \colorbox{red}{$H_{11,9}$} & \colorbox{red}{$H_{11,10}$} & \colorbox{cyan}{$H_{11,11}$} & H_{11,12} & H_{11,13} \\
 & & H_{12,3} & & & \vdots & H_{12,7} & 0 & \colorbox{green}{$H_{12,9}$} & \colorbox{red}{$H_{12,10}$} & \colorbox{red}{$H_{12,11}$} & \colorbox{cyan}{$H_{12,12}$} & H_{12,13} \\
 & & H_{13,3} & & & & H_{13,7} & \vdots & 0 & H_{13,10} & \colorbox{green}{$H_{13,11}$} & \colorbox{red}{$H_{13,12}$} & \colorbox{cyan}{$H_{13,13}$}
\end{pmatrix}. \tag{2.125}$$

Within the blue diagonal entries, the overlap between the new accepted Lanczos vector $|y_j\rangle$ and the new candidate $|\mathscr{C}_{j+B}\rangle$ before orthogonalisation

$$|\mathscr{C}_{j+B}\rangle \rightarrow |\mathscr{C}_{j+B}\rangle - |y_j\rangle \, \langle y_j|\mathscr{C}_{j+B}\rangle \tag{2.126}$$

are contained. The red off-diagonal entries below the diagonal contain the overlap between the new accepted Lanczos vector $|y_j\rangle$ with the old candidates $|\mathscr{C}_k\rangle$ before they are orthogonalised

$$|\mathscr{C}_k\rangle \rightarrow |\mathscr{C}_k\rangle - |y_j\rangle \, \langle y_j|\mathscr{C}_k\rangle . \tag{2.127}$$

The green entries further below the diagonal are the norms of the candidates $|\mathscr{C}_j\rangle$, which are generated by application of the Hamiltonian, once they are normalised to become accepted Lanczos vectors $|y_j\rangle$

$$\langle y_j|\mathscr{C}_j\rangle = \| \, |\mathscr{C}_j\rangle \, \| . \tag{2.128}$$

When vectors are deflated, the overlap between the generating vector $|y_\ell\rangle$ and the new candidate $|\mathscr{C}_{j+B}\rangle$,

$$|\mathscr{C}_{j+B}\rangle \rightarrow |\mathscr{C}_{j+B}\rangle - |y_\ell\rangle \, \langle y_\ell|\mathscr{C}_{j+B}\rangle \tag{2.129}$$

give rise to the orange entries which form a ‘fishbone’ structure. The remaining entries are obtained by complex conjugation, since the Hamiltonian is a Hermitian matrix. Note, that the Band Lanczos algorithm without deflation leads to a band matrix with bandwidth $2B+1$. This bandwidth is reduced by two entries each time deflation occurs, hence the routine to diagonalise the remaining matrix has to be selected accordingly.

In accordance with regular Lanczos ED, one may deal with ‘orthogonality leaks’ via reorthogonalisation w.r.t. saved Lanczos vectors and terminate the procedure once the required number of eigenvalues is converged. Also in analogy to regular Lanczos ED, the eigenenergies of the Hamiltonian are given by the eigenvalues of the Hamiltonian matrix in the basis of Lanczos vectors, whereas the eigenstates follow from the basis transformation (2.110). More details and an explicit listing of the algorithm for Hermitian matrices can be found in [Fre00]. A more general and cleaner presentation for complex $N \times N$-matrices can be found in [Ali+99].

At $T = 0$, regular Lanczos ED is sufficient to determine the ground state. Hence the cluster grand potential can be determined via equation (2.111). However for the single-particle retarded Green’s function of a system with degenerate ground state or due to practical reasons mentioned at the beginning of the section, it is reasonable to employ Band Lanczos ED for construction of the basis of excited states $|\Psi^\pm_\alpha\rangle$. Starting from the set of normalised states $\left\{ |\mathcal{Y}^+_\beta\rangle = |\Psi^+_\beta\rangle / \| \, |\Psi^+_\beta\rangle \, \| \right\}_\beta$ as initial states of the Band Lanczos algorithm allows constructing the basis $\{|y^+_n\rangle\}$. Using this basis for the weights of the single-particle retarded Green’s function yields

$$Q^{(e)}_{\alpha n} Q^{(e)\dagger}_{\beta n} = \| \, |\Psi^+_\alpha\rangle \, \| \cdot \left[\sum_i \langle \mathcal{Y}_\alpha|y^+_i\rangle \, \langle y^+_i|\Psi^+_n\rangle \right] \cdot \left[\sum_j \langle \Psi^+_n|y^+_j\rangle \, \langle y^+_j|\mathcal{Y}^+_\beta\rangle \right] \cdot \| \, |\Psi^+_\beta\rangle \, \| , \tag{2.130}$$

where the second basis $\{|y^+_j\rangle\}$ is needed since $|\mathcal{Y}^+_\beta\rangle$ is **not** a basis vector. Following the first B steps of the Band Lanczos algorithm, the initial vectors are orthogonalised stepwise, which may be rewritten as

$$|\mathcal{Y}^+_\beta\rangle = |\tilde{y}^+_k\rangle + \sum_{i=0}^{k-2} |y^+_i\rangle \, \langle y^+_i|\mathcal{Y}^+_\beta\rangle , \tag{2.131}$$

where $\left\{|y_i^+\rangle\right\}_{i=1,\dots,k-1}$ are normalised Lanczos vectors, while $|\tilde{y}_k^+\rangle$ is not yet normalised. Computing the overlap with a (normalised) Lanczos vector $|y_j^+\rangle$ explicitely

$$\langle y_j^+|\mathcal{Y}_\beta^+\rangle = \|\,|\tilde{y}_k^+\rangle\,\|\delta_{jk} + \delta_{j\in[0,k-2]}\delta_{k\neq 0}\,\langle y_j^+|\mathcal{Y}_\beta^+\rangle \tag{2.132}$$

proves the above claim. Writing the overlap as matrix, one finds a square, upper triangular matrix whose rank is given by the number of initial vectors

$$\langle y_j^+|\mathcal{Y}_\beta^+\rangle = \begin{pmatrix} \|\,|\tilde{y}_0^+\rangle\,\| & \langle y_0^+|\mathcal{Y}_1^+\rangle & \cdots & \cdots & \langle y_0^+|\mathcal{Y}_{B-1}^+\rangle \\ 0 & \|\,|\tilde{y}_1^+\rangle\,\| & \langle y_1^+|\mathcal{Y}_2^+\rangle & \cdots & \langle y_1^+|\mathcal{Y}_{B-1}^+\rangle \\ \vdots & \ddots & \ddots & \ddots & \vdots \\ \vdots & & \ddots & \ddots & \langle y_{B-2}^+|\mathcal{Y}_{B-1}^+\rangle \\ 0 & \cdots & \cdots & 0 & \|\,|\tilde{y}_{B-1}^+\rangle\,\| \end{pmatrix}. \tag{2.133}$$

For the weights, one needs the norms of the initial vectors $\|\,|\Psi_\alpha^+\rangle\,\|$, which can be determined before the Band Lanczos run. During the first B steps of the Band Lanczos algorithm, one computes the overlap between the normalised initial vectors $|\mathcal{Y}_\alpha^+\rangle$ and the Lanczos vectors $|y_i^+\rangle$ filling the matrix (2.133). Diagonalising the Hamiltonian gives the coefficients of the Hamiltonians eigenvectors expressed by the Lanczos vectors $\langle y_i^+|\Psi_n^+\rangle$ as well as the eigenvalues for the poles. The weights for the hole part are

$$Q^{(\mathrm{h})}_{\beta m}Q^{(\mathrm{h})\dagger}_{\alpha m} = \|\,|\Psi_\beta^-\rangle\,\| \cdot \left[\sum_i \langle\mathcal{Y}_\beta|y_i^-\rangle\,\langle y_i^-|\Psi_m^-\rangle\right] \cdot \left[\sum_j \langle\Psi_m^-|y_j^-\rangle\,\langle y_j^-|\mathcal{Y}_\alpha^-\rangle\right] \cdot \|\,|\Psi_\alpha^-\rangle\,\|. \tag{2.134}$$

2 3 4 Chebyshev expansion

◈*Computing the Green's function as expansion of Chebyshev polynomials requires only the evaluation of a recursion relation. Since no basis is constructed, orthogonality does not has to be enforced. Furthermore no diagonalisations have to be performed. It thus provides an alternative representation of the Green's function to be employed with a matrix-product state solver. The presentation follows [Wei+06; BS14].*◈

There appear to be two branches of expanding the single-particle retarded Green's function into orthogonal polynomials, the Kernel polynomial method (KPM) [Wei+06] and a brute-force expansion [BS14]. Here, only Chebyshev polynomials $T_n(x)$ are discussed, although other orthogonal polynomials such as Legendre polynomials [Boe15] are used in practice as well.

Within the KPM [Wei+06], the limit of zero broadening $\eta\rightarrow 0$ is considered, where the imaginary part of the Green's functions' spectral representation of equation (2.112) becomes for real weights a sum of δ-distributions with the Green's functions' poles as roots

$$\begin{aligned}\lim_{\eta\rightarrow 0}\mathrm{Im}[G^{\mathrm{ret}}_{\alpha\beta}(z=E+\mathrm{i}\,\eta)] = &-\pi\sum_n\left[Q^{(\mathrm{e})}_{\alpha n}Q^{(\mathrm{e})\dagger}_{\beta n}\delta(E-E_n^+)\right] \\ &-\pi\sum_m\left[Q^{(\mathrm{h})}_{\beta m}Q^{(\mathrm{h})\dagger}_{\alpha m}\delta(E+E_m^-)\right].\end{aligned} \tag{2.135}$$

The arguments of these δ-distributions are rescaled into the interval $[-1,1]$ as

$$
\begin{aligned}
(E \mp E_n^{\pm}) &\rightarrow \frac{1}{a}\cdot(E \mp E_n^{\pm} - b) = (\tilde{E} \mp \tilde{E}_n^{\pm}) \in [-1,1], && (2.136)\\
a &= \frac{\varepsilon_{\max}^{\pm} - \varepsilon_{\min}^{\pm}}{2-\delta}, && (2.137)\\
b &= \frac{\varepsilon_{\max}^{\pm} + \varepsilon_{\min}^{\pm}}{2} - \varepsilon_0 && (2.138)
\end{aligned}
$$

with $\delta \sim 0.01$ and expanded into Chebyshev polynomials giving 'moments' $\mu_j^{\pm}$ as expansion coefficients

$$
\begin{aligned}
\sum_n Q_{\alpha n}^{(\mathrm{e})} Q_{\beta n}^{(\mathrm{e})\dagger} \delta(\tilde{E} - \tilde{E}_n^{+}) &= -\frac{1}{\sqrt{1-\tilde{E}^2}} \left[\mu_0^{+} + 2\sum_{j=1}^{\infty} \mu_j^{+} T_j(\tilde{E})\right], && (2.139)\\
\mu_j^{+} &= \sum_n Q_{\alpha n}^{(\mathrm{e})} Q_{\beta n}^{(\mathrm{e})\dagger} \int_{[-1,1]} \mathrm{d}x\, \delta(\tilde{E} - \tilde{E}_n^{+}) T_j(\tilde{E})\\
&= \sum_n Q_{\alpha n}^{(\mathrm{e})} Q_{\beta n}^{(\mathrm{e})\dagger} T_j(+\tilde{E}_n^{+}) = \langle \Psi_0 | c_\alpha T_j(\tilde{H} - \tilde{\varepsilon}_0) c_\beta^{\dagger} | \Psi_0 \rangle\,, && (2.140)\\
\sum_m Q_{\beta m}^{(\mathrm{h})} Q_{\alpha m}^{(\mathrm{h})\dagger} \delta(\tilde{E} + \tilde{E}_n^{-}) &= -\frac{1}{\sqrt{1-\tilde{E}^2}} \left[\mu_0^{-} + 2\sum_{j=1}^{\infty} \mu_j^{-} T_j(\tilde{E})\right], && (2.141)\\
\mu_j^{-} &= \sum_n Q_{\beta m}^{(\mathrm{h})} Q_{\alpha m}^{(\mathrm{h})\dagger} \int_{[-1,1]} \mathrm{d}x\, \delta(\tilde{E} + \tilde{E}_n^{-}) T_j(\tilde{E})\\
&= \sum_m Q_{\beta m}^{(\mathrm{h})} Q_{\alpha m}^{(\mathrm{h})\dagger} T_j(-\tilde{E}_n^{-}) = \langle \Psi_0 | c_\beta^{\dagger} T_j(-\tilde{H} - \tilde{\varepsilon}_0) c_\alpha | \Psi_0 \rangle\,. && (2.142)
\end{aligned}
$$

Here and in the remainder of this section, a tilde highlights quantities rescaled according to equation (2.136). By exploiting the recursion relations of the Chebyshev polynomials, the moments $\mu_j^{\pm}$ are constructed in an iterative fashion similar to the Lanczos algorithm

$$
\begin{aligned}
|y_0^{\pm}\rangle &= |\Psi_{\beta,\alpha}^{\pm}\rangle\,, && (2.143)\\
|y_1^{\pm}\rangle &= \tilde{H}\,|y_0^{\pm}\rangle\,, && (2.144)\\
|y_j^{\pm}\rangle &= 2\tilde{H}\,|y_{j-1}^{\pm}\rangle - |y_{j-2}^{\pm}\rangle\,, && (2.145)\\
\hookrightarrow \mu_j^{\pm} &= \langle \Psi_{\alpha,\beta}^{\pm} | y_j^{\pm} \rangle\,. && (2.146)
\end{aligned}
$$

In contrast to Lanczos or Band Lanczos ED, no basis of an invariant subspace is constructed, s.t. no reorthogonalisation is required. Since numerically only a finite expansion order can be handled, the series is truncated. To prevent Gibbs oscillations in the expanded function, additional 'kernel' functions are multiplied to the moments for damping, giving the method its name. These kernel functions also influence the broadening of the spectrum obtained from the Green's function. After the imaginary part of the Green's function is obtained, the real part is constructed as the Hilbert transform of the imaginary part

$$
\mathrm{Re}[G_{\alpha\beta}^{\mathrm{ret}}(\tilde{E})] = -\frac{1}{\pi}\mathcal{P}\int_{[-1,1]} \mathrm{d}E'\, \frac{\mathrm{Im}[G_{\alpha\beta}^{\mathrm{ret}}(E')]}{\tilde{E} - E'}. \qquad (2.147)
$$

Within each step, additional analytical properties of the Chebyshev polynomials can be exploited.

Two major drawbacks prevent using the KPM for VCA. First, it requires an operator whose eigenvalues form the poles of the Green's function which is expanded. At least from the perspective of constructing the moments as matrix elements by applying an operator to states requires the existence of the operator. This might be different from a Quantum Monte Carlo perspective. For the cluster Green's, function the cluster Hamiltonian exists, whereas the CPT Green's function lacks an explicit operator. Having such an operator would simplify VCA enormously and is not likely to be possible. Second, the KPM is restricted to real energies, hence a contour integration with complex energy arguments is not possible. This is related to the limit of zero broadening meaning zero imaginary part of the complex energies. There are implementations of the KPM in combination with Quantum Monte Carlo [Gul+18] using purely imaginary energies, but this is merely a constant phase which can be moved into the function keeping the argument real. In the end, both reasons conspire against the application in VCA. Due to the second issue, one must perform the semi-analytical treatment of VCA described in section 2.3.6, where the Matsubara energy summation/contour integration is performed analytically, leaving only a dependence on real energies. However, the issue of complex energies is replaced by the requirement of knowing the poles of the CPT Green's function. In the context of KPM, this corresponds to knowing the operator having these poles as eigenvalues.

Performing a brute-force expansion into Chebyshev polynomials [BS14] allows explicitely the usage of complex energy arguments. The relevant expressions for $T = 0$ are rederived in the following, since the notation of Braun and Schmitteckert is sometimes unclear and some expressions will be kept in a different form due to the possibility of branch cuts of complex roots. Depending on where the branch cuts of functions are located for a given programming language or library, the domain of the function may have to be altered by shifting its argument [Chy+11].

Starting from the spectral representation of the retarded single-particle Green's function in equation (2.112), one obtains by removing the identity within the excited subspace

$$G^{\mathrm{ret}}_{AB}(z) = G^{+}_{AB}(z) - G^{-}_{BA}(z) \tag{2.148}$$

with the complex energy $z = E + \mathrm{i}\,\eta$, $\eta > 0$, the operators $A = c_\alpha$ $B = c^\dagger_\beta$ as well as the short-hand notation

$$G^{\pm}_{AB}(z) = \langle\Psi_0|A[\pm z - (H - \varepsilon_0)]^{-1}B|\Psi_0\rangle\,. \tag{2.149}$$

Considering only the resolvent function $f^{\pm}_{z}(x) = [\pm z - x]^{-1}$ occuring therein, one can rescale the argument x into the range $[-1, 1]$ using its maximum and minimum values as

$$x \rightarrow \tilde{x} = \frac{x - b}{a} \in [-1, 1], \tag{2.150}$$

$$a = \frac{x_{\max} - x_{\min}}{2 - \delta}, \tag{2.151}$$

$$b = \frac{x_{\max} + x_{\min}}{2}, \tag{2.152}$$

with $\delta \sim 0.01$ to avoid values on the margin. W.r.t. this rescaled argument, the resolvent function becomes

$$f^{\pm}_{z}(\tilde{x}) = a^{-1} \cdot \left[\pm\frac{1}{a}(z \mp b) - \tilde{x}\right]^{-1}. \tag{2.153}$$

Expanding the resolvent function into Chebyshev polynomials yields

$$f_z^{\pm}(\tilde{x}) = a^{-1} \sum_{n=0}^{\infty} \alpha_n^{\pm}\left(\frac{z \mp b}{a}\right) T_n(\tilde{x}) \tag{2.154}$$

with the coefficients

$$\alpha_n^{\pm}(z) = \frac{2/\pi}{1+\delta_{n,0}} \int\limits_{[-1,1]} \mathrm{d}\,x\, \frac{T_n(x)}{\sqrt{1-x^2}} f_z^{\pm}(x). \tag{2.155}$$

Writing the resolvent function therein as Laplace transform

$$f_z^{\pm}(x) = -\mathrm{i} \int_{[0,\pm\infty)} \mathrm{d}\,t\, \exp(\mathrm{i}[\pm z - x]t) \tag{2.156}$$

with $z = E + \mathrm{i}\,\eta$, $\eta > 0$ to ensure convergence and extending the integral range as $[-1,1] \rightarrow \mathbb{R}$ while fixing the domain of the Chebyshev polynomials with $T_n(x)|_{|x|>1} = 0$, one obtains

$$\alpha_n^{\pm}(z) = \frac{-2\,\mathrm{i}/\pi}{1+\delta_{n,0}} \int_{[0,\pm\infty)} \mathrm{d}\,t\, \exp(\pm\,\mathrm{i}\,z t) \int_{\mathbb{R}} \mathrm{d}\,x\, \frac{T_n(x)}{\sqrt{1-x^2}} \exp(-\,\mathrm{i}\,x t). \tag{2.157}$$

Interpreting the second integral as Fourier transform, one obtains with equation 11.4.24 in [AS72]

$$\int_{\mathbb{R}} \mathrm{d}\,x\, \frac{T_n(x)}{\sqrt{1-x^2}} \exp(-\,\mathrm{i}\,x t) = (-\mathrm{i})^n \pi J_n(t), \tag{2.158}$$

where $J_n(t) = (-1)^n J_n(-t)$ is the Bessel function of first kind. After substitution $\tau = \pm t$ and defining $\mathrm{i}\,z \equiv -s$, the coefficients take the form of a Laplace transform

$$\alpha_n^{\pm}(z) = \pm \frac{2(-\mathrm{i})^{n+1}}{1+\delta_{n,0}} \int_{[0,\infty)} \mathrm{d}\,\tau\, \exp(-s\tau) J_n(\pm\tau). \tag{2.159}$$

Using equation 29.3.56 in [AS72] which requires $n > -1$, one ends up with the coefficients

$$\alpha_n^{\pm}(z) = (\pm 1)^{n+1} \frac{2(-\mathrm{i})^{n+1}}{1+\delta_{n,0}} \left(\sqrt{1-z^2} + \mathrm{i}\,z\right)^n \sqrt{1-z^2}^{\,-1}. \tag{2.160}$$

The real and imaginary part of some coefficients on the complex plane are shown in the figures 2.11 and 2.12. Their range is restricted to $[-1,1]$ since everything beyond this range are signatures of poles and branch cuts. Already $\mathrm{Re}[\alpha_{n=0}^{+}(z)]$ exhibits branch cuts along most of the real axis. These discontinuities of multivalued complex functions are more pronounced for higher n, where they show up as boundaries between entirely black and white regions. It appears that besides branch cuts along the real axis they occur in the lower part of the complex plane. For the real part, $n-1$ branch cuts occur for $n \geq 2$, while the imaginary part exhibits $n-2$ branch cuts in case $n \geq 3$.

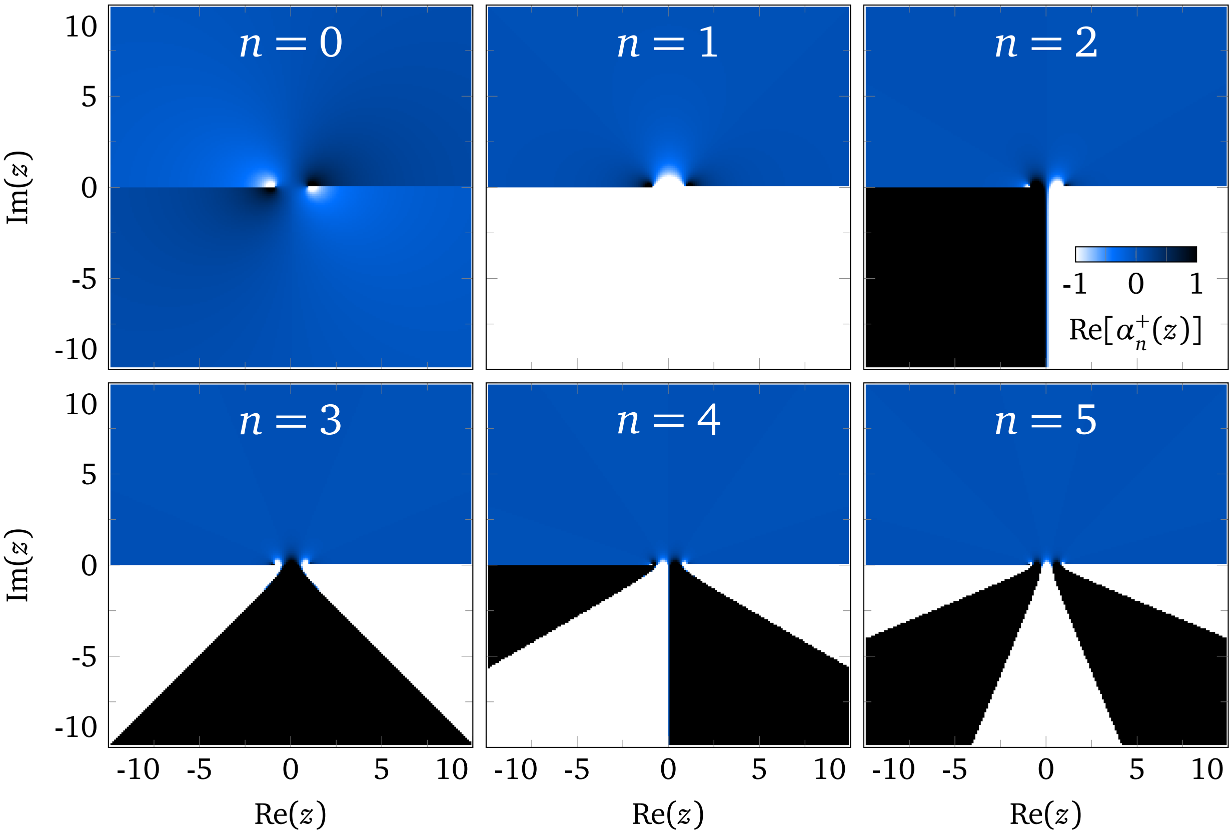

■ **2.11** – Real part of the coefficients $\mathrm{Re}[\alpha_n^+(z)]$ for $n \in \{0,1,2,3,4,5\}$ on the complex plane. Its range is restricted to $[-1,1]$ since everything beyond this range are signatures of poles and branch cuts.

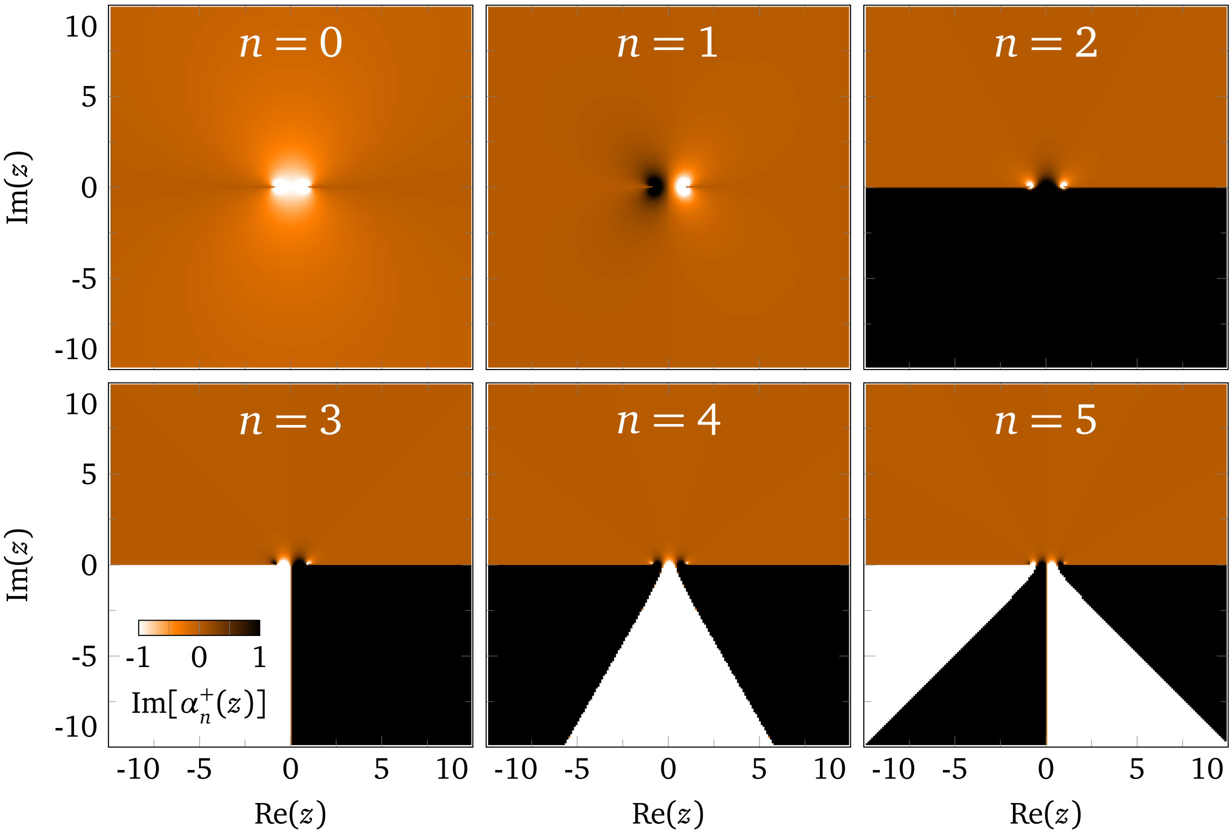

■ **2.12** – Imaginary part of the coefficients $\mathrm{Im}[\alpha_n^+(z)]$ for $n \in \{0,1,2,3,4,5\}$ on the complex plane. Its range is restricted to $[-1,1]$ since everything beyond this range are signatures of poles and branch cuts.

Note that in case of vanishing η, the Laplace transform in equation (2.156) does not yield the resolvent since the limit $L \to \infty$ of the integral

$$-\mathrm{i} \int_{[0,\pm L]} \mathrm{d}\, t \, \exp(\mathrm{i}[\pm z - x]t) = \frac{1 - \exp(\pm\, \mathrm{i}[\pm z - x]L)}{\pm z - x} \tag{2.161}$$

is ambiguous with a purely real z. In practice this turned out to be of no concern.

Coming back to the Green's function in equation (2.149) gives the expression

$$G^{\pm}_{AB}(z) = a^{-1} \sum_{n=0}^{\infty} \alpha^{\pm}_{n} \left(\frac{z \mp b}{a} \right) \langle \Psi_0 | A T_n(\tilde{H} - \tilde{\varepsilon}_0) B | \Psi_0 \rangle \,. \tag{2.162}$$

It is obtained as follows:

1) Determine the scaling parameters a and b via the equations (2.137) and (2.138) by performing two Lanczos runs for each excited state sector. The maximal eigenvalue can be obtained by inverting the sign of the Hamiltonian within the Lanczos algorithm.
2) Compute the ground state within a Lanczos run.
3) Construct the 'moments' up to the desired order N_{mom} using the recursion relations according to equation (2.146).
4) Compute the coefficients $\alpha^{\pm}_{n}$ and assemble the Green's function.

Here two disadvantages of the Chebyshev expansion compared to the spectral representation should be mentioned. First, the Chebyshev expansion does not know about the poles and respective weights of the Green's function. Hence the energy range of the contour integration always has to enclose all poles whose extent is obtained from the scaling parameters as $b \pm a \cdot (2 - \delta)/2$. In contrast, for the spectral representation, poles with negligible weight can be omitted and the integration range reduced. Trying to shorten the integration contour for the Chebyshev representation by performing a bisection did not work, since the data turned out too noisy. Second, the energy-dependent coefficients depend on the scaling parameters a and b which contain the ground state energy. At finite temperatures, this single ground state energy is replaced by the energies of the trace vectors. Hence for each trace vector, the coefficients need to be computed anew. The energy-dependent coefficients and moments are thus intertwined, just like the energy-dependent denominator of the spectral representation is connected to the numerator. In other words: there is the same effort in assembling the Green's function using the Chebyshev expansion as there is for the spectral representation. The speed-up achieved by separating the energy-dependence from the rest of the Green's function via a high-frequency expansion as described in section 2.4.4 should in principle be possible for the Chebyshev expansion. Setting the coefficients a and b used for rescaling for all poles to a sufficiently large value to convert all poles into the range $[-1, 1]$ however gave detrimental results not matching those of the ED solver. Besides these issues, without knowing the poles and weights of the Green's function, the contour integration within the moments cannot be performed analytically as possible for the spectral representation described in section 2.3.6.

2.3.5 Brute-force numerical integration

To compute contributions to the self-energy functional and one-body expectation values, sums over Matsubara energies have to be evaluated. Instead of infinite sums, integrations along contours in the complex plane are performed. These can be deformed to be resilient against numerical errors when low sampling of the contour is chosen to speed up computations. Further speed-up is achieved by a high-frequency expansion to be described in section 2.4.4 which requires the deformation of the contour as well. The presentation follows [LA09].

In order to evaluate the self-energy functional, the terms

$$\mathrm{Tr}\ln(-\boldsymbol{G}^{-1}) = \frac{1}{\beta}\sum_{n=-\infty}^{\infty}\sum_{\alpha}\exp\left(\mathrm{i}E_n 0^+\right)\ln[-\boldsymbol{G}^{\mathrm{M}}(E_n)^{-1}]_{\alpha\alpha} \tag{2.163}$$

have to be computed for the cluster and CPT Green's function. To obtain one-body expectation values of the cluster and CPT system, equation (2.62) has to evaluated. Contributions to the functional and the expectation value are summarised as

$$S = \frac{1}{\beta}\sum_{n=-\infty}^{\infty}\exp\left(\mathrm{i}E_n 0^+\right)g(\mathrm{i}E_n), \tag{2.164}$$

where $g(\mathrm{i}E_n)$ represents the trace-logarithm $\sum_\alpha \ln[-\boldsymbol{G}^{\mathrm{M}}(E_n)^{-1}]_{\alpha\alpha}$ and the Matsubara Green's function $G^{\mathrm{M}}_{\alpha\beta}(E_n)$. The presentation combines the descriptions in [LA09] and [Sén08]. Since the Matsubara energies are the poles of the Fermi distribution $f(z)$ with residue $\mathrm{Res}[f(z), z = \mathrm{i}E_n] = -\beta^{-1}$, the sum over Matsubara energies can be written as contour integral using the residue theorem

$$S = -\frac{1}{2\pi\mathrm{i}}\oint_C \mathrm{d}z\,\exp(z0^+)g(z)f(z) = -\frac{1}{2\pi\mathrm{i}}\oint_C \mathrm{d}z\,F(z), \tag{2.165}$$

where the contour corresponds to circles around the Matsubara energies passed counterclockwise as illustrated in figure 2.13a. Adding zeros by means of Cauchy's integral theorem allows connecting the circular contours as displayed in figure 2.13b. Exploiting the decay of the Green's function at high energy as given in equation (2.219) allows adding further zeros by means of arcs around the positive and negative real axis visible in figure 2.13c. One might also follow Eder [Ede08], who argues that the Green's function is analytical off the real axis. Shrinking the contour to the poles of the finite system along the real axis and extending it to a finite imaginary part δ gives the grey contour in figure 2.13d. The extension to a non-negligible δ serves to achieve a good accuracy while using only few points in the numerical integration. Again, zeros by means of Cauchy's integral theorem are added. This last step makes it possible to decompose the integration into two parts shown in figure 2.13e, a contribution due to the Matsubara energies and a contribution by the poles along the real axis.

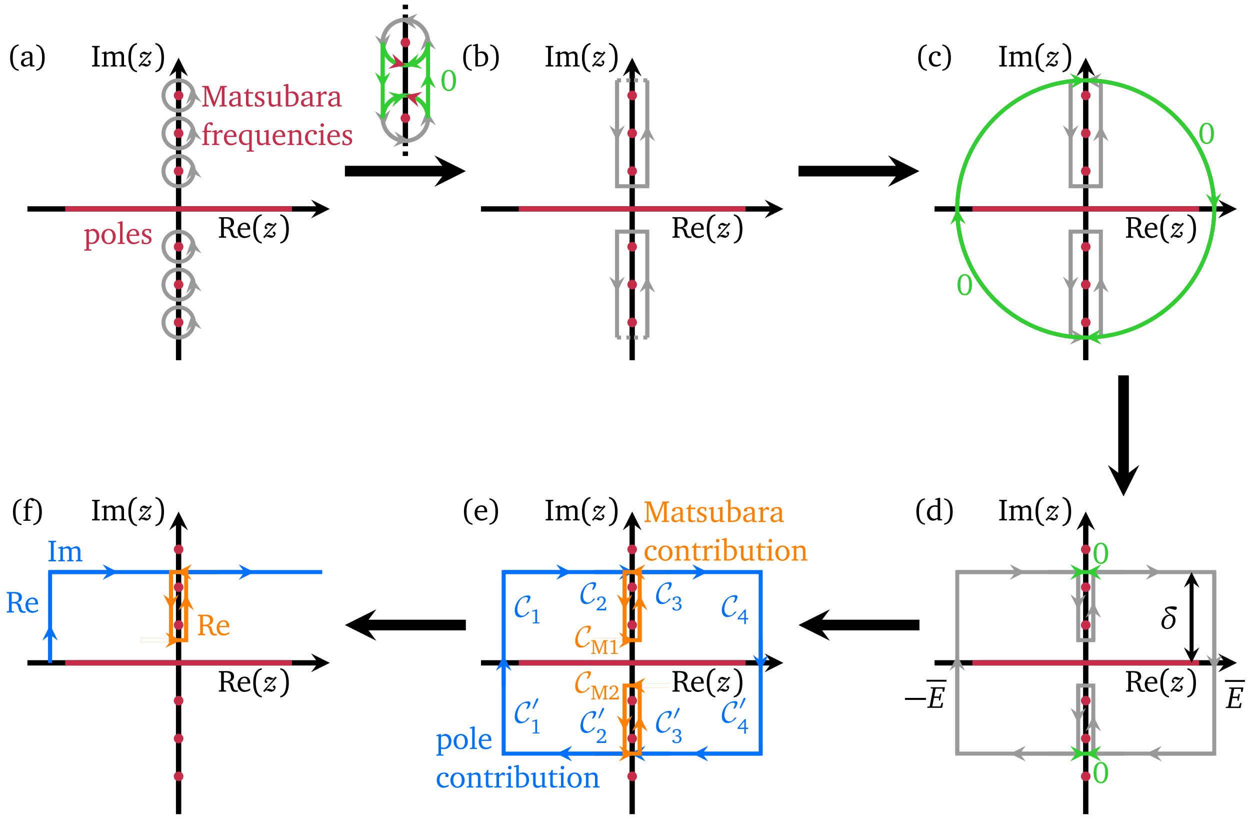
(a)
Im(z)
Matsubara
frequencies
poles
Re(z)
0
(b)
Im(z)
Re(z)
(c)
Im(z)
0
Re(z)
0
(d)
Im(z)
0
δ
$-\overline{E}$
Re(z)
$\overline{E}$
0
(e)
Im(z)
Matsubara
contribution
$\mathcal{C}_1$
$\mathcal{C}_2$
$\mathcal{C}_3$
$\mathcal{C}_4$
$\mathcal{C}_{\mathrm{M1}}$
$\mathcal{C}_{\mathrm{M2}}$
Re(z)
$\mathcal{C}_1'$
$\mathcal{C}_2'$
$\mathcal{C}_3'$
$\mathcal{C}_4'$
pole
contribution
(f)
Im(z)
Im
Re
Re
Re(z)

2.13 – Sequence of contour deformations employed to compute the quantity S. Poles are highlighted in red and zero contributions in green.

However the contour on which the integrand is evaluated can be simplified even further by exploiting the property $G_{\alpha\beta}(z^*) = G_{\beta\alpha}(z)^*$ which can be inferred from the spectral representation at zero and finite temperature (2.112) and (2.190). While the switch in indices can be reversed in the contributions to the self-energy functional $\mathrm{Tr}\ln(-\boldsymbol{G}^{-1})$ due to the trace occuring therein, the operators within one-body expectation values have to be extended to observables $\mathcal{O} = \sum_{\alpha,\beta} s_{\alpha\beta} c^\dagger_\beta c_\alpha / L$ with L being the number of lattice sites of N_{cl} clusters with ℓ sites per cluster and $\boldsymbol{s} = \boldsymbol{s}^\dagger$ a hermitian matrix. Without having to worry about the indices, the integrand above and below the real axis are related via $F(z^*) = F(z)^*$. Hence contour branches above and below the real axis can be combined to give

$$S_{23} = -\frac{1}{2\pi\,\mathrm{i}} \int\limits_{\mathcal{C}_2\cup\mathcal{C}_3\cup\mathcal{C}_2'\cup\mathcal{C}_3'} \mathrm{d}z\, F(z) = -\frac{1}{\pi} \int\limits_{[-\overline{E},\overline{E}]} \mathrm{d}a\, \mathrm{Im}[F](a + \mathrm{i}\,\delta), \tag{2.166}$$

$$S_1 = -\frac{1}{2\pi\,\mathrm{i}} \int\limits_{\mathcal{C}_1\cup\mathcal{C}_1'} \mathrm{d}z\, F(z) = -\frac{1}{\pi} \int\limits_{[0,\delta]} \mathrm{d}b\, \mathrm{Re}[F](-\overline{E} + \mathrm{i}\,b), \tag{2.167}$$

$$S_4 = -\frac{1}{2\pi\,\mathrm{i}} \int\limits_{\mathcal{C}_4\cup\mathcal{C}_4'} \mathrm{d}z\, F(z) = \frac{1}{\pi} \int\limits_{[0,\delta]} \mathrm{d}b\, \mathrm{Re}[F](\overline{E} + \mathrm{i}\,b), \tag{2.168}$$

$$S_{\mathrm{M}} = \frac{1}{\beta} \sum_{\substack{n=-\infty \\ E_n<\delta}}^{\infty} \exp\left(\mathrm{i}\,E_n 0^+\right) g(\mathrm{i}\,E_n) = \frac{2}{\beta} \sum_{\substack{n=0 \\ E_n<\delta}}^{\infty} \mathrm{Re}[\exp\left(\mathrm{i}\,E_n 0^+\right) g(\mathrm{i}\,E_n)], \tag{2.169}$$

s.t. only contour branches with positive imaginary part remain. An additional simplification follows from considering the shape of the Fermi function. At zero temperature it is a step function which permits neglecting the integration contour for $\mathrm{Re}(z) > 0$ entirely. But even at finite temperature, the Fermi function decays exponentially with $\mathrm{Re}(z)$ s.t. by extending the contour for $\mathrm{Re}(z) > 0$ beyond $\overline{E}$ allows neglecting the vertical branch S_4. This corresponds to the contour signified in figure 2.13f. It is the same as employed by Lu and Arrigoni [LA09] and Seki et al. [SSY18] which can be combined with the high-frequency expansion described in section 2.4.4.

The trace occuring within the integrand is split into a trace over discrete quantum numbers such as spin σ or orbital ρ and a summation over reciprocal lattice vectors $\tilde{\boldsymbol{k}}$ with weight $1/N_{\mathrm{cl}}$ associated with the lattice of clusters.

2 3 6 Q-matrix representation & Semi-analytical treatment

◇*Knowing the poles of the cluster and CPT Green's function, the contour integration required for the self-energy functional and one-body expectation values can be performed analytically. They are available when working with the Q-matrix representation of the Green's function. The presentation follows [Sén08].*◇

If the poles of the CPT Green's-function are known, the brute-force contour integration discussed above is not necessary, since the integrals can be computed via the Residue theorem. Assuming the poles of the CPT Green's function to be known, Potthoff [Pot03] obtained an analytical expression for the grand potential

$$\Omega_{\mathrm{CPT}} = \Omega_{\mathrm{cl}} - LT \sum_{\sigma} \sum_{m} \frac{1}{N_{\mathrm{cl}}} \sum_{\tilde{\boldsymbol{k}}} \ln[1 + \exp(-\beta E_{m\sigma}^{(CPT)}(\tilde{\boldsymbol{k}}))] + 2LT \sum_{m} \ln[1 + \exp(-\beta E_{m}^{(\mathrm{cl})})], \tag{2.170}$$

where $L = N_{\mathrm{cl}} \cdot \ell$ are the total number of sites on N_{cl} cluster of ℓ sites each, $E_{m\sigma}^{(CPT)}(\tilde{\boldsymbol{k}})$ are the poles of the CPT Green's function, $E_m^{(cl)}$ are the poles of the cluster Green's function and m enumerates the poles.

A procedure to obtain the poles of the CPT Green's function which is numerically feasible (at least for zero temperature) consists in representing the cluster Green's function in terms of Q-matrices [Aic+06]. Following the presentation by Sénéchal [Sén08], the idea is sketched and relevant expressions are given. First, the electron and hole part $[\boldsymbol{Q}^{(\mathrm{e})}]_{\alpha n}$ and $[\boldsymbol{Q}^{(\mathrm{h})}]_{\alpha n}$ are combined into a matrix by appending the latter complex conjugated below the prior as

$$\boldsymbol{Q} = \begin{pmatrix} \boldsymbol{Q}^{(\mathrm{e})} \\ \boldsymbol{Q}^{(\mathrm{h})*} \end{pmatrix}, \tag{2.171}$$

which gives the cluster Green's function as a product of three matrices

$$\boldsymbol{G}_{\mathrm{cl}}(z) = \boldsymbol{Q}\boldsymbol{g}(z)\boldsymbol{Q}^{\dagger}, \tag{2.172}$$

where $\boldsymbol{g}(z) = (z\mathbb{1} - \boldsymbol{\Lambda})^{-1}$ and $\Lambda_{mn} = \mathrm{diag}(E_m^{(\mathrm{e})}, E_m^{(\mathrm{h})}) = E_m^{(\mathrm{cl})}\delta_{mn}$ contains the poles of the electron and hole part. To obtain the CPT-Green's function

$$\boldsymbol{G}_{\mathrm{CPT}}(z, \tilde{\boldsymbol{k}}) = \left[\boldsymbol{G}_{\mathrm{cl}}^{-1}(z) - \boldsymbol{V}(\tilde{\boldsymbol{k}})\right]^{-1} \tag{2.173}$$

also in terms of Q-matrices, one first pulls out $\boldsymbol{G}_{\mathrm{cl}}^{-1}$ from the denominator, rewrites the remaining fraction as von Neumann series and pulls out $\boldsymbol{Q}\boldsymbol{g}$ to the front and $\boldsymbol{Q}^{\dagger}$ to the back. Next, the series is summed up again and $\boldsymbol{g} = (\boldsymbol{g}^{-1})^{-1}$ is moved into the denominator giving

$$\boldsymbol{G}_{\mathrm{CPT}}(z, \tilde{\boldsymbol{k}}) = \boldsymbol{Q}\tilde{\boldsymbol{g}}(z, \tilde{\boldsymbol{k}})\boldsymbol{Q}^{\dagger}, \tag{2.174}$$

with

$$\begin{aligned} \tilde{\boldsymbol{g}}(z, \tilde{\boldsymbol{k}}) &= [\boldsymbol{g}(z)^{-1} + \boldsymbol{Q}^{\dagger}\boldsymbol{V}(\tilde{\boldsymbol{k}})\boldsymbol{Q}]^{-1} \\ &= [z\mathbb{1} - \boldsymbol{L}(\tilde{\boldsymbol{k}})]^{-1}. \end{aligned} \tag{2.175}$$

Assuming that $\boldsymbol{L}(\tilde{\boldsymbol{k}})$ can be diagonalised as $\tilde{\Lambda}(\tilde{\boldsymbol{k}}) = \boldsymbol{U}^{\dagger}(\tilde{\boldsymbol{k}})\boldsymbol{L}(\tilde{\boldsymbol{k}})\boldsymbol{U}(\tilde{\boldsymbol{k}})$ and pulling out the matrices of eigenvectors $\boldsymbol{U}(\tilde{\boldsymbol{k}})$, one ends up with the CPT Green's function in terms of Q-matrices and poles

$$\boldsymbol{G}_{\mathrm{CPT}}(z) = [\boldsymbol{Q}\boldsymbol{U}(\tilde{\boldsymbol{k}})][z\mathbb{1} - \tilde{\Lambda}(\tilde{\boldsymbol{k}})]^{-1}[\boldsymbol{Q}\boldsymbol{U}(\tilde{\boldsymbol{k}})]^{\dagger} \tag{2.176}$$

This expression for the CPT Green's function can further be used to compute the diagonal of the CPT spectral function

$$S_{\alpha\alpha}(E, \tilde{\boldsymbol{k}}) = \frac{1}{\pi}\sum_{m} \frac{\eta |[\boldsymbol{Q}\boldsymbol{U}(\tilde{\boldsymbol{k}})]_{\alpha m}|^2}{\{E\mathbb{1} - \tilde{\boldsymbol{\Lambda}}_{mm}(\tilde{\boldsymbol{k}})\}^2 + \eta^2\mathbb{1}}, \tag{2.177}$$

to obtain the site resolved CPT DOS

$$\rho_{\alpha}(E) = \frac{1}{N_{\mathrm{cl}}}\sum_{\tilde{\boldsymbol{k}}} S_{\alpha\alpha}(E, \tilde{\boldsymbol{k}}) \tag{2.178}$$

and to perform the contour integration for the CPT one-body expectation values

$$\langle c_{\beta}^{\dagger} c_{\alpha}\rangle = \sum_{\sigma}\sum_{m} \frac{1}{N_{\mathrm{cl}}}\sum_{\tilde{\boldsymbol{k}}} f[E_{m\sigma}^{(CPT)}(\tilde{\boldsymbol{k}})] Q_{\alpha m} Q_{\beta m}^{*}. \tag{2.179}$$

Note that in order to obtain the fully $\boldsymbol{k}$-dependent spectral function, an additional Fourier transform in the cluster sites is needed. Employing the Q-matrices, it is sufficient to use the Fourier transform of the matrix $[\boldsymbol{Q}\boldsymbol{U}(\tilde{\boldsymbol{k}})]$ in equation (2.177). For the DOS, no additional Fourier transform is required, but the sum over $\tilde{\boldsymbol{k}}$ has to include a summation over the cluster site indices.

To obtain the Q-matrices numerically, the Band Lanczos algorithm is required. A set of Lanczos runs is not sufficient, since each run with different initial vector leads to slightly different eigenvectors. The resulting weights thus cannot be grouped into Q-matrices.

When considering finite temperature, the Q-matrices get an additional index replacing the ground state with the trace. Hence one ends up with a tensor instead of a matrix. Combining the indices of the bases in the ground and excited state sector into a multi-index streamlines the appearence and gives again a matrix. However, the dimension of this matrix is $(N_{\mathrm{GS}} \cdot N_{\mathrm{ES}}) \times L$ with N_{GS} (N_{ES}) being the dimensions of the ground state (excited state) sector. However for small systems, the Q-matrix representation is a viable option to perform the VCA by hand and thus useful for testing purposes. Apart from this increase in size, the procedure to construct the Q-matrix representation within a Band Lanczos run requires to include all $(N_{\mathrm{GS}} \times L)$ excited states obtained by applying the construction operators to the trace vectors. This produces a matrix with bandwidth $2(N_{\mathrm{GS}} \times L) + 1$ which causes memory issues for large systems.

2 4 Cluster solvers at finite temperature

The finite temperature versions of the FD, ED and Chebyshev solver are presented. For the latter two types of solvers, traces with exact eigenvectors, with random vectors and a combination of both are discussed. Several additional details relevant for reducing the computation time, new observables and realising different reference systems are given.

2 4 1 FD and ED

The computation of expectation values, the partition function and the Green's function at finite temperature using FD and ED are described. Approximations employed in case of ED are highlighted. Expressions used numerically are explicitely given. The presentation follows [Dag01; Aic04; PB11].

At finite temperature, expectation values become traces as stated in equation (2.22). Knowing the eigenbasis of the Hamiltonian, one can evaluate the trace and compute these expectation values as

$$\Xi = \sum_n \exp(-\beta \varepsilon_n), \tag{2.180}$$

$$\langle \mathcal{O} \rangle = \sum_n \frac{\exp(-\beta \varepsilon_n)}{\Xi} \langle \Psi_n | \mathcal{O} | \Psi_n \rangle \,. \tag{2.181}$$

For small systems ($L = 6$ spinful sites with $N_\mathrm{p} = 6$ particles gives $\dim \mathscr{H} = 924$) this is possible via FD. Larger systems ($L = 8$ spinful sites with $N_\mathrm{p} = 8$ particles gives $\dim \mathscr{H} = 12870$) require the Lanczos or Band Lanczos algorithm. In this case one can approximate the complete trace at a given inverse temperature β by restricting oneself to those eigenstates, which provide a sufficient contribution to it as is done by Seki et al. in [SSY18]. Sufficient means, that the contribution by the nth eigenstate with eigenenergy ε_n should provide a ratio $\exp(-\beta \varepsilon_n)/\exp(-\beta \varepsilon_0) \geq \delta$ with the ground state energy ε_0 and the tolerance δ, for which Seki et al. [SSY18] used 1×10^{-6}. This value amounts to converge all eigenvectors with energies up to $\sim 14 \times T$ ($k_\mathrm{B} \equiv 1$) above the ground state energy. Since every expectation value contains the ratio between Bolzmann factor $\exp(-\beta \varepsilon_n)$ and partition function Ξ, whose largest contribution is $\exp(-\beta \varepsilon_0)$, this approximation is rather precise. For large systems with dense spectrum, it is however costly.

Assume now that one is provided with the vectors $\{|\Psi_n\rangle\}$ forming the trace. This could be due to a previous FD or ED. In order to obtain the expectation value (2.22) one performs several additional Lanczos/Band Lanczos runs of length M with initial states $\{|\Psi_n\rangle\}$. To determine which matrix elements need to be computed during one Lanczos/Band Lanczos run, one makes use of projection operators onto the Krylov subspace initialised by the state $|\Psi_n\rangle$ after m iterations

$$P_m^{(n)} = \sum_{i=0}^{m-1} |x_i^{(n)}\rangle \langle x_i^{(n)}| \,. \tag{2.182}$$

Employing the iteration rule of the Lanczos algorithm connecting three Lanczos vectors, one finds that the combined application of the Hamiltonian $\mathcal{H}$ first and the projection operator $P_m^{(n)}$ afterwards would transfer three Lanczos vectors $|x_{i+1}\rangle$, $|x_i\rangle$, $|x_{i-1}\rangle$ into one Lanczos vector $|x_i\rangle$ as

$$P_m^{(n)} \mathcal{H} = \sum_{i=0}^{m-1} |x_i^{(n)}\rangle \left[\beta_{i+1}^{(n)} \langle x_{i+1}^{(n)}| + \alpha_i^{(n)} \langle x_i^{(n)}| + \beta_i^{(n)} \langle x_{i-1}^{(n)}| \right], \tag{2.183}$$

where $\beta_{i+1} = \| |\tilde{x}_i\rangle \|$ is used. A similar relation holds for the Band Lanczos algorithm, where the central state of the band emerges from itself and B 'old' and B 'new' states if no deflation occurs. For the Lanczos algorithm, this holds up to $m \leq M-1$, while it is restricted to $m \leq M-B$ for the Band Lanczos algorithm. In a nutshell, the action of the Hamiltonian does not lead out of the constructed Krylov subspace but branches only to other Lanczos vectors provided one is far enough away from the last states of the iteration. Since the Lanczos vectors of the Krylov subspace are orthogonal and normalised, applying the projection operator $P^{(n)}_{m+B}$ beforehand does not alter the action of $P^{(n)}_m\mathcal{H}$. Each branch is just transmitted to the right. Also projection operators belonging to later iterations such as $P^{(n)}_M$ do not change the throughput, because all states going beyond the branching give zero contribution due to orthogonality. Hence one can write

$$P^{(n)}_m\mathcal{H} = P^{(n)}_m\mathcal{H}P^{(n)}_{m+B} = P^{(n)}_m\mathcal{H}P^{(n)}_M\,. \tag{2.184}$$

Projection operators $P^{(n)}_{m'}$ with $m < m' < m+B$ however alter the action.

Expanding the exponential inside the density matrix of equation (2.22) sets the task of computing at order k the matrix element $\langle\Psi_n|\mathcal{H}^k\mathcal{O}|\Psi_n\rangle$. Since the initial state $|\Psi_n\rangle$ is proportional or equal to the first Lanczos vector $|x^{(n)}_0\rangle$, which is invariant under the projection operator $P^{(n)}_1$, one can introduce projection operators of later iterations using the resilience described by equation (2.184), giving

$$\begin{aligned}\langle\Psi_n|\mathcal{H}^k\mathcal{O}|\Psi_n\rangle &= \langle x^{(n)}_0|P^{(n)}_1\mathcal{H}^k\mathcal{O}|x^{(n)}_0\rangle \\ &= \langle x^{(n)}_0|P^{(n)}_1\mathcal{H}P^{(n)}_{B+1}\mathcal{H}\ldots\mathcal{H}P^{(n)}_{kB+1}\mathcal{O}|x^{(n)}_0\rangle \\ &= \langle x^{(n)}_0|P^{(n)}_M\mathcal{H}P^{(n)}_M\mathcal{H}\ldots\mathcal{H}P^{(n)}_M\mathcal{O}|x^{(n)}_0\rangle\,.\end{aligned} \tag{2.185}$$

The last step however requires $k \cdot B < M$. Within this restriction the projection operator $P^{(n)}_M$ can be considered as identity matrix of the Krylov subspace. Using the idempotence $[P^{(n)}_m]^2 = P^{(n)}_m$ of projection operators, the matrix element simplifies further to

$$\langle\Psi_n|\mathcal{H}^k\mathcal{O}|\Psi_n\rangle = \langle\Psi_n|[P^{(n)}_M\mathcal{H}P^{(n)}_M]^k\mathcal{O}|\Psi_n\rangle\,, \tag{2.186}$$

where the Hamiltonian is now expressed as matrix in the basis of Lanczos vectors. Inserting formally a real identity matrix on the Krylov subspace given by the eigenvectors of the Hamiltonian $\mathbb{1} = \sum_{n^x=0}^{M-1}|\Psi_{n^x}\rangle\langle\Psi_{n^x}|$ between Hamiltonian and projection operator makes it possible to replace the Hamiltonian by its eigenvalues. Since the projection operators leave the eigenvectors invariant when expanded in the Lanczos basis, they can be omitted except for the outmost ones, since these translate the initial vectors into the Lanczos basis. Employing the orthogonality of the eigenvectors reduces the sums of the prior identities over eigenvectors to one, giving

$$\langle\Psi_n|\mathcal{H}^k\mathcal{O}|\Psi_n\rangle = \sum_{n^x=0}^{M-1}\varepsilon^k_{n^x}\,\langle\Psi_n|P^{(n)}_M|\Psi_{n^x}\rangle\,\langle\Psi_{n^x}|\,P^{(n)}_M\mathcal{O}|\Psi_n\rangle\,. \tag{2.187}$$

Up to this point all expressions are exact but require sufficient iteration steps $M > k\cdot B$ of the Lanczos/Band Lanczos algorithm to be valid. However starting from an exponential series within the density matrix, only part of it is captured when restricting oneself to a reasonable value of M. The approximation consists now in assuming the validity of equation (2.187) for all orders of k by resumming the exponential to obtain

$$\langle \mathcal{O} \rangle \approx \sum_{n} \sum_{n^x=0}^{M-1} \frac{\exp(-\beta \varepsilon_{n^x})}{\Xi} \langle \Psi_n | P_M^{(n)} | \Psi_{n^x} \rangle \langle \Psi_{n^x} | P_M^{(n)} \mathcal{O} | \Psi_n \rangle \tag{2.188}$$

Hence the error of the approximation is $\mathcal{O}(\beta^{M+1})$. Some relevant operators are the partition function

$$\begin{aligned} \Xi &= \sum_{n} \sum_{n^x=0}^{M-1} \exp(-\beta \varepsilon_{n^x}) \langle \Psi_n | P_M^{(n)} | \Psi_{n^x} \rangle \langle \Psi_{n^x} | P_M^{(n)} | \Psi_n \rangle \\ &= \sum_{n} \sum_{n^x=0}^{M-1} \exp(-\beta \varepsilon_{n^x}) \left| \sum_i \langle \Psi_n | x_i \rangle \langle x_i | \Psi_{n^x} \rangle \right|^2 \end{aligned} \tag{2.189}$$

and the finite temperature retarded Green's function

$$\begin{aligned} G^{\mathrm{ret}}_{\alpha\beta}(E) = &\sum_{m,n} \frac{\exp(-\beta \varepsilon_m)}{\Xi} \left[\frac{\left\langle \Psi_m \middle| c_\alpha \middle| \Psi_n^+ \right\rangle \left\langle \Psi_n^+ \middle| c_\beta^\dagger \middle| \Psi_m \right\rangle}{E - E^+_{nm} + \mathrm{i}0^+} \right] \\ + &\sum_{m,n} \frac{\exp(-\beta \varepsilon_m)}{\Xi} \left[\frac{\left\langle \Psi_m \middle| c_\beta^\dagger \middle| \Psi_n^- \right\rangle \left\langle \Psi_n^- \middle| c_\alpha \middle| \Psi_m \right\rangle}{E + E^-_{nm} + \mathrm{i}0^+} \right] \end{aligned} \tag{2.190}$$

with the poles $E^\pm_{nm} = \varepsilon^\pm_n - \varepsilon_m$, the electron weights

$$\begin{aligned} &\frac{\exp(-\beta \varepsilon_m)}{\Xi} \left\langle \Psi_m \middle| c_\alpha \middle| \Psi_n^+ \right\rangle \left\langle \Psi_n^+ \middle| c_\beta^\dagger \middle| \Psi_m \right\rangle = \\ &\frac{\exp(-\beta \varepsilon_{m^x})}{\Xi} \cdot \left[\sum_i \langle \Psi_{m^x} | x_i \rangle \langle x_i | \Psi_{n^x} \rangle \right] \cdot \left[\sum_{j,k} \langle \Psi_{n^x} | x_j \rangle \langle \mathcal{X}^+_{j\alpha} | y^+_k \rangle \langle y^+_k | \Psi^+_{n^y} \rangle \right] \\ &\qquad \cdot \left[\sum_\ell \langle \Psi^+_{n^y} | y^+_\ell \rangle \langle y^+_\ell | \mathcal{Y}^+_\beta \rangle \right] \cdot \| \, | \Psi^+_\beta \rangle \, \| \end{aligned} \tag{2.191}$$

and hole weights

$$\begin{aligned} &\frac{\exp(-\beta \varepsilon_m)}{\Xi} \left\langle \Psi_m \middle| c_\beta^\dagger \middle| \Psi_n^- \right\rangle \left\langle \Psi_n^- \middle| c_\alpha \middle| \Psi_m \right\rangle = \\ &\frac{\exp(-\beta \varepsilon_{m^x})}{\Xi} \cdot \left[\sum_i \langle \Psi_{m^x} | x_i \rangle \langle x_i | \Psi_{n^x} \rangle \right] \cdot \left[\sum_{j,k} \langle \Psi_{n^x} | x_j \rangle \langle \mathcal{X}^-_{j\beta} | y^-_k \rangle \langle y^-_k | \Psi^-_{n^y} \rangle \right] \\ &\qquad \cdot \left[\sum_\ell \langle \Psi^-_{n^y} | y^-_\ell \rangle \langle y^-_\ell | \mathcal{Y}^-_\alpha \rangle \right] \cdot \| \, | \Psi^-_\alpha \rangle \, \|. \end{aligned} \tag{2.192}$$

The following quantities occur within the electron and hole weights:

- $\{|x_i\rangle\}$: basis constructed in the first Lanczos run
- $\langle x_i|\Psi_{n^x}\rangle$: components of the eigenvalues of the Hamiltonian in the Lanczos basis $\{|x_i\rangle\}$ belonging to the eigenenergies ε_{n^x}
- $\langle \mathcal{X}^+_{j\alpha}| = \langle x_j|\, c_\alpha = (c^\dagger_\alpha\, |x_j\rangle)^\dagger$: auxiliary vector of the electron part
- $\langle \mathcal{X}^-_{j\beta}| = \langle x_j|\, c^\dagger_\beta = (c_\beta\, |x_j\rangle)^\dagger$: auxiliary vector of the hole part
- $\{|y^+_k\rangle\}$: basis constructed in the second Lanczos run starting from the initial vector $|\mathcal{Y}^+_\beta\rangle = |\Psi^+_\beta\rangle \,/\, \|\, |\Psi^+_\beta\rangle\, \|$
- $\{|y^-_k\rangle\}$: basis constructed in the second Lanczos run starting from the initial vector $|\mathcal{Y}^-_\alpha\rangle = |\Psi^-_\alpha\rangle \,/\, \|\, |\Psi^-_\alpha\rangle\, \|$
- $\langle y^\pm_k|\Psi^\pm_{n^y}\rangle$: components of the eigenvalues of the Hamiltonian in the Lanczos basis $\{|y^\pm_k\rangle\}$ belonging to the eigenenergies $\varepsilon^\pm_{n^y}$

Depending on which solver (FD, Lanczos ED, Band Lanczos ED) one uses for the matrix elements, one can reduce the number of required matrix elements or set them to the identity implementation-wise. For the case of a one-dimensional Hilbert space, the matrix elements simplify even further, since dot-products give only of a single entry. One has to keep in mind however, that complex couplings can lead to complex Lanczos vectors and eigenvectors which require usage of the correct dot product. For completeness, the respective electron weights are given, which are sorted according to the first and second FD or ED run. The colors highlight the run during which the marked quantities are determined. FD and Lanczos ED require the same matrix elements when used within the first run. For completeness, in case of the one-dimensional Hilbert space, the eigenvector is chosen to be $|\Psi_1^{(+)}\rangle = 1$:

- $\dim \mathscr{H} = 1$, $\dim \mathscr{H} = 1$:

$$\exp(-\beta\varepsilon_m)\left\langle \Psi_m \middle| c_\alpha \middle| \Psi^+_n \right\rangle \left\langle \Psi^+_n \middle| c^\dagger_\beta \middle| \Psi_m \right\rangle = \exp(-\beta\varepsilon_1)\left\langle \Psi_1 \middle| c_\alpha \middle| \Psi^+_1 \right\rangle \left\langle \Psi^+_1 \middle| c^\dagger_\beta \middle| \Psi_1 \right\rangle \tag{2.193}$$

- $\dim \mathscr{H} = 1$, FD:

$$\exp(-\beta\varepsilon_m)\left\langle \Psi_m \middle| c_\alpha \middle| \Psi^+_n \right\rangle \left\langle \Psi^+_n \middle| c^\dagger_\beta \middle| \Psi_m \right\rangle = \exp(-\beta\varepsilon_1)\left\langle \Psi_1 \middle| c_\alpha \middle| \Psi^+_n \right\rangle \left\langle \Psi^+_n \middle| c^\dagger_\beta \middle| \Psi_1 \right\rangle \tag{2.194}$$

- $\dim \mathscr{H} = 1$, Lanczos ED:

$$\begin{aligned} \exp(-\beta\varepsilon_m)\left\langle \Psi_m \middle| c_\alpha \middle| \Psi^+_n \right\rangle \left\langle \Psi^+_n \middle| c^\dagger_\beta \middle| \Psi_m \right\rangle = \exp(-\beta\varepsilon_1)\left\langle \Psi_1 \middle| c_\alpha \middle| y^+_i \right\rangle \left\langle y^+_i \middle| \Psi^+_n \right\rangle \\ \cdot \left\langle \Psi^+_n \middle| y^+_j \right\rangle \left\langle y^+_j \middle| c^\dagger_\beta \middle| \Psi_1 \right\rangle \end{aligned} \tag{2.195}$$

- FD/Lanczos ED, $\dim \mathscr{H} = 1$:

$$\exp(-\beta\varepsilon_m)\left\langle \Psi_m \middle| c_\alpha \middle| \Psi^+_n \right\rangle \left\langle \Psi^+_n \middle| c^\dagger_\beta \middle| \Psi_m \right\rangle = \exp(-\beta\varepsilon_m)\left\langle \Psi_m \middle| c_\alpha \middle| \Psi^+_1 \right\rangle \left\langle \Psi^+_1 \middle| c^\dagger_\beta \middle| \Psi_m \right\rangle \tag{2.196}$$

- FD/Lanczos ED, FD:

$$\exp(-\beta\varepsilon_m)\left\langle \Psi_m \middle| c_\alpha \middle| \Psi^+_n \right\rangle \left\langle \Psi^+_n \middle| c^\dagger_\beta \middle| \Psi_m \right\rangle = \exp(-\beta\varepsilon_m)\left\langle \Psi_m \middle| c_\alpha \middle| \Psi^+_n \right\rangle \left\langle \Psi^+_n \middle| c^\dagger_\beta \middle| \Psi_m \right\rangle \tag{2.197}$$

- FD/Lanczos ED, Lanczos ED:

$$\begin{aligned}\exp(-\beta\varepsilon_m)\left\langle\Psi_m\middle|c_\alpha\middle|\Psi_n^+\right\rangle\left\langle\Psi_n^+\middle|c_\beta^\dagger\middle|\Psi_m\right\rangle = \exp(-\beta\varepsilon_m)\left\langle\Psi_m\middle|c_\alpha\middle|y_i^+\right\rangle\left\langle y_i^+\middle|\Psi_n^+\right\rangle \\ \cdot\left\langle\Psi_n^+\middle|y_j^+\right\rangle\left\langle y_j^+\middle|c_\beta^\dagger\middle|\Psi_m\right\rangle\end{aligned} \tag{2.198}$$

2 4 2 Finite temperature Lanczos method (FTLM)

Within the FTLM, a trace over a complete basis is approximated via an average of independent and identically distributed random vectors of zero mean and the identity as covariance matrix. Increasing the system or employing more random vectors improve this approximation. Expressions and error estimates used numerically are explicitely given. An improvement at low temperature by splitting the trace into a part with exact and random trace vectors is described. The present FTLM implementation using real Gaussian random numbers is contrasted with another FTLM implementation using a split trace and a typicality-based solver employing random phase vectors. The presentation follows [Dag01; Aic04; PB11].

Another way to tackle the problem is the finite temperature Lanczos method (FTLM) [PB11], which approximates the trace formed by the basis $|\Psi_n\rangle$ spanning the N-dimensional Hilbert-space of the system by R random vectors $|r\rangle = \sum_n \alpha_n^r |\Psi_n\rangle$. These random vectors are chosen to have a mean value of zero and to be orthonormal within the statistical expectation [PB11]:

$$\mathbb{E}[\alpha_n^r] = 0, \tag{2.199}$$

$$\mathbb{E}[\alpha_n^r \alpha_{n'}^{r'}] = \delta_{nn'}\delta_{rr'}. \tag{2.200}$$

One can interpret them as Gaussian random variables with zero mean value and the identity matrix as covariance matrix. They can be constructed using independent and identically distributed random numbers employing the central limit theorem, the Box-Muller method or the polar method, just to name the ones implemented. For the computations in this thesis, the polar method is used. Computing on top of the quantum mechanical expectation value the statistical expectation w.r.t. the random numbers $\mathbb{E}[\cdot]$, one ends up with the original expectation value when using a complete basis

$$\begin{aligned}\mathbb{E}[\Xi_r] &= \mathbb{E}[\langle\exp(-\beta\mathcal{H})\rangle_r] = \mathbb{E}[\langle r|\exp(-\beta\mathcal{H})|r\rangle] \\ &= \sum_{n,n'}\mathbb{E}[\alpha_n^r\alpha_{n'}^r]\,\langle\Psi_n|\exp(-\beta\mathcal{H})|\Psi_{n'}\rangle \overset{(2.200)}{=} \sum_n \exp(-\beta\varepsilon_n) = \Xi,\end{aligned} \tag{2.201}$$

$$\begin{aligned}\mathbb{E}[\langle\mathcal{O}\rangle_r] &= \mathbb{E}\left[\left\langle r\middle|\frac{\exp(-\beta\mathcal{H})}{\mathbb{E}[\Xi_r]}\mathcal{O}\middle|r\right\rangle\right] \\ &\overset{(2.200)}{=} \sum_n \frac{\exp(-\beta\varepsilon_n)}{\Xi}\,\langle\Psi_n|\mathcal{O}|\Psi_n\rangle = \langle\mathcal{O}\rangle\,.\end{aligned} \tag{2.202}$$

The approximation consists now in replacing the statistical expectation w.r.t. a probability distribution by an ensemble average with independent and identically distributed random numbers

$$\mathbb{E}[\mathcal{O}] \approx \overline{\mathcal{O}} = \frac{1}{R}\sum_r \mathcal{O}_r. \tag{2.203}$$

Its error can be estimated with the square root of the variance of a trace approximated with random vectors $\mathcal{O}_r = \langle r|\mathcal{O}|r\rangle$. For R uncorrelated samples, the variance is [Jah02]

$$\begin{aligned} \mathrm{Var}[\overline{\mathcal{O}}] &= \mathbb{E}[(\overline{\mathcal{O}} - \mathbb{E}[\overline{\mathcal{O}}])^2] \\ &= \frac{1}{R} \cdot \mathrm{Var}[\mathcal{O}_r]. \end{aligned} \tag{2.204}$$

In analogy to expectation values, $\mathbb{E}[\mathcal{O}_r] = \mathrm{tr}(\mathcal{O})$, while

$$\mathbb{E}[\mathcal{O}_r^2] = \frac{N^2}{N(N+1)}[\mathrm{tr}(\mathcal{O}^2) + \mathrm{tr}(\mathcal{O})^2] \tag{2.205}$$

can be inferred from the Supplementary material of [SS13], with the additional factor N^2 due to the random vectors not being normalised within the statistical expectation as discussed below. Assuming $N \gg 1$, estimating for $N \times N$-matrices $\mathrm{tr}(\mathcal{O}) \sim N$ and $\mathrm{tr}(\mathcal{O}^2) \sim N$, as well as using $\mathbb{E}[\overline{\mathcal{O}}] = \mathrm{tr}(\mathcal{O})$, one finds the relative error

$$\frac{\sqrt{\mathrm{Var}[\overline{\mathcal{O}}]}}{\mathbb{E}[\overline{\mathcal{O}}]} = \frac{1}{\sqrt{R \cdot N}}. \tag{2.206}$$

Hence the quality of the approximation can be improved by incorporating more random vectors or increasing the systems Hilbert-space dimension. Increasing the system size lets the Hilbert-space dimension grow exponentially and is thus advantageous. However within the Lanczos, Band Lanczos and Chebyshev solvers, the overall system size is limited by memory. And once smaller systems have to be investigated to verify the FTLM implementation by comparing with FD, more random vectors can improve the quality as well.

In the context of the Lanczos, Band Lanczos or Chebyshev solvers, the approximated trace vectors are normalised and used as initial states. Due to the identity covariance matrix in equation (2.200), the random vectors are not normalised within the statistical expectation

$$\mathbb{E}[\langle r|r'\rangle] = \sum_{n,n'} \mathbb{E}[(\alpha_n^r)^* \alpha_{n'}^{r'}] \langle \Psi_n|\Psi'_n\rangle \overset{(2.200)}{=} N\delta_{rr'}. \tag{2.207}$$

Approximating the actual norm with its statistical expectation, one sets $|r\rangle \approx N\,|\mathcal{R}\rangle$ with $|\mathcal{R}\rangle = |r\rangle / \|\,|r\rangle\,\|$. In the following, $|r\rangle$ is considered as the normalised vector $|\mathcal{R}\rangle \rightarrow |r\rangle$. This leads to an additional factor N in several expressions. The partition function reads

$$\begin{aligned} \Xi &\approx \frac{N}{R} \sum_{r=0}^{R-1} \langle r|\exp(-\beta\mathcal{H})|r\rangle \\ &= \frac{N}{R} \sum_{r=0}^{R-1} \sum_{n^x=0}^{M-1} \exp(-\beta\varepsilon_{n^x}) \left| \sum_i \langle r|x_i^r\rangle \langle x_i^r|\Psi_{n^x}\rangle \right|^2. \end{aligned} \tag{2.208}$$

To arrive at this expression, an identity $\mathbb{1} = \sum_n |n\rangle\langle n|$ is inserted and approximated by the eigenvectors obtained in a Lanczos/Band Lanczos run. Next, two projectors are inserted to express the approximate eigenstates in the Lanczos basis. For a regular Lanczos run, this simplifies further due to $\langle r|x_i^r\rangle = \delta_{1i}$, which does not hold for Band Lanczos ED. In a similar manner, the weights of the Green's function are obtained:

- LanczosED, $\dim \mathscr{H} = 1$:

$$\begin{aligned} &\exp(-\beta\varepsilon_{m^x}) \left\langle \Psi_m \middle| c_\alpha \middle| \Psi_n^+ \right\rangle \left\langle \Psi_n^+ \middle| c_\beta^\dagger \middle| \Psi_m \right\rangle \\ =&\frac{N}{R} \sum_{i,j} \exp(-\beta\varepsilon_{m^x}) \left\langle r \middle| x_i^r \right\rangle \left\langle x_i^r \middle| \Psi_{m^x} \right\rangle \left\langle \Psi_{m^x} \middle| x_j^r \right\rangle \left\langle x_j^r \middle| c_\alpha \middle| \Psi_1^+ \right\rangle \left\langle \Psi_1^+ \middle| c_\beta^\dagger \middle| r \right\rangle \end{aligned} \tag{2.209}$$

- Lanczos ED, FD:

$$\begin{aligned}&\exp(-\beta\varepsilon_m)\left\langle\Psi_m\middle|c_\alpha\middle|\Psi_n^+\right\rangle\left\langle\Psi_n^+\middle|c_\beta^\dagger\middle|\Psi_m\right\rangle\\=&\frac{N}{R}\sum_{i,j}\exp(-\beta\varepsilon_{m^x})\left\langle r\middle|x_i^r\right\rangle\left\langle x_i^r\middle|\Psi_{m^x}\right\rangle\left\langle\Psi_{m^x}\middle|x_j^r\right\rangle\left\langle x_j^r\middle|c_\alpha\middle|\Psi_n^+\right\rangle\left\langle\Psi_n^+\middle|c_\beta^\dagger\middle|r\right\rangle\end{aligned}\tag{2.210}$$

- Lanczos ED, Lanczos ED:

$$\begin{aligned}&\exp(-\beta\varepsilon_m)\left\langle\Psi_m\middle|c_\alpha\middle|\Psi_n^+\right\rangle\left\langle\Psi_n^+\middle|c_\beta^\dagger\middle|\Psi_m\right\rangle\\=&\frac{N}{R}\sum_{i,j,k,\ell}\exp(-\beta\varepsilon_{m^x})\left\langle r\middle|x_i^r\right\rangle\left\langle x_i^r\middle|\Psi_{m^x}\right\rangle\left\langle\Psi_{m^x}\middle|x_j^r\right\rangle\left\langle x_j^r\middle|c_\alpha\middle|y_k^+\right\rangle\\&\cdot\left\langle y_k^+\middle|\Psi_n^+\right\rangle\left\langle\Psi_n^+\middle|y_\ell^+\right\rangle\left\langle y_\ell^+\middle|c_\beta^\dagger\middle|r\right\rangle\end{aligned}\tag{2.211}$$

Again the overlap between random vectors and Lanczos basis can be simplified in case they are obtained from the same Lanczos run.

In case of a high-dimensional Hilbert space, the matrix elements for the ground state and excited state sector can be obtained either in a Lanczos or a Band Lanczos run. It turned out in practice, that among the four possibilities, a Band Lanczos run for the ground state sector and a Lanczos run for the excited state sector are sufficient. With Band Lanczos ED applied to the ground state sector, degenerate eigenenergies are resolved which are relevant due to the Boltzmann factor, while the excited state sector can be handled with a regular Lanczos run.

In practice, the error of an observable $\mathcal{O}$ can be estimated by approximating the variance within a Jackknife analysis [Jah02]. Considering therein Jackknife blocks of size $R-1$ gives for the variance:

$$\overline{\mathcal{O}}_{-k}=\frac{1}{R-1}\sum_{r\neq k}\mathcal{O}_r,\tag{2.212}$$

$$\overline{\mathcal{O}}=\frac{1}{R}\sum_{r}\mathcal{O}_r,\tag{2.213}$$

$$\mathrm{Var}[\overline{\mathcal{O}}]=\frac{R-1}{R}\sum_{k}(\overline{\mathcal{O}}_{-k}-\overline{\mathcal{O}})^2,\tag{2.214}$$

where $\mathcal{O}_r$ is the expectation value obtained from the rth Green's function.

While this type of error analysis is natural in classical Monte Carlo, where running averages of the observables can be used to reduce the effort, here this treatment is artificial and requires additional effort. In essence, the cluster Green's function for each random vector has to be constructed separately and for each of these Green's functions, the observables have to be computed to obtain their Jackknife variance. In practice, this amounts to arrays of Green's functions and observables, which serve only to compute the error.

A technical advantage of using random trace vectors is that they are independent. Hence the computations starting from different random vectors can be performed in parallel. Specifics on the implementation using OpenMP are given in appendix D.

To improve the low-temperature results, Weiße et al. [Wei+06] divide the trace up into parts with exact and random trace vectors. In practice one first computes the eigenstates with lowest energy. When coming to the Lanczos run starting from a random vector, one orthogonalises the Lanzos basis w.r.t. the eigenstates obtained earlier. In addition one has to keep in mind, that the random contributions are weighted by a factor N/R, while the exact parts have a factor 1. Also, while each exact trace vector belongs to one energy, each random vector is associated with a whole spectrum. After implementing and testing this split trace as solver for the VCA, a study using it in combination with the bare FTLM for spin systems was published by Morita and Tohyama [MT20].

Considering systems small enough for FD to assess the precision of the FTLM show, that the method is insufficient to compute reliable grand potentials as needed in VCA. The comparison between FTLM and a trace determined with Band Lanczos ED for a larger $\sqrt{10}\times\sqrt{10}$ site cluster is shown in figure 4.15. When explicitely orthogonalising the random vectors, the results agree with increasing number with those from FD, because one just selects another basis. When handling part of the trace with exact eigenvectors and part with random vectors as done in [Wei+06], the results improve as well. But the results do not deteriorate when omitting the random vectors. Hence the improvement is only due to the contribution from the exact eigenvectors, which outweigh the random contributions. Hence the FTLM procedure is working as it should, leaving only the random vectors and their insufficient weight as the origin. Including more random vectors did not improve the results as can be seen in figure 4.14.

There is a recent report of a typicality-based VCA solver [Nis+19], which is technically close to the FTLM. However in contrast to the approximation performed in equation (2.188), the Boltzmann factor is not expressed in the eigenbasis but explicitely applied as a truncated series to the trace vectors, following the description of Hyuga et al. [Hyu+14]. In case of the FTLM and the typicality-based solver, these are random vectors. A minor difference is that the FTLM described above employs real Gaussian random variables, while the typicality-based solver employs complex random numbers [Nis+19]. Judging by the use in another implementation of the FTLM [SY20] and the original publication [IE04] arguing that these random phase vectors are superior to real Gaussian variables needing less samples to achieve a reasonable accuracy, one should consider them as a way to improve the implementation.

Since Nishida et al. investigated a single-band Hubbard model with real couplings, a set of real vectors should be sufficient to approximate the trace. The results reported by them are thus interpreted as follows: By applying the Boltzmann factor directly, the weights which are missing in case of the FTLM are explicitely enhanced. This can be understood in terms of the power method, where a Hamiltonian projects onto the eigenstate of (in absolute value) largest eigenvalue when it is just applied enough times to a random initial state.

Attempting to implement the typicality-based solver and applying it to smaller systems led, similar to the FTLM-based solvers, to unsatisfying results.

2.4.3 Chebyshev expansion

At finite temperature, the Chebyshev representation of the Green's function requires proper rescaling of the Hamiltonian during construction of the moments and when assembling the Green's function.

In essence, the Chebyshev expansion of the Green's function at finite temperature consists in applying the expansion discussed at zero temperature for all trace vectors considered. However one intricacy has to be stressed which was already mentioned in section 2.3.4 as a disadvantage, the rescaling.

In case exact trace vectors are employed, the argument $x = H - \varepsilon_0$ within equation (2.149) becomes $x_m = H - \varepsilon_m$ at finite temperature, giving

$$G^{\pm}_{AB}(z) = \sum_m \frac{\exp(-\beta\varepsilon_m)}{\Xi} \langle \Psi_m | A[\pm z - (H - \varepsilon_m)]^{-1} B | \Psi_m \rangle \,. \tag{2.215}$$

Hence the expansion for each trace vector has to be rescaled separately, during computation of the moments and assembly of the Green's function. When using random trace vectors, effectively an identity of exact eigenvectors is inserted as

$$G^{\pm}_{AB}(z) = \frac{N}{R} \sum_r \sum_{m^x} \sum_{i,j} \frac{\exp(-\beta\varepsilon_{m^x})}{\Xi} \langle r | x^r_i \rangle \langle x^r_i | \Psi_{m^x} \rangle \langle \Psi_{m^x} | x^r_j \rangle \langle x^r_j | A[\pm z - (H - \varepsilon_{m^x})]^{-1} B | r \rangle \,. \tag{2.216}$$

and rescaling becomes necessary for each eigenvector associated with the respective trace vector.

Besides having to rescale the Hamiltonian properly during construction and assembly, the resolvent is computed as before using the moments constructed via the recursion relation given in equation (2.146).

2.4.4 High-frequency expansion

The number of iterations needed to assemble the Green's function can be reduced by a factor $\mathcal{O}(10^3)$ by employing a high-frequency expansion for most of the contour integration. The presentation follows [SSY18].

A major obstacle consists in the time needed to assemble the Green's function. For a cluster of $\mathcal{O}(10)$ sites and resolving $\mathcal{O}(10^2)$ eigenstates in the ground state and excited state sector respectively, one has to combine $\mathcal{O}(10^6)$ entries. Using the spectral representation gives an additional factor due to the frequencies for which the Green's function has to be evaluated. Assuming $\mathcal{O}(10^3)$ frequencies leads to $\mathcal{O}(10^9)$ loop iterations until the Green's function is fully combined. This holds independent of using exact trace vectors or random vectors.

To reduce the effort, Seki et al. [SSY18] proposed to use the high-frequency expansion of the spectral representation up to 15th order for complex frequencies whose absolute value is larger than the largest pole. By this, one avoids a factor of $\mathcal{O}(10^3)$ for a considerable portion of frequencies.

In order to obtain a pleasant expression for the moments of the high-frequency expansion, one writes the Green's function using Cauchy's integral formula, uses the geometric series and combines everything apart from the frequency into the moments. This gives the Green's function

$$G_{\alpha\beta}(z) = \oint_{\mathcal{C}} \frac{\mathrm{d}z'}{2\pi\,\mathrm{i}} \frac{G_{\alpha\beta}(z')}{z - z'} = \oint_{\mathcal{C}} \frac{\mathrm{d}z'}{2\pi\,\mathrm{i}} G_{\alpha\beta}(z') \frac{1}{z} \sum_{k=0}^{\infty} \left(\frac{z'}{z}\right)^{k} = \sum_{k=0}^{\infty} \frac{M_{\alpha\beta}^{(k)}}{z^{k+1}} \tag{2.217}$$

with moments

$$M_{\alpha\beta}^{(k)} = \oint_{\mathcal{C}} \frac{\mathrm{d}z'}{2\pi\,\mathrm{i}} G_{\alpha\beta}(z') \cdot (z')^{k}. \tag{2.218}$$

Note, that the integration contour $z' \in \mathcal{C}$ within the moments has to run over frequencies which are in absolute value smaller than the actual frequency argument z of the Green's function. Considering the infinite frequency limit of the spectral representation of the Green's function, one finds

$$\lim_{|z| \to \infty} G_{\alpha\beta}(z) = \lim_{|z| \to \infty} \frac{\delta_{\alpha\beta}}{z} + \mathcal{O}(z^{-2}) \tag{2.219}$$

giving for the moment of zeroth order $M_{\alpha\beta}^{(0)}(z) = \delta_{\alpha\beta}$. Moments of higher order are obtained from the spectral representation of the Green's function as

$$\begin{aligned} M_{\alpha\beta}^{(k>0)} = & \sum_{m,n} (E_{nm}^{+})^{k} \frac{\exp(-\beta\varepsilon_m)}{\Xi} \left\langle \Psi_m \middle| c_\alpha \middle| \Psi_n^{+} \right\rangle \left\langle \Psi_n^{+} \middle| c_\beta^{\dagger} \middle| \Psi_m \right\rangle \\ & + \sum_{m,n} (-E_{nm}^{-})^{k} \frac{\exp(-\beta\varepsilon_m)}{\Xi} \left\langle \Psi_m \middle| c_\beta^{\dagger} \middle| \Psi_n^{-} \right\rangle \left\langle \Psi_n^{-} \middle| c_\alpha \middle| \Psi_m \right\rangle \end{aligned} \tag{2.220}$$

by requiring $|z'| > |E_{nm}^{\pm}|$. This means that only those entries of the Green's function can be expressed via its high-frequency expansion which are evaluated at frequencies with $|z| > |E_{nm}^{\pm}|$, enforcing a deformation of the contour as displayed in figure 2.14. Hence knowing the elements of the spectral representation allows directly the computation of all moments of the high-frequency expansion to arbitrary order. The only restriction on the high-frequency expansion is due to the geometric series. Since the moments can be constructed independent of the frequencies, a factor $\mathcal{O}(10^3)$ of iterations can be prevented.

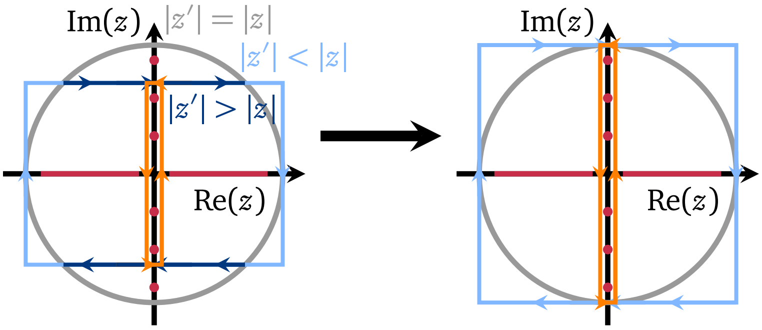

2.14 – Contour deformation necessary to employ the high-frequency expansion. Since $|z'| < |z|$ is required, the contour of figure 2.13e has to be altered to avoid the integration ranges highlighted in dark blue.

2.4.5 Entropy

◈*An expression for the VCA entropy in terms of contour integrals is derived. Focus lies on providing the expressions used numerically. The presentation is motivated by [SSY18], where the respective expressions are given in terms of Matsubara energies.*◈

Going to finite temperature not only makes it possible to consider the temperature-dependence of observables already accessible at zero-temperature, but enables further thermodynamic quantities directly connected to the temperature-dependence of the grand potential Ω. These quantities are the first and second derivative of the grand potential w.r.t. temperature giving the entropy $S = -\mathrm{d}\Omega/\mathrm{d}T$ and the specific heat $C_V = -T\,\mathrm{d}^2\Omega/\mathrm{d}T^2$. In general, the variational parameters λ determined by optimising the grand potential within VCA are temperature dependent. While this temperature dependency drops out in case of the entropy since the grand potential is stationary w.r.t. the variational parameter

$$\mathrm{d}S = -\left.\frac{\partial\Omega}{\partial T}\right|_{\mu,V,\lambda(T)}\mathrm{d}T - \underbrace{\left.\frac{\partial\Omega}{\partial\lambda}\right|_{\mu,V}}_{=0}\frac{\mathrm{d}\lambda}{\mathrm{d}T}\,\mathrm{d}T, \tag{2.221}$$

there remains a temperature derivative of the variational parameters in case of the specific heat

$$C_V = -T\left.\frac{\partial^2\Omega}{\partial T^2}\right|_{\mu,V,\lambda(T)}\mathrm{d}T - T\frac{\partial S}{\partial\lambda}\frac{\mathrm{d}\lambda}{\mathrm{d}T}. \tag{2.222}$$

Since $\lambda(T)$ is not known a-priori and cannot be determined from a one-shot computation, it is not worthwhile spending time on deriving the expression for C_V, but rather to obtain it from finite-differences of the entropy. Without variational parameters an expression for C_V can derived and is given by Seki et al. [SSY18] in terms of Matsubara energies, but this case is usually uninteresting.

Having the expression for the grand potential (2.170) at hand, there are in total three contributions to the entropy

$$-\mathrm{d}\,\Omega|_{\mu,V,\lambda(T)} = -\mathrm{d}\,\Omega_{\mathrm{cl}}|_{\mu,V,\lambda(T)} + \mathrm{d}\,\mathrm{Tr}[\ln(-\boldsymbol{G}_{\mathrm{CPT}}^{-1})] - \mathrm{d}\,\mathrm{Tr}[\ln(-\boldsymbol{G}_{\mathrm{cl}}^{-1})] \tag{2.223}$$

with the VCA-trace $\mathrm{Tr}(\cdot)$. The first is the cluster entropy

$$-\mathrm{d}\,\Omega_{\mathrm{cl}}|_{\mu,V,\lambda(T)} = \frac{1}{T}(\langle H\rangle_{\mathrm{cl}} - \Omega_{\mathrm{cl}})\,\mathrm{d}T \tag{2.224}$$

with $\langle H\rangle_{\mathrm{cl}} = \Xi^{-1}\sum_m \varepsilon_m \exp(-\beta\varepsilon_m)$, which is the average cluster energy [Sch06]. For each of the two remaining contributions, there are two separate temperature dependencies. There are the Boltzmann factors in the Green's functions as well as the Fermi functions within the VCA-trace $\mathrm{Tr}(\cdot)$. Considering differentials of traces of inverse matrices, relations from matrix algebra [Min00] are required. Making use of the three relations

$$\mathrm{d}(\boldsymbol{X}^{-1}) = -\boldsymbol{X}^{-1}(\mathrm{d}\boldsymbol{X})\boldsymbol{X}^{-1}, \tag{2.225}$$

$$\mathrm{tr}[\ln(\boldsymbol{X})] = \ln[\det(\boldsymbol{X})], \tag{2.226}$$

$$\mathrm{d}\ln[\det(\boldsymbol{X})] = \mathrm{tr}(\boldsymbol{X}^{-1}\,\mathrm{d}\boldsymbol{X}) \tag{2.227}$$

for a matrix $\boldsymbol{X}$, one obtains for the term including the cluster Green's function

$$\mathrm{d}\,\mathrm{tr}[\ln(-\boldsymbol{G}_{\mathrm{cl}}^{-1})] = \mathrm{tr}\left[\boldsymbol{G}_{\mathrm{cl}}^{-1}\left\{\sum_{m,n}(\langle H\rangle_{\mathrm{cl}} - \varepsilon_m)\Xi^{-1}\exp(-\beta\epsilon_m)[\boldsymbol{G}_{\mathrm{cl}}^{+} + \boldsymbol{G}_{\mathrm{cl}}^{-}]\right\}\right]\frac{1}{T^2}\,\mathrm{d}T \tag{2.228}$$

and for the one including the CPT-Green's function

$$\mathrm{d}\,\mathrm{tr}[\ln(-\boldsymbol{G}_{\mathrm{CPT}}^{-1})] = \mathrm{tr}\left[(\boldsymbol{G}_{\mathrm{cl}}\boldsymbol{G}_{\mathrm{CPT}}^{-1}\boldsymbol{G}_{\mathrm{cl}})^{-1}\left\{\sum_{m,n}(\langle H\rangle_{\mathrm{cl}} - \varepsilon_m)\Xi^{-1}\exp(-\beta\epsilon_m)[\boldsymbol{G}_{\mathrm{cl}}^{+} + \boldsymbol{G}_{\mathrm{cl}}^{-}]\right\}\right]\frac{1}{T^2}\,\mathrm{d}\,T. \tag{2.229}$$

Looking closer at the combination of these two terms gives the trace of a CPT-variant of the $\boldsymbol{T}$-matrix $\boldsymbol{G}_{\mathrm{CPT}} = \boldsymbol{G}_{\mathrm{cl}} + \boldsymbol{G}_{\mathrm{cl}}\boldsymbol{T}_{\mathrm{CPT}}\boldsymbol{G}_{\mathrm{cl}}$ multiplied by a modified Green's function

$$\begin{aligned}&\mathrm{d}\,\mathrm{tr}[\ln(-\boldsymbol{G}_{\mathrm{CPT}}^{-1})] - \mathrm{d}\,\mathrm{tr}[\ln(-\boldsymbol{G}_{\mathrm{cl}}^{-1})]\\ &= \mathrm{tr}\left[\boldsymbol{T}_{\mathrm{CPT}}\left\{\sum_{m,n}(\langle H\rangle_{\mathrm{cl}} - \varepsilon_m)\Xi^{-1}\exp(-\beta\epsilon_m)[\boldsymbol{G}_{\mathrm{cl}}^{+} + \boldsymbol{G}_{\mathrm{cl}}^{-}]\right\}\right]\frac{1}{T^2}\,\mathrm{d}\,T.\end{aligned} \tag{2.230}$$

In contrast, the parts including derivatives of the Fermi functions

$$\frac{\mathrm{d}\,f(z)}{\mathrm{d}\,T} = f(z)f(-z)z\cdot T^{-2} \tag{2.231}$$

lead for low temperatures to erroneous results. This can be surmised by considering the zero temperature limit, which requires l'Hôpital's rule. To circumvent this expression from appearing, one can perform a variant of partial integration based on Cauchy's integral formula as described in appendix B of [SSY18]. Their argument is repeated here for the sake of completeness and to fill some gaps in their reasoning. First, the temperature derivative is transformed into an energy derivative, since the Fermi function depends only on their ratio

$$\frac{\partial f(z)}{\partial\beta}\frac{\mathrm{d}\,\beta}{\mathrm{d}\,T} = \frac{z}{\beta}\frac{\partial f(z)}{\partial z}\frac{\mathrm{d}\,\beta}{\mathrm{d}\,T}. \tag{2.232}$$

To proceed further, one requires a suitable expression for the Fermi function. This is obtained by considering the function $g(z) = \tanh(\beta z/2)/2$ used in [Nie95], which also has the Matsubara energies as poles and is connected to the Fermi function as $g(z) = 1/2 - f(z)$. Investigating the sum of residues

$$\sum_n \mathrm{Res}[\exp(-0^{+}|z|)g(z)(z'-z)^{-1}, z = \mathrm{i}\,E_n], \tag{2.233}$$

one finds with $\lim\limits_{c\to\infty}\tanh(c\cdot(a+\mathrm{i}\,b)) = \mathrm{sign}(a)$ another expression for $g(z)$

$$g(z) = -\frac{1}{\beta}\sum_n \exp[-0^{+}(|\,\mathrm{i}\,E_n| - |z|)](\mathrm{i}\,E_n - z)^{-1}. \tag{2.234}$$

Setting the converging factor 0^{+} to zero, one obtains for the Fermi function

$$f(z) = \frac{1}{2} + \frac{1}{\beta}\sum_n(\mathrm{i}\,E_n - z)^{-1}. \tag{2.235}$$

Expressing a suitable function with Cauchy's integral formula

$$h(z) = \oint_C \frac{\mathrm{d}\,z'}{2\pi\,\mathrm{i}}\frac{h(z')}{z'-z} \tag{2.236}$$

and computing its m-th derivative

$$\frac{\partial^m}{\partial z^m}h(z) = \oint_C \frac{\mathrm{d}\,z'}{2\pi\,\mathrm{i}}m!\frac{h(z')}{(z'-z)^{m+1}} \tag{2.237}$$

one obtains a similar expression as in the case of the part with derivatives of the Fermi functions. This can be seen with the m-th derivative of the Fermi function

$$\frac{\partial^m}{\partial z^m} f(z) = \frac{1}{\beta} \sum_n m!(\mathrm{i}E_n - z)^{-(m+1)}. \tag{2.238}$$

Combining these relations, one obtains similar to a partial integration

$$\begin{aligned}
\oint_{\mathcal{C}} \frac{\mathrm{d}z'}{2\pi\mathrm{i}} \left(\frac{\partial^m}{\partial z^m} f(z)\right)\bigg|_{z'} h(z') &= \frac{1}{\beta}\sum_n \oint_{\mathcal{C}} \frac{\mathrm{d}z'}{2\pi\mathrm{i}}\, m! \frac{h(z')}{(\mathrm{i}E_n - z')^{m+1}} &(2.239)\\
&= \frac{1}{\beta}\sum_n \left(\frac{\partial^m}{\partial z^m} h(z)\right)\bigg|_{\mathrm{i}E_n} (-1)^{m+1} &(2.240)\\
&= \oint_{\mathcal{C}} \frac{\mathrm{d}z'}{2\pi\mathrm{i}} f(z') \left(\frac{\partial^m}{\partial z^m} h(z)\right)\bigg|_{z'} (-1)^{m+1}. &(2.241)
\end{aligned}$$

Specifically for the part with derivatives of the Fermi functions, one finds

$$\oint_{\mathcal{C}} \frac{\mathrm{d}z'}{2\pi\mathrm{i}} \left(\frac{\partial f(z)}{\partial \beta}\right)\bigg|_{z'} h(z') = \frac{1}{\beta} \oint_{\mathcal{C}} \frac{\mathrm{d}z'}{2\pi\mathrm{i}} f(z') \left[h(z') + z'\left(\frac{\partial h(z)}{\partial z}\right)_{z'}\right] \tag{2.242}$$

With $h(z) = -\operatorname{tr}[\ln(-\boldsymbol{G}_{\mathrm{CPT}}^{-1})] + \operatorname{tr}[\ln(-\boldsymbol{G}_{\mathrm{cl}}^{-1})]$ one obtains the contribution

$$\begin{aligned}
&(-1)\left(-\frac{1}{T}\right)(\Omega_{\mathrm{CPT}} - \Omega_{\mathrm{cl}})\\
&+(-1)\oint_{\mathcal{C}} \mathrm{d}z\, f(z) \operatorname{tr}\left[\boldsymbol{T}_{\mathrm{CPT}} \left\{\sum_{m,n} (Tz)\Xi^{-1} \exp(-\beta\epsilon_m) \left[\frac{\partial \boldsymbol{G}_{\mathrm{cl}}^{+}}{\partial z} + \frac{\partial \boldsymbol{G}_{\mathrm{cl}}^{-}}{\partial z}\right]\right\}\right] \frac{1}{T^2},
\end{aligned} \tag{2.243}$$

where the factor (−1) is due the contour used being left-handed. In total, the entropy is given by

$$S = S_{\mathrm{cl}} + \mathscr{S}_{\mathrm{CPT}} + \mathscr{S}_{\mathrm{cl}} - \frac{1}{T}(\Omega_{\mathrm{CPT}} - \Omega_{\mathrm{cl}}) \tag{2.244}$$

with the contributions

$$\begin{aligned}
S_{\mathrm{cl}} &= -\frac{1}{T}(\Omega_{\mathrm{cl}} - \langle H\rangle_{\mathrm{cl}}), &(2.245)\\
\mathscr{S}_{\mathrm{CPT}} &= \oint_{\mathcal{C}} \mathrm{d}z\, f(z) \operatorname{tr}[(\boldsymbol{G}_{\mathrm{cl}}\boldsymbol{G}_{\mathrm{CPT}}^{-1}\boldsymbol{G}_{\mathrm{cl}})^{-1}\boldsymbol{G}_{\mathrm{mod}}]\frac{1}{T^2}, &(2.246)\\
\mathscr{S}_{\mathrm{cl}} &= \oint_{\mathcal{C}} \mathrm{d}z\, f(z) \operatorname{tr}[(-\boldsymbol{G}_{\mathrm{cl}}^{-1})\boldsymbol{G}_{\mathrm{mod}}]\frac{1}{T^2} &(2.247)
\end{aligned}$$

and the abbreviations

$$\langle H\rangle_{\mathrm{cl}} = \Xi^{-1}\sum_m \varepsilon_m \exp(-\beta\varepsilon_m), \tag{2.248}$$

$$\boldsymbol{G}_{\mathrm{mod}} = \sum_{m,n}(\langle H\rangle_{\mathrm{cl}} - \varepsilon_m)\Xi^{-1}\exp(-\beta\epsilon_m)[\boldsymbol{G}_{\mathrm{cl}}^{+} + \boldsymbol{G}_{\mathrm{cl}}^{-}] - \sum_{m,n}(Tz)\Xi^{-1}\exp(-\beta\epsilon_m)\left[\frac{\partial \boldsymbol{G}_{\mathrm{cl}}^{+}}{\partial z} + \frac{\partial \boldsymbol{G}_{\mathrm{cl}}^{-}}{\partial z}\right]. \tag{2.249}$$

High- and low-temperature limits of the entropy which are useful to check the correct implementation are given in the appendix B.

2.4.6 Cluster-dynamical-impurity approximation (CDIA)

◈*The reference system employed in the CDIA is briefly described. Furthermore, the association of the bath couplings with the cluster Hamiltonian, as well as the on- and inter-cluster part of the V-matrix are explicitely stated. The presentation follows [SSY18].*◈

While VCA incorporates spatial quantum fluctuations, it omits temporal fluctuations which are considered in dynamical mean-field theory. A method that captures both is the cluster-dynamical-impurity approximation (CDIA), where a cluster coupled to additional uncorrelated bath sites is used as reference system.

Since the reference system has more degrees of freedom than the original lattice system, it is expedient to consider an auxiliary system [SSY18] where the uncorrelated bath sites are decoupled from the cluster. Original, auxiliary and reference system are shown in figure 2.15.

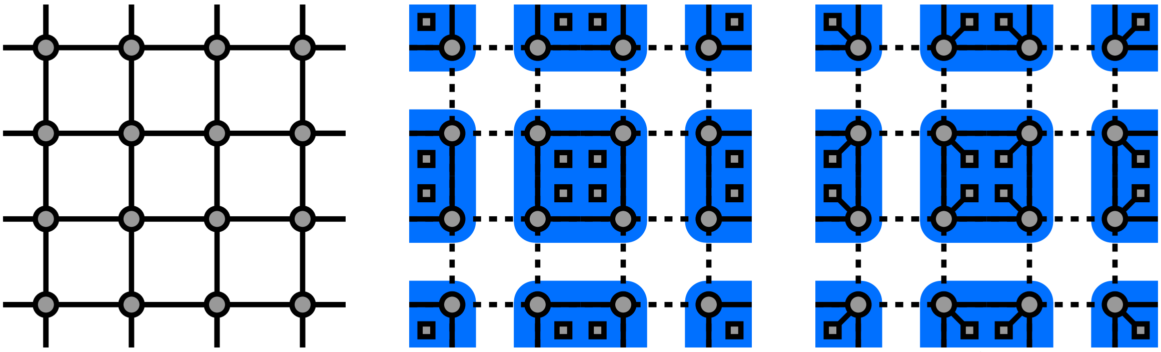
(a) Original system. (b) Auxiliary system. (c) Reference system.

2.15 – Original system, auxiliary and reference system employed in CDIA. Circles denote cluster sites, squares are bath sites. Clusters are highlighted in blue. Solid lines refer to regular hopping, while dashed lines are hoppings between clusters.

For such a system, the partition function factorizes into one for the lattice system and one for the bath sites since the Hamiltonians commute and the subspaces are independent:

$$\Xi_{\mathrm{aux}} = \Xi \cdot \Xi_{\mathrm{bath}}, \tag{2.250}$$

giving the grand potential:

$$\Omega = \Omega_{\mathrm{aux}} - \Omega_{\mathrm{bath}}. \tag{2.251}$$

Approximating now the auxiliary system with the reference system of clusters coupled to the bath sites in a VCA manner finishes the description of CDIA. More details on the derivation can be found in [SSY18].

In practice, the bath sites can be realised as an orbital degree of freedom. The chemical potential of the bath sites enters only the cluster Hamiltonian, while the hybridisation between cluster and bath sites is added to the cluster Hamiltonian and subtracted via the on-cluster part of the V-matrix. In contrast, the lattice hopping enters the cluster Hamiltonian as well as the inter-cluster part of the V-matrix.

Care has to be taken concerning the degree of degeneracy considered. Since electrons on the bath sites are non-interacting, the systems ground state is degenerate by the number of permutations of electrons on the bath sites. Consider the case of a half-filled 2 × 2 cluster forming the ground state. Filling the system with $N = 7$ electrons leads to a 56-fold degenerate ground state at negligible hybridisation. Hence 56 exact eigenvectors have to be considered even at low enough temperatures for zero to low hybridisation.

2.4.7 Setting the filling

◇*The filling or magnetisation of a system can be fixed by optimising the suitably Legendre transformed grand potential w.r.t. the physical chemical potential or a physical magnetic field. The presentation follows [BP10].*◇

In order to set the filling of the system to some value $\overline{N}$, instead of the grand potential, its Legendre transform

$$F = \Omega + \mu\overline{N} \tag{2.252}$$

is considered. Note that μ is the physical chemical potential. Optimising this free energy w.r.t. the physical chemical potential enforces the demanded filling

$$\frac{\partial F}{\partial \mu} = -\langle N \rangle + \overline{N} \overset{!}{=} 0 \tag{2.253}$$

as can be seen from section 2.1.2. Other observables such as the magnetisation can be fixed in a similar fashion which is described in [BP10].

3 Matrix-product state solver for VCA

◇*Using matrix-product states (MPSs) makes it possible to consider larger systems but also requires more time to handle them. It is argued that among the representations of the Green's function presented in section 2.3, the continued fraction and Chebyshev representations are most promising to be constructed using MPS. A proof of principle is given using the continued fraction representation. Issues arising due to loss of orthogonality could be overcome with the Chebyshev representation.*◇

Matrix-product states (MPSs) form an efficient representation of many-body states. By truncating the state space to those with a non-vanishing singular value, the exponential growth of the Hilbert space dimension with increasing system size can – to some degree – be counteracted.

Assuming that the ground state of the system can be found in its MPS representation, the main task is to construct the single-particle Green's function. Since the spectral representation of the Green's function requires the (partial) diagonalisation of the Hamiltonian in the excited state sectors, it is not an option within the MPS representation. This also discards the possibility to construct the Q-matrix representation of the Green's function. In turn only the option to compute the self-energy functional by means of a contour integration in the complex energy plane remains, discarding a purely real or imaginary time-evolution to compute the Green's function. This also implies that the Kernel polynomial method [Wei+06] which has been used for a MPS-based solver for the dynamical mean-field theory [Wol+14] is not available. As it stands, the continued fraction representation [Dag94; Sén08; SSY18] remains as most straight-forward option to reconcile the different requirements. It is described in section 2.3.2 for real couplings.

However, the continued fraction representation rests on the construction of the Lanczos basis in the excited state sectors, which is supposed to be sufficiently orthogonal. Since the basis is expressed in terms of MPSs, the reorthogonalisation is performed variationally. This means that in order to keep the space of MPS small, the next state within the iteration rule is approximated by one representable within the MPS space that is closest to the actual state. Besides requiring more runtime, the truncation eventually leads to a loss of orthogonality. Technical details on the solver can be obtained from [Pae20].

Considering the one-band Hubbard model in one dimension at half-filling while varying the isotropic hopping on the cluster gives the grand potential shown in figure 3.1a. For small systems, the MPS-based solver agrees for the entire parameter range considered with the results obtained using an ED solver. Larger systems exhibit deviations at higher isotropic hoppings. However close to the stationary point, both solvers agree. The run-times necessary to compute one data point are shown in figure 3.1b. In all cases considered, the MPS-based solver needs more time than the ED solver. Once an optimisation algorithm is applied which requires a factor of $\mathcal{O}(10)$ iterations per variational parameter to achieve convergence, the MPS-based solver has to be furher improved. Parallelisation is one option which however collides with the intention of employing larger reference systems. Exhausting the capabilities of the MPS solver and interlocking it with the rest of the implementation by making the solver more accessible would already be sufficient to investigate more interesting systems.

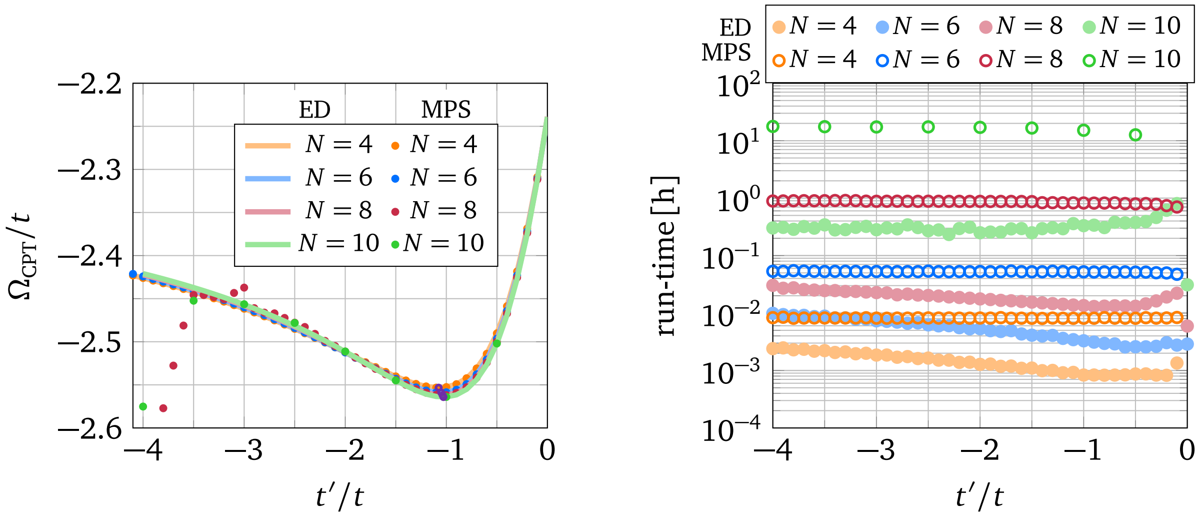

(a) CPT Grand potential. The purple open dots denote the minima.

(b) Run-times.

3.1 – CPT Grand potential Ω_{CPT}/t and run-times needed to compute it vs on-cluster hopping t'/t at $T/t = 0$, $U/t = 4$ for various one-dimensional clusters comparing MPS- and ED-solver.

In the following some technical parameters used to obtain the results in figure 3.1a are listed with a rough description of their implications based on the presentation by Paeckel [Pae20], whose MPS solver was used. General parameters of the simulation are the maximal bond dimension ranging at 20—500 which specifies the rank of the largest matrices occuring in the MPS. The maximal discarded weight in the range $10^{-10} - 10^{-5}$ fixes how strongly the MPSs are truncated by means of neglecting components which have a small singular value. To find the ground state, 40 sweeps through the system are performed, during each of which an effective local Hamiltonian is partially diagonalised within $5-10$ Lanczos iterations until the lowest local eigenenergy changes per iteration by less than $10^{-10} - 10^{-8}$. The solver allows selecting the quantum number sector of the ground state, which amounts here to setting the particle number to half-filling and the total spin to zero. To construct the continued fraction representation of the Green's function, the Hamiltonian is represented as a tridiagonal matrix using the Lanczos algorithm. Besides applying the Hamiltonian to states, the resulting Lanczos vectors have to be orthogonalised w.r.t. each other. As mentioned earlier, this is done variationally for the MPS, which refers to a variational compression with orthogonality to other states as constraint. There, a maximal distance of 10^{-8} between the initial and the variationally compressed state are allowed, while the discarded weight may be at maximum 10^{-6}. A maximum of 20 sweeps through the system are performed. For the continued fraction representation, a maximum of 50 Lanczos iterations of excited states are employed. Each newly constructed Lanczos vector is orthogonalised w.r.t. 5 previously obtained vectors. Once the lowest eigenvalue changes by no more than 10^{-8}, the iteration is stopped as well.

In summary using MPSs is a two-sided coin. On one side, they enable the handling of larger systems since only necessary states are considered. On the other side, the time required to handle these larger systems is increased as well. In addition, the orthogonality of the basis constructed to obtain a tridiagonal Hamiltonian in the excited state sectors is not ensured. How strongly this affects the Green's function as the inverse of the tridiagonal Hamiltonian is unclear. A solution to this issue consists in using the Chebyshev representation put forward in section 2.3.4 which avoids any need for orthogonalisation.

4 One-band Hubbard model: Testing ground

◈*The one-band Hubbard model serves as testing ground for the solvers implemented. Analytical results on one-dimensional one and two site clusters serve to verify the implementation employing FD. The basic implementation of FTLM-based solvers is verified by comparing their results on one-dimensional two and four site clusters with those of FD. For all practical purposes considered, they are restricted to too high temperatures to be of use. Using traces with exact and random vectors makes it possible to reach lower temperatures. Comparing the results obtained using these split traces with literature confirms their implementation. Employing solely exact trace vectors turns out to be the most expedient option. The agreement between results of an ED solver with those of a Chebyshev solver, both using exact trace vectors, verifies the implementation of the Chebyshev solver.*◈

Note that all cluster observables (cluster particle density, cluster kinetic energy) determined in this chapter are obtained from the cluster Green's function. Appendix C discusses discrepancies occuring between cluster expectation values obtained from the eigenstates following equation (2.22) and the cluster Green's function. However the discrepancies discussed in appendix C do not alter the overall conclusion, since it is a systematic error which affects the results from all solvers equally.

4.1 FD, ED and FTLM

4.1.1 Hubbard atom

◈*The implementation of finite temperature VCA using a FD solver is verified on the cluster and CPT level.*◈

One of the simplest exactly solvable models where finite temperature leads to different behaviour is the Hubbard atom. It consists of one site described by the Hubbard model without hopping

$$H_{\mathrm{cl}} = -\mu(n_\uparrow + n_\downarrow) + U n_\uparrow n_\downarrow, \tag{4.1}$$

where μ is the chemical potential, U the Hubbard repulsion and n_σ the number operator counting fermionic particles of spin σ on the site. Since the Hamiltonian (4.1) is diagonal in the site basis, the partition function defined in equation (2.19) can be written down straightforwardly

$$\Xi_{\mathrm{cl}} = 1 + 2\exp\left(\frac{\mu}{T}\right) + \exp\left(-\frac{U-2\mu}{T}\right) \tag{4.2}$$

and allows determining the grand potential Ω defined in equation (2.20). The main quantity of interest is the particle density $\langle n\rangle = (-\partial\Omega/\partial\mu)/\ell$ for one site $\ell = 1$, giving

$$\langle n\rangle_{\mathrm{cl}} = \frac{2}{\Xi_{\mathrm{cl}}} \cdot \left[\exp\left(\frac{\mu}{T}\right) + \exp\left(-\frac{U-2\mu}{T}\right)\right]. \tag{4.3}$$

Combining the numerically obtained cluster particle density from the zero-, one- and two-particle sectors according to equation (A.4), the analytical relation is recovered as can be seen in figure 4.1. Hence for one- and low-dimensional Hilbert-spaces, the implementation of the finite temperature treatment employing FD is verified from the perspective of the cluster particle density.

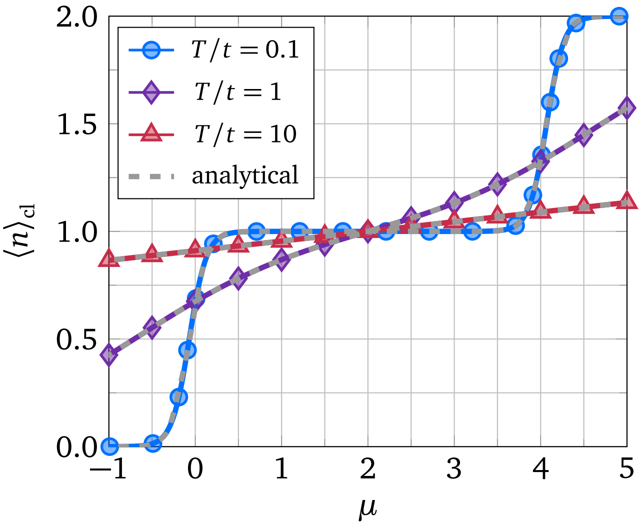

4.1 – Cluster particle density $\langle n \rangle_{\mathrm{cl}}$ vs chemical potential μ for a one site cluster with $U = 4$ at various temperatures. The data is obtained via FD and compared with the analytical relation (4.3).

Solving the equation of motion of the Green's function in energy space without specifying the boundary conditions one finds

$$G^{\mathrm{cl}}_{\sigma\sigma'}(E) = \delta_{\sigma\sigma'} \left[\frac{1}{E+\mu} + \frac{U \langle n_{\bar{\sigma}} \rangle_{\mathrm{cl}}}{(E+\mu)\cdot(E+\mu-U)} \right]. \tag{4.4}$$

By applying a partial fraction decomposition, $G^{\mathrm{cl}}_{\sigma\sigma'}$ can be written in its spectral representation. Employing the Dirac identity [Nol14], the spectral function follows as

$$\begin{aligned} A^{\mathrm{cl}}_{\sigma\sigma'}(E) = \delta_{\sigma\sigma'} \big[&(1-\langle n_{\bar{\sigma}} \rangle_{\mathrm{cl}})\, \delta(E+\mu) \\ &+ \langle n_{\bar{\sigma}} \rangle_{\mathrm{cl}} \delta(E+\mu-U) \big]. \end{aligned} \tag{4.5}$$

Applying the spectral theorem [Nol14] for fermions, the particle density can be expressed in terms of a set of algebraic equations. After solving these for $\langle n_\sigma \rangle$, one obtains the expression (4.3).

Starting from the cluster Green's function (4.4) and considering the inter-atom hopping matrix

$$V_{\sigma\sigma'}(\tilde{k}) = -2t\,\delta_{\sigma\sigma'} \cos(\tilde{k}), \tag{4.6}$$

with the reciprocal lattice vectors of the superlattice $\tilde{k} = \{2\pi n/N_{\mathrm{cl}} | n = 0, 1, \ldots, N_{\mathrm{cl}} - 1\}$ of N_{cl} atoms, the CPT Green's function can be obtained via

$$G^{\mathrm{CPT}}_{\sigma\sigma'}(E, \tilde{k}) = \left[G^{\mathrm{cl}}_{\sigma\sigma'}(E)^{-1} - V_{\sigma\sigma'}(\tilde{k}) \right]^{-1}. \tag{4.7}$$

After a partial fraction decomposition, the CPT Green's function takes the form

$$G^{\mathrm{CPT}}_{\sigma\sigma'}(E, \tilde{k}) = \delta_{\sigma\sigma'} \left[\frac{\varrho_+}{E-\varepsilon_+} + \frac{\varrho_-}{E-\varepsilon_-} \right] \tag{4.8}$$

with weights and poles

$$\varrho_\pm = \pm\frac{\mu - U(1-\langle n_{\bar\sigma}\rangle_{\mathrm{cl}}) + \varepsilon_\pm}{\varepsilon_+ - \varepsilon_-}, \tag{4.9}$$

$$\begin{aligned}\varepsilon_\pm = \frac{1}{2}\Big[&(U - 2\mu - 2t\cos(\tilde{k})) \\ &\pm\sqrt{(U-2t\cos(\tilde{k}))^2 + 8t\cos(\tilde{k})U(1-\langle n_{\bar\sigma}\rangle_{\mathrm{cl}})}\Big].\end{aligned} \tag{4.10}$$

Using again the Dirac identity and the spectral theorem [Nol14], one obtains the CPT particle density as

$$\langle n\rangle_{\mathrm{CPT}} = \frac{1}{N_{\mathrm{cl}}}\sum_{\tilde{k}}[\langle n_\uparrow\rangle_{\mathrm{CPT}}(\tilde{k}) + \langle n_\downarrow\rangle_{\mathrm{CPT}}(\tilde{k})] \tag{4.11}$$

with

$$\langle n_\sigma\rangle_{\mathrm{CPT}}(\tilde{k}) = \varrho_+ f(\varepsilon_+) + \varrho_- f(\varepsilon_-) \tag{4.12}$$

and the Fermi function $f(E) = [\exp(E/T)+1]^{-1}$. Note that this CPT treatment differs from the treatment of Gros and Valentí [GV93], since they formally set $\langle n_{\bar\sigma}\rangle_{\mathrm{cl}} = \langle n_{\bar\sigma}\rangle_{\mathrm{CPT}}$ within equation (4.10) and determine the particle density self-consistently.

Numerically, the different particle number sectors are considered separately and their densities are combined according to equation (A.4) as done for the cluster particle density. The comparison of the CPT particle densities is shown in figure 4.2 with the analytical results as dashed, light grey lines and the numerical results as solid, coloured lines. As it turns out, it is not sufficient to treat each particle number sector separately and combine the results afterwards. Due to the V-matrix, each particle number sector has to be considered, when setting up the cluster Green's function. Apart from the region where two sectors of different particle number contribute, the agreement between analytical and numerical results is of quantitative nature. For higher temperatures, the quantitative agreement extends over the whole range of the chemical potential considered, since each particle number sector contributes uniformly throughout this range. A more general reason for the deviations is the thermodynamic inconsistency of CPT [Sén12].

Thus for the purpose of verifying the implementation, this comparison is not suitable. Hence the calculation leading to equation (4.11) is repeated for the cluster Green's functions of the zero-, one- and two-particle sector separately. These in turn are directly obtained by constructing their spectral representations $G^{(N)}_{\sigma\sigma'}$

$$G^{(0)}_{\sigma\sigma'}(E) = \delta_{\sigma\sigma'}[E+\mu]^{-1}, \tag{4.13}$$

$$G^{(1)}_{\sigma\sigma'}(E) = [G^{(0)}_{\sigma\sigma'}(E) + G^{(2)}_{\sigma\sigma'}(E)]/2, \tag{4.14}$$

$$G^{(2)}_{\sigma\sigma'}(E) = \delta_{\sigma\sigma'}[E-(U-\mu)]^{-1}. \tag{4.15}$$

The combination of the respective particle densities according to equation (A.4) for different temperatures is shown in figure 4.2 as dotted, dark grey lines. Here, numerical and analytical results agree.

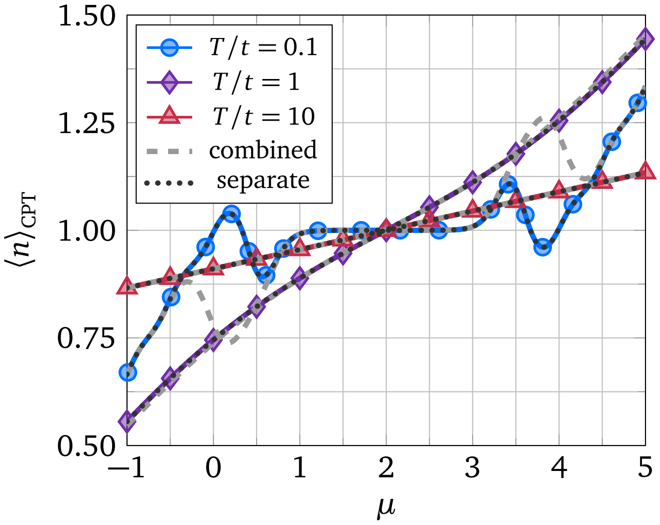

4.2 – CPT particle density $\langle n \rangle_{\mathrm{CPT}}$ vs chemical potential μ for a one site cluster reference system with $U/\mu = 4$ and $N_{\mathrm{cl}} = 24$ at various temperatures. The data (solid, coloured line) is obtained via FD and compared with the analytical relation (4.11), which is evaluated using the cluster Green's function of all particle number sectors combined (dashed, light grey line) and for all particle number sectors treated separately with the densities combined afterwards (dotted, dark grey line).

In the context of CPT, the grand potential is further of importance, since it contains contributions from the cluster grand potential, the cluster Green's function and the CPT Green's function. Employing the analytical expression derived by Potthoff [Pot03], it is given by

$$\begin{aligned}\Omega_{\mathrm{CPT}} &= \Omega_{\mathrm{cl}} + \operatorname{Tr}\ln\left(-G_{\mathrm{CPT}}^{-1}\right) - \operatorname{Tr}\ln\left(-G_{\mathrm{cl}}^{-1}\right) \\ &= \Omega_{\mathrm{cl}} - L\sum_{m,\sigma}\frac{1}{N_{\mathrm{cl}}}\sum_{\tilde{k}}\ln\left[1+\exp\left(\frac{\varepsilon_{m\sigma}^{\mathrm{CPT}}(\tilde{k})}{T}\right)\right] \\ &\quad + 2L\sum_{m}\ln\left[1+\exp\left(\frac{\varepsilon_{m}^{\mathrm{cl}}}{T}\right)\right],\end{aligned} \tag{4.16}$$

where $L = N_{\mathrm{cl}} \cdot \ell$ is the number of all sites on a finite lattice of N_{cl} clusters with ℓ sites each and the sum over m resembles the summation over all poles. The results from the equation of motion, the separately treated particle number sectors and the numerical results are shown in figure 4.3. Again, handling the different particle number sectors separately agrees with the numerical results, while the equation of motion outcomes agree quantitatively apart from where they are expected to differ.

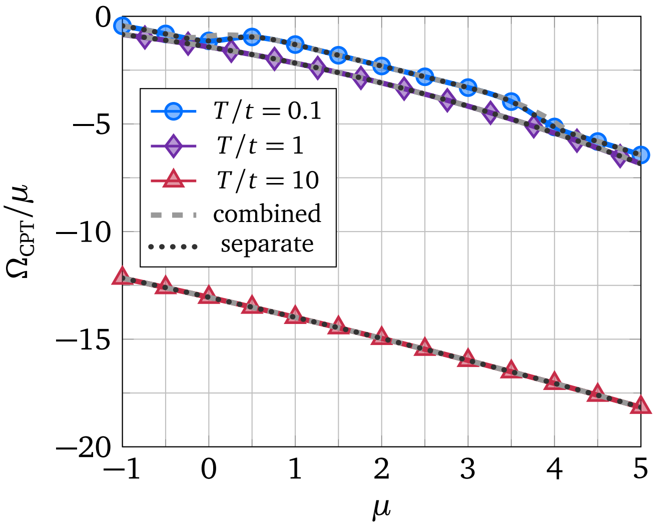

4.3 – CPT grand potential $\Omega_{\mathrm{CPT}}/\mu$ vs chemical potential μ for a one site cluster reference system with $U/\mu = 4$ and $N_{\mathrm{cl}} = 24$ at various temperatures. The data (solid, coloured line) is obtained via FD and compared with the analytical relation (4.16), which is evaluated using the cluster Green's function of all particle number sectors combined (dashed, light grey line) and for all particle number sectors treated separately with the grand potentials combined afterwards (dotted, dark grey line).

Therefore the implementation of the FD solver used for CPT is correct for a one site cluster.

4.1.2 Two site Hubbard cluster

The implementation of finite temperature VCA using a FTLM solver is considered on the cluster and CPT level. There occur discrepancies in the cluster kinetic energy at low temperature.

With two instead of one site, analytical results can be obtained easily and the FTLM can be used as solver. This is not possible for the Hubbard atom due to the small Hilbert space, which is further decomposed into disconnected sectors of spin up and spin down particles. Hence, the Hubbard atom is extended to the full Hubbard model

$$H_{\mathrm{cl}} = -t \sum_{\langle i,j\rangle,\sigma} \left(c^{\dagger}_{i\sigma} c_{j\sigma} + c^{\dagger}_{j\sigma} c_{i\sigma} \right) - \mu \sum_{i\sigma} n_{i,\sigma} + U \sum_{i} n_{i\uparrow} n_{i\downarrow}, \tag{4.17}$$

where t is the hopping amplitude, $\langle i, j\rangle$ denotes all nearest neighbour bonds and $c^{(\dagger)}_{i\sigma}$ annihilates (creates) a fermion at site i with spin σ. Computing the eigenenergies of the Hamiltonian (4.17) for each sector of fixed particle number and total spin separately allows constructing the partition function giving the grand potential and thus all thermodynamic expectation values as derivatives. The eigenenergies within each sector are listed in table 4.1.

4.1 – Eigenenergies ε of the two site Hubbard model, sorted by fixed particle number with given spin.

$N_\uparrow$	$N_\downarrow$	ε
0	0	0
1	0	$-\mu \mp t$
0	1	$-\mu \mp t$
1	1	$U - 2\mu$
		-2μ
		$(U - 4\mu \pm \sqrt{U^2 + 16t^2})/2$
2	0	-2μ
0	2	-2μ
2	1	$U - 3\mu \mp t$
1	2	$U - 3\mu \mp t$
2	2	$2U - 4\mu$

In the following, the observables are computed for each particle number sector separately and combined afterwards via equation (A.4).

Figure 4.4a shows the cluster particle density, where the results using FD and the FTLM coincide with the analytical result. In contrast, the cluster kinetic energy shown in figure 4.4b exhibits deviations of the FTLM result within an intermediate range of the chemical potential for $T/t \in \{0.1, 1\}$, while FD is reliable. When considering the sectors of different particle number separately, the two-particle sector can be identified to give different results for the FTLM and FD. When using combinations of FD and the FTLM for the ground state and excited state sector, each time the trace is performed by the same method (e.g. FD+FD and FD+FTLM or FTLM+FD and FTLM+FTLM), the results agree, while different methods lead to deviations. Hence the origin of these deviations is the stochastic evaluation of the trace using random vectors. Using more random vectors or considering higher temperatures should allow to overcome these discrepancies.

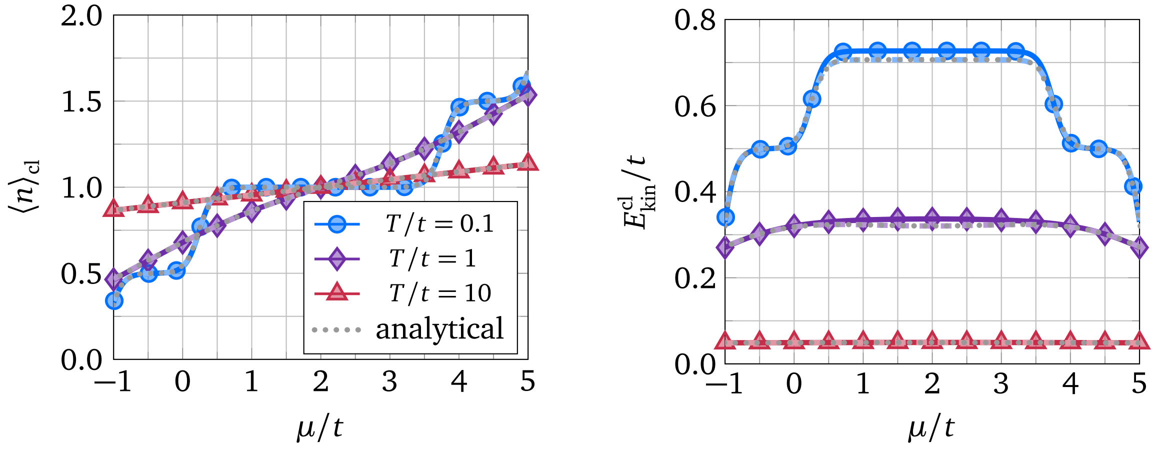

(a) Density.

(b) Kinetic energy.

4.4 – Cluster particle density $\langle n \rangle_{\mathrm{cl}}$ and cluster kinetic energy $E^{\mathrm{cl}}_{\mathrm{kin}}/t$ vs chemical potential μ/t for a two site cluster with $U/t = 4$ at various temperatures. The dashed, light-coloured lines are obtained via FD, while the solid, dark-coloured lines originate from the FTLM employing $R = 75$ random vectors while requiring the convergence of one eigenenergy. Both are compared with the analytical result (dotted, grey line) for which all particle number sectors are treated separately with the observables combined afterwards.

In order to assess the quality of the FTLM as solver within CPT, the CPT particle density obtained via FTLM+CPT is shown in figure 4.5 and compared with the result from FD+CPT. Apart from small deviations at $T/t = 0.1$, both results agree.

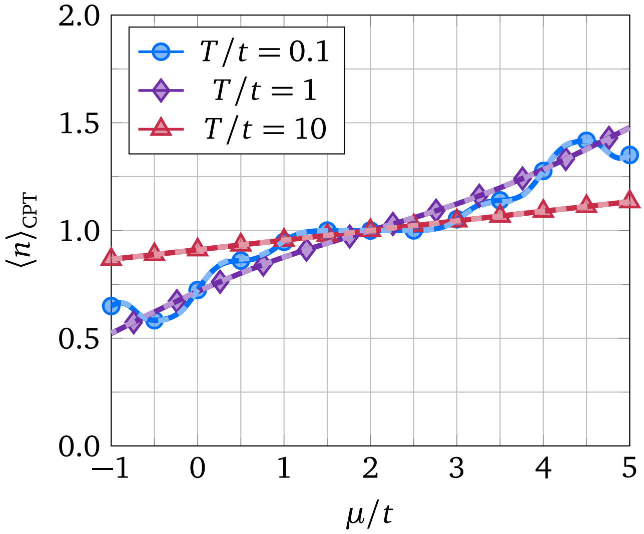

4.5 – CPT particle density $\langle n\rangle_{\mathrm{CPT}}$ vs chemical potential μ/t for a two site cluster reference system with $U/t = 4$ and $N_{\mathrm{cl}} = 24$ at various temperatures. The dashed, light-coloured lines are obtained via FD, while the solid, dark-coloured lines originate from the FTLM employing $R = 75$ random vectors while requiring the convergence of one eigenenergy.

4.1.3 Four site Hubbard cluster

By considering the cluster kinetic energy as reference quantity, the FTLM solver is investigated. Its implementation is verified by constructing an explicit basis of random vectors. The importance of precise low excited states is emphasized. Different combinations of Lanczos and Band Lanczos solvers for the ground and excited state sector are considered. Splitting the trace into exact and random trace vectors makes it possible to investigate lower temperatures.

Verification of the FTLM

Consider an one-dimensional, four site Hubbard cluster with antiferromagnetic (AFM) Weiss field

$$H_{\mathrm{AFM}} = h' \sum_j (-1)^j (n_{j\uparrow} - n_{j\downarrow}) \tag{4.18}$$

entering the cluster Hamiltonian and being subtracted in the V-matrix as reference system. Although the relative error of thermodynamic quantities obtained via FTLM should decrease with increasing system size, considerable deviations in the kinetic energy occur for $N \in [2,6]$ particles on such a cluster. These deviations are random in the sense that expected symmetries (e.g. particle-hole symmetry and spin-flip symmetry) are not satisfied by the kinetic energy. An example for the lack of spin-flip symmetry is shown in figure 4.6 by the blue crosses. To assess, whether the implemented FTLM is correct, the case of two particles on the four site cluster is considered. By orthogonalising the random vectors explicitely w.r.t. each other and considering $R \in \{20, 24, 28\}$ random vectors, two properties of the implemented FTLM are found:

1) When considering $R = 28$ random vectors which is the dimension of the Hilbert space of two particles on a four site cluster, the orthogonalised random vectors form a complete basis. Hence one expects the kinetic energy to agree with the result from FD. This is confirmed by the results in figure 4.6.
2) With less random vectors than the dimension of the Hilbert space, the orthogonalisation improves the results compared to no orthogonalisation. Nevertheless, the spin-flip symmetry is not recovered by an orthogonal but incomplete set of random vectors.

Using the FTLM with orthogonalised random vectors as a means of constructing a basis of random vectors to compute the trace confirms the implementation of the FTLM. However the FTLM is supposed to handle small systems by considering enough random vectors, thus increasing the sample size.

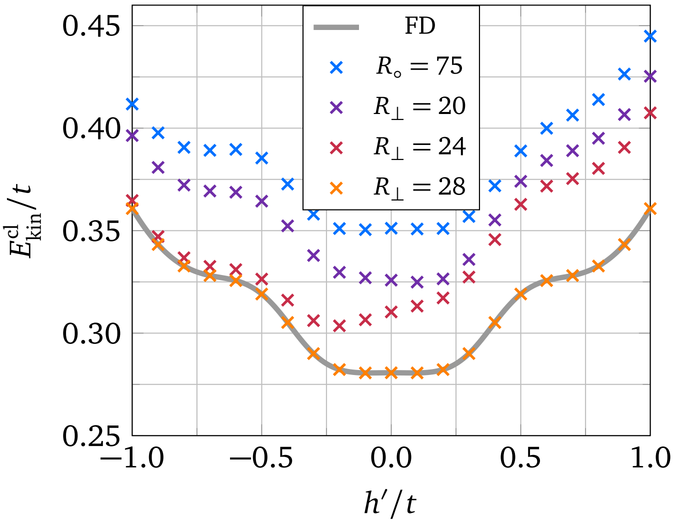

4.6 – Cluster kinetic energy $E^{\mathrm{cl}}_{\mathrm{kin}}/t$ vs AFM Weiss field h'/t of two particles on a four site cluster with $U/t = 4$, $\mu = U/2$, $T/t = 0.1$ for R random vectors. The index '$\circ$' refers to unorthogonalised, '$\perp$' to orthogonal random vectors.

Importance of precise low excited states

When considering the cluster kinetic energy obtained using different seeds for the random number generator as shown in figure 4.7, there appears to be a favour for either $h'/t > 0$ or $h'/t < 0$. A possible reason for this may lie in the overlap of the sets of random vectors with the respective ground state of the system. While a seed of 96 leads to random vectors with a large overlap with the ground state commensurate with $h'/t < 0$, a seed of 756 constructs random vectors which favour the ground state with $h'/t > 0$. This can be inferred from the ground state weight to the partition function

$$\Xi_{\mathrm{GS}}(h') = \sum_i |\langle \mathrm{GS}(h')|r_i\rangle|, \tag{4.19}$$

which is the prefactor of the Boltzmann factor from the ground state energy. For the seed 96 the current implementation gives $\Xi_{\mathrm{GS}}(\pm 0.8t) \approx 2.3, 2.5$, while the seed 756 yields $\Xi_{\mathrm{GS}}(\pm 0.8t) \approx 2.5, 1.8$. Although the difference between these weights seems small, it is amplified by the Boltzmann factor from the ground state, which is for $h'/t = \pm 0.8$ of order $\mathcal{O}\left[\exp(7.1158/0.1) = 8 \cdot 10^{30}\right]$. Thus even a small difference in these weights is punished.

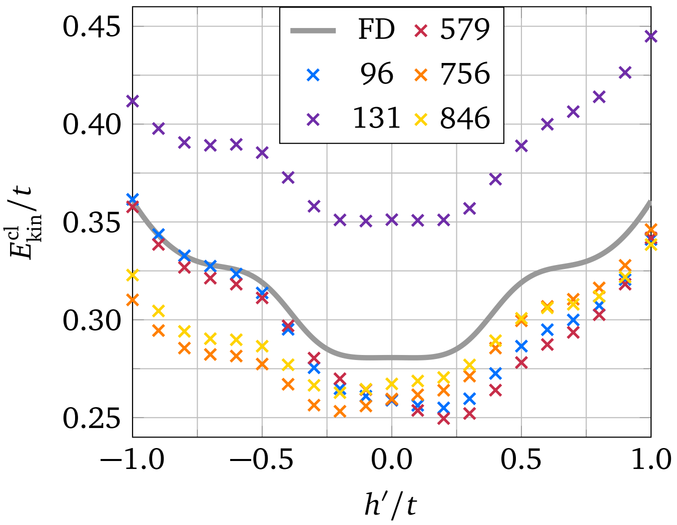

4.7 – Cluster kinetic energy $E_{\mathrm{kin}}^{\mathrm{cl}}/t$ vs AFM Weiss field h'/t of two particles on a four site cluster with $U/t = 4$, $\mu = U/2$, $T/t = 0.1$ for $R = 75$ random vectors generated using the seeds given in the key.

Further methods and their verification

Apart from Lanczos ED to determine the matrix elements contributing to the Green's function, Band Lanczos ED can be used as well. Its advantage lies in the ability to resolve degenerate eigenstates. Hence for systems with degenerate ground or low lying excited states, their contributions to the Green's function can be determined precisely. Since the Green's function contains ingredients from three sectors of different particle number (N, $N \pm 1$ particles), in principle for each of these sectors, the Lanczos basis can be determined either through Lanczos or Band Lanczos ED. Here, the usage of Lanczos or Band Lanczos ED is restricted to the ground state sector with N particles and the excited state sectors with $N \pm 1$ particles. If Band Lanczos ED is applied to the ground state sector, the number of degenerate states N_{deg} expected is specified externally. In practice $N_{\mathrm{deg}} = 8$ is used. Once Band Lanczos ED is used for the FTLM, the number of random vectors R is increased such that N_{deg} becomes a divisor of it, specifically to

$$\tilde{R} = \left\lceil \frac{R}{N_{\mathrm{deg}}} \right\rceil \cdot N_{\mathrm{deg}}. \tag{4.20}$$

When Band Lanczos ED is applied to the excited state sector, the number of excitations fix N_{deg}. For a cluster with ℓ sites, including b orbitals of particles with spin, $N_{\mathrm{deg}} = 2b\ell$. Once Band Lanczos ED is used within the ground and excited state sector, N_{deg} is set externally for the ground state sector and fixed by the number of excitations for the excited state sector. The resulting combinations of Lanczos and Band Lanczos ED are denoted finite temperature Lanczos method (FTLM), finite temperature Band Lanczos method (FTBLM), degenerate finite temperature Lanczos method (DFTLM) and degenerate finite temperature Band Lanczos method (DFTBLM), which are summarised in table 4.2.

4.2 – Abbreviations of the methods emerging by applying Lanczos (L) and/or Band Lanczos (BL) ED within the ground and excited state sectors.

ground state	excited state	abbreviation
L	L	FTLM
L	BL	FTBLM
BL	L	DFTLM
BL	BL	DFTBLM

Note that in the meantime of writing this thesis an implementation using Block Lanczos ED within the FTLM has been presented [SY20].

In order to test the implementations of this range of methods, again the cluster kinetic energy of two particles on a four site cluster are shown in figure 4.8.

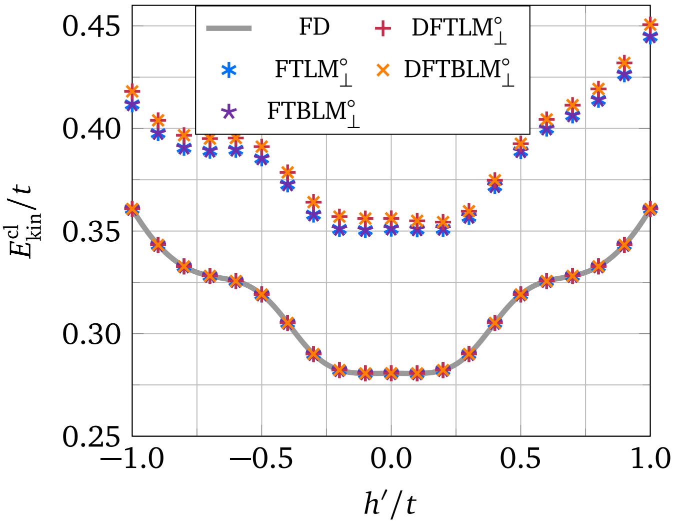

4.8 – Cluster kinetic energy $E^{\mathrm{cl}}_{\mathrm{kin}}/t$ vs AFM Weiss field h'/t of two particles on a four site cluster with $U/t = 4$, $\mu = U/2$, $T/t = 0.1$ for R random vectors while allowing $N_{\mathrm{deg}} = 7$ degenerate vectors. The index '$\circ$' refers to $R = 75$ unorthogonalised, '$\perp$' to $R = 28$ orthogonal random vectors. The data lying far away from the FD results emerge from the unorthogonalised random vectors.

The influence of the method used within the N-particle sector can be seen from the data obtained via unorthogonalised random vectors (far away from the FD results). Employing Band Lanczos ED leads to an overestimation, since more states contribute in each Band Lanczos run than in each Lanczos run. Nevertheless, for a complete basis of random vectors, the FD result is recovered for each method. Hence each of the implementations is confirmed, although the quality of the results depend strongly on the number of random vectors.

Extension to low temperatures

A way to overcome the limitations of high temperature is mentioned by Weiße et al. [Wei+06] in the context of the KPM. There, an inital Lanczos run is used to determine the ground state and several excited states. These states are used as trace vectors to compute contributions. In the next step, random vectors are generated and orthogonalised w.r.t. these eigenvectors, before they are used to stochastically sample the trace and compute matrix elements within the KPM. Details are given in section 2.4.2.

This approach can also be applied to the FTLM and its variants giving satisfying results. Variants of the FTLM combined with an exact contribution to the trace are denoted by a leading ‘ex’ (exFTLM, exFTBLM, exDFTLM, exDFTBLM). The most important question that arises is, whether a partial orthogonalisation is enough to circumvent the asymmetry in figure 4.8. A more practical question is, how many exact and how many random trace vectors are required to get results of satisfying precision. These questions are addressed in figure 4.9. Therein again, the cluster kinetic energy of two particles on a four site cluster is shown, this time for $N_{\mathrm{ex}} \in \{1,2,4,8,16\}$ exact and $R = 25$ random trace vectors, as well as for $N_{\mathrm{ex}} \in \{1,2,4\}$ and $R \in \{50,75\}$.

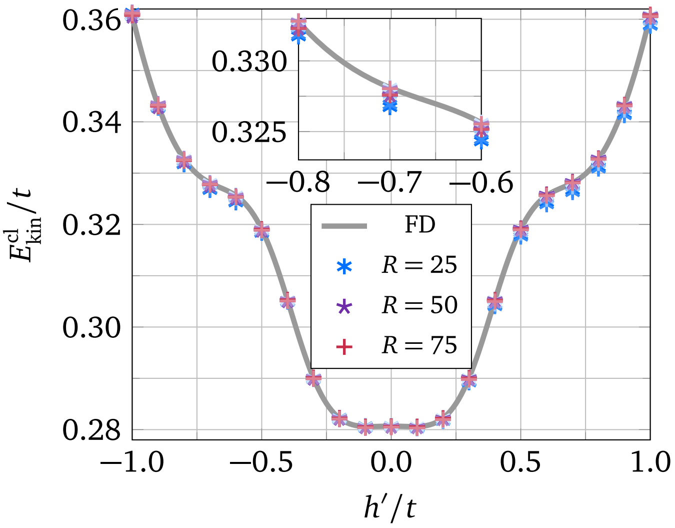

4.9 – Cluster kinetic energy $E^{\mathrm{cl}}_{\mathrm{kin}}/t$ vs AFM Weiss field h'/t of two particles on a four site cluster at $U/t = 4$, $\mu = U/2$ and $T/t = 0.1$ for R random trace vectors. The colour shades refer to the number of exact trace vectors used, with light colours meaning more exact trace vectors $N_{\mathrm{ex}} \in \{1,2,4,8,16\}$.

Already one exact trace vector is enough to achieve quantitatively appealing results. Increasing the number of exact or random trace vectors further improves the agreement. While more exact trace vectors lead to a better agreement, more random trace vectors do not necessarily achieve this.

For larger systems more exact trace vectors are required, since with increasing system size the number of eigenenergies increases and the states become denser in energy. Hence for a given temperature more states contribute significantly to the trace.

An extension of this approach is also possible, since the initial Lanczos run can also be replaced by a Band Lanczos run. This becomes necessary, once the ground state and/or lowest excited states are degenerate. If the number of exact trace vectors desired goes beyond the number of vectors, which can be resolved by a regular Lanczos run, the incorporation of degenerate eigenvectors is required. Variants of the FTLM combined with an exact contribution to the trace obtained via a Band Lanczos run are denoted by a leading 'dex' (dexFTLM, dexFTBLM, dexDFTLM, dexDFTBLM). This happens for instance if $N_{\text{ex}} = 16$ eigenvectors are requested for the system shown in figure 4.9 at $h'/t = 0$. The dimension of the Hilbert space $\dim \mathscr{H} = 28$ decreases from the perspective of the Lanczos algorithm to 14 non-degenerate states, which lies below $N_{\text{ex}} = 16$. Hence for $N_{\text{ex}} = 16$ exact trace vectors, $N_{\text{deg}} = 7$ is used.

Note that in the meantime of writing this thesis two variants denoted by RFTLM and OFTLM using this decomposition of the trace have been presented in [MT20] as mentioned in section 2.4.2.

Application to VCA

In order to use a variant of the FTLM as cluster solver within VCA, the grand potential of the cluster as well as the cluster Green's function have to be determined with sufficient accuracy. To achieve this also at low temperatures, 'enough' eigenvectors have to be taken into account. For a one-dimensional system of two particles on a four site cluster, $N_{\text{ex}} = 2$ are enough according to section 4.1.3, but the question is now, how many eigenstates are needed if FD is no longer applicable. How can one estimate a 'reasonable' number of states? To answer this question one has to give a reason, why using the eigenstates lowest in energy improves the result. The reason is the Boltzmann factor inside the trace, which punishes small errors in the other matrix elements contributing to the trace at low temperatures and low energies. Therefore it is enough to take into account those states of energy ε which satisfy

$$\frac{\exp(-\beta\varepsilon)}{\exp(-\beta\varepsilon_{\text{GS}})} > \eta_{\text{tol}}, \tag{4.21}$$

with a small tolerance η_{tol} as done in [SSY18] and mentioned in section 2.4.1. It is important to note, that the existence of degenerate states at low energy make it necessary to employ Band Lanczos ED to compute the eigenstates.

This criterion can however only be applied consistently for the exact part of the trace. For the FTLM part, the different trace vectors cannot be associated with a specific Boltzmann factor. Hence the criterion might limit the number of Lanczos runs, but not the number of trace vectors.

Consider as an example four particles on a 2×2 site cluster in two dimensions on a square lattice, which is still tractable via FD. Part of the energy spectrum of the cluster obtained via FD is shown in figure 4.10a. It is divided into four groups of states which are considered as contributions to the trace. As can be seen from the energy difference in the states, $N_{\text{ex}} = 16$ eigenstates should be sufficient to recover the FD results up to $T/t \approx 1$. To convince oneself of this assumption, figure 4.10b shows the AFM magnetisation obtained via VCA $\langle m \rangle_{\text{VCA}}$ vs temperature T/t and recovers in the case $N_{\text{ex}} = 16$ the result from FD when employing Band Lanczos ED to determine the eigenvectors.

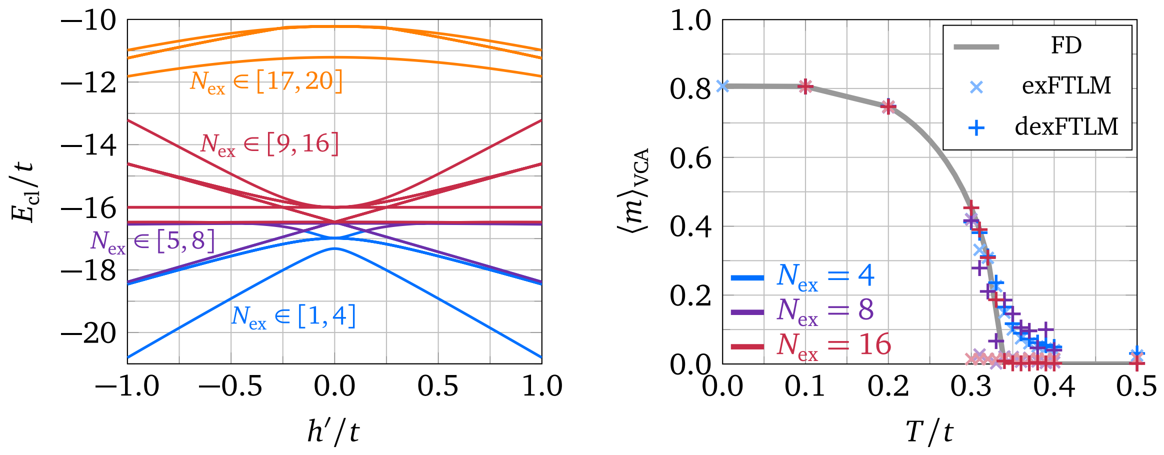

(a) Cluster eigenenergies.

(b) AFM magnetisation.

4.10 – Lowest cluster eigenenergies E_{cl}/t vs AFM Weiss field h'/t and AFM magnetisation $\langle m \rangle_{\mathrm{VCA}}$ vs temperature T/t. The reference system consists of four particles on a 2×2 square cluster with $U/t = 8$, $\mu = U/2$ and is solved via FD. The states in figure 4.10a are divided into four, color-coded groups and are used together with $R = 75$ random vectors as trace vectors to compute the magnetisation in figure 4.10b. Therein, besides the different symbols, the data obtained with exFTLM is coloured lighter than the data obtained with dexFTLM to make the figure less busy.

Another point verified is the requirement, that Band Lanczos ED is necessary to recover all low energy eigenstates since they are degenerate. While the Band Lanczos run resolves all lowest energy eigenstates, a Lanczos run obtains only one representative among the degenerate states. Further states found by the Lanczos run are higher in energy and thus less relevant due to the Boltzmann factor. Nevertheless, the deterioration of the results from exFTLM with increasing N_{ex} is sobering.

4 1 4 Comparison to solvers in literature

The agreement of FD and ED results with those from literature confirm the implementation.

CT-QMC solver [Li+09]

Coming back to the thermodynamic properties at finite temperature, the central quantity is the grand potential. A comparison with the FD data used by Li et al. [Li+09] to gauge their implementation of VCA with a Quantum Monte Carlo (QMC) solver serves as further check.

First, the cluster grand potential as function of the chemical potential is compared in figure 4.11. While the data belonging to the one and two site clusters agree, the three site cluster clearly differs for small chemical potential μ. This is a miscalculation in the paper, since even when considering all sectors of different particle number while building the respective Hamiltonian matrix by hand, the results still differ in disfavour of Li et al. The argument of thermodynamic consistency valid for CPT cannot be invoked since these are results on a finite system.

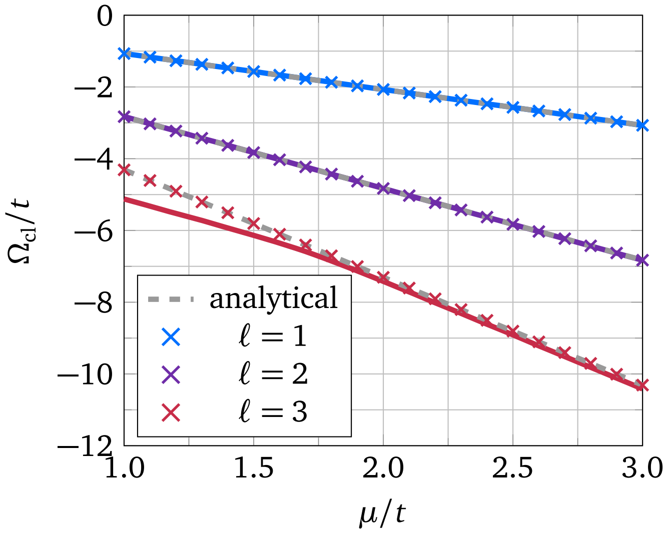

4.11 – Cluster grand potential Ω_{cl}/t vs chemical potential μ/t for one-dimensional clusters of ℓ sites with $U/t = 4$, $T/t = 0.1$. Results from FD (×) combining all particle sectors, as well as (semi-)analytic calculations employing Python including all particle sectors (dashed, grey lines) are compared with those of Li et al. [Li+09] (solid, coloured lines).

In order to check the CPT implementation at finite temperature, the CPT grand potential Ω_{CPT} of the Hubbard model is computed for a 2×2 cluster at half-filling, meaning $\mu = U/2$ and four particles. The CPT part consists of an AFM Weiss field

$$H_{\mathrm{AFM}} = h' \sum_{i} (-1)^{i_x + i_y} (n_{i\uparrow} - n_{i\downarrow}), \tag{4.22}$$

which is added to the cluster Hamiltonian and subtracted via the V-matrix. A comparison with the data from Li et al. is shown in figure 4.12. For large values of $U/t \in [2, 4]$, the grand potential agrees qualitatively with the paper. In contrast for lower U/t, the grand potential seems to saturate faster with increasing h'/t than in the paper. Results from FD and dexFTLM are consistent. Attempting to combine multiple particle sectors may not lead to a better agreement, since CPT is not thermodynamically consistent.

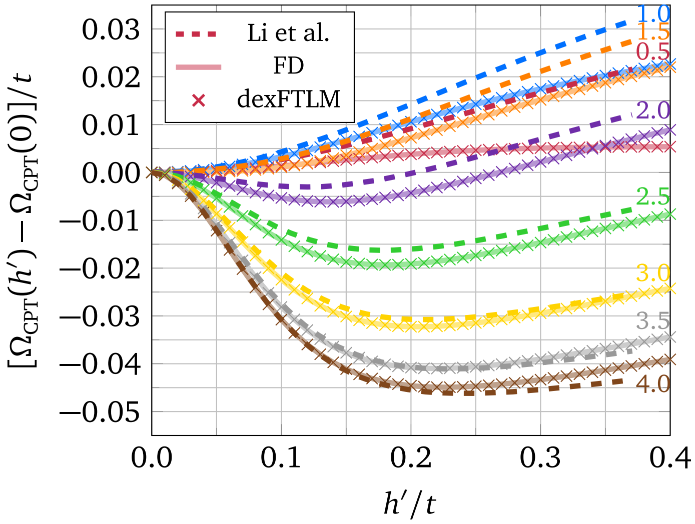

4.12 – CPT grand potential Ω_{CPT}/t vs AFM Weiss field h'/t for a half-filled 2×2 cluster with $U/t \in \{0.5, 1, \ldots, 4\}$, $\mu = U/2$ and $T/t = 0.2$. Results from FD (solid, light-coloured lines) and the dexFTLM using $N_{\mathrm{ex}} = 16$ eigenvectors and $R = 75$ random vectors (×) are compared with those of Li et al. [Li+09] (dashed, dark-coloured lines).

FTLM solver [Aic04]

Using the cluster Green's function within CPT, highly resolved spectral functions can be obtained. In order to assess the quality of the implementation of the FTLM, the spectra for a one-dimensional Hubbard chain of eight sites are compared with those of Aichhorn [Aic04] in figure 4.13. For higher temperature, it is sufficient to require the convergence of one eigenenergy to achieve an almost quantitative agreement apart from some wiggles. At lower temperature, more wiggles appear and make it necessary to require the convergence of more eigenvalues. Demanding more converged eigenvalues while not using the respective eigenvectors as trace vectors poses a missed opportunity.

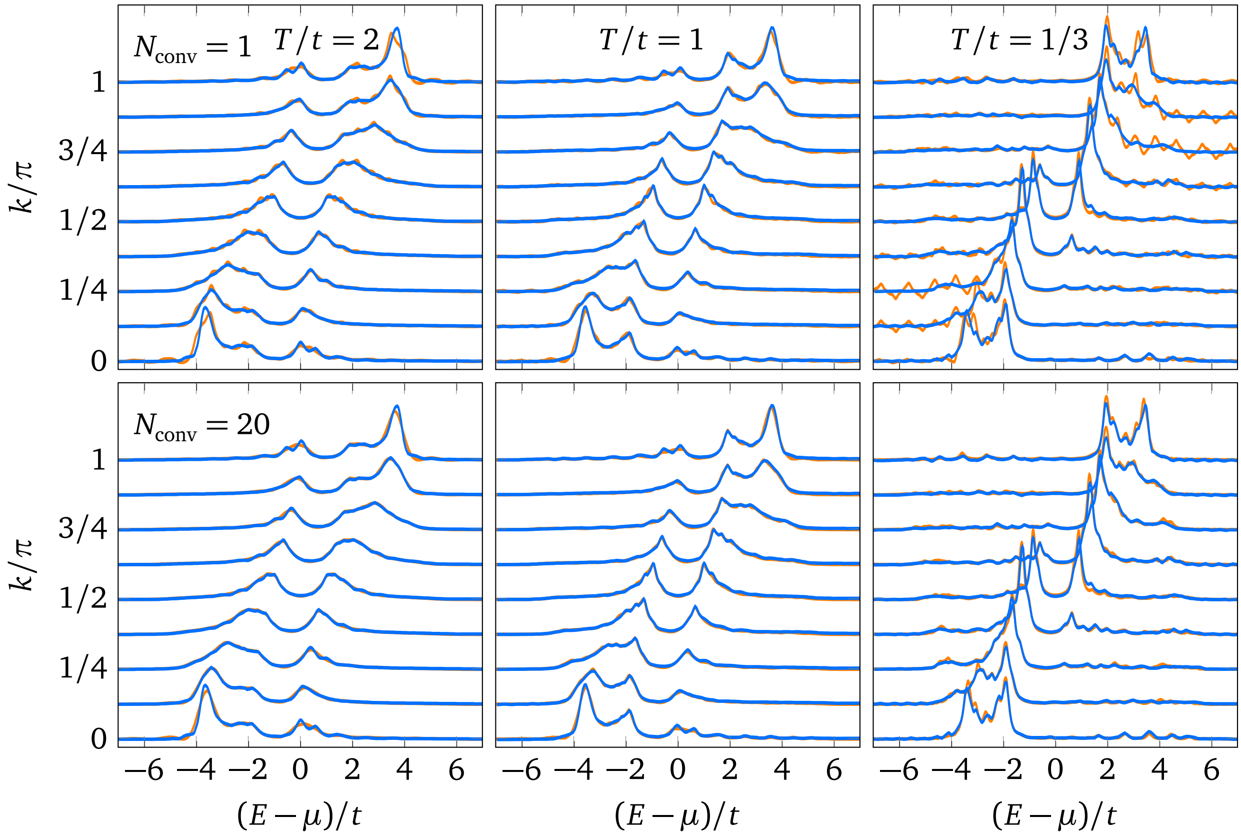

4.13 – CPT spectral function for a one-dimensional Hubbard cluster of eight sites with $U/t = 4$ at half-filling $\mu = U/2$ obtained via the FTLM employing $R = 75$ random vectors while requiring the convergence of N_{conv} eigenenergies for several temperatures T/t. Orange lines are numerical data, whereas blue lines are taken from Aichhorn [Aic04].

FD and ED solver [SSY18]

Approximating a full trace with a restricted number of converged eigenvectors from ED can be systematically improved by incorporating more eigenstates. By the same measure, the validity of the approximation can be extended to higher temperatures. In contrast, FTLM-based approximations of a full trace as realised in this thesis do not systematically improve with more trace vectors.

A direct comparison of how more exact and random trace vectors affect the precision of the grand potential is shown in figure 4.14. Sweeps of the Weiss field with $N_{\mathrm{ex}} = 20$ exact and $R = 60$ random trace vectors show an overall good agreement with the grand potential of Seki et al. However the location of the minimum (+) becomes less precise with increasing temperature, starting at $T/t = 0.25$. The amount of exact and random trace vectors is not sufficient to determine the Néel temperature, which marks the phase transition from AFM to paramagnet (PM). Increasing the number of exact trace vectors reproduces the results of Seki et al. With more random vectors, the Néel temperature can be determined correctly as well. However the deviation from the ED results upon approaching the phase transition is significant and puts into question how reliable FTLM-based solvers are at low temperature.

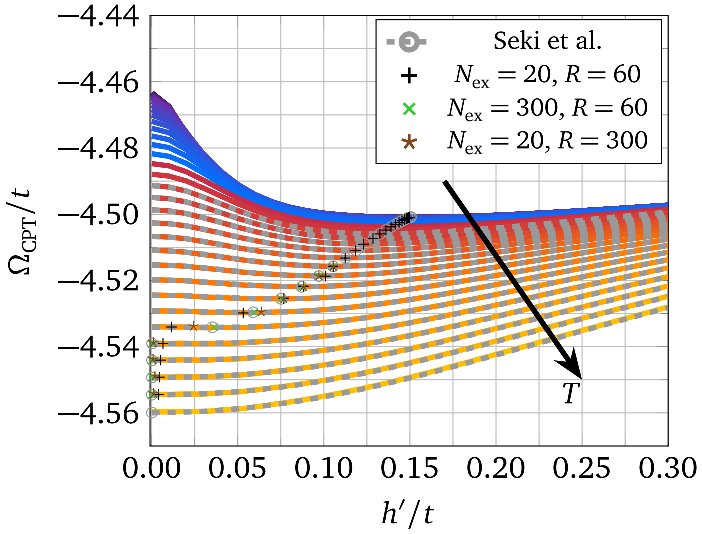

4.14 – CPT grand potential Ω_{CPT}/t as function of the AFM Weiss field h'/t for a half-filled 4×2 cluster with $U/t = 8$ and $\mu = U/2$ at several temperatures T/t. Results from ED (solid, coloured lines, +, × and stars) are compared with those of Seki et al. [SSY18] (dashed, grey lines, open dots).

To illustrate the discrepancy between exact and random trace vectors further, figure 4.15 shows the cluster and CPT grand potential for a $\sqrt{10} \times \sqrt{10}$ site cluster obtained using either type of trace vectors exclusively. While on the cluster level, the difference is less apparent, the CPT grand potential obtained using random vectors lacks even the basic feature of being symmetric w.r.t. flipping the direction of the AFM Weiss field. Within this scenario, where the random vectors are supposed to be advantageous due to a larger cluster, this comparison exhibits how inaccurate the results using the FTLM-based solvers are.

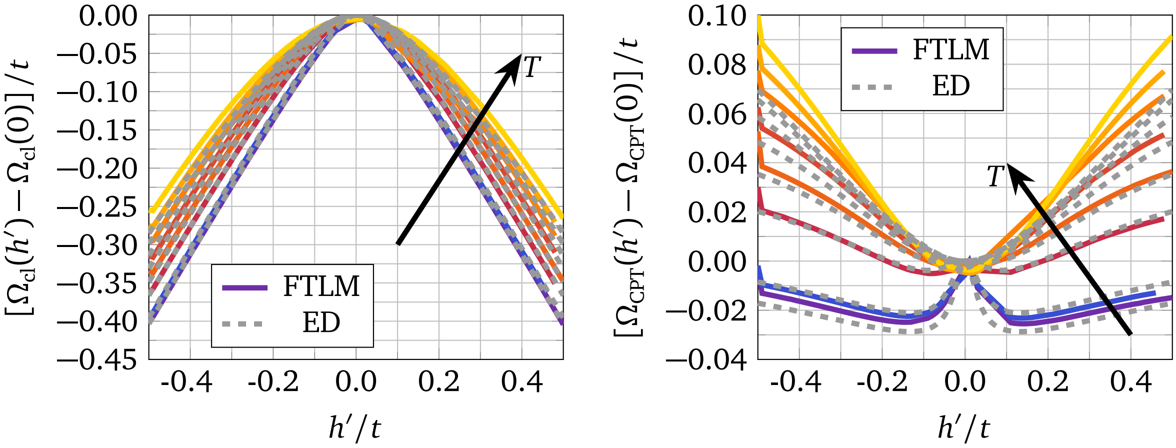

(a) Cluster grand potential. (b) CPT grand potential.

4.15 – Cluster and CPT grand potential Ω_{cl} and Ω_{CPT} as function of the AFM Weiss field amplitude h'/t for a $\sqrt{10} \times \sqrt{10}$ site cluster with $U/t = 8$ and $\mu = U/2$ at several temperatures $T/t \in \{0.10, 0.15, \ldots, 0.50\}$ excluding $T/t = 0.20$. Results from FTLM (solid, coloured lines) with $R = 100$ random trace vectors are compared with those from ED (dashed, grey lines) with $N_{\mathrm{ex}} = 120$ exact trace vectors allowing an $N_{\mathrm{deg}} = 8$ fold degeneracy.

In summary, FTLM-based solvers exhibit a worse precision than using exact trace vectors. They are restricted to high temperatures due to approximating the trace by a stochastic average with a uniform distribution. For FTLM-based solvers, large reference systems allow to reduce the number of random trace vectors. However this requires a longer time to compute the required matrix elements than reference systems of moderate size. For moderate and small reference systems, a sufficiently large number of random trace vectors is needed to achieve sufficient sampling for reliable averages. Both measures make the method numerically more expensive. Technically, for FTLM-based solvers more data has to be assembled when constructing the cluster Green's function. By including more exact trace vectors, one can systematically and reliably improve the cluster Green's function and grand potential.

Hence an FTLM-based solver is supposed to be operated for as big of a reference system as possible, while for the VCA the reference system has to be solved multiple times. Therefore FTLM-based solvers are better suited for one-shot computations than as a solver for the VCA. Increasing the number of exact trace vectors is therefore advantageous compared to adding more random vectors.

When considering finite temperature, entropy as the change of the grand potential with temperature can be computed. In order to verify the implementation using equation (2.244) combined with FD, first the numerically obtained values S_{CPT} are compared to the derivative in terms of finite differences of the grand potential $-(\Delta\Omega_{\mathrm{CPT}}/\Delta T)$. As can be seen from the filled and empty dots in figure 4.16, the combination of both give an almost continously looking line. Comparing both with the results of Seki et al. is another indication that the implementation is correct.

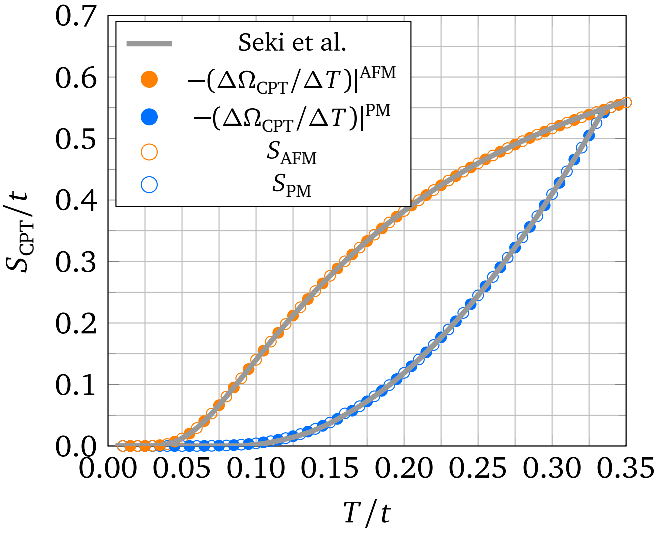

4.16 – CPT entropy S_{CPT} for a half-filled 2×2 cluster at $U/t = 8$ and $\mu = U/2$ for the AFM and PM solution as function of the temperature T/t. Results from FD (solid and open dots) are compared with those of Seki et al. [SSY18] (grey lines).

For a larger cluster with 4×2 sites, the paramagnetic entropy for all particle number sectors is computed separately, combined and shown in figure 4.17. Since the chemical potential is chosen as $\mu = U/2$, it suffices to consider only part of the sectors due to particle-hole symmetry. Looking at the different particle number sectors separately as shown in figure 4.17a, with increasing temperature the entropy per cluster site approaches the limiting value $\lim_{T\to\infty} S_{\mathrm{CPT}} = \ln(\dim \mathscr{H}_N)/(4\times 2)$ derived in appendix B. Combining the entropy from all particle number sectors according to equation (A.3) agrees with the paramagnetic entropy by Seki et al. as shown in figure 4.17b.

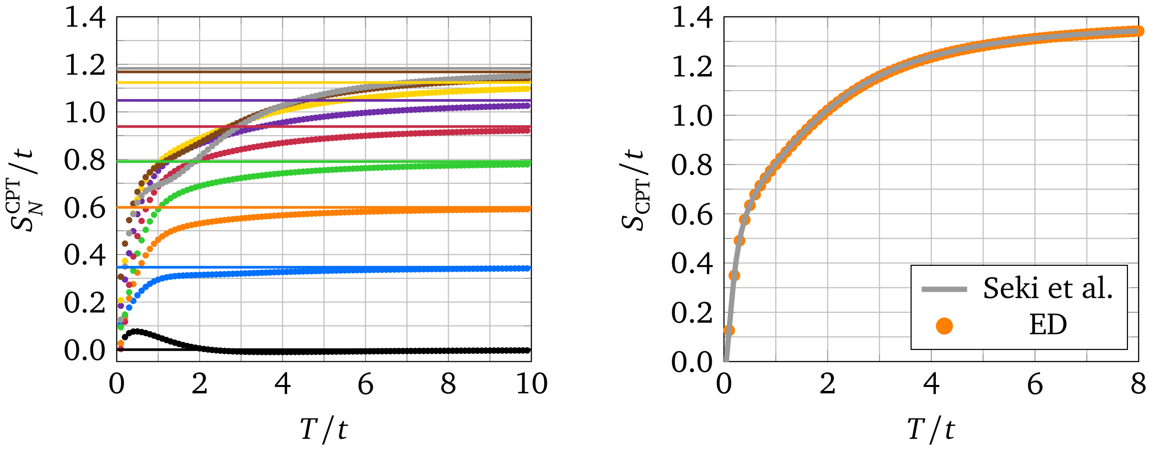

(a) Separate sectors.
(b) Combined sectors.

4.17 – CPT entropy S_{CPT} for several fillings of a 4×2 cluster at $U/t = 8$, $\mu = U/2$ in the PM phase as function of the temperature T/t. In case of small particle numbers $N \leq 3$, the FD solver is used, while for $3 < N \leq 8$ particles, the ED solver with $N_{\mathrm{ex}} = 20$ exact, $N_{\mathrm{deg}} = 8$ fold degenerate trace vectors and $R = 60$ random trace vectors are employed. The combination of all available particle number sectors is compared to those of Seki et al. [SSY18] (grey line).

Besides ordered phases, also dynamical properties characterising the system can be investigated. To capture the metal-insulator transition in the one-band Hubbard model, another type of reference system has to be considered. The cluster-dynamical-impurity approximation (CDIA) described in section 2.4.6 employs a cluster coupled to uncorrelated bath sites as reference system. Considering the hybridisation with the bath sites as variational parameter, insulator and metal are characterised by a minimum in the grand potential at low and high hybridisation strength, respectively. The deeper minimum determines the phase.

Figure 4.18 shows the grand potential of the auxiliary system introduced within CDIA for a 2×2 cluster with one bath site per cluster site at $T/t = 0.015$. It is obtained by combining the grand potentials of all particle number sectors available for the reference system according to equation (A.2). Since the chemical potentials are chosen to give a particle-hole symmetric Hamiltonian with $\mu = U/2$ and $\mu_{\text{bath}} = 0$, it suffices to consider only the particle number sectors with $N = 0, 1, \dots, 8$ particles. While for the case of $N \in \{0, 1, 2, 3, 4, 5\}$ particles, $\{1, 16, 120, 500, 1000, 4368\}$ iterations within Band Lanczos ED are enforced to construct the entire Hilbert spaces, for $N \in \{6, 7, 8\}$ particles, the number of iterations is restricted to at maximum 4000. For $N \in \{0, 1\}$ particles, the number of degenerate vectors is restricted to $\{1, 16\}$ and for the remaining sectors to 70, which is the number of possibilities to position four particles on the eight uncorrelated bath sites including spin. The additional contributions within figure 4.18 are the bath grand potential per cluster site $\Omega_{\text{bath}}/\ell = -T \ln(4^{\ell})/\ell$ and the Legendre transform to the free energy with $N = 1$.

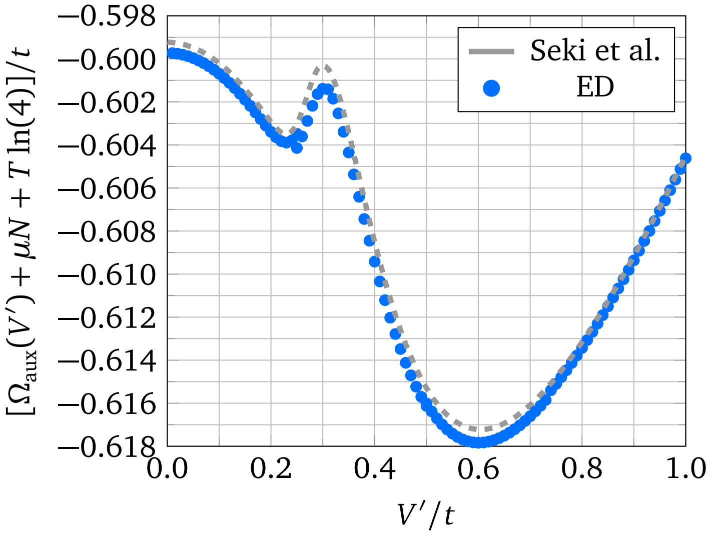

4.18 – CPT grand potential Ω_{CPT} as function of the hybridisation Weiss field amplitude V'/t for a 2×2 cluster with one bath site per cluster site and $U/t = 5.4$, $\mu = U/2$ at $T/t = 0.015$. Results using an ED-solver are compared with those of Seki et al. [SSY18].

The steps in the combination of all sectors originates from steps in the separate sectors. They originate from the decomposition of the hybridisation-sweep into multiple sections. Since the $N \in \{5, 6, 7\}$ particle sectors contributions are significant, deviations of $\mathcal{O}(10^{-3})$ in the grand potential at these steps translate into visible steps. Hence in case CDIA is used in ‘production’ runs, one has to be careful about precision and might need to take additional measures to improve it. These steps do not occur on the cluster level.

4 2 Chebyshev expansion

Comparing the results employing the ED solver with those of the Chebyshev solver confirms the latter one. Depending on the number of Chebyshev moments, the runtimes are comparable.

Besides expressing the Green's function in its spectral representation, one can also expand the resolvent into Chebyshev polynomials as described in the sections 2.3.4 and 2.4.3. As a proof of principle, figure 4.19 shows the grand potential of the one-band Hubbard model on a $\sqrt{10} \times \sqrt{10}$ site cluster with $U/t = 8$ and $\mu = U/2$ at half-filling for various temperatures employing different numbers of moments, i.e. expansion orders. Already $N_{\text{mom}} = 10$ moments are sufficient to quantitatively reproduce the grand potential. Other cluster sizes exhibit the same agreement between Chebyshev and ED results.

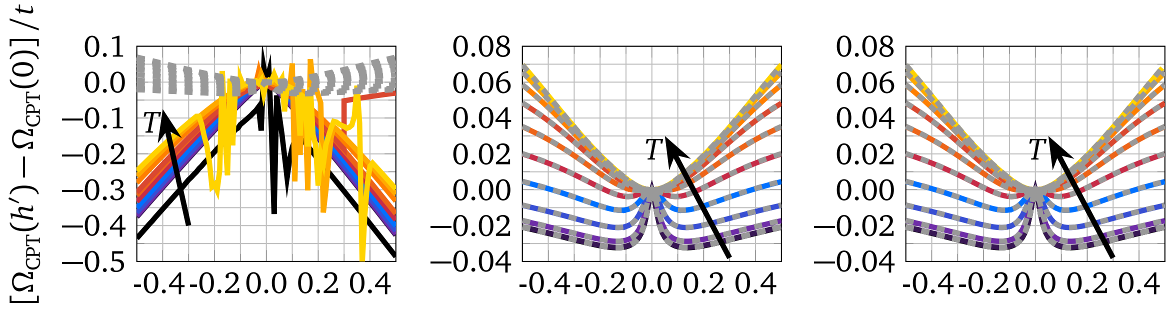

(a) $N_{\text{mom}} = 1$. (b) $N_{\text{mom}} = 10$. (c) $N_{\text{mom}} = 100$.

4.19 – CPT grand potential Ω_{CPT} as function of the AFM Weiss field amplitude h'/t for a $\sqrt{10} \times \sqrt{10}$ site cluster with $U/t = 8$ and $\mu = U/2$ at several temperatures $T/t \in \{0.00, 0.05, \ldots, 0.50\}$. Results via Chebyshev expansion (solid, coloured lines) for different number of moments $N_{\text{mom}} \in \{1, 10, 100\}$ are compared with those obtained from ED (dashed, grey lines). Both solvers employ $N_{\text{ex}} = 120$ exact trace vectors while allowing a $N_{\text{deg}} = 8$ fold degeneracy.

A comparison of the runtimes while using either the Chebyshev or the spectral representation is shown in figure 4.20. For several clusters of different size and shape at different temperatures, the runtimes per Ω-value averaged over 101 computations for different Weiss fields are depicted therein. While the spectral representation can make use of the high-frequency expansion, the Chebyshev representation can restrict the number of moments and thereby perform similarly. Hence compared to the performance of the MPS-based solver using the continued fraction representation in figure 3.1b, the Chebyshev representation is rather promising.

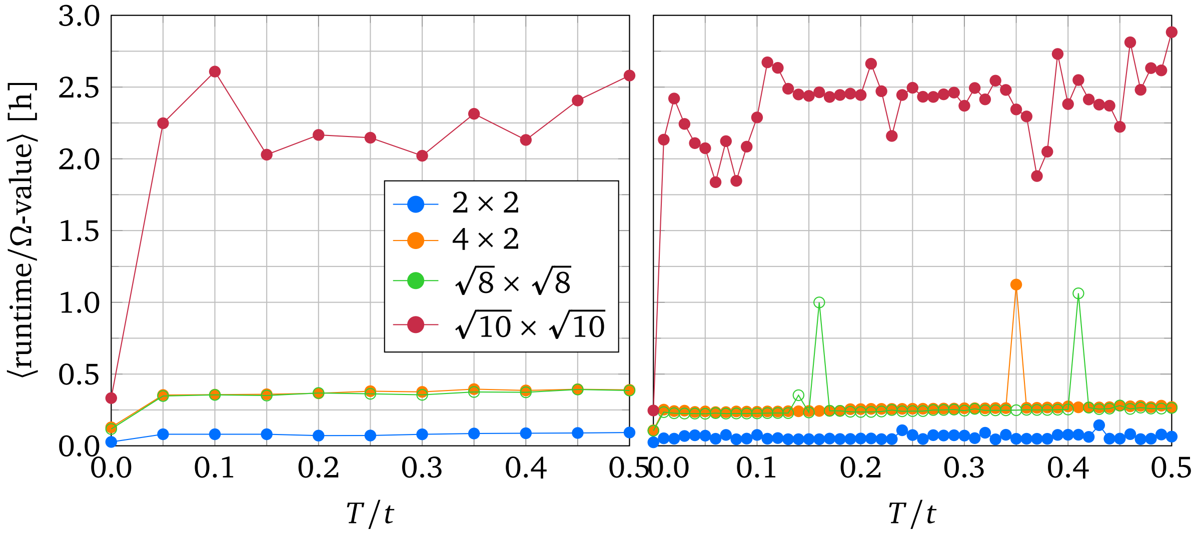

(a) Chebyshev. (b) ED, FD.

4.20 – Average runtimes per datapoint of the grand potential for several cluster sizes using different solvers. For the Chebyshev solver, $N_{\mathrm{mom}} = 100$ moments are used, while the FD and ED solvers employ the high-frequency expansion. For the 2×2 site cluster, $N_{\mathrm{ex}} = 60$ is used for the Chebyshev solver and FD is applied in comparison, whereas for larger clusters $N_{\mathrm{ex}} = 120$ exact trace vectors are employed in both cases.

4 3 Conclusion

As the test cases exemplified, exact trace vectors should be used instead of random ones. Employing a combination of exact and random trace vectors appears to increase the workload without providing benefits. The solver used to obtain the exact trace vectors should be capable of resolving degenerate eigenstates. For the sector of excited states this is irrelevant and a regular Lanczos solver can be used. Besides the spectral representation, the Chebyshev representation of the Green's function can be used efficiently at finite temperature.

5 Three-band Hubbard model: Physical application

5 1 d^5 configuration: Sr_2IrO_4

Here a three-band Hubbard model with five electrons is used to investigate the AFM to PM phase transition in Sr_2IrO_4 employing the VCA. The magnetic signatures in the spectrum and the orbital responsible for them are identified. Within VCA, a local self-energy omitting nonlocal quantum fluctuations is sufficient to qualitatively reproduce the spectra of magnetically ordered systems. Yet such a treatment overestimates the magnetic orders stability and misses spectral features in the unoccupied states. In order to contribute to the discussion, whether the Mott- or Slater-type insulating mechanism dominates in Sr_2IrO_4, VCA is not sufficient and a CDIA study should be attempted.

From the perspective of orbital physics, the compound Sr_2IrO_4 is interesting since it exhibits upon lowering the temperature the opening of an insulating gap close to the Néel temperature $T_N = 240\,K$ [Li+13] with the insulator being enabled by spin-orbit coupling (SOC) [Kim+08]. The scenario deduced from first-principles bandstructure calculations [Kim+08] is illustrated in figure 5.1 and can be summarised as:

1) Octahedral crystal field (CF) splits the 5d states into low energy t_{2g} and high energy e_g subspaces.
2) SOC splits the t_{2g} subspace into a half-filled high energy $j_{\mathrm{eff}} = 1/2$ and a completely filled low energy $j_{\mathrm{eff}} = 3/2$ subspace.
3) Realistic Hubbard repulsion U splits the half-filled $j_{\mathrm{eff}} = 1/2$ subspace into a lower and an upper Hubbard band.

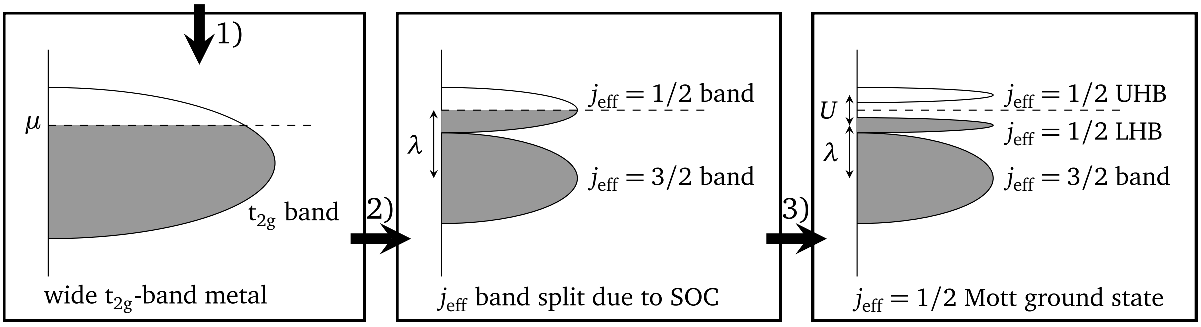
1)
μ
t_{2g} band
wide t_{2g}-band metal
2)
$j_{\mathrm{eff}} = 1/2$ band
λ
$j_{\mathrm{eff}} = 3/2$ band
j_{eff} band split due to SOC
3)
U
λ
$j_{\mathrm{eff}} = 1/2$ UHB
$j_{\mathrm{eff}} = 1/2$ LHB
$j_{\mathrm{eff}} = 3/2$ band
$j_{\mathrm{eff}} = 1/2$ Mott ground state

5.1 – Scenario leading to a Mott insulator driven by SOC λ. After the octahedral CF splits t_{2g} and e_g states, SOC goes on to split the t_{2g} states into $j_{\mathrm{eff}} = 1/2$ and 3/2 states. The half-filled $j_{\mathrm{eff}} = 1/2$ states are then split by a realistic value for the Hubbard interaction U into lower and upper Hubbard band (LHB, UHB). Reproduced from [Kim+08].

Several subsequent publications using tight-binding models obtained via density functional theory (DFT) investigated the influence of correlations on the mean-field level [Jin+09] and on a cluster mean-field level [WSY10; SWY10]. All of these detected the $j_{\mathrm{eff}} = 1/2$ character of the ground state/lowest unoccupied excited state.

The importance of structural distortions besides SOC for the system to be insulating was addressed using DFT+DMFT [Mar+11]. Since single site DMFT was used, the system was considered in its paramagnetic phase. From their DFT results they deduce that the system is spin-orbitally ordered, while there is neither orbital nor spin order on its own. To assess the importance of structural distortions and SOC, the critical value of U/t necessary for the Mott metal-insulator transition was monitored. Without either structural distortions or SOC as well as without both, the critical interaction strength is larger than when including both.

Another paper by the same group [Mar+18] aimed at improving the theoretically obtained single-particle spectral function on a qualitative level. In order to capture the effects of AFM fluctuations in the paramagnetic phase, an oriented cluster was used as the impurity. Adding nonlocal quantum fluctuations in such a manner makes the lowest unoccupied excited $j_{\mathrm{eff}} = 1/2$ state more dispersive as was observed in experiment. Comparing the angle-resolved photoemission spectra measured above and below the Néel temperature implies that the spectral properties are insensitive to the presence or absence of magnetic order.

A topic related to this observation is the question, whether the magnetic order is the result or partially the origin of the insulating behaviour [Ari+12; Li+13; WSY14]. In a Mott-type insulator, the Coulomb interaction opens the insulating gap with the AFM being a secondary effect. Within a Slater-type insulator, the insulating gap is opened by the AFM order breaking the translational symmetry, meaning that the band structure is relevant for the insulators stability.

An investigation of Sr_2IrO_4 via DFT+DMFT [Ari+12] concludes that the compound is a Slater-type insulator, which is a consequence of Mott correlations. On the theoretical side, the Hartree part of the self-energy driving the Slater insulator is not sufficient for the insulating gap to open, while a contribution characteristic for the AFM order helps opening the gap. In experiment, the insulating gap size measured in scanning tunneling spectroscopy [Li+13], which behaves with temperature similar to a mean-field AFM order parameter, hints only at a Slater-type origin of the metal-insulator transition.

The question of Mott- vs Slater-type insulator was picked up again in a variational Monte Carlo study [WSY14] which considered the different energy gain mechanisms to distinguish the types of insulators. A Mott-type insulator is considered interaction-energy driven, while a Slater-type insulator is promoted through the band-energy gained. For low interaction strength U/t, the AFM insulator is stabilised opposed to the paramagnetic metal through the interaction energy U'/t. At large interaction U/t, the band energy E_{kin} stabilises the AFM insulator w.r.t. the paramagnetic insulator. When the paramagnet is a metal, the band-energy is lost during the transition to the AFM insulator as compared to the transition from the paramagnetic insulator, where band-energy is gained. For the region of intermediate interaction U/t, both gain mechanisms are active due to the strong renormalisation of the paramagnetic metal. With Sr_2IrO_4 residing at intermediate interaction strength, Slater- as well as Mott-type behaviour are expected to be observed.

In this chapter, the following questions are addressed using VCA:

- What are the spectral signatures of the AFM? Which orbitals are relevant for the magnetism?
- Does an extended cluster with local self-energy capture the essential physics as compared to a cluster with nonlocal self-energy? What is the influence of nonlocal quantum fluctuations onto spectral properties?
- Can VCA contribute to the discussion of Mott- vs Slater-type insulator or should the reference system be extended to include bath sites leading to CDIA?

5.1.1 Hamiltonian, basis and orders

As hinted at in figure 5.1, the CF splits the 5d states such, that only the t_{2g} states are of relevance. Hence the Hamiltonian considered is a three-band Hubbard model with interactions of Kanamori form [GMM13; Ole83]

$$H = H_{\text{kin}} + H_{\text{int}} + H_{\text{SOC}} + H_{\text{CF}} + H_{\mu} \tag{5.1}$$

with the kinetic part

$$\begin{aligned} H_{\text{kin}} = &- t_1 \sum_{\langle i,j\rangle_1,\sigma} (c^{\dagger}_{i,\text{xy},\sigma} c_{j,\text{xy},\sigma} + c^{\dagger}_{j,\text{xy},\sigma} c_{i,\text{xy},\sigma}) - t_2 \sum_{\langle i,j\rangle_2,\sigma} (c^{\dagger}_{i,\text{xy},\sigma} c_{j,\text{xy},\sigma} + c^{\dagger}_{j,\text{xy},\sigma} c_{i,\text{xy},\sigma}) \\ &- t_3 \sum_{\langle i,j\rangle_3,\sigma} (c^{\dagger}_{i,\text{xy},\sigma} c_{j,\text{xy},\sigma} + c^{\dagger}_{j,\text{xy},\sigma} c_{i,\text{xy},\sigma}) \\ &- t_1 \sum_{\langle i,j\rangle_{1,\text{y}},\sigma} (c^{\dagger}_{i,\text{yz},\sigma} c_{j,\text{yz},\sigma} + c^{\dagger}_{j,\text{yz},\sigma} c_{i,\text{yz},\sigma}) - t_1 \sum_{\langle i,j\rangle_{1,\text{x}},\sigma} (c^{\dagger}_{i,\text{xz},\sigma} c_{j,\text{xz},\sigma} + c^{\dagger}_{j,\text{xz},\sigma} c_{i,\text{xz},\sigma}), \end{aligned} \tag{5.2}$$

the interaction part

$$\begin{aligned} H_{\text{int}} = &\, U \sum_{i,\alpha} n_{i\alpha\uparrow} n_{i\alpha\downarrow} + U' \sum_{i,\alpha,\beta\neq\alpha} n_{i\alpha\uparrow} n_{i\beta\downarrow} + (U' - J) \sum_{i,\alpha,\beta>\alpha,\sigma} n_{i\alpha\sigma} n_{i\beta\sigma} \\ &- J \sum_{i,\alpha,\beta\neq\alpha} c^{\dagger}_{i\alpha\uparrow} c_{i\alpha\downarrow} c^{\dagger}_{i\beta\downarrow} c_{i\beta\uparrow} + J \sum_{i,\alpha,\beta\neq\alpha} c^{\dagger}_{i\alpha\uparrow} c^{\dagger}_{i\alpha\downarrow} c_{i\beta\downarrow} c_{i\beta\uparrow}, \end{aligned} \tag{5.3}$$

the SOC

$$H_{\text{SOC}} = \frac{\lambda}{2} \sum_{i} (c^{\dagger}_{i,\text{yz},\uparrow}, c^{\dagger}_{i,\text{yz},\downarrow}, c^{\dagger}_{i,\text{xz},\uparrow}, c^{\dagger}_{i,\text{xz},\downarrow}, c^{\dagger}_{i,\text{xy},\uparrow}, c^{\dagger}_{i,\text{xy},\downarrow}) \begin{pmatrix} \mathbf{0} & -\mathrm{i}\boldsymbol{\sigma}_{\text{z}} & \mathrm{i}\boldsymbol{\sigma}_{\text{y}} \\ \mathrm{i}\boldsymbol{\sigma}_{\text{z}} & \mathbf{0} & -\mathrm{i}\boldsymbol{\sigma}_{\text{x}} \\ -\mathrm{i}\boldsymbol{\sigma}_{\text{y}} & \mathrm{i}\boldsymbol{\sigma}_{\text{x}} & \mathbf{0} \end{pmatrix} \begin{pmatrix} c_{i,\text{yz},\uparrow} \\ c_{i,\text{yz},\downarrow} \\ c_{i,\text{xz},\uparrow} \\ c_{i,\text{xz},\downarrow} \\ c_{i,\text{xy},\uparrow} \\ c_{i,\text{xy},\downarrow} \end{pmatrix}, \tag{5.4}$$

the CF splitting

$$H_{\text{CF}} = \Delta \sum_{i,\sigma} n_{i,\text{xy},\sigma} \tag{5.5}$$

and the chemical potential

$$H_{\mu} = -\mu \sum_{i,\alpha,\sigma} n_{i\alpha\sigma}. \tag{5.6}$$

Within this enumeration, the following conventions are used:

- The meaning of the angular brackets $\langle \boldsymbol{i}, \boldsymbol{j} \rangle_{1,2,3}$ is illustrated in figure 5.2. They refer to the bonds consisting of a site $\boldsymbol{i}$ and its first, second or third nearest neighbouring site $\boldsymbol{j}$. In case of the first nearest neighbours, the labels x and y added in $\langle \boldsymbol{i}, \boldsymbol{j} \rangle_{1,\text{x}}$ and $\langle \boldsymbol{i}, \boldsymbol{j} \rangle_{1,\text{y}}$ refer to the first nearest neighbouring sites along the x- or y-direction.
- $\boldsymbol{\sigma}_{\text{x,y,z}}$ refer to the Pauli matrices.

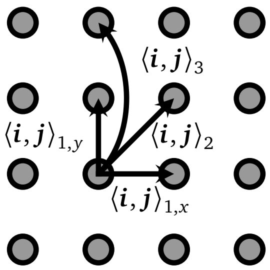

5.2 – Illustration of the various hoppings present within the kinetic part (5.2).

The hoppings and SOC used within the Hamiltonian are approximately taken from [SWY10], while CF splitting is motivated by [Kim+14; Bog+15]. Hunds coupling is inferred from [Li+13] and [Mar+11]. In contrast, the Hubbard-repulsion is adapted to match the insulating gap measured in [Li+13]. In summary, the parameters amount to:

- $t_1 = 0.36\,\mathrm{eV} \equiv t$
- $t_2 = 0.18\,\mathrm{eV} = t/2$
- $t_3 = 0.09\,\mathrm{eV} = t/4$
- $\lambda = 0.36\,\mathrm{eV} = t$
- $\Delta = t/2 = 0.18\,\mathrm{eV}$
- $U = 1.8\,\mathrm{eV} = 5t$
- $J = 0.7t \approx 0.25\,\mathrm{eV}$
- $U' = U - 2J = 3.6t \approx 1.3\,\mathrm{eV}$

Conversely, the chemical potential is determined such, that the system is filled by one hole per site as described in section 2.4.7. In practice, the nearest neighbour hopping of the xy-orbital forms the unit of energy and is denoted by t.

As mentioned in the introduction, the systems ground state was argued several times to be of $j_{\mathrm{eff}} = 1/2$ character [Jin+09; WSY10; SWY10], indicating that j_{eff} forms a good quantum number. Hence instead of looking at the decomposition of the spectral properties in terms of the t_{2g} orbitals, the $j_{\mathrm{eff}} = 1/2$ and $3/2$ states are used. Since these states are also denoted as Kramers doublets A ($j_{\mathrm{eff}} = 1/2$), B and C ($j_{\mathrm{eff}} = 3/2$) in the literature [SWY10; Sch16; Fel19] this notation is used in the rest of the chapter. In essence, they are the eigenstates of an atomic Hamiltonian including only SOC and CF splitting. For completeness, the Kramers doublets as used in [Fel19] and within this thesis are given by

$$c^{\dagger}_{A,\pm} = \sin(\theta)c^{\dagger}_{\mathrm{xy},\sigma} + \frac{1}{\sqrt{2}}\cos(\theta)(\pm c^{\dagger}_{\mathrm{yz},\bar{\sigma}} + \mathrm{i}\, c^{\dagger}_{\mathrm{xz},\bar{\sigma}}), \tag{5.7}$$

$$c^{\dagger}_{B,\pm} = -\frac{1}{\sqrt{2}}(\pm c^{\dagger}_{\mathrm{yz},\sigma} + \mathrm{i}\, c^{\dagger}_{\mathrm{xz},\sigma}), \tag{5.8}$$

$$c^{\dagger}_{C,\pm} = \cos(\theta)c^{\dagger}_{\mathrm{xy},\sigma} - \frac{1}{\sqrt{2}}\sin(\theta)(\pm c^{\dagger}_{\mathrm{yz},\bar{\sigma}} + \mathrm{i}\, c^{\dagger}_{\mathrm{xz},\bar{\sigma}}), \tag{5.9}$$

where ± denotes the pseudospin of the Kramers doublets. The angle θ depends on SOC λ and CF Δ in the following fashion

$$\cos(\theta) = \frac{1}{\sqrt{2}}\sqrt{1 + \frac{\lambda/2 + \Delta}{R}}, \tag{5.10}$$

$$\sin(\theta) = \frac{1}{\sqrt{2}}\sqrt{1 - \frac{\lambda/2 + \Delta}{R}}, \tag{5.11}$$

$$R = \sqrt{\frac{9}{4}\lambda^2 + \Delta^2 + \lambda\Delta}. \tag{5.12}$$

However not only spectral properties are decomposed into contributions from Kramers doublets, but also the fillings and orders considered. The orders considered take the general form

$$H = h' \sum_j \Lambda_j \exp(\mathrm{i}\boldsymbol{q} \cdot \boldsymbol{j}), \tag{5.13}$$

where Λ_j is a one-body operator and $\boldsymbol{q}$ the ordering wavevector. In practice, AFM and ferromagnetic (FM) orderings expressed in the cubic harmonics (C) and the Kramers (K) basis with different spin orientations (x,z) are investigated:

- CAFM: $\Lambda_j = \sum_{\alpha \in \{\mathrm{xy,yz,xz}\}} (n_{j\alpha\uparrow} - n_{j\alpha\downarrow})$, $\boldsymbol{q} = (\pi, \pi)$,
- CFM: $\Lambda_j = \sum_{\alpha \in \{\mathrm{xy,yz,xz}\}} (n_{j\alpha\uparrow} - n_{j\alpha\downarrow})$, $\boldsymbol{q} = (0, 0)$,
- KAFM S_z: $\Lambda_j = \sum_{\alpha \in \{\mathrm{A,B,C}\}} (n_{j\alpha+} - n_{j\alpha-})$, $\boldsymbol{q} = (\pi, \pi)$,
- KFM S_z: $\Lambda_j = \sum_{\alpha \in \{\mathrm{A,B,C}\}} (n_{j\alpha+} - n_{j\alpha-})$, $\boldsymbol{q} = (0, 0)$,
- KAFM S_x: $\Lambda_j = \sum_{\alpha \in \{\mathrm{A,B,C}\}} (c^\dagger_{j\alpha+} c_{j\alpha-} + c^\dagger_{j\alpha-} c_{j\alpha+})$, $\boldsymbol{q} = (\pi, \pi)$,
- KFM S_x: $\Lambda_j = \sum_{\alpha \in \{\mathrm{A,B,C}\}} (c^\dagger_{j\alpha+} c_{j\alpha-} + c^\dagger_{j\alpha-} c_{j\alpha+})$, $\boldsymbol{q} = (0, 0)$,

with $n_{j\alpha\sigma} = c^\dagger_{j\alpha\sigma} c_{j\alpha\sigma}$. The in-plane orderings employing the pseudospin components in x-direction S_x are obtained via a SU(2) spin-rotation applied to the creation/annihilation operators as used in [Sch16], meaning

$$c^\dagger_{j\alpha+_\mathrm{x}} = (c^\dagger_{j\alpha+} + c^\dagger_{j\alpha-})/\sqrt{2}, \tag{5.14}$$

$$c^\dagger_{j\alpha-_\mathrm{x}} = (-c^\dagger_{j\alpha+} + c^\dagger_{j\alpha-})/\sqrt{2}. \tag{5.15}$$

For the investigation of small reference systems such as the 1 and 2 × 1 site clusters, FD is employed at zero and finite temperature. In case of the larger 2 × 2 site cluster illustrated in figure 2.9, all computations are performed with $N_\mathrm{ex} = 60$ exact trace vectors, which are obtained by performing a maximum of 1800 Band Lanczos iterations allowing $N_\mathrm{deg} = 8$ starting vectors. The excited state sectors are handled with a regular Lanczos solver with a maximum of 800 iterations. For the construction of the Green's function, the high-frequency expansion is employed up to 15th order.

As for the modus operandi, first the free energy as a function of the physical and cluster chemical potential μ and μ' is evaluated on a grid. This is done for the PM phase with $h'/t = 0$ for three temperatures $T/t \in \{0, 0.01, 0.1\}$ to assess which optima survive to finite temperature. After an estimate of both parameters is obtained with a resolution of $\Delta\mu/t = 0.1 = \Delta\mu'/t$, the corresponding optimum is determined starting from the estimate. Starting from this optimum, the free energy is computed for a range of Weiss field amplitudes $h'/t \in \{0.00, 0.01, \ldots, 0.20\}$ at all temperatures considered, while optimising the two chemical potentials. The free energies obtained allow to determine the optimal magnetic Weiss field with a resolution of $\Delta h'/t = 0.01$. For the computation of further observables, the system is evaluated at the optimum.

5 1 2 2 × 1 site cluster

Starting with a small 2 × 1 site cluster, various magnetic orders are compared at zero temperature $T/t = 0$ as shown in figure 5.3. Among all orders shown, the AFM ones exhibit minima at finite Weiss field $|h'/t| > 0$, while the FM ones have a maximum at $h'/t = 0$. Since the lowest minimum is interpreted as being realised, the Kramers in-plane ordering 'KAFM S_x' will be considered in the following. The interaction strength $U/t = 5$ is chosen such, that the gap in the DOS belonging to the KAFM S_x order amounts to ~ 0.2 eV as found experimentally at the lowest temperature reached [Li+13].

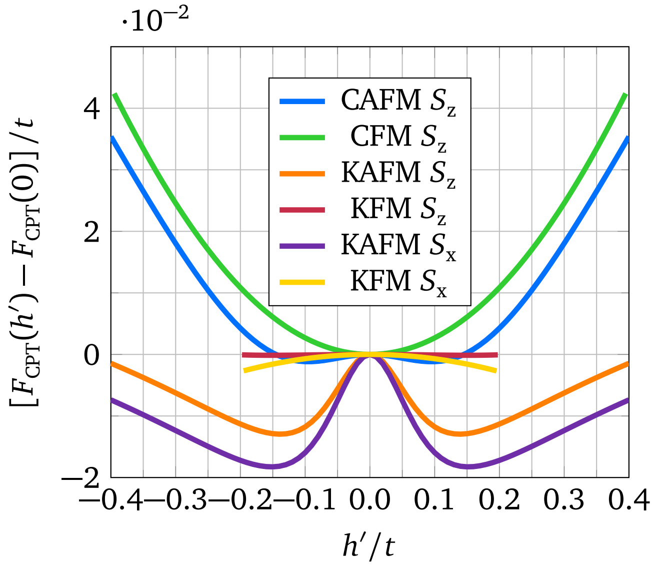

5.3 – CPT free energy F_{CPT} as function of several Weiss fields amplitudes h'/t at $T/t = 0$ and $U/t = 5$. The Weiss fields considered induce AFM and FM orderings expressed in the cubic harmonics (C) and the Kramers (K) basis, where different spin orientations (x,z) are used.

Upon raising the temperature, the minimum associated with the KAFM S_x order shifts to smaller values of the Weiss field, until it vanishes at the Néel temperature $T_N/t = 0.2$. This can be inferred from figure 5.4. It signals a transition from the KAFM S_x order to a paramagnet. Since in order to fix the particle number, the free energy is optimised w.r.t. the chemical potential μ/t and the cluster chemical potential μ'/t, the Weiss field h'/t is only scanned with a resolution of $\delta h'/t = 0.01$. Hence the rough looking behaviour of the highlighted minima.

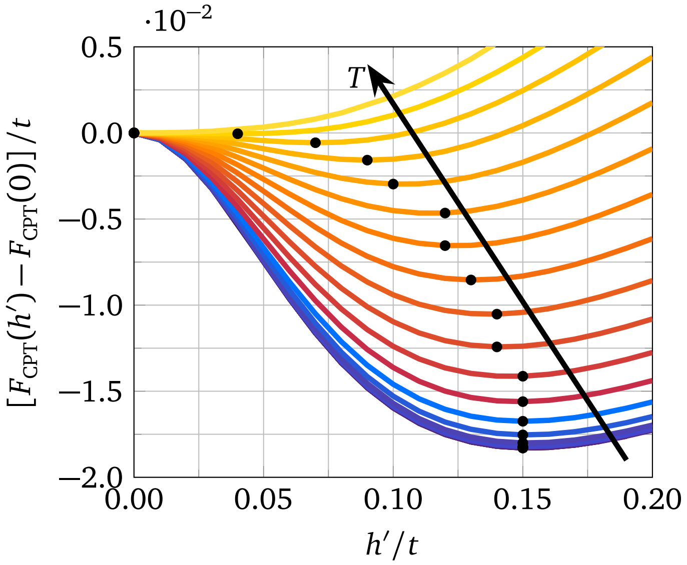

5.4 – CPT free energy F_{CPT} as function of the KAFM S_{x} Weiss field amplitudes h'/t for several temperatures $T/t \in \{0.0, 0.01, \ldots, 0.20\}$.

In order to evaluate the spectral properties of the system, the variational parameters are fixed to those of the minima highlighted in figure 5.4.

The DOS for the different temperatures is shown in figure 5.5. While the left-hand figure 5.5a shows the DOS for all temperatures as computed, the DOS is shifted within the right-hand figure 5.5b such that any change of the gap with temperature can be inferred.

Up to $T/t = 0.07$, the chemical potential changes almost linearly with temperature. While it first resides at the lower edge of the gap, it shifts with increasing temperature to its center where it stays until the maximum temperature $T/t = 0.3$ is reached. Starting at $T/t = 0.16$, a peak develops at the lower edge of the gap, while the upper edge starts to develop a shoulder which spreads into the gap. When considering the DOS in figure 5.5b with the upper edges of the gap shifted on top of each other, within the KAFM S_{x} phase the gap shrinks starting from its lower edge. In the paramagnetic phase, this extension of the lower gap boundary slows down, however a peak in the gap starts to emerge making the base of the gap asymmetric. This can be seen by the slope of the blue and orange lines, which serve as guides to the eye for the lower edge of the gap marked by points where the DOS takes the value 0.3.

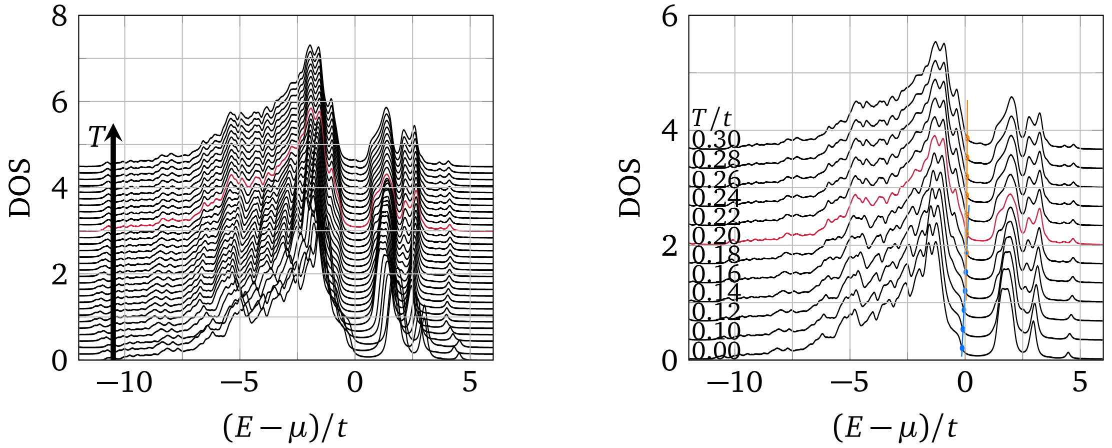

(a) Total DOS as is.

(b) Shifted DOS.

5.5 – Total DOS as is and energy shifted onto the $T/t = 0$ total DOS for different temperatures $T/t \in \{0.00, 0.01, \ldots, 0.30\}$ in (a) and specified in (b). The red curve highlights the phase transition at T_{N}. To illustrate the difference in how the gap closes in the AFM and PM phase, the blue and orange lines serve as guides to the eye for the points which mark the energy, where the DOS takes the value 0.3.

Considering the spectral function with its additional dependence on the reciprocal vectors in figure 5.6 encompasses further information on the magnetic features and how they vanish with increasing temperature. Since the contributions for different signs of m_{j_eff} are the same, only those with positive sign are shown and denoted by a plus sign.

The main feature associated with magnetism is the dispersive arc around $\boldsymbol{k}/\pi = (1,0)$ [SWY10], which is visible for all j_eff states at $T/t = 0.01$. With increasing temperature, this arc flattens in case of the $j_\text{eff} = 1/2$ state and vanishes for the $j_\text{eff} = 3/2$ states until it is gone for all orbitals at the Néel temperature $T_\text{N}/t = 0.2$. Another subtle hint at the connection to an AFM order is the peak within the occupied states around $\boldsymbol{k}/\pi = (1/2, 1/2)$. For a perfect AFM, the points $\boldsymbol{k}/\pi = (1,0)$ and $\boldsymbol{k}/\pi = (1/2, 1/2)$ are equivalent. Due to nonlocal quantum fluctuations, this is not the case. However the presence of peaks at $\boldsymbol{k}/\pi = (1,0)$ and $\boldsymbol{k}/\pi = (1/2, 1/2)$ can be interpreted as remnants of the perfect AFM.

Coming back to the gap and how it shrinks with increasing temperature, the path considered suggests at low temperature weight of the unoccupied states extending at the point $\boldsymbol{k}/\pi = (1/2, 1/2)$ into the gap, which changes at higher temperature to $\boldsymbol{k}/\pi = (0,0)$. This bending of the dispersion around $\boldsymbol{k}/\pi = (0,0)$ has been identified by Seki et al. [SSY18] as a signature of the AFM state in case of the one-band Hubbard model. Given the spectrum in the AFM phase, this change is expected. Due to doubling of the unit cell in a perfect AFM, the band weights at $\boldsymbol{k}/\pi = (0,0)$ and $\boldsymbol{k}/\pi = (1,1)$ are expected to be at the same energy. Within the PM phase however, the point $\boldsymbol{k}/\pi = (0,0)$ is expected to be of lower energy than the one at $\boldsymbol{k}/\pi = (1,1)$, which is the change observed.

Similar to how the magnetic feature is most pronounced in the $j_\text{eff} = 1/2$ spectrum, the lowest unoccupied states keep their $j_\text{eff} = 1/2$ character [WSY10; SWY10] as temperature is raised.

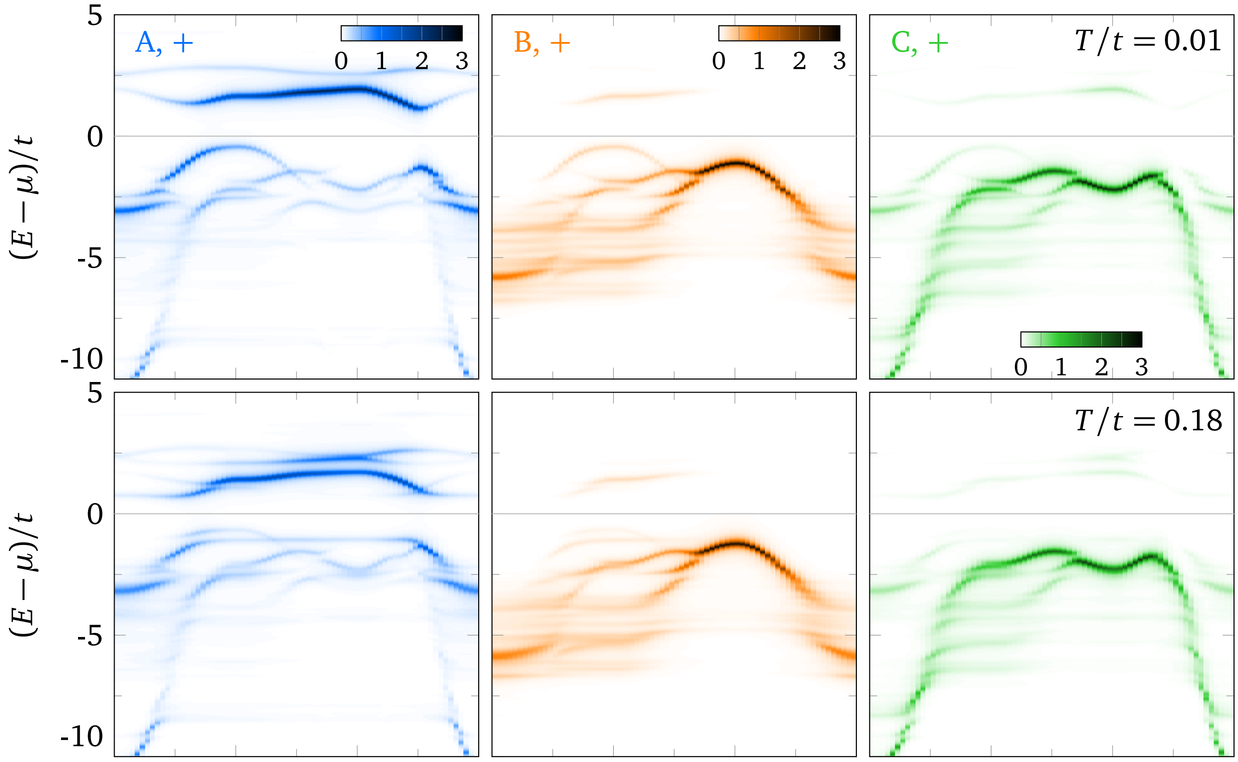

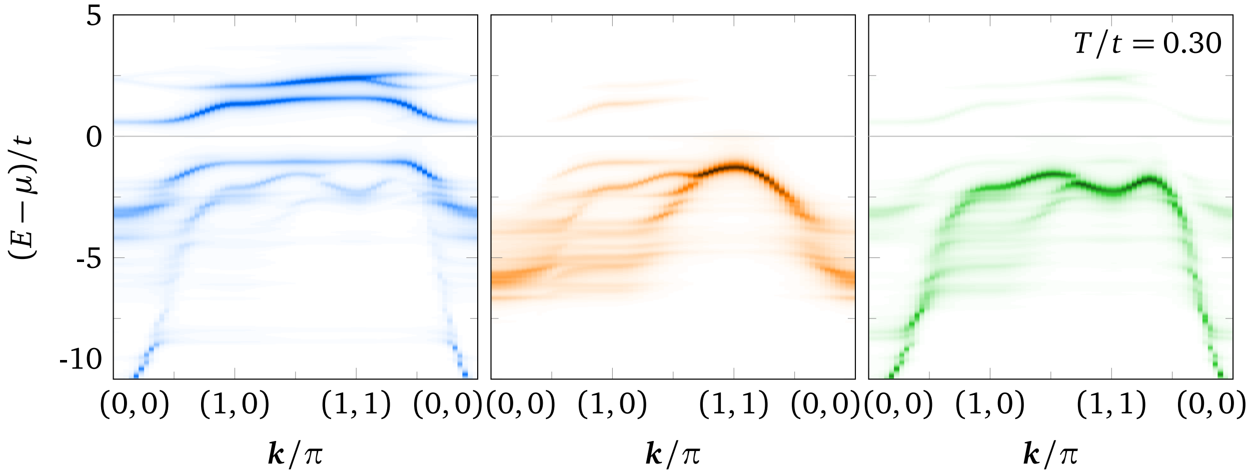

5.6 – Spectral function decomposed into contributions from the atomic states $|\mathrm{A},+\rangle = |j_{\mathrm{eff}} = 1/2, m_{j_{\mathrm{eff}}} = 1/2\rangle$, $|\mathrm{B},+\rangle = |j_{\mathrm{eff}} = 3/2, m_{j_{\mathrm{eff}}} = 3/2\rangle$ and $|\mathrm{C},+\rangle = |j_{\mathrm{eff}} = 3/2, m_{j_{\mathrm{eff}}} = 1/2\rangle$ for different temperatures T/t.

The $j_{\mathrm{eff}} = 1/2$ character of the lowest unoccupied states can also be inferred from the respective DOS shown in figure 5.7. Since one edge of the gap is essentially formed by the $j_{\mathrm{eff}} = 1/2$ states, it determines how the gap is reduced.

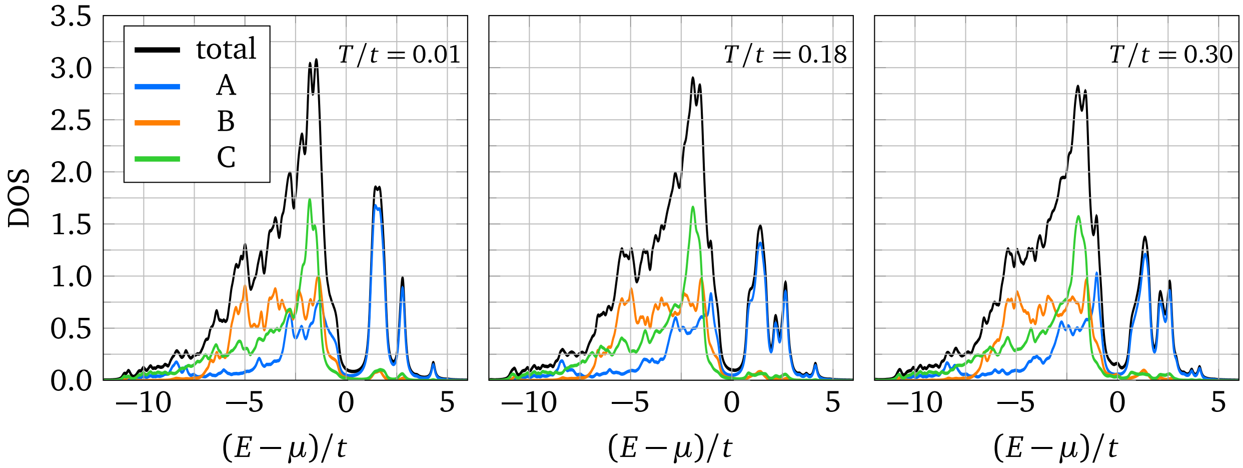

5.7 – Total and orbital resolved DOS for temperatures used for the spectra in figure 5.6.

Looking at the occupations of the respective states in figure 5.8, for the entire range of temperatures considered, the $j_{\text{eff}} = 3/2$ states remain occupied, while the $j_{\text{eff}} = 1/2$ states stay half-filled.

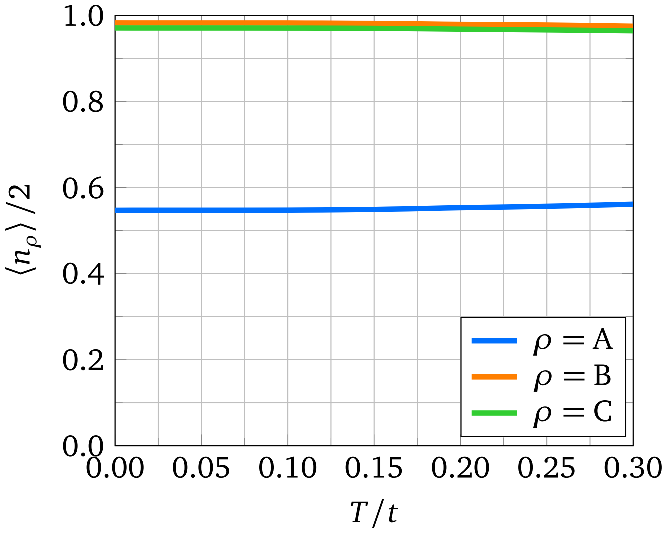

5.8 – Occupations per site and spin (electron perspective) as a function of temperature.

5.1.3 1 site cluster

Since a single site cluster cannot accommodate an AFM order, figure 5.9 shows only the low-temperature spectrum in the PM phase. As seen for the high-temperature PM phase for the 2×1 site cluster in figure 5.6, the states below the chemical potential are very much dispersionless away from the center $\boldsymbol{k}/\pi = (0,0)$ of the Brillouin-zone. The unoccupied hole in turn exhibits a free dispersion in two dimensions as promoted by the free hopping between the clusters.

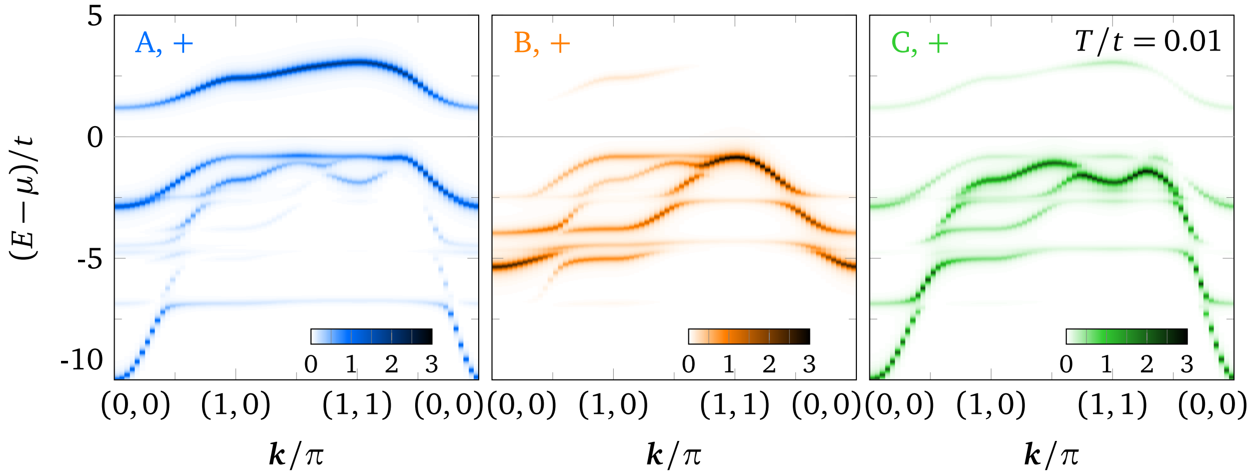

5.9 – Spectral function decomposed into contributions from the atomic states $|\mathrm{A},+\rangle = |j_{\text{eff}} = 1/2, m_{j_{\text{eff}}} = 1/2\rangle$, $|\mathrm{B},+\rangle = |j_{\text{eff}} = 3/2, m_{j_{\text{eff}}} = 3/2\rangle$ and $|\mathrm{C},+\rangle = |j_{\text{eff}} = 3/2, m_{j_{\text{eff}}} = 1/2\rangle$ for the temperature $T/t = 0.01$.

5 1 4 2 × 1 site cluster with local self-energy

A local self-energy similar to single site DMFT [Mar+11] is achieved by treating all hoppings perturbatively. In practice, all hoppings entering the cluster Hamiltonian are moved into the V-matrix. The KAFM S_x order being local is still optimised, as well as the chemical potential. This approach is similar to the comparison performed in the supplementary material of [Mar+18], where the oriented cluster DMFT is employed for a single site.

In contrast to the VCA results in figure 5.4, the optimal Weiss field in figure 5.10 first increases and then decreases with increasing temperature, while it kept decreasing within VCA. Due to this detour, the Néel temperature $T_N/t = 0.25$ turns out to be larger compared to VCA.

A possible explanation is that the reference system is not well suited to capture the magnetic features of the original system. Since the cluster sites of the reference system have no means of exchanging particles via hopping, they are decoupled and an effective superexchange interaction between the sites cannot emerge. The reference system itself thus has no mechanism to stabilise a magnetic order which should therefore be entirely driven by the Weiss field. With increasing temperature, more excited states of the ground state sector become relevant. In order to preserve the magnetic order which resembles the original system, the Weiss field has to enforce magnetic states as the lowest excited states and thus first increases with temperature. Once the temperature is too high, the Weiss field cannot ensure that only magnetic states contribute and the system starts to approach a PM.

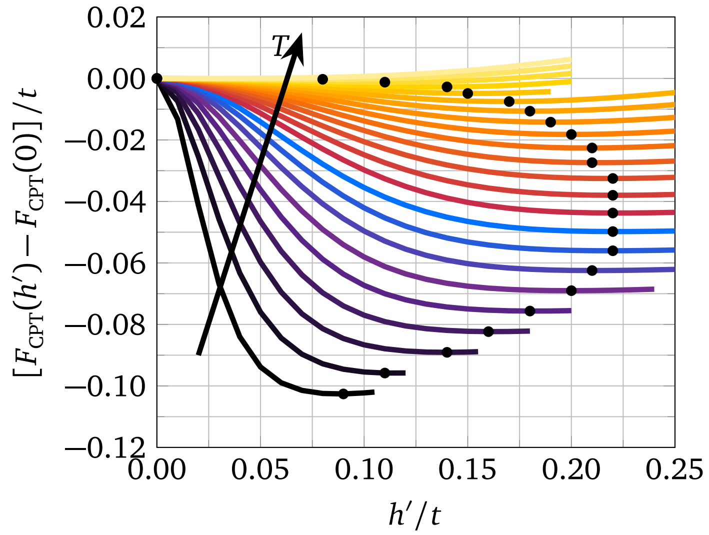

5.10 – CPT free energy F_{CPT} as function of the KAF S_x Weiss field amplitudes h' for several temperatures $T/t \in \{0.03, 0.04, \ldots, 0.25\}$.

Concerning the magnetic features in the spectral function, figure 5.11 shows, that the arc at $\boldsymbol{k}/\pi = (1, 0)$ is present at low temperature and vanishes above the Néel temperature as observed before. However compared to VCA, all states A, B and C exhibit such an arc, which remains visible also up to higher temperature.

Besides the magnetic features, the wavevectors forming the edges of the gap and the lowest unoccupied state being of $j_{\mathrm{eff}} = 1/2$ character are captured qualitatively by the local self-energy. Subtle differences are sharper features for the local self-energy, missing features above the chemical potential and a bigger gap between occupied and unoccupied states.

In comparison to the 2 × 1 and 2 × 2 site cluster with nonlocal self-energy a band with incoherent weight is missing. Considering the unoccupied states as those of a one-band Hubbard model [Kim+08], it describes the hole-dynamics of the respective low-energy t-J-model [Dag94].

The increased gap is accompanied in the supplementary material of [Mar+18] with a constant energy map strongly differing from the one with an oriented cluster as reference system.

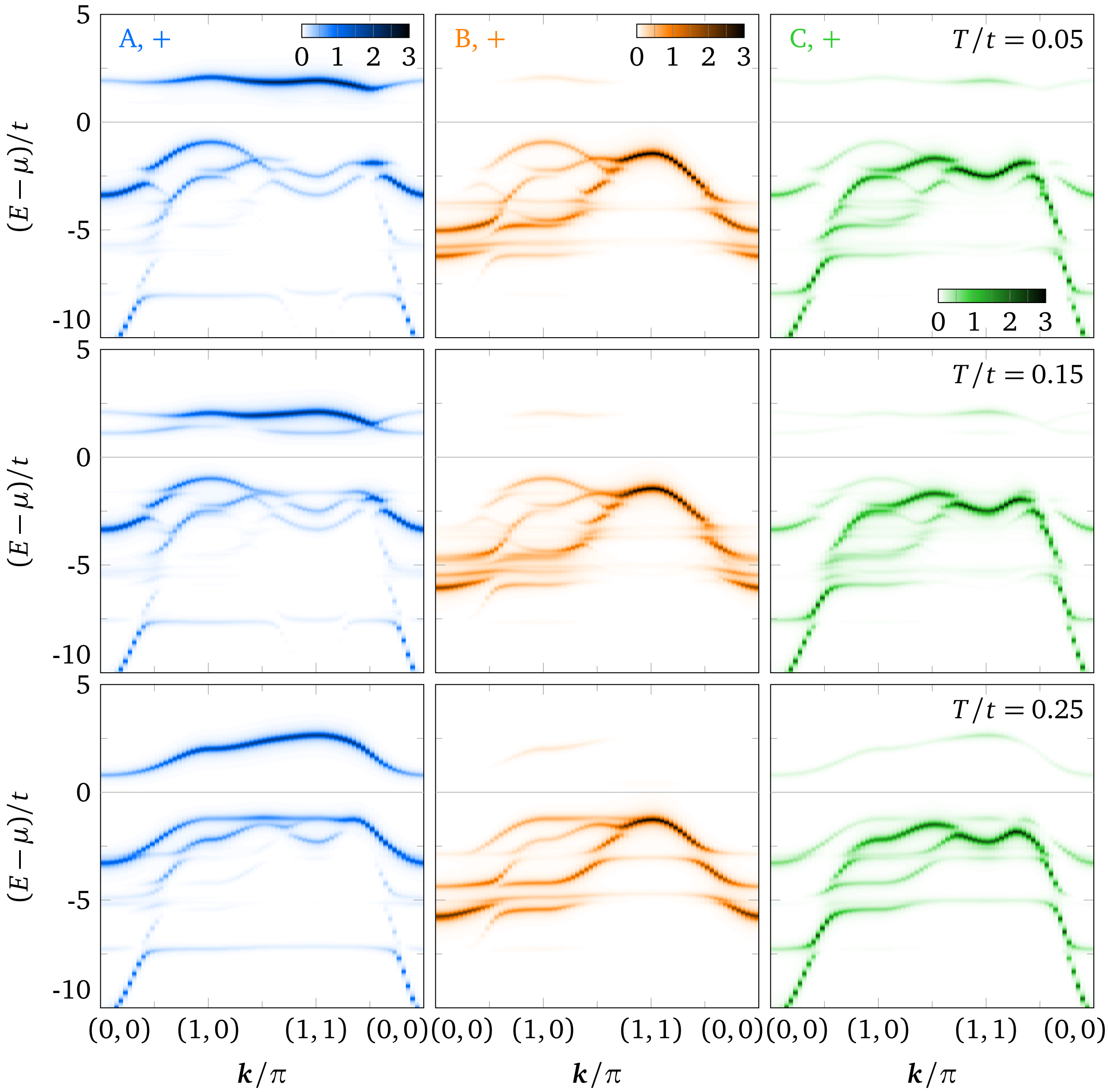

5.11 – Spectral function decomposed into contributions from the atomic states $|\mathrm{A},+\rangle = |j_\mathrm{eff} = 1/2, m_{j_\mathrm{eff}} = 1/2\rangle$, $|\mathrm{B},+\rangle = |j_\mathrm{eff} = 3/2, m_{j_\mathrm{eff}} = 3/2\rangle$ and $|\mathrm{C},+\rangle = |j_\mathrm{eff} = 3/2, m_{j_\mathrm{eff}} = 1/2\rangle$ for different temperatures T/t.

5 1 5 2 × 2 site cluster

To check the stability of the observations made with the 2 × 1 site cluster, a larger 2 × 2 site cluster as reference system is investigated.

The free energy shown in figure 5.12 behaves similar to the 2 × 1 site cluster in the sense, that the Weiss field is continuously reduced until it vanishes at the Néel temperature. Compared to the smaller reference system, the Néel temperature $T_N/t = 0.18$ is reduced as expected, since according to the Mermin-Wagner theorem [GN01] breaking of a continuous symmetry leading to the system ordering cannot occur in a two-dimensional system at finite temperature.

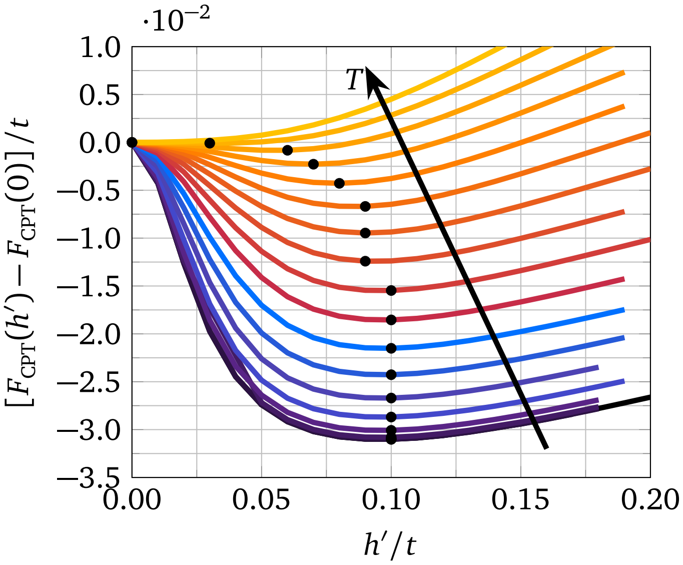

5.12 – CPT free energy F_{CPT} as function of the KAF S_x Weiss field amplitudes h' for several temperatures $T/t \in \{0.00, 0.01, \ldots, 0.18\}$.

Considering the DOS in figure 5.13, going from zero to non-zero temperature, the chemical potential exhibits a jump. This is most likely a numerical artifact due to the small weight in the gap allowing for a range of chemical potentials to realise the filling intended. In the range of $T/t \in [0.01, 0.06]$, the chemical potential shifts again almost linearly with temperature. For higher temperature, the chemical potential remains in the same order of magnitude. Just as in case of the 2 × 1 site cluster, the lower gap edge develops a peak, while the upper one exhibits a shoulder. Comparing the KAFM S_x phase with the PM phase, the gap closes rapidly in the prior one starting from the lower edge of the gap, while a peak emerges in the latter making the gap asymmetric. The speed by which the gap closes from its lower edge can be assessed from the blue and orange lines, which serve as guides to the eye for the points which refer to a value of 0.8 in the DOS. Both features of the gap closing are the same as for the 2 × 1 site cluster.

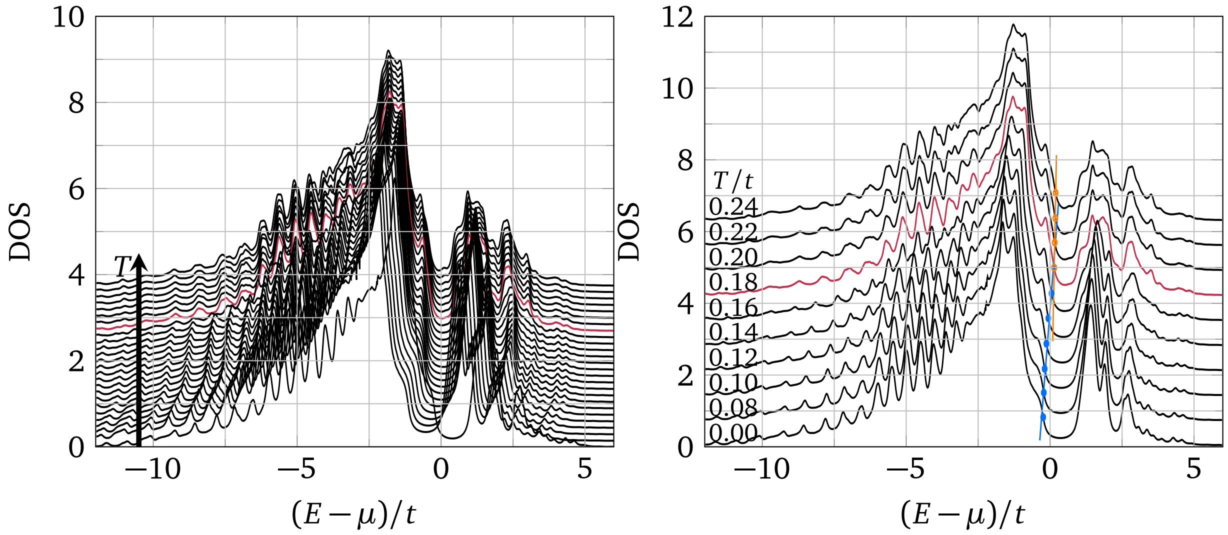

(a) Total DOS as is.

(b) Shifted DOS.

5.13 – Total DOS as is and energy shifted onto the $T/t = 0$ total DOS for different temperatures $T/t \in \{0.00, 0.01, \ldots, 0.25\}$ in (a) and specified in (b). The red curve highlights the phase transition at T_N. To illustrate the difference in how the gap closes in the AFM and PM phase, the blue and orange lines serve as guides to the eye for the points which mark the energy, where the DOS takes the value 0.8.

As for the 2×1 site cluster, the arc at $\boldsymbol{k}/\pi = (1,0)$ remains as feature of the magnetic order as shown in figure 5.14 when going to a larger reference system. In constrast to the smaller reference system, the arc seems to flatten by moving towards the chemical potential. Just as in case of the smaller cluster, the arc is present at low temperature for all states, while it flattens for the $j_{\text{eff}} = 1/2$ states and vanishes for the $j_{\text{eff}} = 3/2$ states when going beyond the Néel temperature.

The gap seems to keep closing from the point $\boldsymbol{k}/\pi = (1/2, 1/2)$, since the weight previously present around $\boldsymbol{k}/\pi = (0,0)$ is missing.

In addition, the $j_{\text{eff}} = 1/2$ character of the lowest unoccupied states is pronounced further compared to the 2×1 site cluster since weight from the $j_{\text{eff}} = 3/2$ states is missing above the chemical potential.

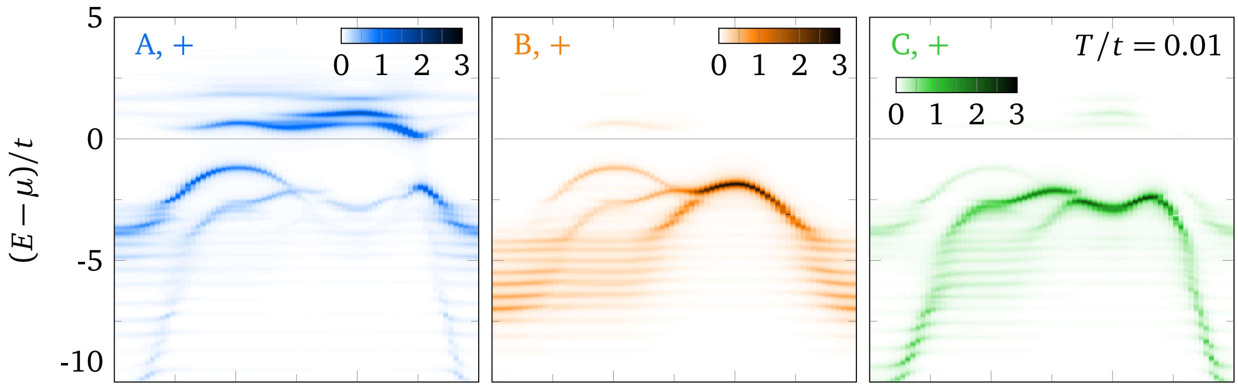

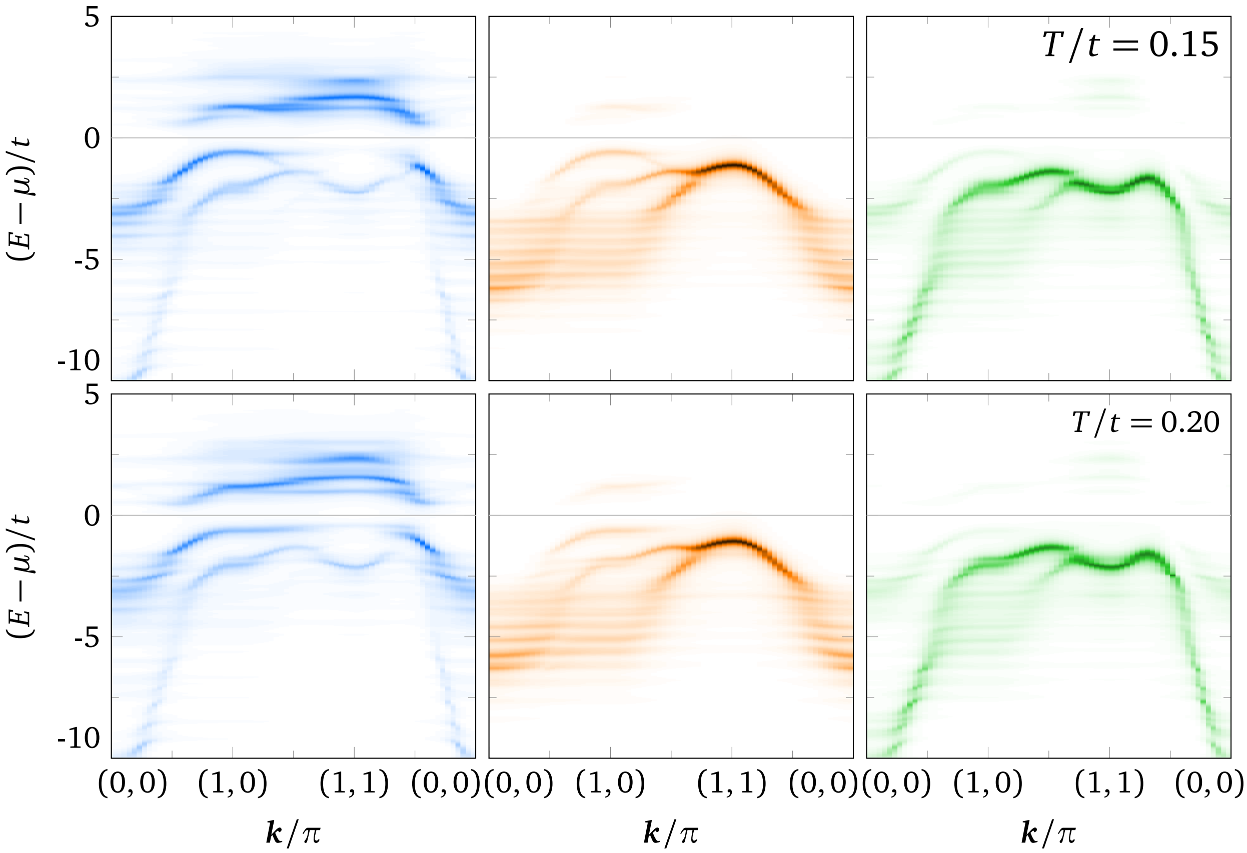

5.14 – Spectral function decomposed into contributions from the atomic states $|\mathrm{A},+\rangle = |j_{\mathrm{eff}} = 1/2, m_{j_{\mathrm{eff}}=1/2}\rangle$, $|\mathrm{B},+\rangle = |j_{\mathrm{eff}} = 3/2, m_{j_{\mathrm{eff}}=3/2}\rangle$ and $|\mathrm{C},+\rangle = |j_{\mathrm{eff}} = 3/2, m_{j_{\mathrm{eff}}=1/2}\rangle$ for different temperatures T/t.

As for the 2×1 site cluster, the $j_{\mathrm{eff}} = 1/2$ character of the lowest unoccupied states is visible within the respective DOS shown in figure 5.15. The $j_{\mathrm{eff}} = 1/2$ states determine how the gap is reduced. In contrast to the 2×1 site cluster, it seems that the asymmetry in the gap of the total DOS is entirely determined by the asymmetry of the gap in the $j_{\mathrm{eff}} = 1/2$ DOS.

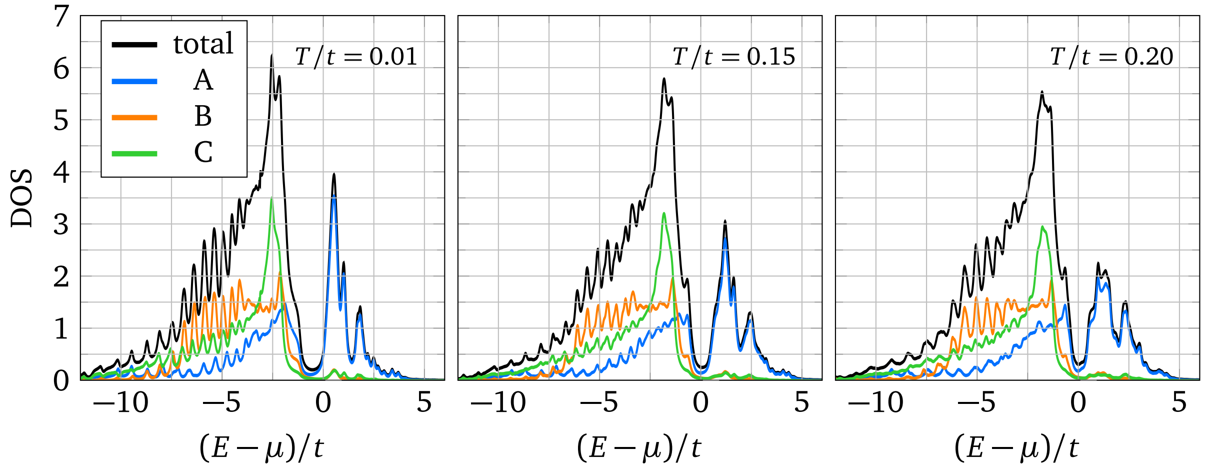

5.15 – Total and orbital resolved DOS for temperatures used for the spectra in figure 5.14.

On the front of the states occupation shown in figure 5.16 nothing changes compared to the 2 × 1 site reference system. The $j_{\mathrm{eff}} = 1/2$ states are approximately half-filled while the $j_{\mathrm{eff}} = 3/2$ states are completely occupied over the entire temperature range considered.

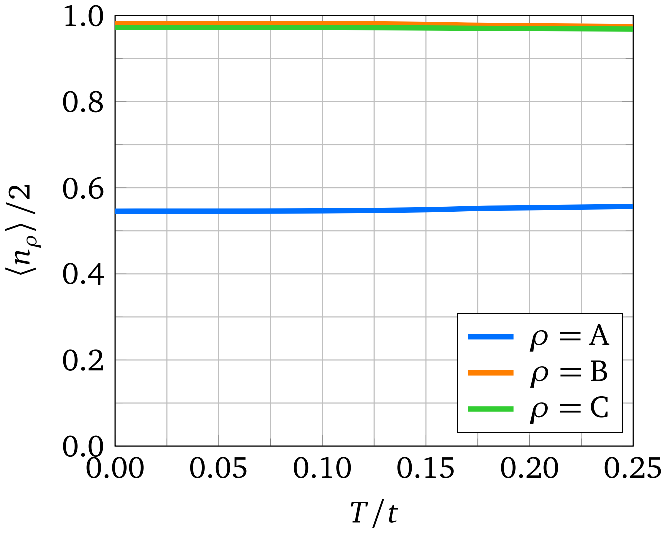

5.16 – Occupations per site and spin (electron perspective) as a function of temperature.

5.1.6 Néel temperature

As a summary, figure 5.17a shows the magnetisation as a function of temperature for the various reference systems. In case of the 2 × 1 site cluster with local self-energy Σ_{loc}, the amplitude of the magnetisation as well as the stability of the magnetic phase are overestimated. This behaviour is expected, since a local, atom-like self-energy lies closer to the mean-field limit than the self-energy of a cluster with local degrees of freedom. In the latter case, nonlocal quantum fluctuations can inhibit ordering.

With a nonlocal self-energy, the amplitude of the magnetisation drops and remains at low temperature independent of the size of the reference system. Furthermore, the Néel temperature is reduced from local to nonlocal self-energy to larger reference system. The latter is expected from the Mermin-Wagner theorem [GN01].

Further signatures of the KAFM S_x phase are the kink in the entropy and the resulting peak in the specific heat at the Néel temperature visible in the figures 5.17b and 5.17c.

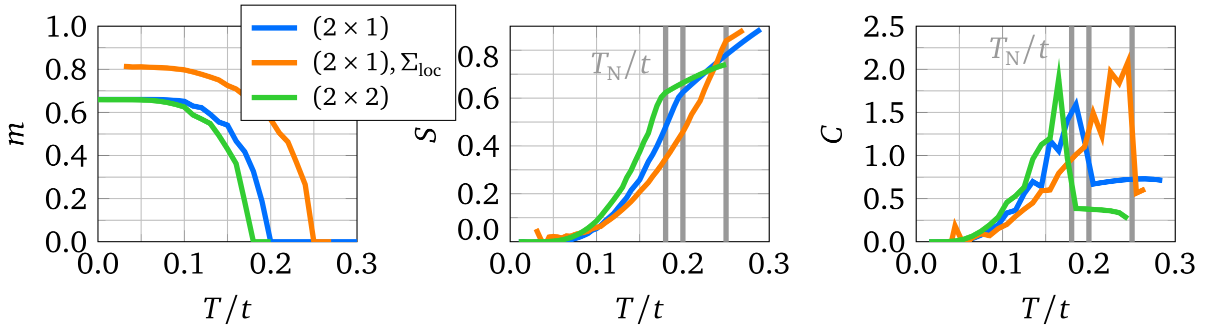

(a) Magnetisation. (b) Entropy. (c) Specific heat.

5.17 – Magnetisation, entropy and specific heat as function of temperature for the 2×1 site cluster with full and single site self-energy as well as for the 2 × 2 site cluster.

5.1.7 Conclusion and Outlook

To answer the questions raised at the beginning of this chapter:

- The AFM is characterised by an arc around the point $\boldsymbol{k}/\pi = (1,0)$ which vanishes with increasing temperature. Within the unoccupied states, the dispersion at the point $\boldsymbol{k}/\pi = (0,0)$ flips [SSY18] for a 2×1 site reference cluster. Such a behaviour cannot be confirmed for the larger 2×2 site reference system, where weight around this point is missing.

  The orbitals responsible for the magnetic ordering are the $j_{\text{eff}} = 1/2$ states. When going above the Néel temperature, the occupation of the states does not change.
- A local self-energy within the VCA qualitatively reproduces the spectra of the magnetically ordered system. However it overestimates the magnetic order's stability (larger Néel temperature, larger spectral gap) and misses out on spectral features in the unoccupied states, which show up when considering nonlocal quantum fluctuations.
- Within VCA, the insulating gap changes with temperature only marginally. The gap filling up above and below the Néel temperature appear to be different. However this occurs in such a faint manner, that definitive conclusions cannot be drawn.

  Trying to describe a metallic state with a finite cluster as reference system can be improved by adding bath sites and performing CDIA instead of VCA [BHP08; SSY18]. Since the d^5 system investigated within this section allows for a 2×2 site reference cluster in VCA, a CDIA reference system of a 2×1 site cluster with one bath-site per cluster site should be in reach. Hence the question of Mott- vs Slater-type insulator should be revisited within CDIA.

  As a side note, the number of variational parameters should first be restricted to the system, cluster and a bath chemical potential to fix the filling. Once a suitable starting point with satisfying filling is found, one can start sweeping the bath hybridisation. Similar to the one-band Hubbard model [SSY18], a minimum at low hybridisation is expected to hint at an insulator, while a minimum at higher hybridisation should imply a metal. By finally comparing the PM computation with a hybridisation sweep with finite AFM field on the reference cluster or even sweeping an AFM Weiss field and comparing the DOSs should give an indication which scenario might be occuring.
- Another way to investigate the question of Mott- vs Slater-type insulator would be to perform a parameter study similar to the one for the half-filled one-band Hubbard model [SSY18]. There, the paramagnetic entropy, specific heat and double occupation $\langle \hat{D} \rangle = \partial_U \Omega$ for all particle number sectors combined are computed for a large range of temperature and Hubbard repulsion U. Peaks in the specific heat highlight spin and charge excitations. Regions with $\partial_U S = -\partial_T \langle \hat{D} \rangle > 0$ mark spin fluctuations which increase the entropy by means of increased U. Their origin can be motivated by a double-occupancy susceptibility $\chi_{\mathrm{D}} = -T\,\partial_U \langle \hat{D} \rangle$ and the superexchange coupling constant $J = 4t^2/U$. Comparison with other studies allowed to assign the spin-fluctuations at small U to the Slater-type insulator and the ones at large U to the Mott-type insulator. The entropy and specific heat presented may serve as a starting point for such a study.

For a three-band Hubbard model, such a study will be more involved, since more couplings are present, which are usually chosen to depend on each other. Another point worth mentioning is the fixed filling of the present system. In order to enforce a specific filling in a thermodynamically consistent way, the physical chemical potential and a cluster chemical potential have to be optimised. This leads to the question, whether it is sufficient to perform the optimisation only in the particle number sector corresponding to this fixed filling and use the chemical potentials obtained in the other particle number sectors. A numerically more expensive approach would be to optimise for arbitrary fillings which can be realised within CDIA.

5.2 d^4 configuration: Ca_2RuO_4

Another compound described by a three-band Hubbard model but with four electrons is Ca_2RuO_4. Using VCA, SOC is found to destabilize the magnetic order. However it seemingly does not affect the Néel temperature which is most likely a finite-size effect. With increasing temperature, the capability of SOC to mix different orbitals becomes less effective. The combination with signatures of orbital fluctuations and the absence of real orbital order [Por+18] suggests phase fluctuations between the orbital components which are no longer fixed by SOC as the origin of these fluctuations. The results presented here have in part been published in [LD21].

Another compound interesting for its orbital physics is Ca_2RuO_4 [Bur08]. In contrast to Sr_2IrO_4 discussed in the previous section, it hosts two holes in 4d orbitals. Similar to the prior compound, CF splitting leads to the four electrons occupying the t_{2g} orbitals indicating a system with three active orbitals. With increasing temperature, Ca_2RuO_4 starts off at low temperature as an AFM insulator until it reaches its Néel temperature $T_N = 110\,K$. At $T_{MIT} = 360\,K$, the paramagnetic insulator transitions further into a paramagnetic metal. In between, at $T_{OO} = 260\,K$, the transition from an orbitally ordered into a disordered state may [Zeg+05] or may not [Por+18] be present.

After finding, that the orbital occupation changes strongly with temperature and attributing this to strong SOC [Miz+01], Hotta and Dagotto [HD01] predicted an orbital ordered (OO) state responsible for this behaviour. Several groups [HD01; Jun+03; FNT04] argued in favour of an orbital order, however the actual order as well as the stabilisation mechanism remained debated. Experimentally, Zegkinoglou et al. [Zeg+05] associated the order parameter-like vanishing of the (100) reflex of the L_2-edge at $T_{OO} \approx 260\,K$ with the orbital order, while the phase at $T_N \leq T \leq T_{OO}$ was identified as a paramagnet.

A DFT+DMFT study [Gor+10] argued, that structural change with temperature is the main driver of the orbital order accompanying the insulator-metal transition, which prevails against an orbital-selective Mott phase due to CF splitting dominating over the bandwidths influence. This study as well as another one by the same group [ZP17] attributed the metal-insulator transition (MIT) occuring at $T_{MIT} = 360\,K$ [Bur08] to the structural change as well. The second publication [ZP17] claimed, based on the local spectral function, that SOC on the LDA-level, an anisotropic, orbital dependent Coulomb interaction and magnetic ordering are not decisive for the MIT.

A thorough resonant elastic x-ray scattering study [Por+18] brought the conclusion by Zegkinoglou et al. of orbital order into question. At $T_{OO} = 260\,K$, no abrupt behaviour was detected in the x-ray reflex at (013) of the L_2-edge addressing the same order parameter as the one at (100) of the L_2-edge and hence the assignment of an orbital-order phase transition to this temperature should be reanalysed. However the continuous decrease in the above mentioned reflexes cannot be explained entirely by the contraction of the octahedra, allowing for a complex phase relation in the (yz, xz)-subspace.

As for this chapter, the influence of SOC and CF splitting onto the temperature-dependence of static quantities as well as of dynamic properties is investigated following the treatment at zero temperature [Fel19]. The prior comprises magnetisation, specific heat and orbital occupation, while the latter refers to the DOS and spectral function. Furthermore, the cluster expectation value of projectors onto the local LS-coupled states $|J = 0, 1, 2\rangle$ is determined. The overall focus lies on the magnetic phase transition and features in the above mentioned observables hinting at orbital-selective behaviour. An attempt to model the metal-insulator transition by means of CDIA turned out difficult already while searching for a starting point at zero temperature.

5.2.1 Hamiltonian, observables and orders

Since only the t_{2g} states are of relevance, the Hamiltonian considered is again a three-band Hubbard model with interactions of Kanamori form [GMM13; Ole83]

$$H = H_{\text{kin}} + H_{\text{int}} + H_{\text{SOC}} + H_{\text{CF}} + H_{\mu} \tag{5.16}$$

with the kinetic part

$$\begin{aligned} H_{\text{kin}} =& -t \sum_{\langle i,j\rangle_1,\sigma} (c^{\dagger}_{i,\text{xy},\sigma} c_{j,\text{xy},\sigma} + c^{\dagger}_{j,\text{xy},\sigma} c_{i,\text{xy},\sigma}) \\ & - t \sum_{\langle i,j\rangle_{1,\text{y}},\sigma} (c^{\dagger}_{i,\text{yz},\sigma} c_{j,\text{yz},\sigma} + c^{\dagger}_{j,\text{yz},\sigma} c_{i,\text{yz},\sigma}) - t \sum_{\langle i,j\rangle_{1,\text{x}},\sigma} (c^{\dagger}_{i,\text{xz},\sigma} c_{j,\text{xz},\sigma} + c^{\dagger}_{j,\text{xz},\sigma} c_{i,\text{xz},\sigma}), \end{aligned} \tag{5.17}$$

the interaction part

$$\begin{aligned} H_{\text{int}} = & U \sum_{i,\alpha} n_{i\alpha\uparrow} n_{i\alpha\downarrow} + U' \sum_{i,\alpha,\beta\neq\alpha} n_{i\alpha\uparrow} n_{i\beta\downarrow} + (U' - J) \sum_{i,\alpha,\beta>\alpha,\sigma} n_{i\alpha\sigma} n_{i\beta\sigma} \\ & - J \sum_{i,\alpha,\beta\neq\alpha} c^{\dagger}_{i\alpha\uparrow} c_{i\alpha\downarrow} c^{\dagger}_{i\beta\downarrow} c_{i\beta\uparrow} + J \sum_{i,\alpha,\beta\neq\alpha} c^{\dagger}_{i\alpha\uparrow} c^{\dagger}_{i\alpha\downarrow} c_{i\beta\downarrow} c_{i\beta\uparrow}, \end{aligned} \tag{5.18}$$

the SOC

$$H_{\text{SOC}} = \frac{\lambda}{2} \sum_{i} (c^{\dagger}_{i,\text{yz},\uparrow}, c^{\dagger}_{i,\text{yz},\downarrow}, c^{\dagger}_{i,\text{xz},\uparrow}, c^{\dagger}_{i,\text{xz},\downarrow}, c^{\dagger}_{i,\text{xy},\uparrow}, c^{\dagger}_{i,\text{xy},\downarrow}) \begin{pmatrix} \mathbf{0} & -\mathrm{i}\boldsymbol{\sigma}_{\text{z}} & \mathrm{i}\boldsymbol{\sigma}_{\text{y}} \\ \mathrm{i}\boldsymbol{\sigma}_{\text{z}} & \mathbf{0} & -\mathrm{i}\boldsymbol{\sigma}_{\text{x}} \\ -\mathrm{i}\boldsymbol{\sigma}_{\text{y}} & \mathrm{i}\boldsymbol{\sigma}_{\text{x}} & \mathbf{0} \end{pmatrix} \begin{pmatrix} c_{i,\text{yz},\uparrow} \\ c_{i,\text{yz},\downarrow} \\ c_{i,\text{xz},\uparrow} \\ c_{i,\text{xz},\downarrow} \\ c_{i,\text{xy},\uparrow} \\ c_{i,\text{xy},\downarrow} \end{pmatrix}, \tag{5.19}$$

the tetragonal CF splitting

$$H_{\text{CF}} = \Delta \sum_{i,\sigma} n_{i,\text{xy},\sigma} \tag{5.20}$$

and the chemical potential

$$H_{\mu} = -\mu \sum_{i,\alpha,\sigma} n_{i\alpha\sigma}. \tag{5.21}$$

The coupling parameters used are approximately taken from [Fel19]. Since anisotropic first nearest neighbour, second nearest neighbour, and inter-orbital hopping do not alter the results significantly, only isotropic first nearest neighbour hopping is considered. Most values for SOC are chosen as $\lambda/t > 0.4$ since at $T/t = 0$, excitonic AFM order with ordering wavevector $\boldsymbol{q}/\pi = (1,1)$ dominates. For $\lambda/t \leq 0.4$ a stripy pattern with ordering wavevectors $\boldsymbol{q}/\pi = (0,1)$ for spins and $\boldsymbol{q}/\pi = (1,0)$ for orbitals is realised, which is not of interest. CF splitting and interaction parameters are taken from [Fel19] in order to realise an excitonic AFM order and are further motivated by [Gre+19; Sut+17; Por+18; Gor+10; Miz+01]. Altogether, the coupling parameters used in practice are given below:

- $t = 0.2\,\mathrm{eV}$
- $\lambda \in \{0, 0.1, 0.6, 0.8, 1\}t = \{0, 0.02, 0.12, 0.16, 0.2\}\,\mathrm{eV}$
- $\Delta \in \{0, 1.5, 5\}t = \{0, 0.3, 1\}\,\mathrm{eV}$
- $U = 12.5t = 2.5\,\mathrm{eV}$
- $J = 2.5t = 0.5\,\mathrm{eV}$
- $U' = (U - 2J) = 7.5t = 1.5\,\mathrm{eV}$

Besides these parameters, the chemical potential is fixed s.t. the system is filled by two holes per site as described in section 2.4.7. The unit of energy used in practice is given by the nearest neighbour hopping of the xy-orbital denoted by t.

In order to assess the influence of SOC on the magnetic and orbital composition, the squared absolute value of the overlap of the local LS-coupled states $|J = 0, 1, 2\rangle$ with the cluster ground state were considered at zero temperature [Fel19]

$$\langle J \rangle = |\langle \Psi_0 | J \rangle|^2. \tag{5.22}$$

This overlap can be extended to finite temperature by interpreting it as the expectation value of a projector onto the LS-coupled states, which gives at finite temperature

$$\begin{aligned} \langle J \rangle &= \mathrm{Tr}(\varrho\, |J\rangle \langle J|) &(5.23)\\ &= \sum_n \frac{\exp(-\beta \varepsilon_n)}{\Xi} |\langle \Psi_n | J \rangle|^2, &(5.24) \end{aligned}$$

where in practice the sum is truncated to the exact trace vectors determined by the cluster solver. Computing the overlap on a VCA level is not possible, since only the single-particle Green's function containing one-body operators is available, while the overlap is a two-body observable. One may argue that this overlap yields information on the local magnetic and orbital composition of a cluster embedded in its environment. Note that also the expectation values of projectors including other states can be computed in order to characterise the system.

Since this cluster expectation value is computed from the eigenstates following equation (2.22) and not from the cluster Green's function, the discrepancies discussed in appendix C do not affect the results presented in this section.

The orders considered within VCA take the general form

$$H = h' \sum_j \Lambda_j \exp(\mathrm{i}\boldsymbol{q} \cdot \boldsymbol{j}), \tag{5.25}$$

where Λ_j is a one-body operator and $\boldsymbol{q}$ the ordering wavevector. In practice, the following orders are investigated:

- CAFM S_z: $\Lambda_j = \sum_{\alpha \in \{\mathrm{xy,yz,xz}\}} (n_{j\alpha\uparrow} - n_{j\alpha\downarrow})$, $\boldsymbol{q} = (\pi, \pi)$,
- CAFM S_x: $\Lambda_j = \sum_{\alpha \in \{\mathrm{xy,yz,xz}\}} (c^\dagger_{j\alpha\uparrow} c_{j\alpha\downarrow} + c^\dagger_{j\alpha\downarrow} c_{j\alpha\uparrow})$, $\boldsymbol{q} = (\pi, \pi)$,

with $n_{j\alpha\sigma} = c^\dagger_{j\alpha\sigma} c_{j\alpha\sigma}$. The in-plane orderings employing the spin components in x-direction S_x are obtained via a SU(2) spin-rotation applied to the creation/annihilation operators as used in [Sch16], meaning

$$\begin{aligned} c^\dagger_{j\alpha\uparrow_\mathrm{x}} &= (c^\dagger_{j\alpha\uparrow} + c^\dagger_{j\alpha\downarrow})/\sqrt{2}, &(5.26)\\ c^\dagger_{j\alpha\downarrow\mathrm{x}} &= (-c^\dagger_{j\alpha\uparrow} + c^\dagger_{j\alpha\downarrow})/\sqrt{2}. &(5.27) \end{aligned}$$

The reference system considered for the major part is a 2 × 1 site cluster. At zero temperature, a 2 × 2 site cluster can be employed as reference system [Fel19], while tests at finite temperature showed that ~ 20 converged exact trace vectors obtained after $\sim 1600-2000$ Lanczos iterations already form a limit, since the optimisation requires multiple evaluations of the grand potential. To assess the size dependence and local character of the observations, a 1 site cluster is employed.

Technically, for finite temperature all computations for the 2 × 1 site cluster are performed with $N_{\mathrm{ex}} = 120$ exact trace vectors, which are obtained by performing a maximum of 800 Band Lanczos iterations allowing $N_{\mathrm{deg}} = 8$ starting vectors. The excited state sectors are handled with a regular Lanczos solver with a maximum of 800 iterations. In case of the 1 site cluster, FD and all exact trace vectors are used. For the construction of the Green's function, the high-frequency expansion is employed up to 15th order for both cluster sizes.

Employing the Band Lanczos and Lanczos solver instead of FD for the 2 × 1 site cluster is due to the latter taking too much time to construct the Green's function. Details on this can be found in appendix D.2. The restriction to $N_{\mathrm{ex}} = 120$ exact trace vectors is used, since it turned out to be sufficient for large clusters of the one-band Hubbard model. In general, the decision to restrict the number of trace vectors instead of setting them depending on the temperature [SSY18] is discussed in appendix D.2.

As for the modus operandi, first the free energy as a function of the physical and cluster chemical potential μ and μ' is evaluated on a grid. This is done for the PM phase with $h'/t = 0$ for three temperatures $T/t \in \{0, 0.01, 0.1\}$ to assess which optima survive to finite temperature. After an estimate of both parameters is obtained with a resolution of $\Delta\mu/t = 0.1 = \Delta\mu'/t$, the corresponding optimum is determined starting from the estimate. Starting in case of the 2 × 1 site cluster from this optimum, the free energy is computed for a range of the magnetic Weiss field amplitudes $h'/t \in \{0.00, 0.01, \ldots, 0.20\}$ at all temperatures considered while optimising the two chemical potentials. The free energies obtained allow to determine the optimal magnetic Weiss field with a resolution of $\Delta h'/t = 0.01$. For the 1 site cluster this step is omitted, since such a cluster does not allow for an AFM order. For the computation of further observables, the system is evaluated at the optimum.

5 2 2 Zero tetragonal CF splitting

As a reference, first the system without tetragonal CF splitting $\Delta/t = 0$ is considered. According to investigations at zero temperature [Fel19], the interaction parameters under consideration lead to an AFM order with the spin pointing out-of plane and S_{z} as relevant spin component to quantify the order.

Figure 5.18 shows the free energy for three values of SOC $\lambda/t \in \{0.6, 0.8, 1\}$ as a function of the AFM S_{z} Weiss field h'/t for several temperatures $T/t \in \{0.00, 0.01, \ldots, T_{\mathrm{N}}/t\}$. Within these images, the optimal Weiss field decreases with increasing temperature for all SOCs considered. Interpreting the depth of the free energy minimum as a measure of stability, smaller SOC leads to a more stable AFM S_{z} order. This is reasonable, since larger SOC implies the system to lie closer to a PM [Fel19]. However the Néel temperature does not seem to depend on the SOC as inferred from the values considered. Besides the possibility of strong finite-size effects, another explanation lies in the system being close to the stripy phase for lowest SOC $\lambda/t = 0.6$ considered, which could affect the stability of the magnetic order in that limit.

In order to fix the particle number, the free energy is optimised w.r.t. the chemical potential μ/t and the cluster chemical potential μ'/t. Thus the Weiss field h'/t is only scanned with a resolution of $\Delta h'/t = 0.01$ leading to the discrete appearance of the highlighted minima.

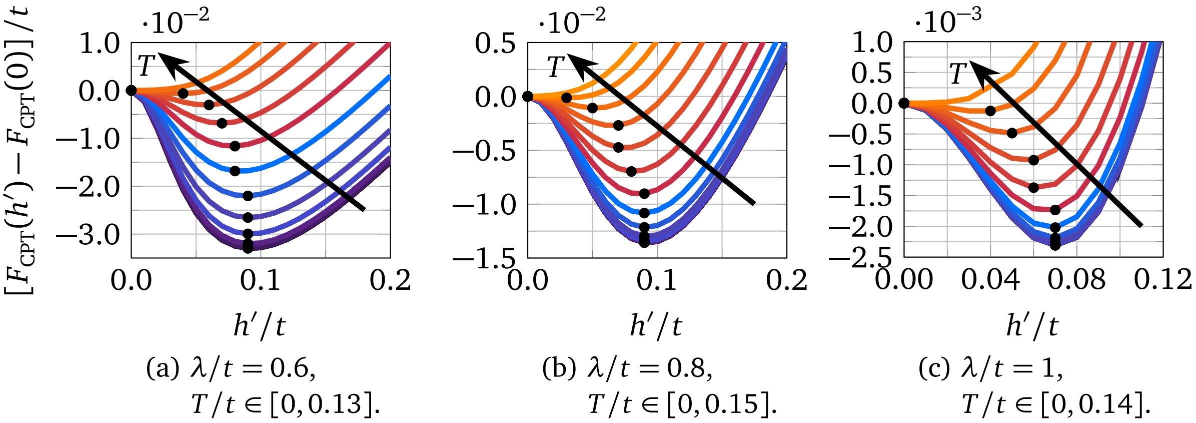

(a) $\lambda/t = 0.6$, $T/t \in [0, 0.13]$.
(b) $\lambda/t = 0.8$, $T/t \in [0, 0.15]$.
(c) $\lambda/t = 1$, $T/t \in [0, 0.14]$.

5.18 – CPT free energy F_{CPT}/t at the given SOC λ/t as function of the AFM S_z Weiss field amplitudes h'/t for several temperatures $T/t \in \{0.00, 0.01, \dots, T_{\mathrm{N}}/t\}$.

A direct measure of the AFM S_z order is the AFM magnetisation shown in figure 5.19a as function of temperature. Its saturation value at low temperature decreases with increasing SOC. This can be understood in terms of the atomic limit, where SOC promotes a singlet state [Fel19]. Given the resolution of the Weiss field, the magnetisation amounts to its saturation value up to rather large temperatures $T/t = 0.07$ for $\lambda/t = 0.6$ and $T/t = 0.09$ for $\lambda/t \in \{0.8, 1\}$. However the Néel temperature does not seem to depend on SOC.

The Néel temperature can also be inferred from the kink visible in the entropy displayed in figure 5.19b. However with increasing SOC, the kink becomes less distinct and the entropy at a given temperature decreases.

The specific heat shown in figure 5.19c as function of temperature exhibits up to two peaks, depending on the SOC. At low and intermediate SOCs $\lambda/t \in \{0.6, 0.8\}$ only one peak close to T_{N} is present. Its height decreases with increasing SOC. Since it lies close to the Néel temperature, it is identified as signature of AFM fluctuations. Only for high SOC $\lambda/t = 1$, a second, broader peak occurs at higher temperature $T_{\mathrm{C2}}/t = 0.225$.

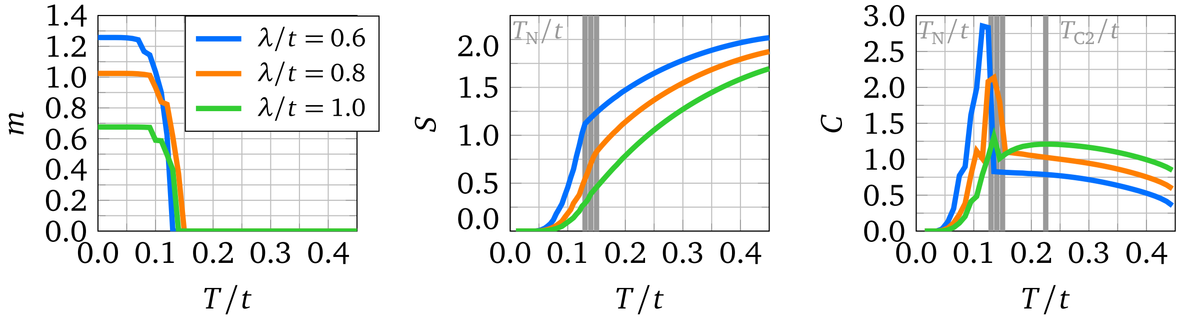

(a) Magnetisation.
(b) Entropy.
(c) Specific heat.

5.19 – Magnetisation, entropy and specific heat as function of temperature for $\lambda/t \in \{0.6, 0.8, 1\}$.

To get an overview of the local magnetic and orbital composition of a cluster embedded in its environment, the overlaps introduced in equation (5.24) as a function of temperature are shown in figure 5.20. For all SOCs considered, the overlaps remain almost constant below the Néel temperature T_N. Starting at T_N, the overlaps start to change significantly. The overlap $\langle J = 0\rangle$ decreases rapidly, while $\langle J = 1\rangle$ and $\langle J = 2\rangle$ increase.

An increase in $\langle J = 1\rangle$ during the transition from AFM to PM deviates from what is observed when this transition is mimicked at zero temperature by considering the system at optimal (AFM) and at zero (PM) AFM S_z Weiss field [Fel19]. There, weight seemingly shifts from $\langle J = 1\rangle$ to $\langle J = 0\rangle$ upon setting the AFM S_z Weiss field to zero. While for the artificial transition at zero temperature the spectrum is altered via the Weiss field, the finite temperature treatment leads besides that also to more states contributing to the trace. Hence a PM state of the system is induced partially also by including PM excited states while the ground state may still be an AFM enforced by the Weiss field.

With increasing SOC, $\langle J = 0\rangle$ starts for low temperatures at a higher value at the expense of $\langle J = 1\rangle$, leading to the intersection of both shifting to higher temperatures. Expressed differently, a higher temperature is required to mix different J-states into the system. This can be understood by considering the atomic limit, where the level splitting is proportional to the SOC [Fel19]. Hence a higher temperature is required to populate these states.

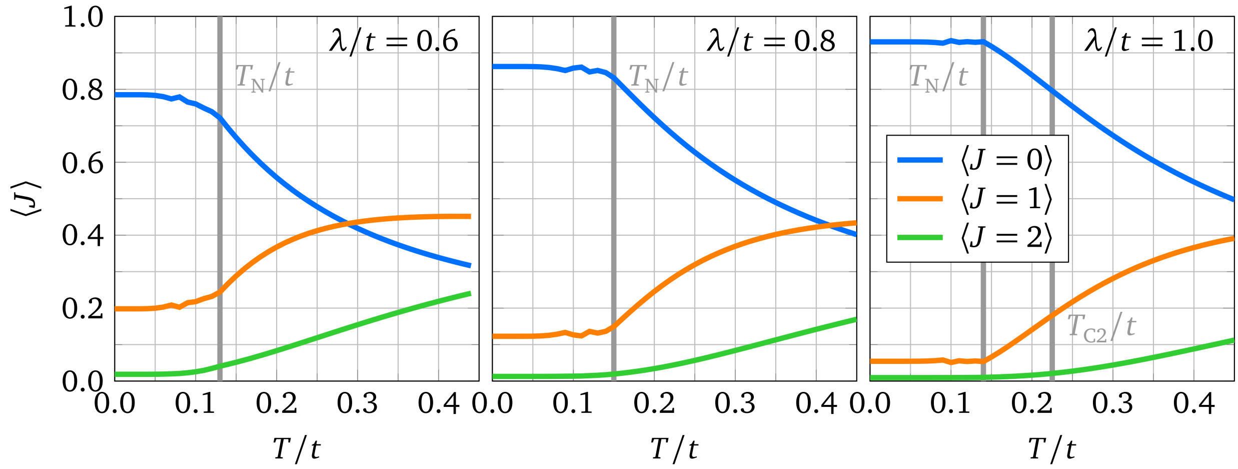

5.20 – Overlaps as functions of temperature at $\lambda/t \in \{0.6, 0.8, 1\}$ considering holes.

Coming to dynamic properties, the DOS for various temperatures is shown in figure 5.21. It exhibits three occupied bands below the chemical potential related to Hunds coupling [Sut+17]. For all SOCs, there occurs a drift in the chemical potential until the transition to the PM. The small detour in the drift when going from finite to zero temperature as well as the jump for $\lambda/t = 1$ at $T/t = 0.14$ is due to the chemical potential deviating from the tendency at the other temperatures. It seems the chemical potential fixed by the filling depends more on the AFM S_z Weiss field than on temperature. This is reasonable, since temperature itself may broaden the states in the DOS or provide them with weight, which fills up the gap eventually. However in case of an insulator, the chemical potential lying in the gap may only be affected by this at high temperature or small gaps. At small and intermediate SOCs, the gaps shape remains more or less the same. Small shoulders start to emerge from the borders of the gap somewhat above the transition to the PM. For large SOC, first a shoulder and later a peak emerges from the lower edge of the gap at the temperature which may belong to the second peak in the specific heat.

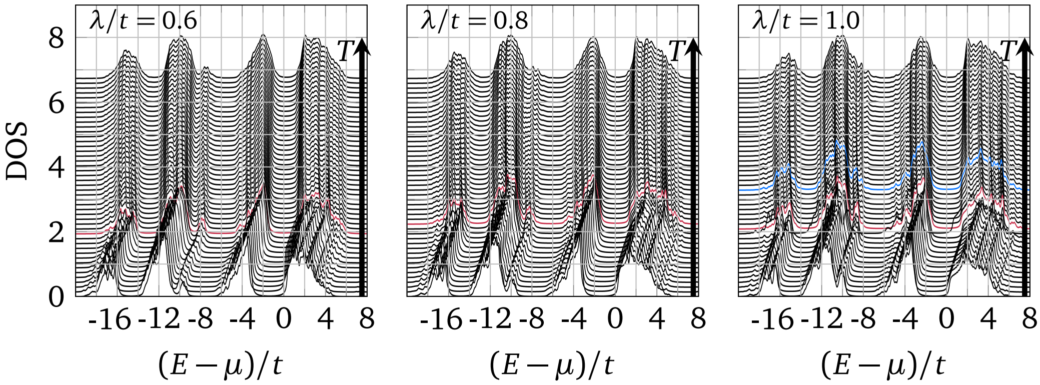

5.21 – Total DOS considering electrons at $\lambda/t \in \{0.6, 0.8, 1\}$ for different temperatures $T/t \in \{0.00, 0.01, \ldots, 0.45\}$. The red curve highlights the phase transition at T_{N}, while the blue curve refers to the temperature closest to, but below the second peak in the specific heat at T_{C2}.

Aligning the DOS within the AFM S_z phase and thus removing the shift due to the chemical potential is shown in figure 5.22. Within the AFM S_z phase, the gap size decreases slightly with increasing temperature until the system enters the PM phase. Past this temperature there occurs almost no change in the gap size as can be inferred from figure 5.21. Furthermore, a peak present at the upper edge of the highest occupied band becomes less sharp and decreases in height with increasing temperature. This behaviour is most noticeable for $\lambda/t \in \{0.8, 1\}$.

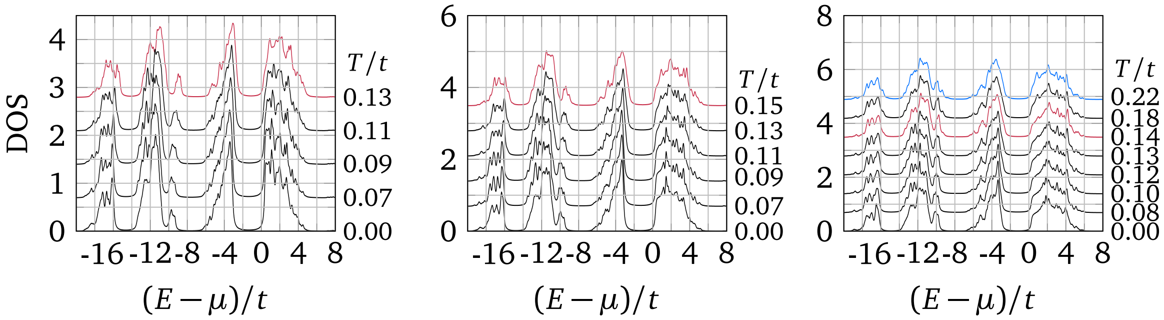

(a) $\lambda/t = 0.6$. (b) $\lambda/t = 0.8$. (c) $\lambda/t = 1$.

5.22 – Total DOS shifted onto the $T/t = 0$ total DOS at $\lambda/t \in \{0.6, 0.8, 1\}$ for several temperatures. The red curve highlights the phase transition at T_{N}, while the blue curve refers to the temperature closest to, but below the second peak in the specific heat at T_{C2}.

In order to highlight the features discussed in the spectral function, the dispersion relations of several tight-binding models are shown in figure 5.23. The AFM order is realised by considering a system with doubled unit cell. Its dispersion relation shown in figure 5.23a can be considered as being the PM dispersion mirrored around the chemical potential. A comparison of the dispersions of one-dimensional chains embedded in a two-dimensional system with the complete two-dimensional dispersion is shown in figure 5.23b. While the chain along the x-direction is dispersionless in y-direction, the opposite is true for the chain in y-direction. The two-dimensional system is only dispersionless for a small plateau around $\boldsymbol{k}/\pi = (1, 0)$.

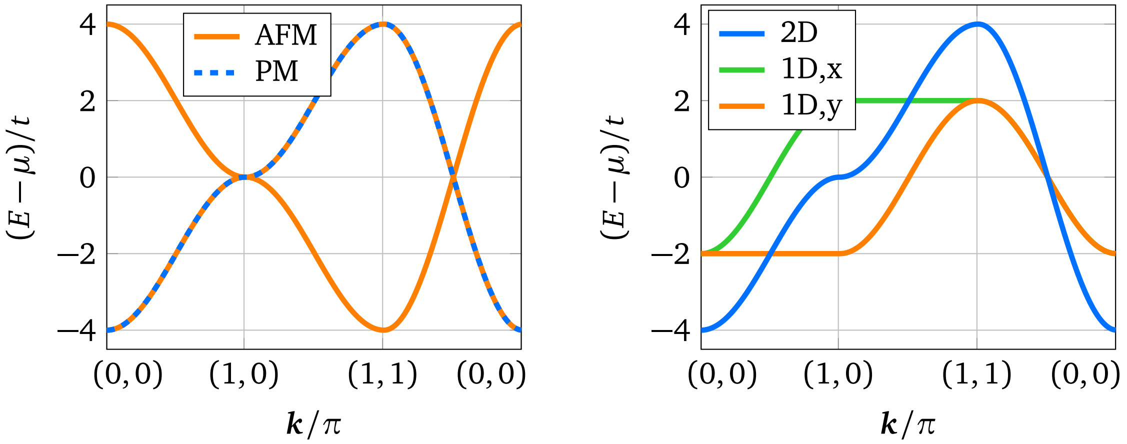

(a) Dispersion relations of an AFM and a PM square system in two dimensions.

(b) Dispersion relations of chains in x- and y-direction as well as of a two-dimensional square system.

5.23 – Illustration of tight-binding dispersions comparing those of a PM and an AFM system as well as hoppings of different dimensionality.

While the total DOS enabled only a rough overview of the energetics, the orbital-resolved spectral function for $\lambda/t = 0.8$ shown in figure 5.24 makes it possible to identify hallmarks of the AFM S_z order. It is characterised by an arc within the unoccupied states at $\boldsymbol{k}/\pi = (1, 1)$ which vanishes at T_N. While this feature occurs in the spectral contributions from all orbitals, it is most noticeable for the xy-orbital. Comparing the spectra with the dispersion relation of a perfect AFM as shown in figure 5.23a confirms the arc as a signature of the AFM order since it resembles the mirrored dispersion relation.

The spectral weight at $\boldsymbol{k}/\pi = (0, 0)$ of the unoccupied states does not switch from bending up- to downwards upon transition from the AFM to the PM as observed for the half-filled one-band Hubbard model [SSY18]. For the three-band Hubbard model associated with Sr_2IrO_4 with one hole shown in figure 5.6 however, such a bending is present. One may be inclined to argue that the system is closer to the Hubbard-I approximation of ordered local moments than a mean-field theory of long-range order since here the spectral weight keeps facing downwards throughout the entire AFM phase [SSY18]. However the analogy with one-band results may be restricted further to systems with an active half-filled band as seems to be the case for Sr_2IrO_4. Considering the Hubbard-I and a self-consistent SDW mean-field approximation for one- and three-band models at different fillings may provide clarity if there is a change in the limiting cases considered.

Apart from the signatures of magnetism, the dimensionality of the orbital-resolved highest occupied and lowest unoccupied band changes with temperature. Just considering the kinetic term of the Hamiltonian, the xy-orbital exhibits a two-dimensional dispersion relation, while the xz- and yz-orbital are supposed to have a one-dimensional dispersion relation as those shown in figure 5.23b. Since the Hamiltonian describes holes while the spectral function is shown for electrons, focus lies on the unoccupied band which signifies the hole-dynamics. While the unoccupied xy-orbital keeps its two-dimensional dispersion relation at higher temperatures, the xz- and yz-orbital change from a two- to a more one-dimensional dispersion.

Spectra employing the other SOCs $\lambda/t \in \{0.6, 1\}$ considered exhibit similar features and are omitted here.

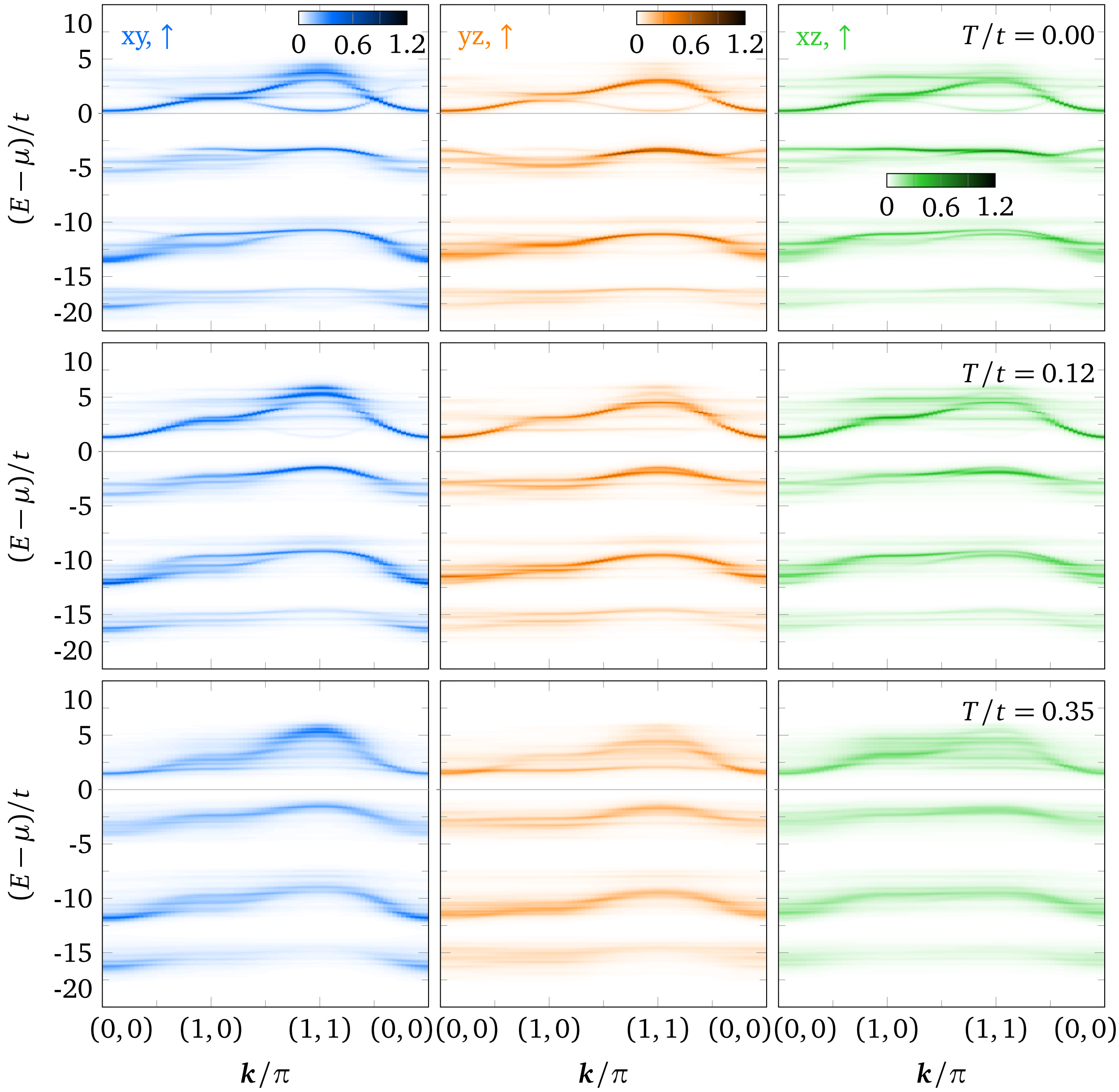

5.24 – Orbital-resolved spectral function considering electrons at $\lambda/t = 0.8$ for two temperatures below and one above $T_\mathrm{N}/t = 0.15$.

Taking a step back, figure 5.25 shows the orbital-resolved DOS at the temperatures used within figure 5.24. At zero temperature, there occur peaks at the lower edge of the gap formed by the yz- and xz-orbitals and a peak at the upper edge of the gap belonging to the xy-orbital. Judging by the energy, the latter belongs to features at the boundary of the Brillouin zone due to the doubled unit cell within the AFM phase which show up at $\boldsymbol{k}/\pi = (1,0)$ and $\boldsymbol{k}/\pi = (1/2, 1/2)$. The former peaks might compensate the missing electrons in the xy-orbital to realise a filling of two holes per site.

This compensation can be argued in a simple manner by considering the available space in terms of orbitals and the fixed filling. Since one orbital can host two particles, the integral of the orbital-resolved DOS over the entire energy range yields two for each orbital. Therefore an increase in the orbital-resolved DOS at one energy leads to a decrease in the orbital-resolved DOS at other energies. Enforcing a certain filling implies for an integral of the total DOS up to the chemical potential to return this filling. If for one orbital the weight of the orbital-resolved DOS shifts above the chemical potential, the other orbitals have to compensate this and accumulate weight below the chemical potential.

The height of the peaks decreases with increasing SOC. With increasing temperature, the different orbitals start to contribute weight of similar order of magnitude in the bands above and below the chemical potential.

As for the arc, it forms the sharp edge of unoccupied states above the gap.

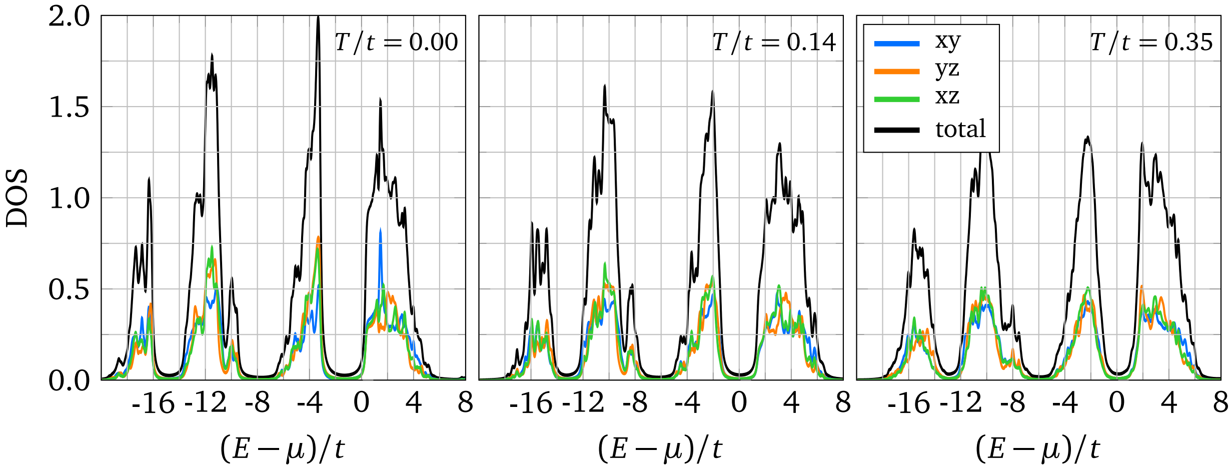

5.25 – Total and orbital-resolved DOS at $\lambda/t = 0.8$ for two temperatures below and one above $T_\mathrm{N}/t = 0.15$ also used for the spectra in figure 5.24.

In comparison to $T/t = 0.14$ and $T/t = 0.35$ the orbital-resolved DOS at the temperature $T/t = 0.22$ closest to, but below $T_{\mathrm{C}2}/t$ shows no prominent features or significant differences. All orbitals contribute above and below the gap which itself is rather symmetric.

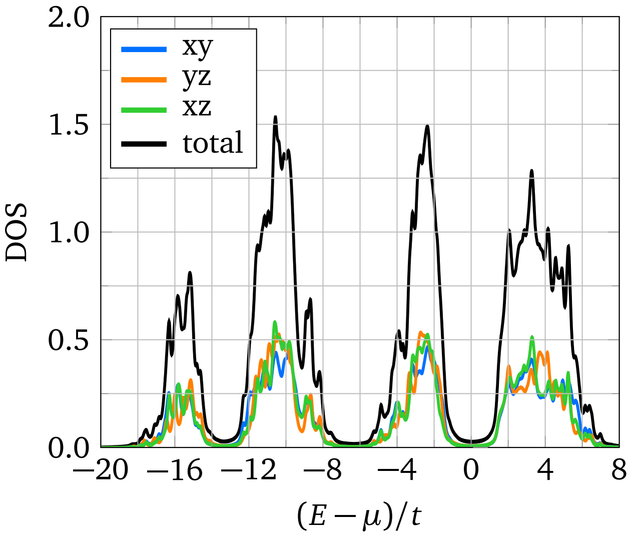

5.26 – Total and orbital-resolved DOS at $\lambda/t = 1$ for $T/t = 0.22$ which is closest to, but below the second peak of the specific heat in figure 5.19c.

Coming back to static observables, the orbital occupations as function of the temperature are shown in figure 5.27. Below the Néel temperature, the xy-orbital is less occupied than the (almost) equally occupied yz- and xz-orbital. Above T_N, all three orbitals are (almost) equally occupied. Upon closer inspection, crossings between the different orbital occupations occur at T_N and T_C2. For $\lambda/t = 0.6$, the xy- and xz-orbital neither cross nor touch, while the yz-orbital crosses the xy-orbital close to T_N. At $\lambda/t = 0.8$, the xy- and xz-orbital touch at T_N, while for $\lambda/t = 1$, both orbitals cross at T_N and T_C2.

Differences between the yz- and xz-orbital occpations are due to magnetic symmetry breaking below T_N and due to the cluster geometry. Hence crossings between one of these orbitals with the xy-orbital is considered to hold for both and may be signatures of the characteristic temperatures T_N and T_C2.

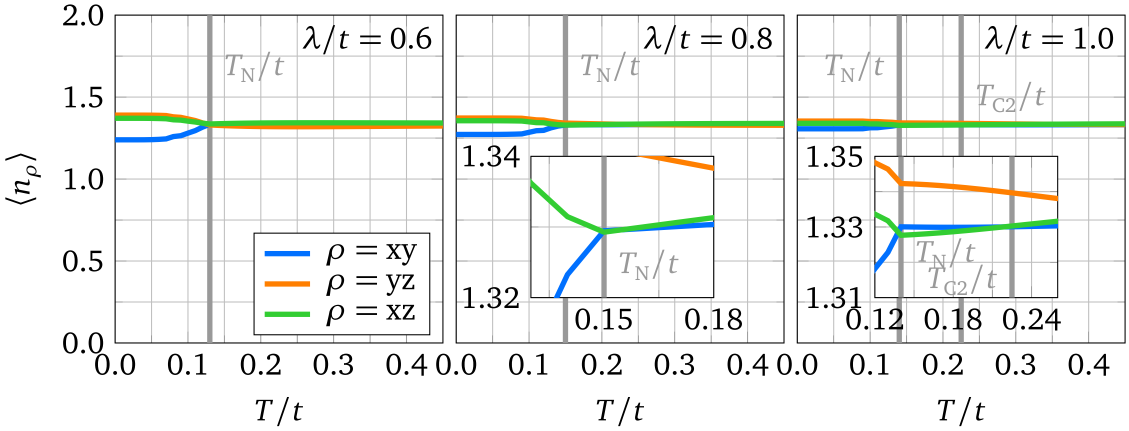

5.27 – Occupations (electron perspective) as a function of temperature at $\lambda/t \in \{0.6, 0.8, 1\}$.

5.2.3 Dominant tetragonal CF splitting

Now the case of dominant tetragonal CF splitting $\Delta/t = 5$ which separates the xy-orbital from the yz- and xz-orbital and thus orbitally polarises the system is considered. Following again the incentive of zero temperature investigations [Fel19], the interaction parameters under consideration lead to an AFM order with the spin lying in-plane and S_x as relevant spin component to quantify the order.

The free energy as a function of AFM S_x Weiss field h'/t for two values of SOC $\lambda/t \in \{0.1, 0.8\}$ at temperatures $T/t \in \{0.00, 0.01, \dots, T_\mathrm{N}/t\}$ is shown in figure 5.28. In contrast to no CF splitting, the optimal Weiss field first increases with increasing temperature before decreasing at low SOC $\lambda/t = 0.1$. At intermediate SOC $\lambda/t = 0.8$, the optimal Weiss field keeps decreasing with increasing temperature as is the case for all SOCs considered without CF splitting. In agreement with the case of no CF splitting, smaller SOC gives a more stable AFM S_x order in terms of a lower free energy minimum. However, here the influence of SOC is reduced. This can be seen already from the zero temperature phase diagram obtained via VCA [Fel19], where at significant CF splitting a larger SOC is required to reach the PM. While the Néel temperature changes from zero to finite CF splitting, SOC has no significant influence on T_N in both cases.

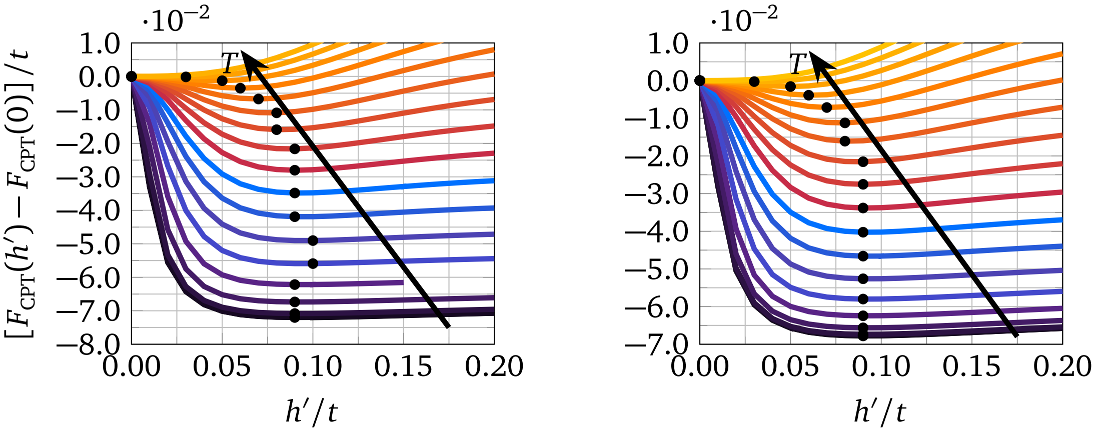

(a) $\lambda/t = 0.1$, $T/t \in [0, 0.17]$.

(b) $\lambda/t = 0.8$, $T/t \in [0, 0.18]$.

5.28 – CPT free energy F_{CPT}/t at the given SOC λ/t as function of the AFM S_x Weiss field amplitudes h'/t for several temperatures $T/t \in \{0.00, 0.01, \ldots, T_N/t\}$.

As for the signature of the AFM S_x phase, the magnetisation shown in figure 5.29a exhibits the same features as at zero CF splitting just with another direction of the ordering moments. The magnetisation's saturation value at low temperature decreases with increasing SOC. Yet the saturation value here is significantly higher than at zero CF splitting and corresponds with close to $m = 2$ to a perfect ordering of spin-one magnetic moments. Furthermore, the temperature range over which the magnetisation amounts to its saturation value ranges only up to a lower temperature $T/t \approx 0.05$ as compared to zero CF splitting.

The Néel temperature and active degree of freedom can also be deduced from the entropy shown in figure 5.29b. While the kink marks the prior, the plateau value $S_1 = \ln(3)$ amounts to the entropy of a single spin-one degree of freedom.

In contrast, the specific heat in figure 5.29c lacks the broad humps for small and intermediate SOCs $\lambda/t \in \{0.6, 0.8\}$ present at zero CF splitting. This could be connected to the orbital polarisation which prevents orbital mixing. The peak close to T_N is associated with AFM fluctuations.

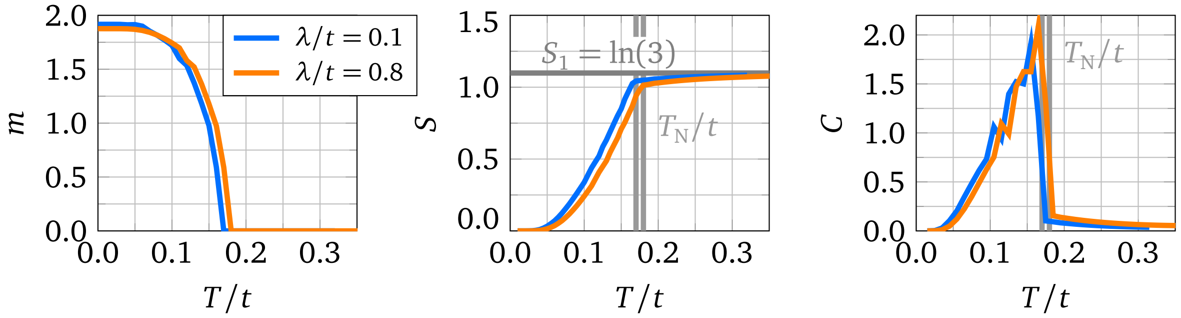

(a) Magnetization.

(b) Entropy.

(c) Specific heat.

5.29 – Magnetization, entropy and specific heat as function of temperature for $\lambda/t \in \{0.1, 0.8\}$.

For low SOC $\lambda/t = 0.1$, the overlaps defined in equation (5.24) and shown in figure 5.30 are separated in the order $\langle J = 2\rangle > \langle J = 1\rangle > \langle J = 0\rangle$ opposite to the order for zero CF splitting at low temperatures. Furthermore in contrast to zero CF splitting, the overlaps change below T_N and remain almost constant above it. Thereby, $\langle J = 0\rangle$ and $\langle J = 2\rangle$ decrease, while $\langle J = 1\rangle$ increases with temperature.

With moderate SOC $\lambda/t = 0.8$, the overlaps change continuously over the entire temperature range considered. No kinks remain from the cases with zero CF splitting and low SOC. Upon increasing SOC, $\langle J = 0\rangle$ is raised, while the other two overlaps are lowered as happens at zero CF splitting. This leads to an intersection between the $\langle J = 0\rangle$ and $\langle J = 1\rangle$ overlap occuring below the Néel temperature.

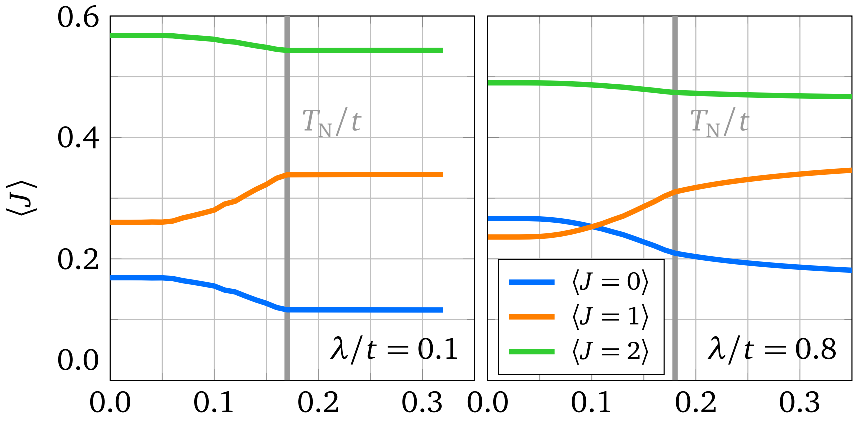

5.30 – Overlaps as functions of temperature at $\lambda/t \in \{0.1, 0.8\}$ considering holes.

The orbital-resolved occupation displayed in figure 5.31 confirms the orbital polarisation. From an electron perspective, the xy-orbital is fully occupied, while the yz- and xz-orbitals are half-filled over the entire temperature range considered.

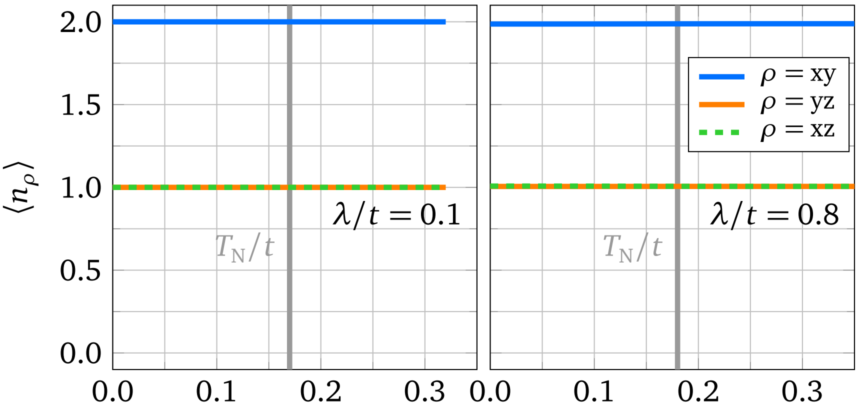

5.31 – Occupations (electron perspective) as a function of temperature at $\lambda/t \in \{0.1, 0.8\}$.

5 2 4 Realistic tetragonal CF splitting

Finally, the case of moderate tetragonal CF splitting $\Delta/t = 1.5$, for which the model lies closer to the compound Ca_2RuO_4 [Fel19], is considered. As for dominant CF splitting, the ordering considered is an AFM order with the spin lying in-plane and S_x as relevant spin component to quantify the order.

Figure 5.32 displays the free energy evaluated as a function of the AFM S_x Weiss field h'/t for four values of SOC $\lambda/t \in \{0, 0.6, 0.8, 1\}$ at various temperatures $T/t \in \{0.00, 0.01, \ldots, T_N/t\}$ and shares the features present at dominant CF splitting discussed in section 5.2.3.

At low SOC, the optimal Weiss field first increases before decreasing, while it keeps decreasing for intermediate and large SOC. Again, smaller SOC gives a more stable AFM order (lower free energy) having less of an impact compared to zero CF splitting but affecting the stability more than at dominant CF splitting. Just as SOC has no significant influence on the Néel temperature, going from dominant to realistic CF splitting does not change T_N either.

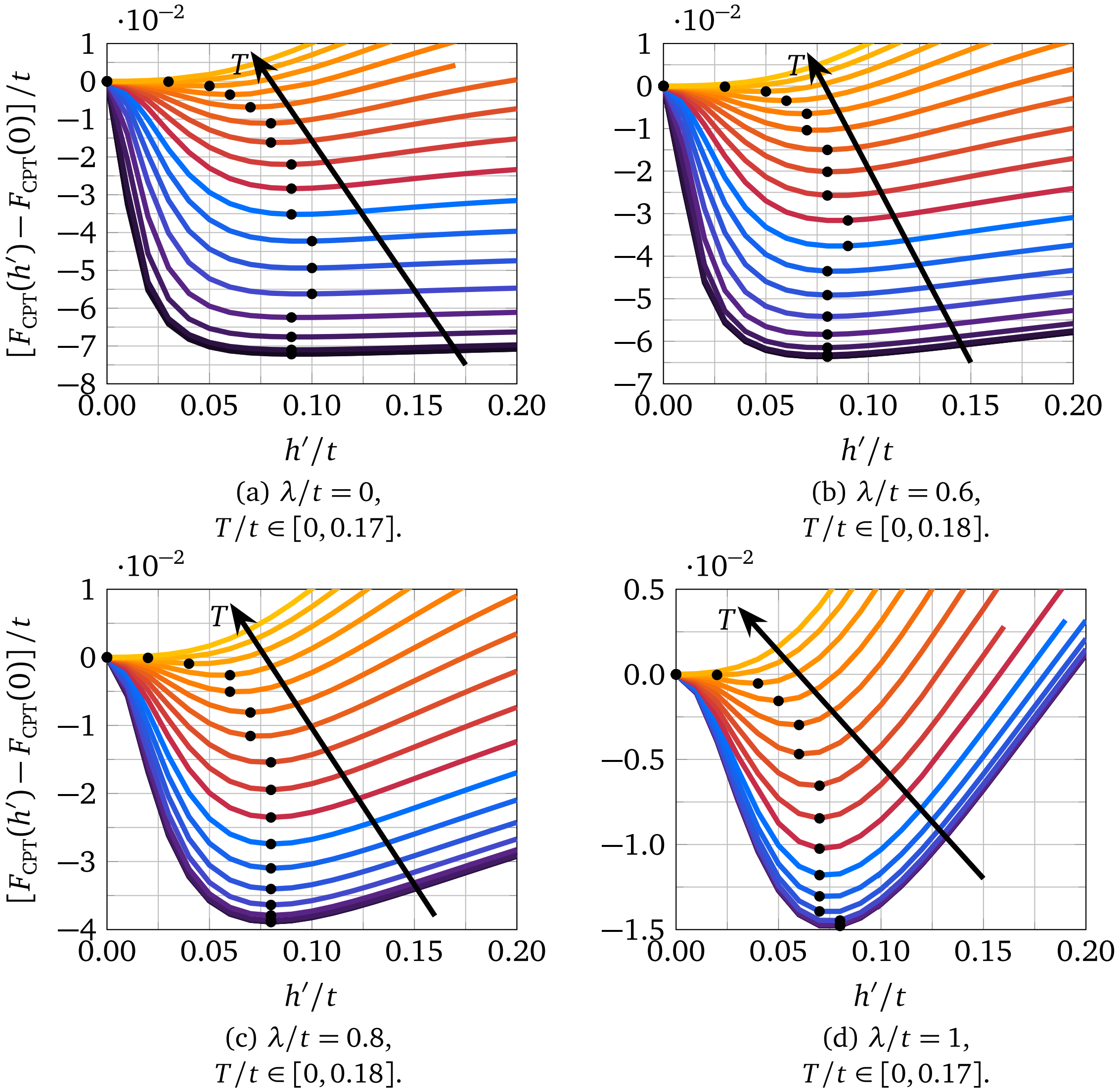

(a) $\lambda/t = 0$, $T/t \in [0, 0.17]$.

(b) $\lambda/t = 0.6$, $T/t \in [0, 0.18]$.

(c) $\lambda/t = 0.8$, $T/t \in [0, 0.18]$.

(d) $\lambda/t = 1$, $T/t \in [0, 0.17]$.

5.32 – CPT free energy F_CPT/t at the given SOC λ/t as function of the AFM S_x Weiss field amplitudes h'/t for several temperatures $T/t \in \{0.00, 0.01, \dots, T_\mathrm{N}/t\}$.

Also the magnetisation visible in figure 5.33a agrees with the trends observed before in section 5.2.3. Its saturation value decreases with increasing SOC, yet it is significantly higher than at zero CF splitting. At zero SOC, the saturation value lies close to $m = 2$ which corresponds to a perfect ordering of spin-one magnetic moments. The temperature range over which the magnetisation assumes its saturation value does not change compared to dominant CF splitting.

Compared to dominant CF splitting, the entropy shown in figure 5.33b exhibits no plateau. However the kink still marks the Néel temperature and the entropy at a given temperature decreases with increasing SOC.

In contrast to zero and dominant CF splitting, the specific heat shown in figure 5.33c exhibits two peaks for all SOCs considered. The first peak slightly below T_N is associated with AFM fluctuations. Its height decreases with increasing SOC. Since all SOCs exhibit a second peak, the peaks dependence on SOC can be inferred. With increasing SOCs $\lambda/t \in \{0, 0.6, 0.8, 1\}$ the peaks temperature $T_{\mathrm{C2}}/t \in \{0.315, 0.335, 0.365, 0.375\}$ increases. This suggests a connection between the second peak and the impact of SOC mixing the orbitals. In turn the lack of broad humps for dominant CF splitting in figure 5.29c would be due to the suppression of orbital mixing.

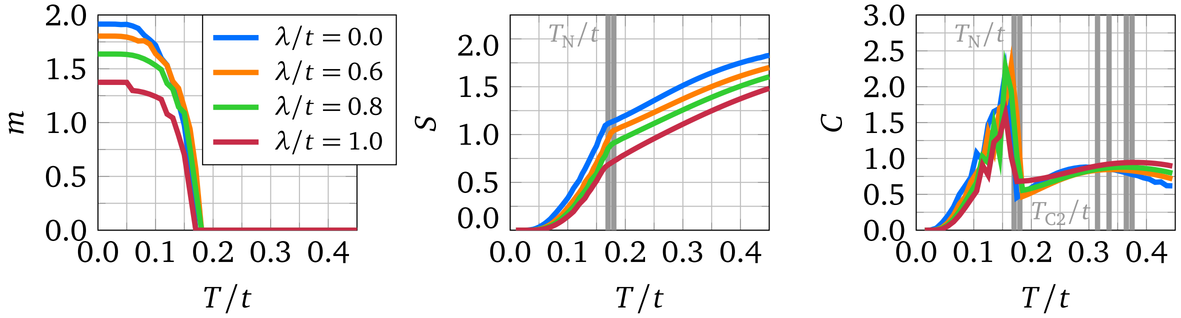

(a) Magnetisation. (b) Entropy. (c) Specific heat.

5.33 – Magnetisation, entropy and specific heat as function of temperature for $\lambda/t \in \{0, 0.6, 0.8, 1\}$.

To obtain a more refined picture of the magnetic and orbital composition, the overlap introduced in equation (5.24) is shown in figure 5.33 as function of temperature.

The case of zero SOC matches that of dominant CF splitting and low SOC. All overlaps are separated in the order $\langle J = 2\rangle > \langle J = 1\rangle > \langle J = 0\rangle$. They change below T_N and remain almost constant above it. $\langle J = 0\rangle$ and $\langle J = 2\rangle$ decrease, while $\langle J = 1\rangle$ increases with temperature.

With finite SOC, the overlaps change continuously over the entire temperature range considered. No kinks remain from the cases with zero CF splitting and zero SOC. The overlaps $\langle J = 1\rangle$ and $\langle J = 2\rangle$ appear to be fixed relative to each other, with an intersection close to $T/t = 0.15$ for $\lambda/t \in \{0.6, 0.8\}$ and $T/t = 0.19$ for $\lambda/t = 1$. There is almost no shift relative to each other. Apart from their absolute position, the overlaps behaviour resembles that visible at zero CF splitting.

With increasing temperature, the overlap $\langle J = 0\rangle$ decreases, while the other two increase leading to multiple intersections between them. Upon increasing SOC, $\langle J = 0\rangle$ is raised, while the other two overlaps are lowered. An increase in the $\langle J = 0\rangle$-contribution with increasing SOC thus survives from zero to finite CF splitting. Intersections between $\langle J = 0\rangle$ and the other overlaps thereby shift to higher temperatures. Hence, a higher temperature is required to mix different J-states into the system.

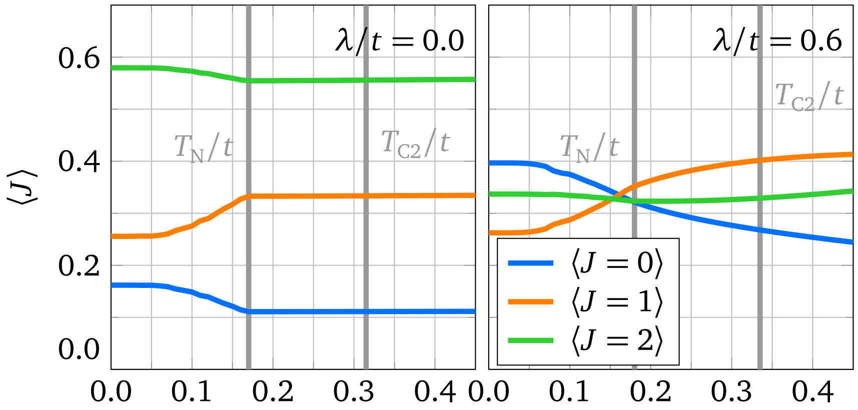

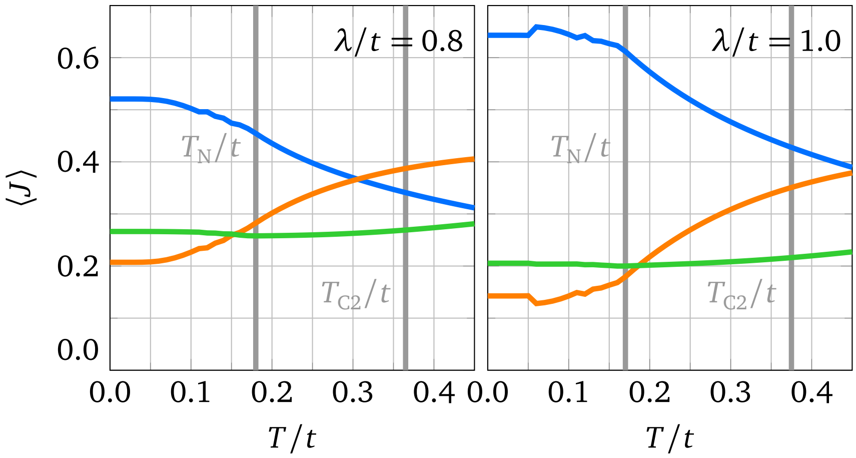

5.33 – Overlaps as functions of temperature at $\lambda/t \in \{0, 0.6, 0.8, 1\}$ considering holes.

Concerning dynamic observables, the rough shape of the DOS shown in figure 5.34 stays the same as for zero CF splitting described in section 5.2.2. Already there, three occupied bands are present and the chemical potential drifts with occasional 'jumps' until the Néel temperature is reached.

However there is a change in the highest occupied band. Compared to zero CF splitting, a peak previously located at the edge of the gap lies now at the center of the band. This peak signals the Néel temperature, since it vanishes at this temperature among the surrounding band. Above T_{N} and for all finite SOCs considered $\lambda/t \in \{0.6, 0.8, 1\}$, small shoulders develop at the upper edge of the gap. At the temperature belonging to the second peak in the specific heat, nothing noteworthy is observed.

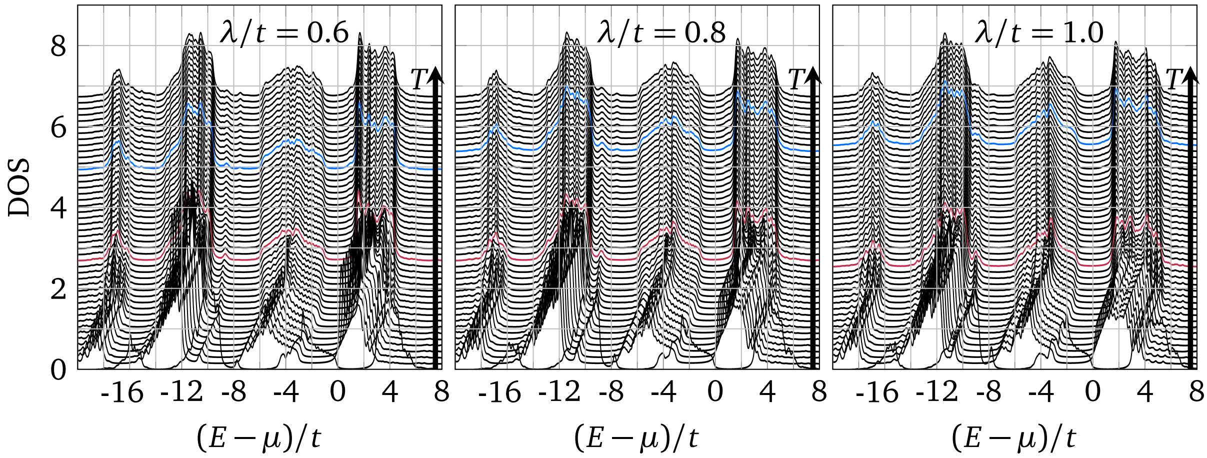

5.34 – Total DOS at $\lambda/t \in \{0.6, 0.8, 1\}$ for different temperatures $T/t \in \{0.00, 0.01, \ldots, 0.45\}$. The red curve highlights the phase transition at T_{N}, while the blue curve refers to the temperature closest to, but below the second peak in the specific heat at T_{C2}.

To infer changes in the DOS below T_{N} besides the drift in the chemical potential, figure 5.35 shows the aligned DOSs. Similar to zero CF splitting, the gap size decreases slightly with increasing temperature below T_{N}. Within the PM phase, the gap size remains almost unchanged, as can be seen in figure 5.34. The height of the peak located at the center of the highest occupied band, which vanishes at the Néel temperature decreases with increasing SOC.

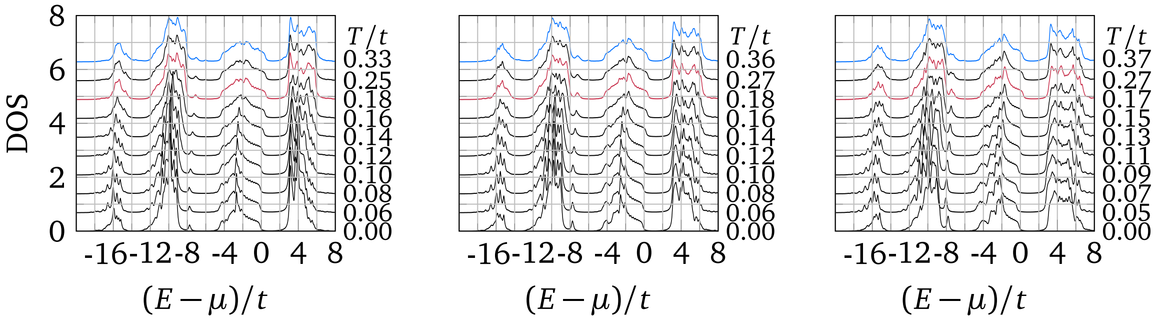

(a) $\lambda/t = 0.6$. (b) $\lambda/t = 0.8$. (c) $\lambda/t = 1$.

5.35 – Total DOS shifted onto the $T/t = 0$ total DOS at $\lambda/t \in \{0.6, 0.8, 1\}$ for several temperatures. The red curve highlights the phase transition at T_N, while the blue curve refers to the temperature closest to, but below the second peak in the specific heat at T_C2.

Going beyond the total DOS, the orbital-resolved spectral function for $\lambda/t = 1$ shown in figure 5.36 provides additional information about the bandstructure of the system. All orbitals exhibit a faint lowest and a well visible middle occupied band. While the xy-orbital dominates the highest occupied band, the yz- and xz-orbitals have a more pronounced unoccupied band.

In comparison to the spectral function at zero CF splitting in figure 5.24, the feature of AFM ordering is still an arc within the unoccupied states centered around $\boldsymbol{k}/\pi = (1, 1)$ which vanishes at T_N. Comparing the spectral function to the tight-binding dispersion in figure 5.23a confirms the arc as signature of AFM order. However besides highlighting in-plane ordering, the arc is most prominent in the yz- and xz-orbitals in contrast to zero CF splitting. The domination of these two orbitals is due to orbital polarisation via CF splitting as can be inferred by comparing figures 5.27 and 5.37. In addition, there are faint traces of the highest occupied band bending upward at $\boldsymbol{k}/\pi = (0, 0)$ for all orbitals. Both features are signatures of an AFM, whose doubled unit cell implies weight at the same energy for $\boldsymbol{k}/\pi = (0, 0)$ and $\boldsymbol{k}/\pi = (1, 1)$.

Besides the arc, the peak at the center of the highest occupied band in the total DOS also vanishes at T_N. Since the highest occupied band is dominated by the xy-orbital, the vanishing peak appears in the spectral function as broadening of the band around $\boldsymbol{k}/\pi = (1, 0)$ and $\boldsymbol{k}/\pi = (1/2, 1/2)$ which mark the boundary of the Brillouin zone due to the doubled unit cell.

Just as for zero CF splitting, there is no real bending of the dispersion of unoccupied states as compared to the one-band Hubbard model [SSY18]. There is only a loss of upward bending weight in the yz-orbital at the point $\boldsymbol{k}/\pi = (0, 0)$, while downwards bending weight remains. Whether this behaviour can be interpreted in the limits of the one-band Hubbard model [SSY18] or requires investigation of the respective limits of the three-band Hubbard model is an open question.

Similar to the case without CF splitting, the dimensionality of the dispersion for several orbitals changes with temperature. As a reference, one- and two-dimensional dispersions are illustrated in figure 5.23b. Focussing first on the unoccupied band, at zero temperature the dominating features resemble a two-dimensional dispersion relation for all orbitals. With increasing temperature, the xy-orbital stays two-dimensional, while the yz- and xz-orbitals turn one-dimensional and become more incoherent, i.e. diffusive. The yz-orbital propagates in y- and the xz-orbital in x-direction. Since these coincide with the dispersion relations of the orbitals within the Hamiltonian without SOC, the influence of SOC to couple the orbitals appears to be reduced with increasing temperature.

Concerning the occupied states, the highest occupied band of the xy-orbital keeps its two-dimensional dispersion upon increasing temperature. The occupied yz- and xz-orbitals, in turn become more coherent, i.e. sharper, when going from zero to finite temperature and thereby unveil a rather one-dimensional dispersion. This unconventional behaviour can be related to a study focussing on these states. It shows that AFM order in a strong-coupling t-J-like model without SOC induces ladder-like spectral features [Kło+20]. The loss of magnetic order thus lets the underlying dispersion be seen more easily. Since the occupied bands of the yz- and xz-orbitals exhibit a rather one-dimensional dispersion at higher temperature, SOC appears to be less effective for higher binding energies. This is in agreement with results on metallic Sr_2RuO_4 [Kim+18], where SOC is not needed to explain features of the spectral function further away from the chemical potential.

Spectra employing the other SOCs $\lambda/t \in \{0.6, 0.8\}$ considered exhibit similar features and are omitted here.

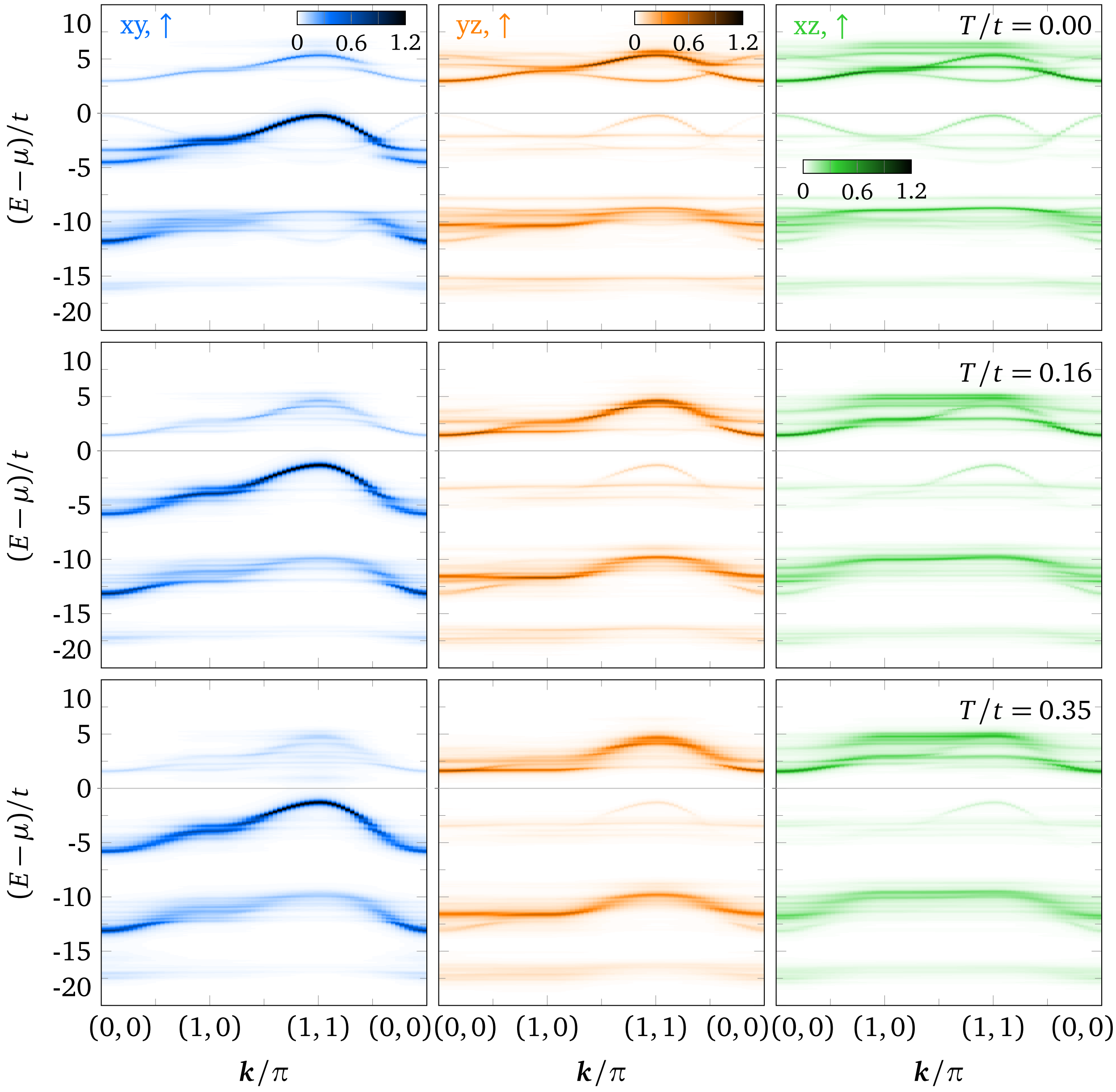

5.36 – Orbital-resolved spectral function considering electrons at $\lambda/t = 1$ for one temperature below, one at and one above $T_N/t = 0.14$.

To get an overview of how the orbital-resolved bands change compared to zero CF splitting, figure 5.37 shows the total and orbital-resolved DOS at the temperatures used for the spectra in figure 5.36. Compared to zero CF splitting, the roles of the xy-orbital on one side and the yz- and xz-orbital on the other side have switched. The band below the chemical potential is almost entirely characterised by the xy-orbital, while the band above the chemical potential is determined by the yz- and xz-orbital. In contrast to zero CF splitting, this orbital polarisation remains intact with increasing temperature. Since CF splitting determines the spectrum and temperature affects the weights of states, the latter cannot compensate for contributions of states dominated by the yz- and xz-orbital being shifted to higher energies by the former.

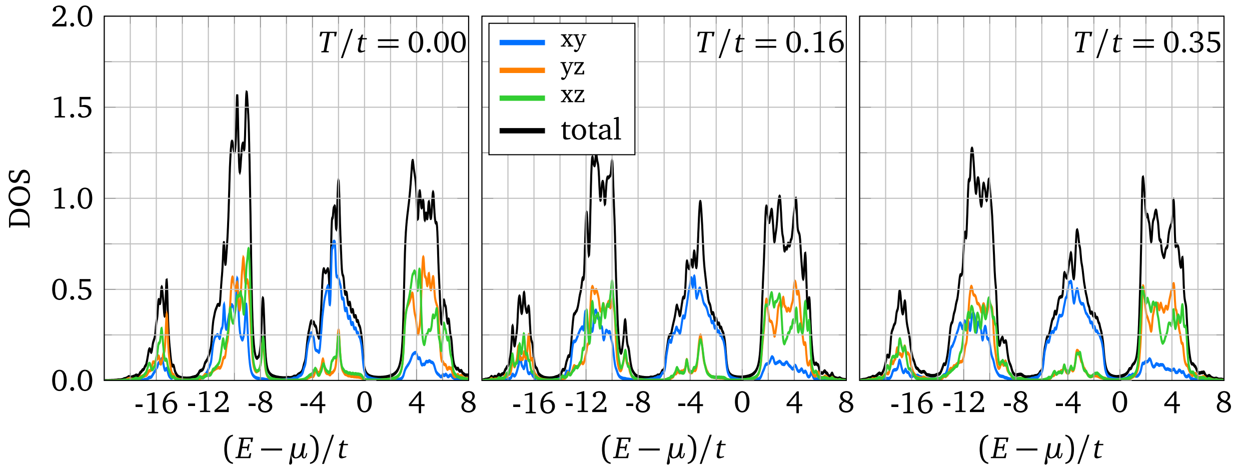

5.37 – Total and orbital-resolved DOS at $\lambda/t = 1$ for one temperature below, one at and one above $T_\mathrm{N}/t = 0.14$ also used for the spectra in figure 5.36.

Since changes in the orbital occupation of Ca_2RuO_4 with temperature [Miz+01] is one of the observations that sparked interest in the compound, figure 5.37 shows this change of the electron filling with temperature for various SOCs considered. Due to CF splitting, the xy-orbital is almost full, while the yz- and xz-orbital are almost half-filled. Differences between occupation of the yz- and xz-orbitals below T_N are due to the magnetic symmetry breaking. Above the Néel temperature, the xy-occupation is reduced, while the yz- and xz-orbital are filled upon increasing the temperature. A crossing does not occur within the temperature range considered. The overall change in occupation is reduced with increasing SOC. This change also occurs for zero SOC, where holes induced in the xy-orbital at temperatures above T_N correspond to the orbital fluctuations forming the second peak in the specific heat.

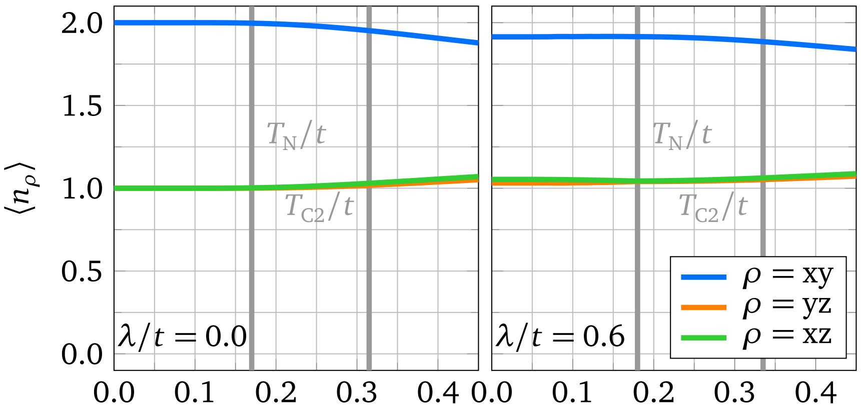

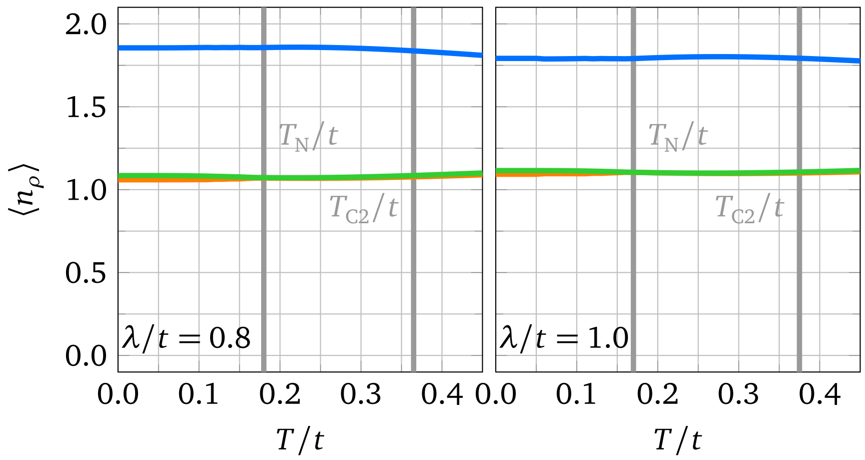

5.37 – Occupations (electron perspective) as a function of temperature at $\lambda/t \in \{0, 0.6, 0.8, 1\}$.

5 2 5 1 site cluster

In order to assess how the features related to orbital mixing change with cluster size, a 1 site cluster is considered. Such a cluster also serves to infer how local in nature the orbital mixing is. Note, that a 1 site cluster is not sufficient as a unit cell for AFM order which will thus not be considered here. Throughout this section, different CF splittings $\Delta/t = \{0, 1.5, 5\}$ will be considered, while SOC is fixed to $\lambda/t = 0.8$.

Considering the entropy shown in figure 5.38a, it exhibits qualitatively similar features as the 2×1 site cluster. The kink which previously marked the Néel temperature is smoothened out. However increasing CF splitting still reduces the high-temperature value of the entropy and leads to a plateau for dominant CF splitting $\Delta/t = 5$ at $S_1 = \ln(3)$ marking a spin-one degree of freedom.

For the specific heat displayed in figure 5.38b, also qualitatively similar trends as for the 2×1 site cluster can be inferred. While zero and dominant CF splittings exhibit one distinct peak, moderate CF splitting $\Delta/t = 1.5$ shows two. However while the peak for $\Delta/t = 0$ decays slowly with increasing temperature, it decays fast for dominant CF splitting. The low temperature peak, which is likely related to AFM spin fluctuations shifts with increasing CF splitting to lower temperature.

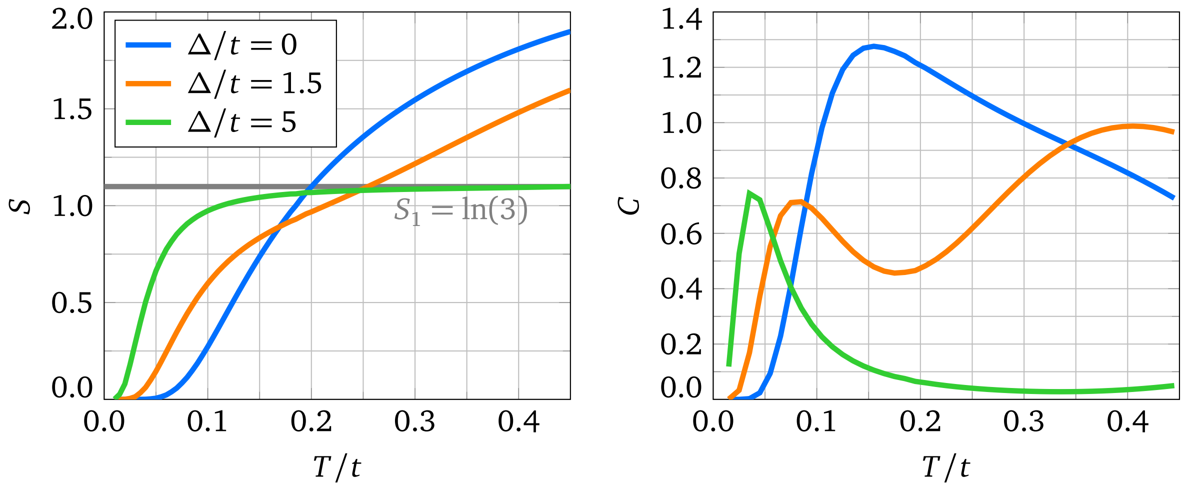

(a) Entropy. (b) Specific heat.

5.38 – Entropy and specific heat as function of temperature for $\Delta/t \in \{0, 1.5, 5\}$ and $\lambda/t = 0.8$.

Also the overlaps defined in equation (5.24) and shown in figure 5.39 agree qualitatively with those of the larger cluster. Specifically the sequence of states and the temperatures where they cross match. While the weight of the $J = 2$ state increases and decreases with temperature at zero and dominant CF splitting, it remains almost unchanged for moderate $\Delta/t = 1.5$. For all CF splittings, the $J = 1$ state gains weight, mostly at the expense of the $J = 0$ state.

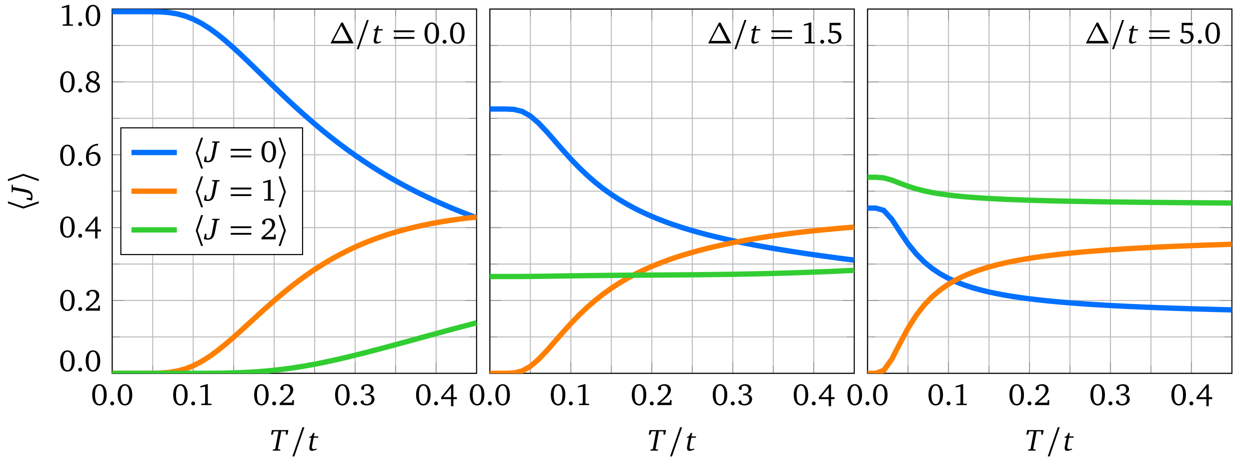

5.39 – Overlaps as functions of temperature at $\Delta/t \in \{0, 1.5, 5\}$ and $\lambda/t = 0.8$ considering holes.

Without magnetic order present, the orbital occupation at zero CF splitting shown in figure 5.40 is unpolarized throughout the entire temperature range. In contrast for dominant CF splitting $\Delta/t = 5$, the system is fully orbitally polarised over the entire temperature range, unchanged as compared to when magnetic order is present. For moderate $\Delta/t = 1.5$, the system is orbitally polarised as well, with the orbital occupation changing only marginally and non-monotonously with increasing temperature.

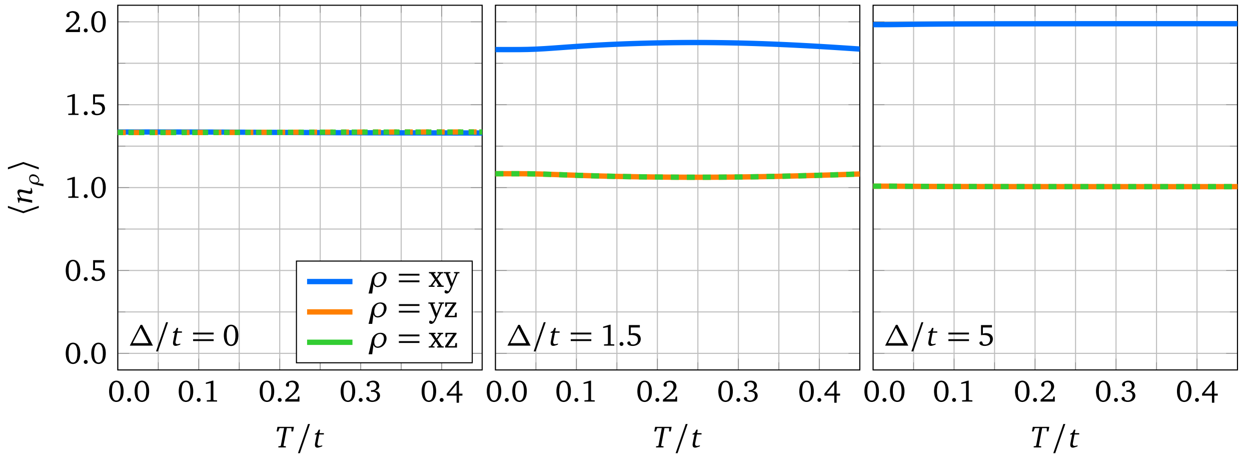

5.40 – Occupations (electron perspective) as a function of temperature at $\Delta/t \in \{0, 1.5, 5\}$ and $\lambda/t = 0.8$.

Considering the spectral function shown in figure 5.36, signatures of the AFM order are missing, since only the PM phase is investigated. The transition from a two-dimensional dispersion at low temperature to a one-dimensional dispersion at high temperature is still present and can best be seen from weights of the unoccupied yz- and xz-orbitals.

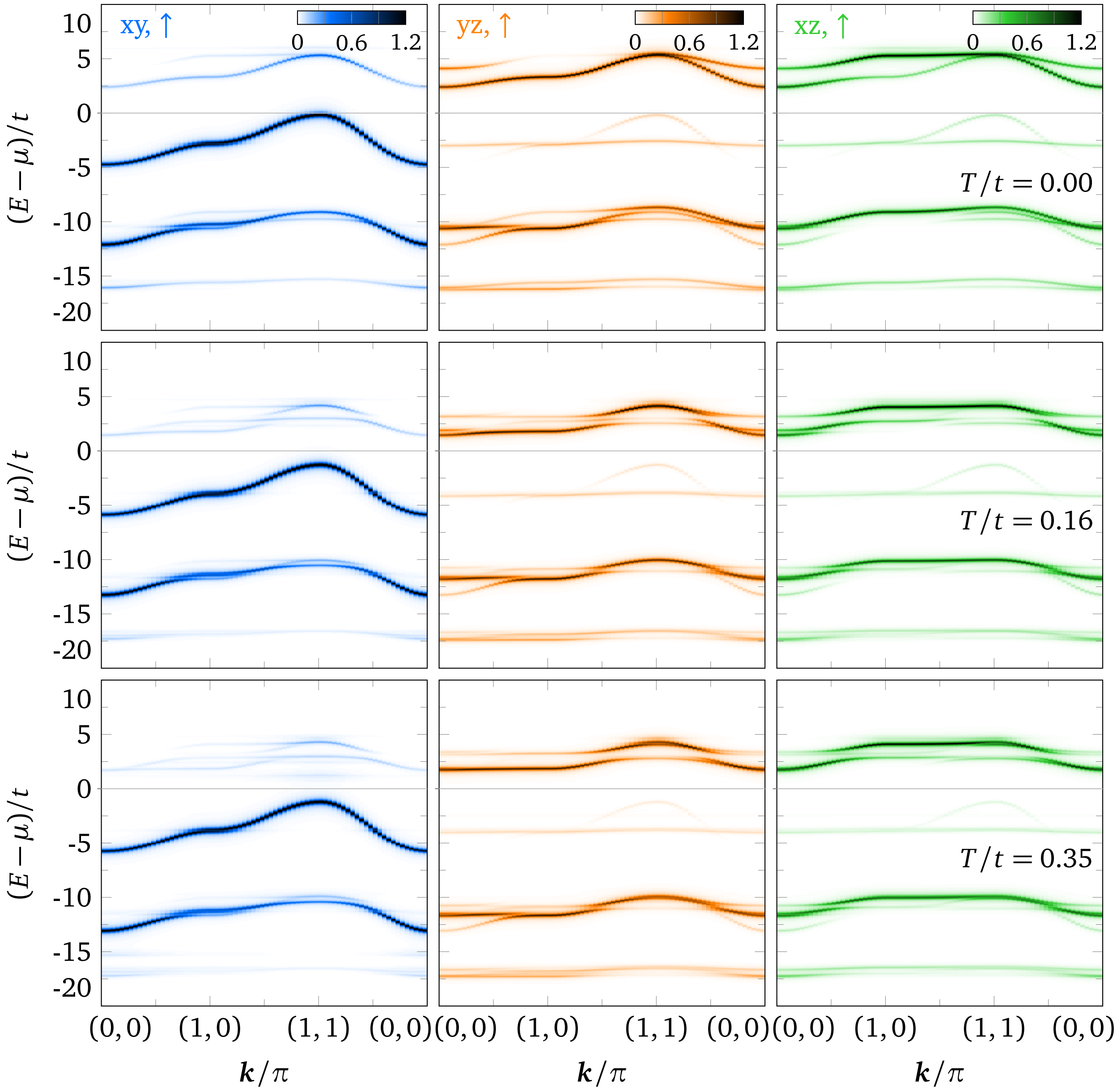

5.41 – Orbital-resolved spectral function considering electrons at $\Delta/t = 1.5$ and $\lambda/t = 0.8$ for the same temperatures as in figure 5.36.

Since the behaviour of all observables presented here agree qualitatively with those of the larger 2 × 1 site cluster, orbital mixing is local in nature and thus not significantly affected by the finite cluster size.

5.2.6 Conclusion and Outlook

First, the implications of SOC and tetragonal CF splitting for the magnetic order and its signatures in dynamic observables, both at finite temperature, are summarised.

Increasing SOC $\lambda/t = 0.6 \rightarrow 1$ destabilizes the magnetically ordered phase at low temperature for zero, realistic and dominant CF splittings $\Delta/t \in \{0, 1.5, 5\}$ as expected from the atomic limit [Fel19]. Signatures of this are shallower free energy minima, a reduced saturation value of the magnetisation at low temperature, a peak in the specific heat associated with AFM fluctuations whose height decreases with increasing SOC and the overlap with the non-magnetic $|J = 0\rangle$-state increasing with SOC. However the Néel temperature does not seem to be affected when increasing SOC. This might be a finite-size effect or due to the systems proximity to a stripy magnetic phase at low SOC [Fel19]. From zero to realistic CF splitting $\Delta/t = 1.5$, the Néel temperature increases but does not alter any further when going to dominant CF splitting $\Delta/t = 5$.

Features of the AFM order in the total DOS are a peak located at the upper edge of the highest occupied band at zero CF splitting and at the center of this band at realistic CF splitting $\Delta/t = 1.5$ which vanishes at the Néel temperature. Considering the orbital-resolved DOS, at zero CF splitting, this peak is formed by the yz- and xz-orbital while at realistic CF splitting $\Delta/t = 1.5$ the xy-orbital dominates.

In the spectral function, magnetism shows up as an arc in the unoccupied states implying a doubled unit cell which vanishes upon reaching the Néel temperature. At zero CF splitting, it occurs within all orbitals, most noticeable in the xy-orbital, at $\boldsymbol{k}/\pi = (1, 1)$. Due to the orbital polarisation at realistic CF splitting $\Delta/t = 1.5$, the arc appears in the yz- and xz-orbital at $\boldsymbol{k}/\pi = (1, 1)$.

Next, orbital-selective features observed in the spectral function, specific heat, overlap and orbital occupation are surveyed.

At low temperatures, all orbitals exhibit a two-dimensional dispersion despite the yz- and xz-orbital being restricted to one-dimensional motion by their bare dispersion relations. Increasing temperature makes the dispersion of the unoccupied yz- and xz-orbital more one-dimensional. Thus SOC becomes less effective with increasing temperature in mixing the yz- and xz-orbitals.

For zero CF splitting and high SOC $\lambda/t = 1$, a second peak appears in the specific heat. In case of a realistic CF splitting $\Delta/t = 1.5$, it is present for all SOCs considered $\lambda/t \in \{0, 0.6, 0.8, 1\}$ and shifts with increasing SOC to higher temperature. At dominant CF splitting $\Delta/t = 5$, such a second peak is suppressed. This suppression is associated with the polarisation of the orbital occupation visible at realistic CF splitting in the orbital-resolved DOS with the highest occupied band being of xy-character, while the lowest unoccupied band is of yz- and xz-character. Hence the presence of such a peak in the specific heat hints at orbital fluctuations.

The overlaps with local LS-coupled states $\langle J\rangle$ providing information on the magnetic and orbital composition change strongly with temperature leading at finite SOC and CF splitting to crossings. These changes suggest the presence of orbital fluctuations. At zero CF splitting and finite SOC $\lambda/t \in \{0.6, 0.8, 1\}$, the overlaps start to change significantly with temperature above the Néel temperature, while at realistic CF splitting $\Delta/t = 1.5$ and zero SOC, the overlaps vary for temperatures below T_N. In case both CF splitting and SOC are somewhat larger than zero, the overlaps change over the entire temperature range. Comparing different parameter sets, overlaps at zero SOC and realistic CF splitting resemble those at dominant CF splitting orbitally polarising the system. However at realistic CF splitting and finite SOC, they lie closer to the unpolarised case of zero CF splitting.

Also the orbital-resolved occupations $\langle n_\rho\rangle$ change comparably strong with temperature, albeit without crossings. Again, this hints at orbital fluctuations being present. Its behaviour is somewhat in contrast with the overlaps. At zero CF splitting, the occupations change mostly below the Néel temperature while above T_N the orbitals are more or less equally occupied. For realistic CF splitting $\Delta/t = 1.5$, the occupations stay almost constant below the Néel temperature and start to change once the temperature increases beyond it. The latter behaviour is associated with the second peak in the specific heat. At dominant CF splitting $\Delta/t = 5$, the orbital occupations remain the same over the entire temperature range considered, just as the second peak in the specific heat is suppressed.

Without a real orbital order possible as it is denied by the findings of Porter et al. [Por+18], a complex phase relation in the (yz, xz)-subspace remains as explanation for the orbital fluctuations observed here. These phase fluctuations can be understood in the following manner: In order to realise the $|J = 0\rangle$-state preferred by SOC at low temperatures, each spin projection has to have a specific phase relation between the orbital components. In contrast at higher temperature, no definite phase relations can be expected, since SOC does not suffice to enforce mostly non-magnetic contributions. Since the signatures of these orbital fluctuations are also found for a 1 site cluster, they are expected to be local in nature.

Once sufficiently high temperatures are reached, eigenstates from other particle number sectors become relevant besides those of the ground state sector. In an attempt to reach higher temperatures and to detect the metal-insulator transition expected, a CDIA study was initiated. The reference system consists of a 1-site cluster described by the three-band Hubbard model with realistic CF splitting $\Delta/t = 1.5$ connected to an uncorrelated bath site with three bands as well. In practice, this is achieved by considering the site type (correlated, bath) as a new quantum number.

While the magnetic order can no longer be captured with such a cluster, three additional variational parameters enter the problem. Due to the realistic CF splitting $\Delta/t = 1.5$, two bath chemical potentials μ_xy and $\mu_\mathrm{yz,xz}$ for the xy- and (yz, xz)-orbital are considered as well as the hybridisation between cluster and bath. However the investigation is stuck at the determination of the bath chemical potentials. Starting from a half-filled reference system with six particles on two sites with three orbitals and two spin-orientations and requiring the correlated cluster site to be occupied by two particles leaves two scenarios for the bath occupation. Either the xy-orbital is full and the yz- and xz-orbital together are half-filled or the xy-orbital is empty and the remaining two orbitals are full. However up to now for both scenarios no reliable optimas were found to which the system could be fixed when raising the temperature.

6 Kondo lattice model

Motivated by a zero temperature study [Len16], the half-filled Kondo lattice model is investigated with finite temperature VCA. Considering the AFM magnetisation, the AFM and PM specific heat as well as the on-site spin-spin correlator allows constructing a phase diagram. The characteristic temperatures lead to three phases: an AFM, a PM of Kondo singlets and a thermal PM. Looking at the DOS and the spectral function provides information on the fate of the Kondo singlets with increasing temperature as well as their signatures compared to the thermal PM.

Physically, the Kondo lattice model (KLM)

$$H = -t \sum_{\langle i,j\rangle,\sigma} c^{\dagger}_{i\sigma} c_{j\sigma} + J \sum_{i} \boldsymbol{S}_i \cdot \boldsymbol{s}_i \tag{6.1}$$

with hopping conduction electrons created by $c^{\dagger}_{i\sigma}$ at site i with spin σ and localised spins $\boldsymbol{S}_i$ coupled to conduction electron spins $[\boldsymbol{s}_i]^{\alpha} = \sum_{s,s'} c^{\dagger}_{is}[\boldsymbol{\sigma}_{s,s'}]^{\alpha} c_{is'}$ describes a regular lattice of magnetic impurities [Col15]. In practice, it can be used to model heavy fermion systems and Kondo insulators. Compared to normal metals, heavy fermion metals exhibit a strongly increased effective mass. This is encapsulated in the model via the singlet formation induced by the Kondo coupling J. Kondo insulators emerge in the limit of dominant J and are paramagnets formed by Kondo singlets at each site.

As the name implies, the KLM is the lattice version of the Kondo model which was used to describe the increase in resistivity as the temperature is lowered once magnetic impurities are present in a metal. The scattering associated with this increase induces Friedel oscillations in the spin DOS which extend over some range around the impurity. Within a regular lattice of magnetic impurities, these Friedel oscillations lead to an interaction between localised spins called RKKY interaction named after Ruderman, Kittel, Kasuya and Yosida. Typically, it gives rise to an AFM ordering of the localised moments with the Néel temperature $T_{\mathrm{N}} \sim J^2\rho(E_{\mathrm{F}})$ and $\rho(E_{\mathrm{F}})$ as the DOS at the Fermi energy.

Upon increasing the Kondo coupling, the AFM order induced by the RRKY interaction starts to compete with the singlet formation between the localised and the conduction electron spins leading to a PM. An interaction induced phase transition at zero temperature denoted as ‘quantum phase transition’ occurs at a critical coupling strength.

While the AFM phase is characterised by the RKKY interaction and separated from the thermal PM at the Néel temperature, the PM of local Kondo singlets (KS) is also distinct from the thermal PM. The temperature describing the crossover between resonant and coherent elastic scattering of conduction electron spins via singlet formation and free spins is called Kondo temperature $T_{\mathrm{K}} = D\exp\{-1/[J\rho(E_{\mathrm{F}})]\}$ with D being half the bandwidth of the Hamiltonian as defined in [Col15]. It emerges within the ‘Poor man’s’ scaling treatment of the Kondo model as the energy scale, where coming from higher temperature the dimensionless coupling constant $g = J\rho(E_{\mathrm{F}})$ diverges which is associated with singlet formation. Within a generalised variant of the KLM, it determines the gap size stabilising the singlet.

In theory, the presence of a singlet on a lattice site i can be inferred from the spin-spin correlator

$$\langle \boldsymbol{S}_i \cdot \boldsymbol{s}_i \rangle = \frac{1}{2}[\langle (\boldsymbol{S}_i + \boldsymbol{s}_i)^2 \rangle - \langle \boldsymbol{S}_i^2 \rangle - \langle \boldsymbol{s}_i^2 \rangle]. \tag{6.2}$$

For pure spin states present at low temperature, the expectation values of the separate spins amount to $\langle \boldsymbol{S}_i^2 \rangle = S(S+1)$ and $\langle \boldsymbol{s}_i^2 \rangle = s(s+1)$ with quantum numbers S and s. At elevated temperature, mixed states $\varrho = \exp(-\beta H)/\Xi$ have to be considered. Upon considering a KS, the total spin amounts to zero, giving $\langle (\boldsymbol{S}_i + \boldsymbol{s}_i)^2 \rangle = 0$. For localised and conduction electron spins 1/2, this leads to the following limiting cases:

- KS, small T/t: $\langle \boldsymbol{S}_i \cdot \boldsymbol{s}_i \rangle = -3/4$
- KS, large T/t: $\langle \boldsymbol{S}_i \cdot \boldsymbol{s}_i \rangle = -3/8$ ($\varrho \rightarrow 1/2$)
- PM, large T/t: $\langle \boldsymbol{S}_i \cdot \boldsymbol{s}_i \rangle = 0$

With the DOS being the $\boldsymbol{k}$-integrated single-particle spectral function, it measures the energetics of single-particle excitations. In the KLM, each site has the possibility to host a Kondo singlet. Upon adding one particle to or removing one particle from the system of conduction electrons, a Kondo singlet can be destroyed. The localised spin can neither couple to a missing electron nor to a non-magnetic singlet of conduction electrons. Hence peaks in the DOS of conduction electrons at energy $(E-\mu)/t \approx 3J/4$ are signatures of KSs as well.

In case of a metallic system, another way to assess the presence of KSs is the Fermi surface. Invoking the Luttinger sum rule, the volume of the Fermi surface counts the number of fermions forming the Fermi liquid. This implies, that at low Kondo coupling without KSs only conduction electrons are counted, while at larger J with KSs also the localised spins contribute to the number of electrons as they now belong to the heavy Fermi liquid. The Fermi surface is thus increased in the latter case.

The present investigation of the KLM is motivated by the one by Lenz [Len16] employing zero temperature VCA using mostly a 3×2 site cluster as reference system. In the following, his results for a half-filled system are summarised with a focus on the observables he investigated and their implications.

Lenz considered the PM and AFM phase in the half-filled and doped case as well as the possibility of s- and d-wave superconductivity. The main observables for the half-filled case are the magnetisation, the spin-spin correlator $\sum_i \langle \boldsymbol{S}_i \cdot \boldsymbol{s}_i \rangle$, the DOS and the spectral function. Considering sufficient doping to reach a metal, the emerging Fermi surface becomes available and the size of the quasiparticle gap can be assessed. Technically, the PM phase is realised by optimising the grand potential w.r.t. the on-cluster hopping, while for the AFM phase an AFM Weiss field is added to the set of variational parameters.

Quantitative observations in the half-filled case include comparisons with QMC results. The finite-size scaled quasiparticle gap in the PM phase for reasonable Kondo coupling and the finite-size scaled critical Kondo coupling where the AFM transitions into a PM lie within the error bars of the QMC treatment. On the qualitative side, a kink occuring in the spin-spin correlator $\sum_i \langle \boldsymbol{S}_i \cdot \boldsymbol{s}_i \rangle$ at the critical Kondo coupling provides other means to distinguish the AFM and PM phase. However the main question is whether the KSs present in the PM phase break up at the critical Kondo coupling or if this Kondo breakdown occurs at lower couplings. The prior case is dubbed unconventional quantum critical point (QCP), while the latter is a conventional QCP. Considering the spin-spin correlator $\sum_i \langle \boldsymbol{S}_i \cdot \boldsymbol{s}_i \rangle$ and trying to identify which peaks in the DOS describe the destruction of KSs leads to the conclusion of a conventional QCP. In case of a doped system, a change in the Fermi surface within the AFM phase may indicate the Kondo coupling where all KSs are destroyed, however this cannot be confirmed. Hence the question remains at which Kondo coupling the Kondo breakdown occurs.

More details on the doped system and superconductivity therein can be found in [Len16].

As for the finite temperature behaviour, Zerec et al. [ZST06] investigated the KLM in its PM phase on an $\sqrt{8} \times \sqrt{8}$ site cluster with open and periodic boundary conditions employing the FTLM. The observables considered comprise the specific heat, the on-site spin-spin correlator of the localised and conduction electrons spin $\langle \boldsymbol{S}_i \cdot \boldsymbol{s}_i \rangle$, the inter-site spin-spin correlators of the localised spins $\langle \boldsymbol{S}_i \cdot \boldsymbol{S}_j \rangle$, the magnetic susceptibility as well as the total local magnetic moments $\langle (\boldsymbol{S}_i + \boldsymbol{s}_i)^2 \rangle$. Here, the correlators and the local moment are measured only for one site/between sites in the center of the cluster.

Characteristic temperatures obtained from these observables are the peak temperatures of the specific heat and susceptibility, as well as the temperatures belonging to the inflection point of the on- and inter-site spin-spin correlators normalised w.r.t. their zero temperature values. Within the phase diagram these characteristic temperatures of different quantities show up as one characteristic temperature of the system. This characteristic temperature scales at low Kondo coupling as $(J/t)^2$ associated with the RKKY interaction and at high coupling as J/t connected to the formation of on-site KSs.

Further details on the scaling behaviour of on- and inter-site spin-spin correlators as well as the implications of open and periodic boundary conditions can be inferred from [ZST06].

A follow-up investigation by the same group [Sia+12] of the correlated KLM, which extends the tight-binding part of the conduction electrons to the Hubbard model, asked about the influence of correlations on the Kondo temperature scale. It turned out to scale linearly as U/t at small correlations until it reaches a plateau at high enough temperature coinciding with the highest excitation enegies present in the system. Also interesting is the cooperation and competition of correlations with the formation of KSs and the RKKY interaction. Increasing U/t promotes the localisation of conduction electrons simplifying the formation of KSs. Small correlations support the RKKY interaction and enhance the inter-site correlator of localised spins. Larger correlations inducing a superexchange interaction however counteract the RKKY interaction and lead to a reduction of the inter-site correlators.

Motivated by the zero temperature results obtained using the VCA and at finite temperature with the FTLM, here the half-filled KLM is investigated employing the finite temperature VCA. Initially, several results of the zero temperature VCA treatment are reproduced to establish the correctness of the model implementation. Then, the Néel temperature of the magnetisation, as well as the characteristic temperature scales of the PM and AFM specific heat and the temperature scale of the on-site spin-spin correlator are extracted. The kink observed at zero temperature at $J/t \approx 2.05$ of the on-site spin-spin correlator is quantified via its derivative and shown as a function of temperature. These energy scales are summarised in a phase diagram. Afterwards, the fate of KSs with increasing temperature is considered by observing the DOS and the spectral function. Lastly, the filling of a PM system as a function of the chemical potential is considered to show the attempt to investigate a doped system with a Fermi surface.

6.1 Hamiltonian, observables and orders

In practice, the Kondo Hamiltonian of equation (6.1) is implemented as a spinfull two orbital model. The requirement for one localised spin on each lattice site is realised explicitely by restricting the state space of the reference cluster. When constructing the cluster Green's function, the contribution by the orbital resembling the localised spins is omitted.

An observable specific to the KLM is the on-site spin-spin correlator. Following the definition of the grand potential and expectation values at finite temperature, it is obtained as derivative

$$\sum_i \langle \boldsymbol{S}_i \cdot \boldsymbol{s}_i \rangle = \frac{\partial \Omega}{\partial J} \tag{6.3}$$

and abbreviated in the following as $\langle \boldsymbol{S} \cdot \boldsymbol{s} \rangle$.

The PM order is realised by optimising the grand potential w.r.t. the (isotropic) on-cluster hopping. In case of the AFM order, the Weiss field

$$H = h' \sum_j \Lambda_j \exp(\mathrm{i}\boldsymbol{q} \cdot \boldsymbol{j}), \tag{6.4}$$

with one-body operator $\Lambda_j = (n_{j\uparrow} - n_{j\downarrow})$ and ordering wavevector $\boldsymbol{q} = (\pi, \pi)$ is considered in addition to the on-cluster hopping.

Technically, for finite temperature all computations are performed with $N_{\mathrm{ex}} = 120$ exact and $R = 60$ random trace vectors. While the exact trace vectors are obtained by performing a maximum of 1200 Band Lanczos iterations allowing $N_{\mathrm{deg}} = 8$ starting vectors, the random trace vectors employ at maximum 800 iterations of a regular Lanczos solver. The excited state sectors are handled with a regular Lanczos solver with a maximum of 800 iterations. For the construction of the Green's function, the high-frequency expansion is employed up to 15th order.

As discussed in section 4.1.4, using random trace vectors is not expedient. Their usage here is a remnant of when this was not yet clear. Considering the cases with Kondo couplings $J/t \in \{1.5, 2, 2.5\}$ with only $N_{\mathrm{ex}} = 120$ exact trace vectors and comparing the optimised grand potential, the magnetisation as well as the optimal Weiss fields, there occur no significant deviations in either quantity within the temperature range $T/t \in [0.01, 0.50]$ as compared to runs employing the additional random vectors.

The reference system considered is formed by a 2 × 2 site cluster with two orbitals and two spin orientations. At zero [Len16] and finite temperature a larger cluster with 3 × 2 sites can be employed. Both clusters and the lattice vectors of the superlattice are given in section 2.2.2. However for the purpose of constructing a phase diagram with sufficient temperature resolution, the smaller cluster is chosen to achieve lower run-times.

As for the modus operandi, first the grand potential at zero temperature is evaluated as function of the Kondo coupling J/t while optimising the on-cluster hopping in case of the PM and in addition the AFM Weiss field for the AFM solution. Starting from the optimal variational parameters at zero temperature, the optimisations are performed at finite temperatures $T/t \in \{0.01, 0.02, \ldots 0.50\}$. Special observables such as entropy, DOS and spectral function are computed afterwards using the optimal variational parameters.

6.2 Comparisons at zero temperature

First only the PM solution of the KLM is considered. For this purpose, the grand potential is optimised w.r.t. the (isotropic) on-cluster hopping. The optimised grand potential Ω/t of a 2×2 site cluster and the optimal values of the variational parameter t'/t of a 2×2 and 3×2 site cluster as function of the Kondo coupling shown in figure 6.1 agree with those of Lenz [Len16]. While the on-cluster hopping diverges monotonously with lowering J/t in case of the 2×2 site cluster, it exhibits a minimum in case of the 3×2 site cluster before diverging as well.

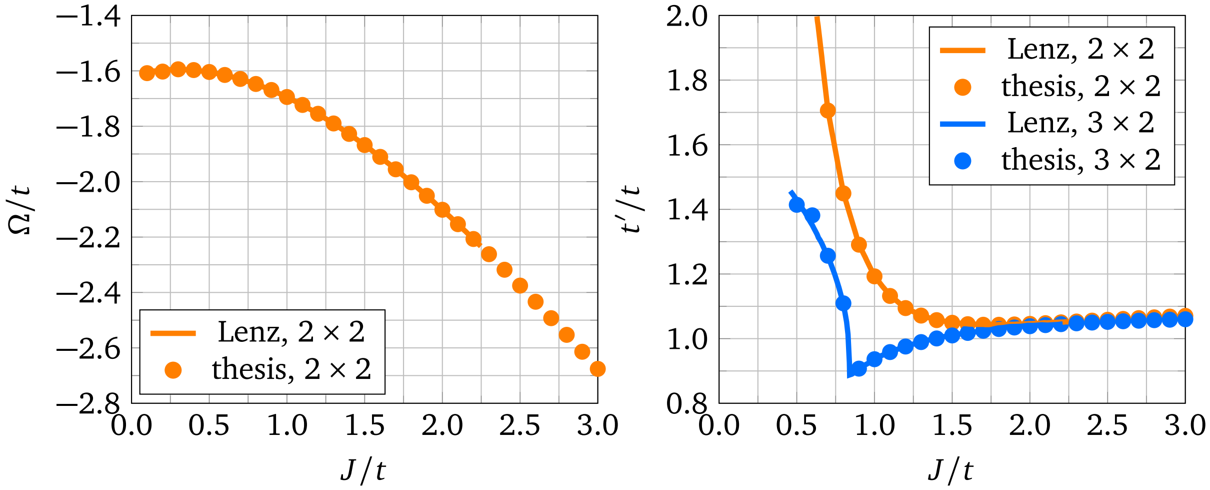

(a) CPT grand potential.

(b) Variational parameter.

6.1 – CPT grand potential Ω and variational hopping amplitude t' belonging to its minima as function of the Kondo coupling J/t at $T/t = 0$. The results are compared to those of Lenz [Len16].

Allowing for an AFM solution, the system exhibits a finite magnetisation which is compared for a 2×2 and a 3×2 site cluster in figure 6.2a to those of Lenz [Len16]. The critical Kondo coupling where the AFM transitions into a PM lies at $J_c/t \approx 2$ for the 2×2 and at 2.1 in case of the 3×2 site cluster. Furthermore, figure 6.2b displays the on-site spin-spin correlator $\langle \boldsymbol{S} \cdot \boldsymbol{s} \rangle$ with a kink well visible at the respective critical Kondo coupling. It is highlighted by fitting the correlator before and after the critical value with a second order polynomial whose derivative $\partial_J \langle \boldsymbol{S} \cdot \boldsymbol{s} \rangle$ is shown in the figure as well. The correlator approaches with increasing Kondo coupling the limit of one KS per site, $-3/4$.

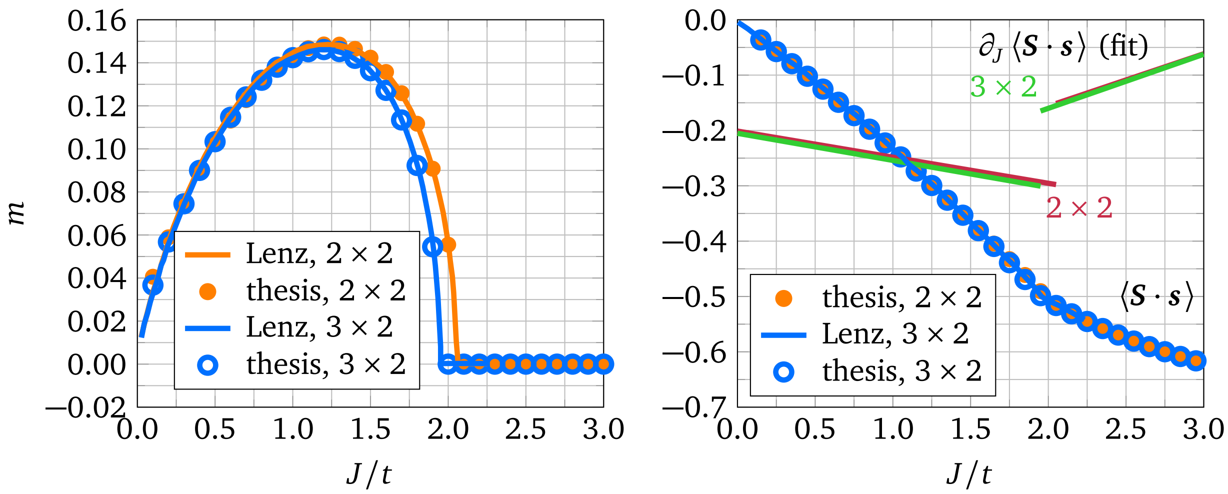

(a) Magnetisation.

(b) Spin-spin correlator $\langle \boldsymbol{S} \cdot \boldsymbol{s} \rangle$ and its J-derivative $\partial_J \langle \boldsymbol{S} \cdot \boldsymbol{s} \rangle$.

6.2 – AFM magnetisation m of the conduction electrons and spin-spin correlator $\langle \boldsymbol{S} \cdot \boldsymbol{s} \rangle$ between localised and conduction electron spin at $T/t = 0$ of a 2 × 2 and a 3 × 2 site cluster. The results are compared to those of Lenz [Len16].

Another way to quantify the presence of KSs described in the introduction is the DOS whose peaks at the energy $3J/4$ indicate breaking of KSs in case these are present. Figure 6.3 displays the DOS for the 2 × 2 and 3 × 2 site cluster with different broadenings $\eta/t \in \{0.05, 0.1\}$. Within the reference [Len16], three different peaks in the PM DOS are considered significant, the side resonance SR and the two peaks MR_1 and MR_2 of the split main resonance as labeled in figure 6.3c. Since here the smaller 2 × 2 site cluster is used as reference system, some peaks may not be sufficiently developed as can be seen by comparing the DOS of the different clusters, figure 6.3b for the 2 × 2 and figure 6.3c for the 3 × 2 site cluster. In the following, the DOS is evaluated for the 2 × 2 site cluster and the slightly larger broadening $\eta/t = 0.1$ as illustrated in figure 6.3a.

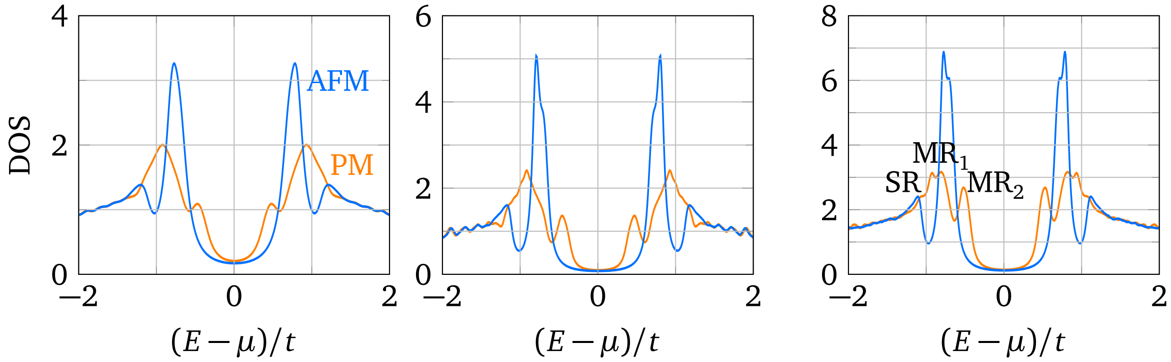

(a) 2 × 2 site cluster with $\eta/t = 0.1$.

(b) 2 × 2 site cluster with $\eta/t = 0.05$.

(c) 3 × 2 site cluster with $\eta/t = 0.05$.

6.3 – DOS of the conduction electrons for $J/t = 1.5$ at $T/t = 0$ of a 2 × 2 site cluster for two broadenings $\eta/t \in \{0.05, 0.1\}$ and a 3 × 2 site cluster for $\eta/t = 0.05$.

6 3 Finite temperature

Allowing for finite temperature provides an additional path from the AFM to a PM phase. This thermal PM is however distinct from the PM phase of KSs emerging at the critical Kondo coupling J_c/t since it consists of more than a pure state. The transition temperature from AFM to thermal PM is the Néel temperature T_N where the AFM magnetisation becomes zero. It can be inferred from figure 6.4, where the magnetisation is shown as function of temperature for several Kondo couplings. Given the temperature resolution $\Delta T/t = 0.01$, the Néel temperature appears to remain the same below $J/t = 1.7$ while it changes above the given value. Increasing J/t at zero temperature leads to a transition from the AFM to a PM phase at $J_c/t = 2.1$ as shown in figure 6.2a. This is reflected here by the magnetic moment vanishing at $J/t = 2.1$ for all temperatures.

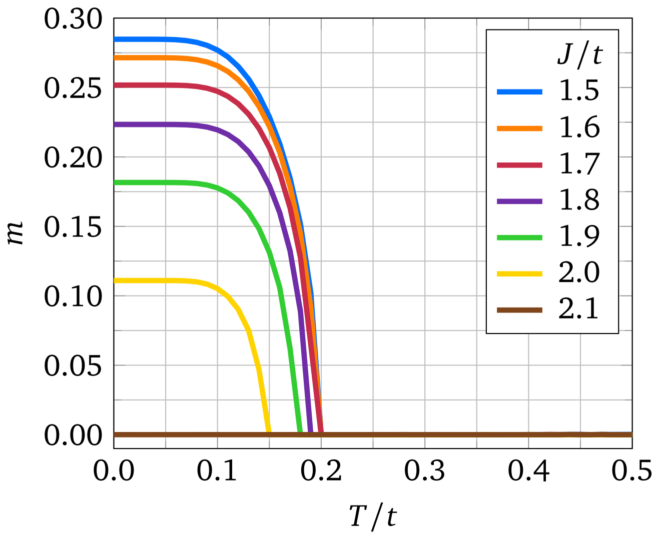

6.4 – AFM magnetisation m of the conduction electrons as function of the temperature T/t of a 2×2 site cluster at several Kondo couplings $J/t \in \{1.5, 1.6, \ldots, 2.1\}$.

Another observable providing a characteristic temperature is the specific heat. Obtained as the temperature derivative of the entropy shown in figure 6.5a for the PM and AFM solution at $J/t = 1.5$, the respective specific heats shown in figure 6.5b both exhibit a peak at temperatures T_{PM} and T_{AFM}. While the PM specific heat is smooth, the high temperature flank of the peak in the AFM specific heat appears to exhibit a jump. Going beyond the example of $J/t = 1.5$ given here, T_{AFM} follows the Néel temperature, while T_{PM} increases linearly with Kondo coupling J/t as can be seen in the phase diagram 6.8. The behaviour of the PM specific heat agrees with the observations of Zerec et al. [ZST06] at elevated Kondo couplings which confirms the present investigation.

Judging from the increase of the specific heat above $T/t \approx 0.3$, a second peak occurs at higher temperature. It is likely related to charge excitations [Sia+12; SSY18] and could be considered within a correlated Kondo lattice model [Sia+12] to check its dependence on the Hubbard repulsion.

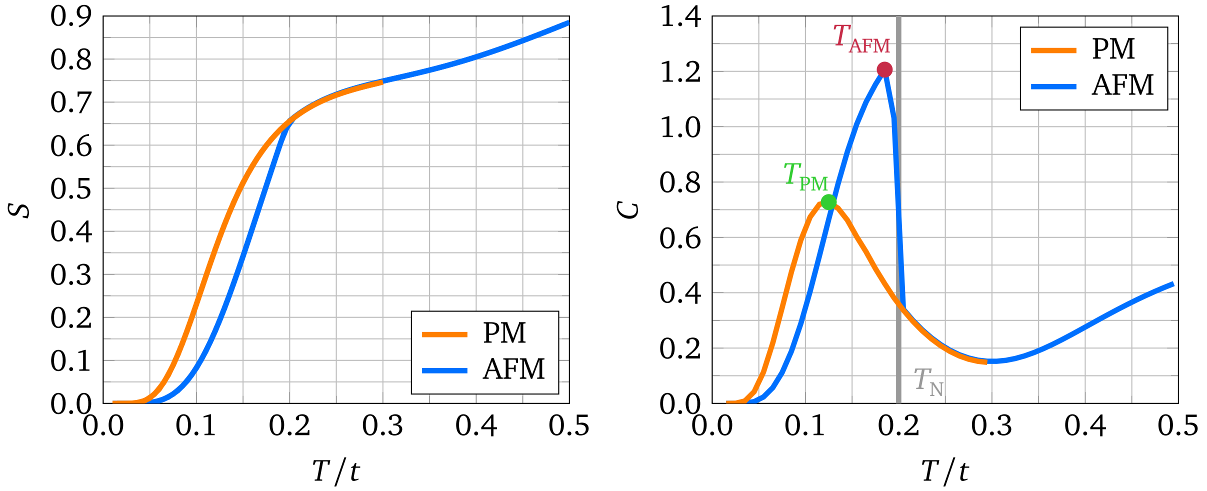

(a) Entropy.

(b) Specific heat.

6.5 – Entropy and specific heat as function of the temperature T of a 2×2 site cluster at $J/t = 1.5$. The peaks of the PM and AFM specific heat are highlighted in green and red.

Following the observation of Lenz [Len16] the on-site spin-spin correlator $\langle \boldsymbol{S} \cdot \boldsymbol{s} \rangle$ is considered as function of the Kondo coupling. Fitting the correlator by two second order polynomials, one below and one above $J/t \in \{1.75, 1.85, \dots, 2.25\}$ aims at capturing kinks possibly present at these Kondo couplings. J-derivatives of these fits exhibit a jump and thereby provide a measure of the kinks occuring at a given J/t. Figure 6.6a illustrates this at the temperature $T/t = 0.1$ for a kink at $J/t = 2.05$. Since this jump is obtained by fitting over restricted ranges of the Kondo coupling, it must be taken with a grain of salt. This can be seen by considering the example shown in figure 6.6a and the summary in figure 6.6b where all values of J/t imply a significant kink. Following the observation at zero temperature [Len16] according to which the kink is located at the critical Kondo coupling J_c/t where the system transitions into a PM, the respective curves in figure 6.6b are highlighted by a darker colour (purple, red, orange). The curves are chosen to overlap due to the finite resolution in J/t.

As for its meaning, the jump is a measure of how much the change with J/t of the (absolute value of the) spin-spin correlator decreases at the critical value J_c/t. It thus splits the system into different regimes depending on how it reacts to the KSs starting to dominate.

Considering the critical Kondo coupling at low temperature given by the dark, puple curve, the change to the PM is associated with the largest jump. In addition the case of Kondo couplings below and above the critical value can be distinguished qualitatively. Below J_c/t, the jump shows a peak, whose temperature decreases with increasing Kondo coupling. Above the critical value, the jump decreases and exhibits an inflection point. At J_c/t, the jump seems to have a saddlepoint. Passing the Néel temperature depending on the Kondo coupling, the jump remains non-zero up to a temperature $T/t \sim 0.45$, signifying the PM of KSs before ending in a thermal PM.

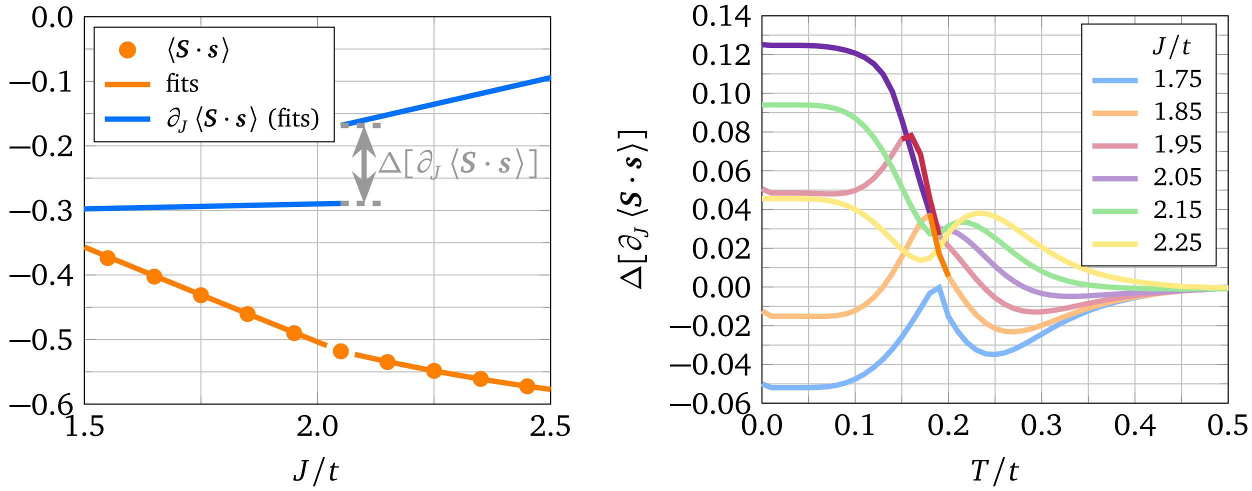

(a) Spin-spin correlator $\langle \boldsymbol{S}\cdot\boldsymbol{s}\rangle$ and its J-derivative $\partial_J \langle \boldsymbol{S}\cdot\boldsymbol{s}\rangle$ at $T/t = 0.1$ as function of J/t.

(b) Jump in the J-derivative of the spin-spin correlator $\Delta[\partial_J \langle \boldsymbol{S}\cdot\boldsymbol{s}\rangle]$ for several J/t.

6.6 – Spin-spin correlator $\langle \boldsymbol{S}\cdot\boldsymbol{s}\rangle$ and its J-derivative $\partial_J \langle \boldsymbol{S}\cdot\boldsymbol{s}\rangle$ at $T/t = 0.1$ as function of J/t as well as the jump occuring in the latter, $\Delta[\partial_J \langle \boldsymbol{S}\cdot\boldsymbol{s}\rangle]$, for $J/t \in \{1.75, 1.85\ldots, 2.25\}$ as function of T/t. Dark curves highlight the critical Kondo coupling J_c/t where the system transitions into a PM.

Perceiving the on-site spin-spin correlator as function of temperature as done by Zerec et al. [ZST06] provides another means to determine a characteristic temperature scale. The normalised correlator as function of the scaled temperature T/J shown in figure 6.7a illustrates the decay of spin correlations with increasing temperature (lower absolute value of correlator). In agreement with Zerec et al. [ZST06], the spin-spin correlator scales as J/t. ‘Scaling as’ means, that when displaying the spin-spin correlator as function of T/J, the curves for different coupling J/t collapse on top of each other.

The characteristic temperature scale is obtained as the temperature of the inflection point which corresponds to the maximum in the T-derivative shown in figure 6.7b. It is summarised in the phase diagram 6.8.

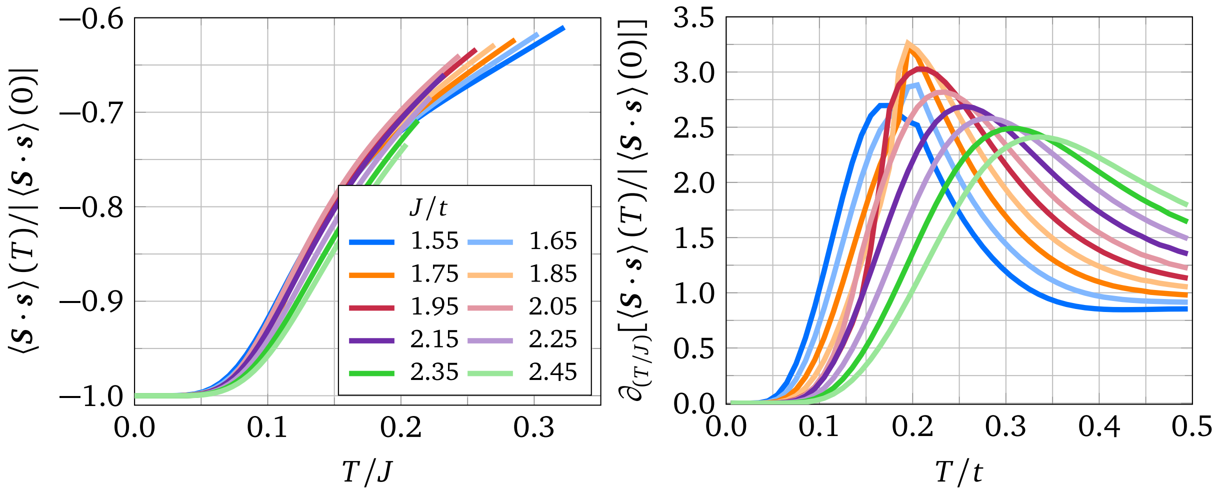

(a) Normalised spin-spin correlator.

(b) Numerical derivative of the normalised spin-spin correlator.

6.7 – Normalised spin-spin correlator and its numerical derivative used to determine the inflection point and thus the temperature scale of onsite correlations $T_{\langle \boldsymbol{S}\cdot\boldsymbol{s}\rangle}$.

In order to summarise the characteristic temperatures of the observables investigated up to now, figure 6.8 displays the corresponding phase diagram.

The AFM phase is highlighted by blue squares whose shade refers to the magnetisation. Its boundary to the thermal PM phase coincides with the peak of the specific heat upon including an AFM order T_{AFM} which is shown in red. This peak thus describes the AFM spin fluctuations. The peak of the specific heat when restriciting oneself to the PM solution T_{PM} is shown in green. Its temperature increases linearly with increasing Kondo coupling J/t. Following the reasoning of Zerec et al. [ZST06], this peak is associated with the breaking of KSs. Fitting this temperature with a linear function in J/t yields $(J/t)(T=0) \approx 1$. A temperature scale describing both types of spin fluctuations is the inflection point of the spin-spin correlator $T_{\langle S \cdot s \rangle}$ as a function of temperature T/t shown in purple. It interpolates between both temperature scales. Since the spin-spin correlator considered as a function of the Kondo coupling J/t exhibits a kink at the critical value, the jump introduced in figure 6.6 is shown for the low-temperature case of $J_{\mathrm{c}}/t = 2.05$. The transition to a thermal PM coincides with the fast decay of the jump. A plateau in the jump remains, until the temperature T_{PM}/t is passed.

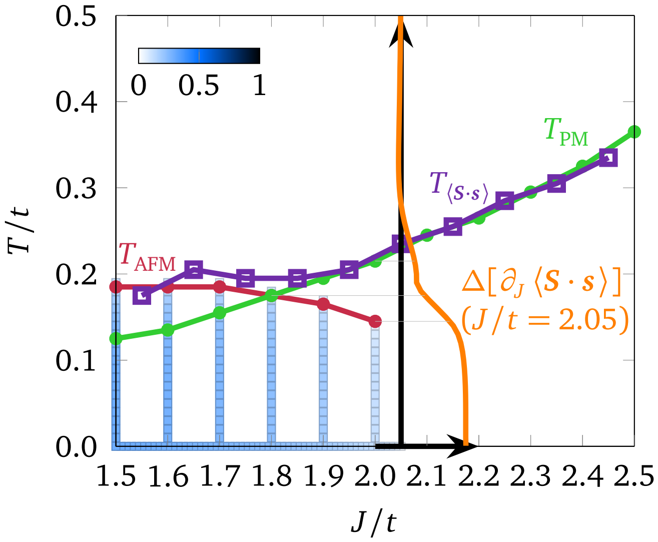

6.8 – T-J phase diagram of the half-filled Kondo model with a 2×2 site cluster as reference system. Blue squares highlight the AFM region with the shade representing the magnetisation. Peak positions of the specific heat introduced in figure 6.5b are shown in red for the AFM phase, T_{AFM}, and in green for the PM phase, T_{PM}. The temperature scale of onsite correlations $T_{\langle S \cdot s \rangle}$ is given in purple. A measure of the kink in the spin-spin correlator $\Delta[\partial_J \langle \boldsymbol{S} \cdot \boldsymbol{s} \rangle]$ introduced in figure 6.6 at $J/t = 2.05$ is depicted in orange.

After having discussed the thermodynamics of the KLM, dynamical observables are considered to shed more light onto the fate of the KSs. Figure 6.9 shows the DOS for several temperatures $T/t \in \{0.00, 0.01, \ldots, 0.30\}$ in case of $J/t = 1.5$ for the PM and AFM solution as well as for $J/t = 2$ in the AFM case. The green and red DOS highlight the temperature closest to but below T_{PM} and T_{AFM}. Note that $T_{\mathrm{PM}} < T_{\mathrm{AFM}}$ in case of $J/t = 1.5$ but $T_{\mathrm{PM}} > T_{\mathrm{AFM}}$ for larger $J/t = 2$. Orange lines highlight the peaks occuring in the DOS up to $T/t = 0.30$ while the orange dots at the top refer to the location of peaks at $T/t = 0.50$. Blue arrows denote the energy required to break a KS at low and high temperature as given in the introduction. Since the KLM is considered at half-filling, the DOS is symmetric around $(E-\mu)/t = 0$ due to particle-hole symmetry.

In case of the PM DOS at $J/t = 1.5$, two peaks occur at low temperature $T/t < T_{\mathrm{PM}}/t$ below the chemical potential. The one closer to the chemical potential lies near the energy required to break a KS. It survives up to $T/t \approx T_{\mathrm{PM}}/t$. For the temperature range $T_{\mathrm{PM}}/t \lesssim T/t \lesssim T_{\mathrm{AFM}}/t$ only one peak is present in the DOS. Slightly above T_{AFM} a new peak emerges in the gap and can be associated with a thermal PM phase since it requires less energy than breaking a KS. At even higher temperature, additional peaks occur in the gap whose position at $T/t = 0.5$ is highlighted by the orange dots.

For the AFM DOS at $J/t = 1.5$ also two peaks occur at low temperature $T/t < T_{\mathrm{AFM}}/t$ below the chemical potential. Since these peaks merge at the Néel temperature, they are associated with the AFM order. This assessment is confirmed upon considering the 'staggered-average local DOS' considered by Lenz [Len16] which measures the imbalance of the spin-resolved DOS on the sublattices formed by the AFM order. Adopting the labels used by Lenz, the presence of a SR and MR peak are signatures of the AFM phase. Besides these signatures, there is no peak visible close to the energy required to break a KS. Slightly above T_{AFM}/t a new peak emerges in the gap and can be associated with a thermal PM phase since it requires less energy than breaking a KS. Going to even higher temperature, additional peaks occur in the gap.

In contrast closer to the PM of KSs at the Kondo coupling at $J/t = 2$, three peaks occur at low temperature $T/t < T_{\mathrm{AFM}}/t$ below the chemical potential. The peak MR_2 closest to the chemical potential lies near the energy required to break a KS. It survives slightly past T_{PM}/t. The remaining two peaks MR_1 and SR merge at the Néel temperature. Slightly above T_{AFM}/t a new peak emerges in the gap and can be associated for $T_{\mathrm{AFM}}/t \lesssim T/t \lesssim T_{\mathrm{PM}}/t$ with the energy required to break a KS at high temperature. Hence there exists a temperature range where the low- and high-temperature KSs coexist. The transition AFM→KS at low T/t may at higher temperature eventually result in a thermal PM phase, since the peak in the gap moves back towards the chemical potential as can be inferred from the orange dots.

The DOS at $J/t = 2.5$ not illustrated here, exhibits a coexistence of the low-temperature KS and further PM peaks. The KS peak starting out for $T/t = 0$ at $(E-\mu)/t = 0.98 \approx 0.9375 = (1/2)\cdot 3J/4$ vanishes for $T/t = 0.43$ at $(E-\mu)/t = 1.06$. PM peaks emerge for $T/t = 0.26$ at $(E-\mu)/t = 0.02$ moving to higher energies until they reach $(E-\mu)/t = 0.27$ for $T/t = 0.5$. This is below the pure KS at high temperature $(1/2)\cdot 3J/8 = 0.46875$.

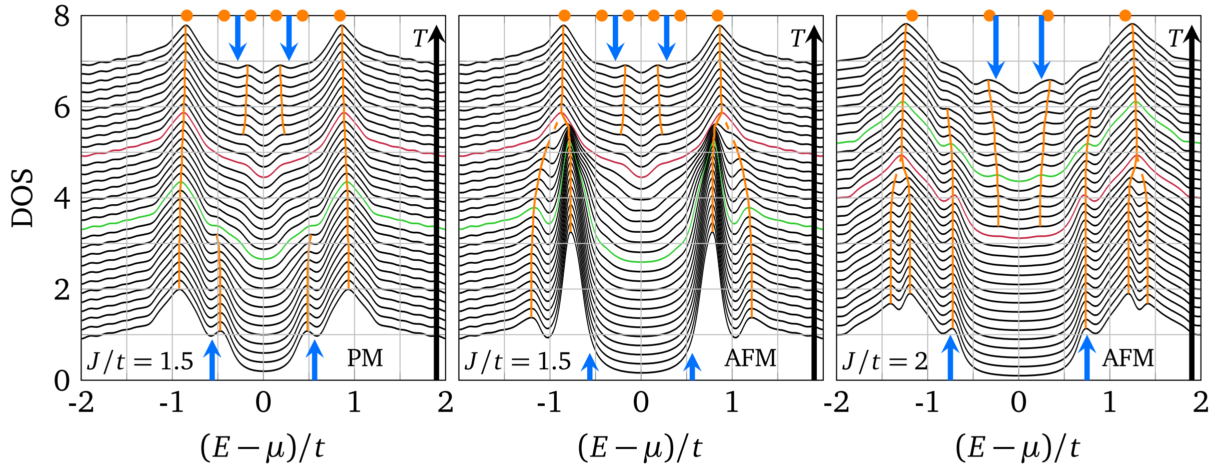

6.9 – DOS of the conduction electrons for two Kondo couplings $J/t \in \{1.5, 2\}$ at several temperatures $T/t \in \{0.00, 0.01, \ldots, 0.30\}$. For $J/t = 1.5$, the DOS is evaluated once for a PM system and once allowing an AFM order among the conduction electrons. Peak positions of the specific heat introduced in figure 6.5b are shown in red for the AFM phase and in green for the PM phase. Relevant peaks in the DOS are highlighted with orange lines and for $T/t = 0.5$ as dots at the top. Blue arrows emerging from the bottom and top highlight the energy needed to break a KS at low and high temperature, $3J/4$ and $3J/8$.

After discussing the energetics of the system in terms of the DOS, the structural dependence within the spectral function follows. Figure 6.10 shows the spectral function for three Kondo couplings $J/t \in \{1.5, 2, 2.5\}$ and three temperatures $T/t \in \{0.01, 0.15, 0.5\}$.

Signatures of the AFM phase corresponding to the splitting between SR and MR_1 occur along the path $\boldsymbol{k}/\pi = (0,1) \rightarrow (1,0)$ which is the boundary of the Brillouin zone due to the doubled unit cell within the AFM phase. Within the AFM phase, the KS is located around $\boldsymbol{k}/\pi = (1,1)$ in the occupied band and $\boldsymbol{k}/\pi = (0,0)$ in the unoccupied bands since these $\boldsymbol{k}$-points are equivalent in the doubled unit cell. It vanishes with increasing temperature. However depending on the Kondo coupling J/t, its signature survives to large temperatures. Since for the Kondo couplings considered, the KS is a localised object due to the local spin, it is not dispersive and stays at $\boldsymbol{k}/\pi = (0,0)$. The thermal PM shows signatures within the gap along the path $\boldsymbol{k}/\pi = (0,1) \rightarrow (1,0)$ corresponding to the boundary of the Brillouin zone due to the doubled unit cell. Thermal PM and KS are therefore distinct.

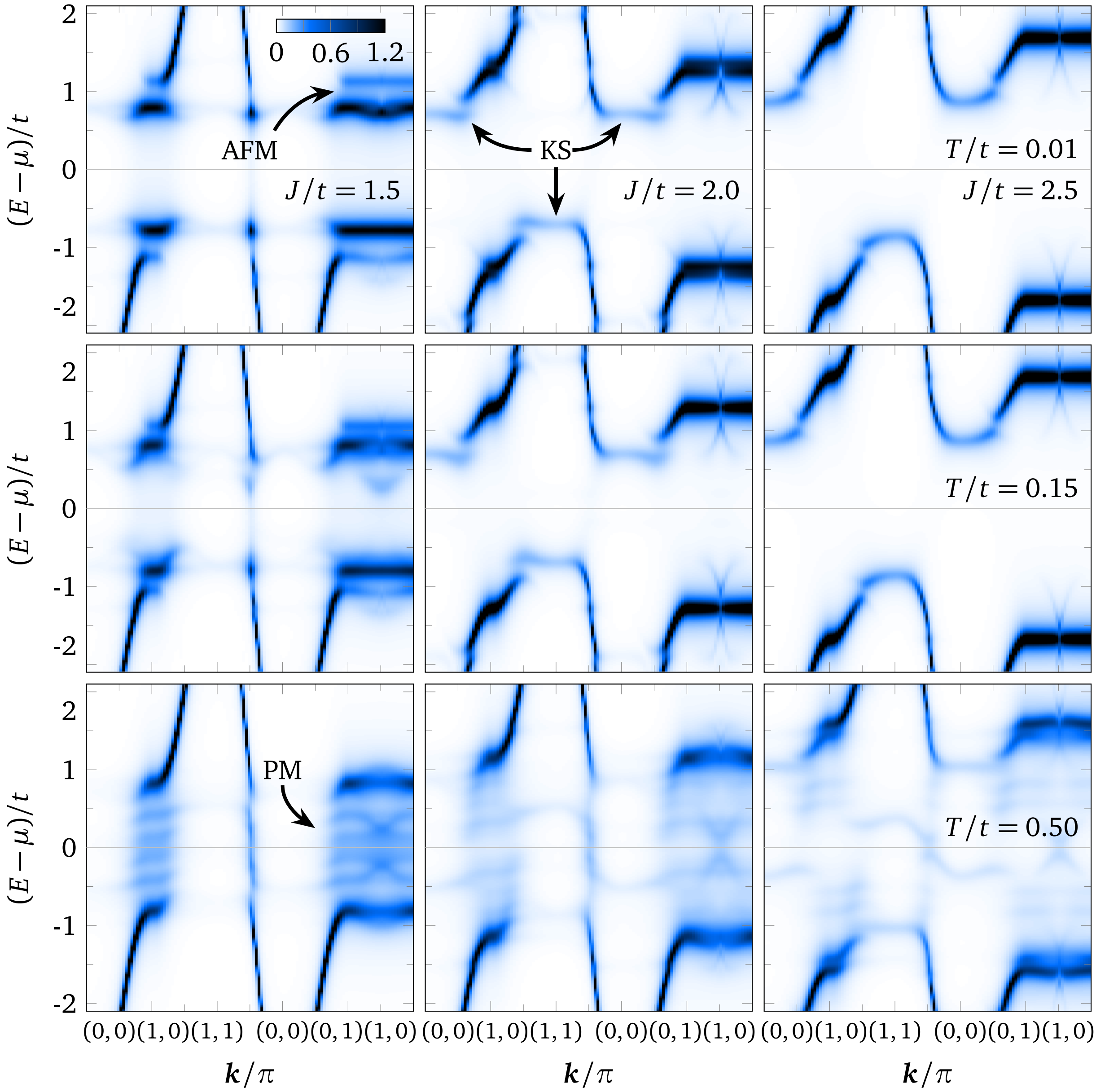

6.10 – Spectral function for different Kondo couplings at several temperatures. KS refers to signatures of the Kondo singlets.

6.4 Doped paramagnet

In order to investigate the effect of KSs on the Fermi surface, a metallic system has to be considered which can be reached by doping the KLM. In practice, doping entails two additional variational parameters, the physical chemical potential μ to fix the filling and the cluster chemical potential μ' to determine the filling in a thermodynamically consistent fashion. The idea behind this is described in section 2.4.7. Figure 6.11 shows the filling of a PM system at $T/t = 0$ as function of the physical chemical potential for two cluster sizes. The variational parameters considered are the on-cluster hopping and the cluster chemical potential. While the fillings observed here appear erratic, those presented by Lenz [Len16] are smooth. This discrepancy is likely due to the usage of a self-refining grid from the CUBA library within the $\boldsymbol{k}$-space integration employed by Lenz.

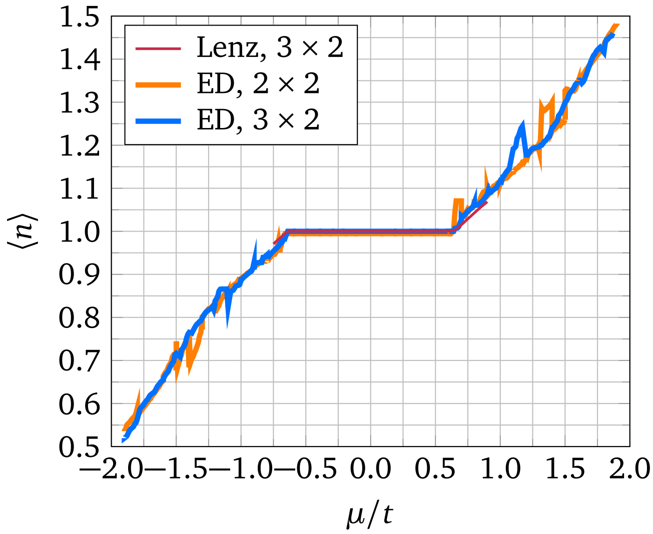

6.11 – Accessible fillings as function of the chemical potential μ/t for $J/t = 2$ at $T/t = 0$ employing a grid of 100×100 $\boldsymbol{k}$-vectors. The results are compared to those of Lenz [Len16].

6.5 Conclusion and Outlook

The characteristic temperature scales obtained from the AFM magnetisation, the specific heat and the on-site spin-spin correlator are summarised in the phase diagram 6.8. A definite phase boundary is formed between the AFM and thermal PM by the Néel temperature and the peak temperature of the specific heat for the AFM solution. In contrast, the peak temperature of the specific heat for the PM solution appears to be more of a crossover temperature between PM of KSs and thermal PM. Fitting this temperature with a linear function in J/t yields a crossover at zero temperature for $(J/t)(T = 0) \approx 1$. The entire thermal PM is separated from the low-temperature phases by the temperature associated with the inflection point of the on-site spin-spin correlator. Hence three phases can be identified.

The DOSs displayed in figure 6.9 exhibit features of the AFM phase, the PM of KSs and the thermal PM as well. A merger of two peaks at the Néel temperature denotes the transition from the AFM to the thermal PM. Each peak is associated with the magnetisation on one sublattice of the AFM. Peaks at the energy required to break a KS at low and high temperature signify the presence of KSs. Additional peaks at lower energies hint at a thermal PM. However there is no sharp transition but a coexistence of the KS peak with further PM peaks before the prior vanishes with increasing temperature. Furthermore it is difficult to distinguish between the peak of a KS at high temperature and peaks related to a thermal PM. Thus the KS to thermal PM transition is considered to be a crossover.

For the spectral function shown in figure 6.10, the split peaks of the AFM present in the DOS show up as two almost dispersionless, split bands along the boundary of the Brillouin zone $\boldsymbol{k}/\pi = (0,1) \rightarrow (1,0)$ related to the doubled unit cell. Signatures of the KSs are also almost dispersionless and occur at $\boldsymbol{k}/\pi = (0,0)$ and $\boldsymbol{k}/\pi = (1,1)$. For the thermal PM, the gap is flooded along the boundary of the Brillouin zone $\boldsymbol{k}/\pi = (0,1) \rightarrow (1,0)$ with spectral weight. Hence for the spectral function the distinction between KS and thermal PM is better visible.

Sticking to the half-filled system, observables of the converged reference cluster such as the PM total moment, the inter-site correlator or the spin susceptibility as done in [ZST06] may provide further characterisation of the KLM.

However the more interesting prospect lies in modelling a metallic system close to half-filling. This would enable the quasiparticle gap and the Fermi surface as well as their behaviour with temperature as observables. The transition from a small Fermi surface counting only the conduction electrons to a large Fermi surface which includes the localised spins would serve as additional temperature scale to characterise the PM of KSs. Another interesting topic is the emergence of non-Fermi liquid behaviour, such as deviations from the T-linear term in the specific heat or the electrical resistivity from the expected T^2 dependence, in heavy fermion metals [GSS08]. On a microscopic level, the energy-dependence of the cluster self-energy can be investigated [Nol14].

7 Conclusion and Outlook

In this thesis, the implementation details of several cluster solvers used for the VCA at finite temperature have been described. The most reliable, sufficiently benchmarked and best performing solver among them (see below) was then used to investigate the magnetic and orbital properties of Sr_2IrO_4 and Ca_2RuO_4 described by three-band Hubbard models, as well as the Kondo model at half-filling.

It was shown, that MPSs can be used within a cluster solver for VCA to construct the continued fraction representation of the cluster Green's function and obtain results in agreement with an ED solver.

For future attempts to use MPSs in a cluster solver, the following points should be kept in mind. First, suitable hardware should be used, since access to larger reference systems comes at the price of longer runtimes. Second, the Chebyshev representation of the Green's function should be considered, since it avoids the technical issue of loosing the basis orthogonality when constructing the continued fraction representation. Third, specifically concerning the solver employed in this thesis, its accessibility should be improved. With the given solver, a staggered AFM order, which is the default order used to benchmark the VCA, could not be investigated.

Concerning the solvers for finite temperature VCA, the FD as well as ED and Chebyshev solvers using exclusively exact trace vectors were reliable and performed well when making use of the high-frequency expansion or when using a moderate number of Chebyshev moments. The exact trace vectors should be obtained with a solver capable of resolving degenerate or clustered eigenvalues like a Band Lanczos solver. In case of the excited state sector for ED, a regular Lanczos solver is sufficient.

For all practical purposes considered, random trace vectors did not provide any advantage compared to their exact counterparts. Using purely random trace vectors within the FTLM gives insufficient results within the temperature range of interest where phase transitions occur and restricts its application to high temperatures. To obtain reliable results within FTLM, a large system or a sufficient number of random trace vectors is required. However to solve larger systems, more time is needed. Hence the FTLM is better suited for one-shot computations than for VCA, where the system has to be solved multiple times to find the optimal variational parameters. Increasing the number of random trace vectors also makes the solver numerically more expensive. When trying to improve the FTLM by requiring more converged eigenvalues one misses the opportunity of using them as exact trace vectors while having to compute them multiple times.

Splitting the trace into an exact and a random part, i.e. employing exact and random trace vectors, is unnecessary when already using exact trace vectors. At low temperature, the exact trace vectors are sufficient. When higher temperatures are of interest, the results can be improved systematically by incorporating more exact eigenvectors. In contrast it is unclear how many random vectors are required for a given temperature to achieve a satisfying precision.

Apart from being perceived as a SOC enabled Mott insulator at low temperature, the investigation of Sr_2IrO_4 was motivated by two questions. On the practical side the question was posed, whether the insulator emerging when going below the Néel temperature is more of Mott- or Slater-type [Ari+12; Li+13; WSY14]. This could not be answered using VCA, since the insulating gap changed only marginally. The closing of the gap with increasing temperature above and below the Néel temperature appeared to proceed at different rates. However this occured in such a faint manner, that definitive conclusions could not be drawn. Future attempts to address this question should be directed towards a CDIA study or a parameter study similar to the one conducted for the half-filled one-band Hubbard model [SSY18].

A more academic question concerned the necessity of nonlocal quantum fluctuations to properly capture the spectral features of magnetically ordered systems [Mar+18]. As far as the spectral function along the path $\boldsymbol{k}/\pi = (0,0) \rightarrow (1,0) \rightarrow (1,1) \rightarrow (0,0)$ is concerned, nonlocal quantum fluctuations are not required to qualitatively reproduce the spectra of the magnetically ordered system modelling Sr_2IrO_4. Besides overestimating the stability of the order considered (larger Néel temperature, larger spectral gap) which can be anticipated for meanfield theories, the spectral function missed features in the unoccupied states.

In contrast to the previous compound, in Ca_2RuO_4 the transition from AFM to PM is separated from the insulator to metal transition. The question motivating the investigation concerned the temperature range between these two transitions, more specifically whether the system changes from an orbitally ordered state into a disordered state [Zeg+05] or not [Por+18].

It was observed, that with increasing temperature, the capability of spin-orbit coupling to mix different orbitals became less effective. Combined with signatures of orbital fluctuations and the absence of real orbital order [Por+18], this suggested fluctuations in the phase between the orbital components, which is no longer fixed by spin-orbit coupling, as the origin of these orbital fluctuations.

Motivated by a VCA study at zero temperature [Len16] and a FTLM study at finite temperature [ZST06], the half-filled Kondo lattice model was investigated with finite temperature VCA. Considering the AFM magnetisation, the AFM and PM specific heat as well as the on-site spin-spin correlator made it possible to construct a phase diagram. The characteristic temperatures led to three phases: an AFM, a PM of Kondo singlets and a thermal PM. While the thermal PM is the final high temperature phase for all Kondo couplings J/t considered, there exists a range $J/t \in [1.8, 2.05]$ where increasing the temperature destroys the AFM order but leaves a PM of Kondo singlets before the thermal PM is reached.

Looking at the DOS and the spectral function provided information on the fate of the Kondo singlets with increasing temperature as well as their signatures compared to the thermal PM.

Having access to finite temperature but being restricted to commensurate fillings and insulating reference systems allows one only to witness the passive action of temperature which dilutes the ground state character with other states of higher energy. If doping could provide states within the insulating gap, a metallic system with a Fermi surface could be investigated or a metal-insulator transition could be captured and thus should allow more interesting dynamics in the spectral function like spectral weight shifting. Focus should be directed towards achieving a reliable level of doping and to properly use the CDIA.

Numerically, the Chebyshev representation of the Green's function should be used in combination with a MPS-based cluster solver and applied to realistic physical problems like Ca_2RuO_4, where larger clusters are in reach. To consider finite temperature, random trace vectors can be employed which should give reliable results with the larger system sizes accessible to a MPS-based solver.

A Mixed ensemble

In general, symmetries of the Hamiltonian which are compliant with the boundary conditions can be exploited to reduce the effort of calculations. Since these symmetries imply conserved quantities, the Hamiltonian and the conserved quantity share a common eigenbasis. Hence, the eigenvalues of the conserved quantity can be used as quantum numbers to characterize the states. If the physical problem at hand fixes the conserved quantity, the space of states used in setting up the Hamiltonian can be restricted.

In the present work, all Hamiltonians considered are particle-number conserving. Thus only states with a specific number of particles are considered. In context of the VCA, this restriction is in contradiction to the notion of a grand potential of the grand canonical ensemble. Working in a subspace with fixed particle number while computing observables in a grand canonical scheme is denoted in the following as working in a mixed ensemble.

To obtain observables within the grand canonical ensemble, one has to combine the observables measured in the different particle-number sectors in a suitable manner. Recalling the connection between the partition functions of the grand canonical ensemble $\Xi(\mu, V, T)$ and the canonical ensemble $\Xi(N, V, T)$,

$$\Xi(\mu, V, T) = \sum_N \Xi(N, V, T) \cdot \exp\left(-\frac{(-\mu N)}{T}\right), \tag{A.1}$$

the full grand potential $\Omega(\mu, V, T)$ can be expressed via the grand potential in the mixed ensemble $\Omega_N(\mu, V, T)$ as

$$\Omega(\mu, V, T) = -\frac{1}{\beta} \ln \left\{ \sum_N \exp\left[-\frac{\Omega_N(\mu, V, T)}{T}\right] \right\}. \tag{A.2}$$

Equation (A.2) forms the dictionary between the mixed and the grand canonical ensemble. Observables within the grand canonical ensemble are obtained by computing the derivative of the grand potential $\Omega(\mu, V, T)$. Identifying the derivatives on the r.h.s. with the observables measured within the mixed ensemble in various particle-number sectors gives the recipe of how to assemble the observables. An important observable in this context is the entropy whose expression is derived in section 2.4.5. To obtain the entropy in the grand canonical ensemble from the quantities measured in the mixed ensemble, one has to assemble the derivative

$$\begin{aligned} S(\mu, V, T) &= -\frac{\partial}{\partial T}\Omega(\mu, V, T) \\ &= -\beta\Omega(\mu, V, T) + \beta \left\langle \Omega_N(\mu, V, T) \right\rangle_N + \left\langle S_N(\mu, V, T) \right\rangle_N \end{aligned} \tag{A.3}$$

with the average

$$\left\langle \mathcal{O}(N, V, T) \right\rangle_N = \left\{ \sum_N \exp[-\beta\Omega_N(\mu, V, T)] \right\}^{-1} \left\{ \sum_N \exp[-\beta\Omega_N(\mu, V, T)]\mathcal{O}(N, V, T) \right\}. \tag{A.4}$$

B High- and low-temperature limits

The easiest route to the high- and low temperature limits of the entropy is to express each quantity in equation (A.3) in terms of the partition function of the mixed ensemble

$$\Xi_N(\mu,V,T)=\exp[-\beta\Omega_N(\mu,V,T)], \tag{B.1}$$

which gives for the entropy of the grand canonical ensemble

$$\begin{aligned}S(\mu,V,T)=\ln\left[\sum_N \Xi_N(\mu,V,T)\right]-\left[\sum_N \Xi_N(\mu,V,T)\right]^{-1}\left[\sum_N \Xi_N(\mu,V,T)\ln[\Xi_N(\mu,V,T)]\right]\\ +\langle S_N(\mu,V,T)\rangle_N\,.\end{aligned} \tag{B.2}$$

Employing the analytical expression for the CPT grand potential provided in equation (2.170), one can see in the limit of high and low temperature

$$\lim_{T\to\infty}\beta\Omega_N(\mu,V,T)=\lim_{T\to\infty}\beta\Omega_{\mathrm{cl}}, \tag{B.3}$$

$$\lim_{T\to 0}\beta\Omega_N(\mu,V,T)=\lim_{T\to 0}\beta\Omega_{\mathrm{cl}}. \tag{B.4}$$

At high temperature, the remaining terms cancel, while at zero temperature, each remaining term vanishes separately. Considering the cluster partition function of equation (2.19) with the trace represented by the eigenstates of the Hamiltonian, it becomes at high temperature the dimension of the Hilbert space of the respective particle number sector, while at zero temperature only the g_N-fold degenerate ground state contributes significantly

$$\lim_{T\to\infty}\Xi_{\mathrm{cl}}=\dim\mathscr{H}_N, \tag{B.5}$$

$$\lim_{T\to 0}\Xi_{\mathrm{cl}}=\lim_{T\to 0}g_N\exp(-\beta E_0). \tag{B.6}$$

Similar to the CPT grand potential, the entropy given in equation (2.244) approaches its cluster counterpart in the high- and low temperature limit. In case of the high-temperature limit, blatantly setting $\beta=0$ gives $\mathscr{S}_{\mathrm{CPT}}=0$, $\mathscr{S}_{\mathrm{cl}}=0$. Since the CPT grand potential becomes the cluster grand potential, only the cluster entropy remains

$$\lim_{T\to\infty}S_N(\mu,V,T)=\lim_{T\to\infty}S_{\mathrm{cl}}. \tag{B.7}$$

The limit of zero temperature is more involved. One may follow the physical reasoning of Seki et al. [SSY18], who start from the internal energy $E_N=\Omega_N(\mu,V,T)+TS_N(\mu,V,T)$ and argue that it should approach the grand potential upon lowering the temperature. Comparing the different expressions leads to a cancellation of all but the cluster entropy within $S_N(\mu,V,T)$. Here, a more technical argument is presented. Following the derivation of the expression for the entropy presented in section 2.4.5, one can identify

$$-\frac{\partial[\Omega_N(\mu,V,T)-\Omega_{\mathrm{cl}}]}{\partial T}=\mathscr{S}_{\mathrm{CPT}}+\mathscr{S}_{\mathrm{cl}}-\frac{[\Omega_N(\mu,V,T)-\Omega_{\mathrm{cl}}]}{T}. \tag{B.8}$$

Considering the zero temperature limit of this equality and applying l'Hôpital's rule one expects

$$\lim_{T\to 0} \frac{[\Omega_N(\mu,V,T)-\Omega_{\mathrm{cl}}]}{T} = \lim_{T\to 0} \frac{\partial[\Omega_N(\mu,V,T)-\Omega_{\mathrm{cl}}]}{\partial T} \tag{B.9}$$

and hence

$$\lim_{T\to 0} (\mathscr{S}_{\mathrm{CPT}} + \mathscr{S}_{\mathrm{cl}}) = 0, \tag{B.10}$$

leaving only the cluster contribution to the entropy

$$\lim_{T\to 0} S_N(\mu,V,T) = \lim_{T\to 0} S_{\mathrm{cl}}. \tag{B.11}$$

With the average cluster energy given by equation (2.248) not scaling with temperature in the high temperature limit, its contribution to the cluster entropy (2.245) vanishes

$$\lim_{T\to\infty} \beta \langle H\rangle_{\mathrm{cl}} = 0. \tag{B.12}$$

This leaves for the high temperature limit of the entropy in the mixed and grand canonical ensemble

$$\lim_{T\to\infty} S_N(\mu,V,T) = \ln[\dim \mathscr{H}_N], \tag{B.13}$$

$$\lim_{T\to\infty} S(\mu,V,T) = \ln\left[\sum_N \dim \mathscr{H}_N\right]. \tag{B.14}$$

In the low temperature limit, only the g_N-fold degenerate ground state contributes, giving

$$\lim_{T\to 0} S_{\mathrm{cl}} = \lim_{T\to 0} [\ln(g_N) - \beta E_0 + \beta E_0] = \ln(g_N). \tag{B.15}$$

For the zero temperature limits of the mixed and grand canonical entropy thus follows

$$\lim_{T\to 0} S_N(\mu,V,T) = \ln(g_N), \tag{B.16}$$

$$\lim_{T\to 0} S(\mu,V,T) = \ln\left(\sum_{\{N\}} g_N\right) - \left(\sum_{\{N\}} g_N\right)^{-1} \cdot \left[\sum_{\{N\}} g_N \ln(g_N)\right], \tag{B.17}$$

where $\{N\}$ refers to case of degenerate ground states within different particle number sectors.

C Finite temperature expectation values

At finite temperature, the expectation values obtained numerically from the cluster Green's function appear to differ in specific cases from those obtained as a trace over the eigenstates. Intuitively, this discrepancy follows from erroneously using the hole and the electron part of the Green's function to compute expectation values. The deviation can be quantified by evaluating the integral (2.165) starting from the grey contour shown in figure 2.13d which encircles the poles of the Green's function on the real axis as well as using $f(\varepsilon) = 1 - f(-\varepsilon)$ for the Fermi function and gives

$$
\begin{aligned}
-\frac{1}{2\pi \mathrm{i}} \oint_C \mathrm{d}z\, G_{\alpha\beta}(z) f(z) &= \sum_{m,n} \frac{\exp(-\beta\varepsilon_m)}{\Xi} f(\varepsilon_n^+ - \varepsilon_m)\, \langle \Psi_m | c_\alpha | \Psi_n^+ \rangle\, \langle \Psi_n^+ | c_\beta^\dagger | \Psi_m \rangle \\
&\quad + \sum_{m,n} \frac{\exp(-\beta\varepsilon_m)}{\Xi} f(\varepsilon_m - \varepsilon_n^-)\, \langle \Psi_m | c_\beta^\dagger | \Psi_n^- \rangle\, \langle \Psi_n^- | c_\alpha | \Psi_m \rangle \\
&= \langle c_\beta^\dagger c_\alpha \rangle + \sum_{m,n} \frac{\exp(-\beta\varepsilon_m)}{\Xi} f(\varepsilon_n^+ - \varepsilon_m)\, \langle \Psi_m | c_\alpha | \Psi_n^+ \rangle\, \langle \Psi_n^+ | c_\beta^\dagger | \Psi_m \rangle \\
&\quad - \sum_{m,n} \frac{\exp(-\beta\varepsilon_m)}{\Xi} f(\varepsilon_n^- - \varepsilon_m)\, \langle \Psi_m | c_\beta^\dagger | \Psi_n^- \rangle\, \langle \Psi_n^- | c_\alpha | \Psi_m \rangle\,, \qquad \text{(C.1)}
\end{aligned}
$$

where the electron and hole part are explicitely denoted by ± and the expectation value is given according to equation (2.22). If the additional terms besides the expectation value neither vanish nor cancel, the integral over the Green's function is different from the expectation value. Considering the shape of the Fermi function, the difference compared to the expectation value consists mostly in states with $\varepsilon_n^\pm < \varepsilon_m$ which lead to poles illustrated in figure C.1 for $T/t > 0$.

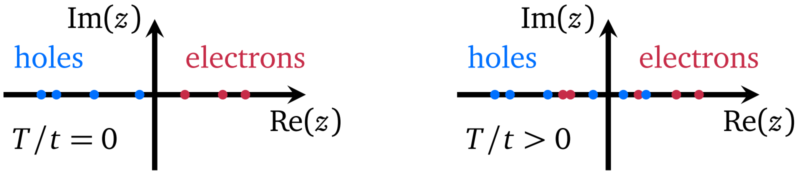

C.1 – Relevant poles of the electron and hole part of the Green's function at zero and finite temperature.

A specific example for this discrepancy is shown for the kinetic energy in figure C.2 for a half-filled one-band Hubbard model with $U/t = 8$ on a 2×2 site cluster. In contrast, the density is captured correctly via the contour integral.

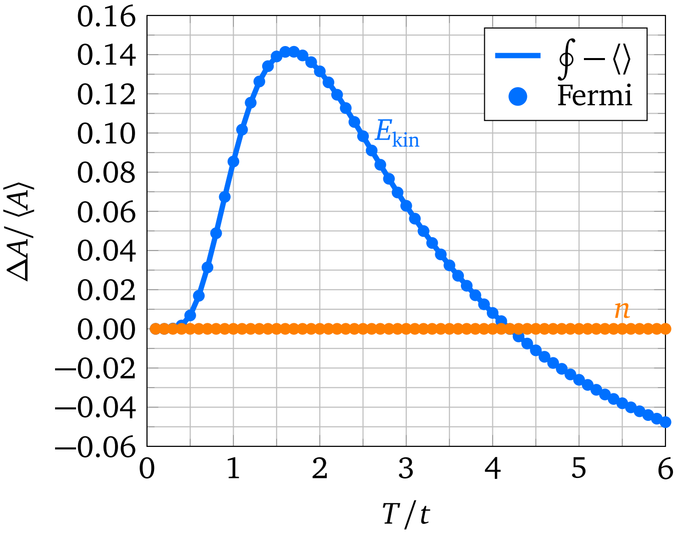

C.2 – Illustration of the discrepancies ΔA motivated in equation (C.1) for the cluster kinetic energy and cluster density $A \in \{E_{\text{kin}}, n\}$. Lines mark the difference between the expectation values obtained via contour integration and trace, while dots refer to the expression containing Fermi functions. The differences are normalised w.r.t. the expectation value obtained via the trace $\langle A \rangle$.

Analytically, the additional terms are prevented by evaluating the Matsubara function at suitable imaginary times as done in equation (2.62). This implies a phase factor in the Fourier series of the Matsubara function which formally allows extending the contour with arcs around the positive and negative real axis as described in section 2.3.5. Missing this phase factor gives different results as is illustrated in two exercises in [Nol14] for the diagonal Matsubara function.

At zero temperature, such a phase factor is not required, since the poles of the hole and electron part are well separated as sketched in figure C.1 and the Fermi function only includes the poles of the hole part since $f(E) \to \Theta(-E)$.

Considering the contour motivated in section 2.3.5, the effect of such a phase factor is limited. Due to the infinitesimal 0^+ in the exponent, the real part of z could be ignored, while a change in the sign of the imaginary part may lead to a sign change. However adding phase factors of different size $0^+ \in \{10^{-6}, 10^{-3}, 10^{-1}\}$ or replacing the phase factor by $\exp[\mathrm{i}\,\mathrm{Im}(z)]$, $\mathrm{sign}[\mathrm{Im}(z)]$ or $\mathrm{i}\,\mathrm{sign}[\mathrm{Im}(z)]$ within the numerical integration does not get rid of the discrepancy. Hence the question remains of how to prevent the electron part from contributing.

Besides altering the cluster expectation values, it is unclear how this affects the expectation values obtained from the CPT Green's function.

Among the cluster observables presented in chapter 4, the discrepancies discussed here do not alter the overall conclusion, since it is a systematic error which affects the results from all solvers equally. Differences between solvers thus do not originate from these discrepancies. Within section 5.2, the overlaps computed on the cluster are obtained via the trace, which yields the correct results.

D Parallelisation

To reduce the execution time, the evaluation of the trace using random vectors is executed in parallel using OpenMP. The respective loop is parallelised via OpenMP leading to several *threads* executing separate iteration steps in parallel.

Since the Hamiltonian matrix scales with the system size and is not modified within Lanczos ED, it is shared among the threads. Thus switching between the ground-state and excited-state sector requires synchronisation of the threads using a *barrier*. Furthermore, the Hamiltonian is updated by only one thread using a *single construct*.

To ensure thread-safety each thread is endowed with its own seed for the random number generator (RNG) used to construct the random vectors. The RNG is contained in a *critical section*, which allows only one thread at a time to execute its contents. Each thread updates its own seed once the random vector is generated.

In order to avoid blocking the execution due to barriers when some threads finish their share of jobs, the total number of loop iterations is reduced to be divisible by the number of maximally available threads. For the remaining loop iterations, the number of threads is reduced. After all loop iterations are performed, the number of threads is reset again. Thus, the available threads are used best.

Arrays and variables used within the subroutines running in parallel are declared *thread-private* to avoid accidental data sharing and overwriting.

Besides the computation and output to file, the input from file to construct the Green function as spectral representation is parallelised as well. This can also be used in case the trace vectors are determined via FD or ED. To avoid race conditions while combining the data, there are two possibilities:

1) Each thread has a private variable to store the partial sum. After the loop is finished, the partial sums are combined in a critical section by one thread at a time.
2) A shared array of Green functions is used, where each thread changes the entries specified by the trace vector. After the loop is finished, the input is combined in a serial manner.

The first case coincides with the *reduction* clause of OpenMP, while the second is required for the error analysis.

D 1 Improved IO

In order to exploit the enhanced speed in computation, writing the components to disk and reading them to assemble the Green function has to be improved too. First, the number of files used is reduced since the operating system/hard drive limits the time to find the file to be read. Next, raw IO is used to keep the disk space small. A symbiosis of these points is that raw output allows storing whole matrices with their internal structure maintained thus reducing the number of files by at least two indices and more indices by appending similar quantities to the same file.

It has to be noted that using Band Lanczos ED compared to Block Lanczos or regular Lanczos ED for the excited subspaces is slower. The convergence of the lowest eigenvalue is determined by the number of times the Hamiltonian is applied to a single state. Since regular Lanczos ED has only one state and in Block Lanczos ED, the Hamiltonian can be applied to multiple states in parallel, they converge similarly fast. For Band Lanczos ED, deflation [Fre00] can occur which reduces the bandwidth of the Hamiltonian matrix in the Lanczos basis. Therefore, the Hamiltonian cannot be applied to all states in parallel, since some states may not contribute and an explicit orthogonalisation w.r.t. deflated Lanczos vectors might be necessary.

D 2 Debatable implementation choices

This paragraph aims at pointing out some aspects of the implementation, where efficiency and quality of life features were sacrificed for the purpose of a slim code base and efficiency of other parts of the code. These are aspects, that have led in practice to (counter-intuitively) using one solver over the other and it may be reasonable to adapt them in the future.

When allowing for a FD solver for ‘small’ systems and ED solvers for ‘larger’ systems, both at finite temperature, one has to decide between less compact code and redundant computations.

In case a Lanczos solver is intended for the excited state sectors, the trace vectors and excitations are handled in a loop, each excitation on top of a trace vector is used as initial vector of a Lanczos run. This is similar to a Band Lanczos solver, where all excitations are handled at once, but the trace vectors are treated in series. For FD, the Hamiltonian of the excited state sectors in principle has to be diagonalised only once. Hence either the FD solver is separated from the ED solvers, meaning less compact code, or the FD is performed multiple times within the loop required by the Lanczos or Band Lanczos solvers, leading to a redundancy in computation. Instead of diagonalising the Hamiltonian of the excited state sectors once, it is diagonalised $N_{\mathrm{GS}} \times \ell = \mathcal{O}(10^3)$ times, with N_{GS} being the dimension of the ground state Hilbert space and ℓ the number of cluster sites, including spin and orbital degrees of freedom.

The latter option was chosen, meaning that for each exactly obtained trace vector and each excitation, the Hamiltonian in the excited state sector is diagonalised. In case of the d^4 configuration of section 5.2, this led to the use of Band Lanczos and Lanczos solvers although the system is small enough for FD. The time it takes to solve the system with the redundancy described simply turned out to be too long for sufficient optimisation steps. For two particles in a three-band Hubbard model, a 792-dimensional Hamiltonian is diagonalised 495 × 12 times.

Since performance of the FD solver became important eventually, it was separated from the Lanczos and Band Lanczos solvers. However the d^4 configuration of section 5.2 was already investigated using Band Lanczos and Lanczos solvers at the time where the number of exact trace vectors was restricted to $N_{\mathrm{ex}} = 120$ at all finite temperatures.

A quality of life feature used by Seki et al. [SSY18] is the automatic use of ‘sufficient’ trace vectors for a given temperature. This has been mentioned in section 2.4.2 and amounts to requiring a sufficiently large ratio of Boltzmann factors between an excited state and the ground state of the ground state sector. This automatic feature is not implemented, since it cannot be applied straightforwardly to the FTLM and misses the original aim of restricting the number of trace vectors depending on their weight. Since originally, a FTLM solver was intended as use-case and exact and random trace vectors used the same routine, additional flags would have been necessary. Also, when splitting the trace into an exact and a random part, the mentioned criterion cannot assess how many exact trace vectors are required compared to additional random trace vectors.

Since the FTLM turned out to be unreliable and unnecessary and performance of using exact trace vectors became important, a redundant copy of the original routine was added with minor details changed. Hence now the automatic adaptation of exact trace vectors can be added to the code.

Zusammenfassung

In dieser Arbeit wurde die Implementation mehrerer Cluster-Solver für VCA bei endlichen Temperaturen beschrieben. Der verlässlichste, hinreichend getestetste und performanteste Solver wurde anschließend dazu verwendet den Magnetismus und die Orbitalphysik von Sr_2IrO_4 und Ca_2RuO_4, beschrieben durch Drei-Band Hubbard Modelle, sowie das halbgefüllte Kondo Gittermodell zu untersuchen.

Es wurde gezeigt, dass MPSs in einem Cluster-Solver von VCA verwendet werden können um die Kettenbruchdarstellung der Greenschen Funktion zu konstruieren und daraus ein Selbstenergiefunktional zu erhalten, welches mit denen eines ED-Solvers übereinstimmt.

Für zukünftige Versuche MPSs in einem Cluster-Solver zu verwenden sollten folgende Punkte beachtet werden. Erstens sollte angemessene Hardware verwendet werden, da der Zugang zu größeren Referenzsystemen durch längere Laufzeiten erkauft wird. Zweitens sollte die Chebyshev-Darstellung der Greenschen Funktion verwendet werden, da auf diese Weise technische Komplikationen in Form des Verlusts der Orthogonalität der Basis bei Konstruktion der Kettenbruchdarstellung vermieden werden. Drittens sollte die in der Arbeit verwendete Implementation der MPSs zugänglich gestaltet sein. In der vorhandenen Version konnte keine AFM Ordnung untersucht werden, was in der Praxis die Standard-Ordnung zum Testen von VCA darstellt.

Unter den präsentierten Solvern für VCA bei endlichen Temperaturen stellten sich der FD-, ED- und Chebyshev-Solver mit exakten Spurvektoren als zuverlässig heraus. In Kombination mit der Hochfrequenzentwicklung, bzw. einer moderaten Anzahl an Chebyshev Momenten sind sie darüber hinaus performant. Die verwendeten exakten Spurvektoren sollten mit einem Solver bestimmt werden, welcher in der Lage ist entartete oder geclusterte Eigenwerte aufzulösen, z.B. einem Band Lanczos Solver. Im Fall des Sektors angeregter Zustände bei ED reicht ein Lanczos Solver aus.

In allen betrachten Fälle wiesen die Zufallsvektoren keinerlei Vorteile gegenüber ihren exakten Pendants auf. Die reine Verwendung von Zufallsvektoren in FTLM führt zu fehlerbehafteten Ergebnissen innerhalb des Temperaturbereichs von Interesse in welchem Phasenübergänge auftreten und beschränkt den Anwendungsbereich des Solvers damit auf hohe Temperaturen. Um mit FTLM zuverlässige Ergebnisse zu erhalten müssen große Systeme oder eine hinreichend hohe Anzahl an Zufallsvektoren verwendet werden. Allerdings benötigen größere Systeme mehr Zeit um sie exakt zu diagonalisieren. Aus diesem Grund ist die FTLM besser für einmalige Rechnungen geeignet als für VCA, bei welcher das System mehrfach exakt diagonalisiert werden muss um die optimalen Variationsparameter zu bestimmen. Mehr Zufallsvektoren lassen den Solver ebenfalls numerisch teurer werden. Beim Versuch die FTLM zu verbessern indem mehr Eigenwerte zur Konvergenz gebracht werden, verpasst man die Gelegenheit die exakten Eigenvektoren in der Spur zu verwenden, während sie für jeden Zufallsvektor erneut berechnet werden.

Eine Aufspaltung der Spur in einen exakten und einen zufälligen Anteil, d.h. die Verwendung exakter und zufälliger Spurvektoren, ist unnötig da bereits exakte Vektoren verwendet werden. Bei niedrigen Temperaturen genügen die exakten Eigenvektoren. Sofern höhere Temperaturen von Interesse sind, können die Ergebnisse systematisch verbessert werden, indem mehr exakte Eigenvektoren in der Spur hinzugenommen werden. Im Gegenzug ist unklar, wie viele Zufallsvektoren benötigt werden um bei einer gegebenen Tempe-ratur eine zufriedenstellende Präzision zu erreichen.

Neben der Erkenntnis, dass Sr_2IrO_4 bei niedrigen Temperaturen ein durch Spin-Bahn Kopplung induzierter Mott-Isolator ist, war die Untersuchung dieser Verbindung durch zwei Fragen motiviert. Auf der praktischen Seite wurde die Frage gestellt, ob der Isolator welcher unterhalb der Néel Temperatur auftritt eher Mott- oder Slater-artig ist [Ari+12; Li+13; WSY14]. Dies konnte mit VCA nicht eindeutig beantwortet werden, da sich die isolierende Bandlücke nur geringfügig änderte. Die Art wie sich die Bandlücke mit zunehmender Temperatur füllt unterscheidet sich unter- und oberhalb der Néel Temperatur. Allerdings findet das Auffüllen in so geringen Maßen statt, dass eindeutige Schlussfolgerungen nicht gezogen werden können. Zukünftige Versuche diese Frage zu beantworten sollten in Form einer CDIA Studie oder eine Parameterstudie ähnlich jener für das Ein-Band Hubbad Modell [SSY18] durchgeführt werden.

Eine eher akademische Frage befasste sich mit der Notwendigkeit nicht-lokaler Quantenfluktuationen um spektrale Signaturen magnetisch geordneter Systeme zu reproduzieren [Mar+18]. Was die Spektralfunktion entlang des Pfades $\boldsymbol{k}/\pi = (0,0) \rightarrow (1,0) \rightarrow (1,1) \rightarrow (0,0)$ anbelangt, so werden keine nicht-lokale Quantenfluktuationen benötigt um qualitativ die Spektren des magnetisch geordneten Systems welches Sr_2IrO_4 modelliert zu erhalten. Neben einer Überschätzung der Stabilität der Ordnung (höhere Néel Temperatur, größere Bandlücke) welche für Molekularfeldtheorien zu erwarten ist, fehlen Signaturen der unbesetzten Zustände in der Spektralfunktion.

Im Gegensatz zur vorherigen Verbindung treten die Übergänge vom AFM zum PM und vom Isolator zum Metall in Ca_2RuO_4 bei unterschiedlichen Temperaturen auf. Die Frage, welche diese Untersuchung motivierte betraf den Temperaturbereich zwischen diesen beiden Übergängen, nämlich ob das System von einem orbital geordneten Zustand in einen ungeordneten Zustand übergeht [Zeg+05] oder nicht [Por+18].

Es konnte beobachtet werden, dass mit zunehmender Temperatur die Fähigkeit der Spin-Bahn Kopplung unterschiedliche Orbitale zu mischen abnimmt. In Kombination mit Signaturen von Orbitalfluktuationen und der Abwesenheit reeller Orbitalordnung [Por+18] suggeriert dies Phasenfluktuationen zwischen den verschiedenen Orbitalkomponenten, welche nicht mehr durch Spin-Bahn Kopplung fixiert sind und als Ursprung der Orbitalfluktuationen angesehen werden können.

Motiviert durch eine VCA Studie beim absoluten Temperaturnullpunkt [Len16] und einer FTLM Studie bei endlicher Temperatur [ZST06] wurde das Kondo Gittermodell bei halber Füllung mit VCA bei endlicher Temperatur untersucht. Anhand der AFM Magnetisierung, der AFM und PM spezifischen Wärmekapazität sowie des lokalen Spin-Spin Korrelators konnte ein Phasendiagramm konstruiert werden. Die charakteristischen Temperaturen führen zu drei Phasen: ein AFM, ein PM aus Kondo Singuletts und ein thermischer PM. Während der thermische PM für alle berücksichtigen Kondo-Kopplungen J/t die endgültige Hochtemperaturphase darstellt, existiert ein Bereich $J/t \in [1.8, 2.05]$ in welchem die Temperatur die AFM Ordnung zerstört und eine PM Ordnung von Kondo Singuletts verbleibt, bis schließlich ein thermischer PM erreicht wird.

Die Zustandsdichte und Spektralfunktion erlaubten Rückschlüsse auf das Schicksal der Kondo Singuletts mit steigender Temperatur und ihre Signaturen in Abgrenzung zum thermischen PM.

Der Zugang zu endlichen Temperaturen bei gleichzeitiger Einschränkung der Füllungen auf jene, welche mit dem Cluster als Referenzsystem realisierbar sind und auf isolierende Referenzsysteme, ist unbefriedigend. Auf diese Weise wird nur die passive Wirkung der Temperatur erfasst, welche den Grundzustandscharakter durch Zustände höherer Energie abschwächt. Wenn Dotierung für Zustände in der isolierenden Bandlücke sorgen könnte, so könnten ein metallisches System mit einer Fermi-Fläche untersucht oder ein Metall-Isolator Übergang modelliert werden. Dies könnte ein interessanteres Verhalten in der Spektralfunktion mit sich bringen, wie etwa die Verschiebung spektralen Gewichts.

Auf numerischer Seite sollte die Chebyshev-Darstellung der Greenschen Funktion in Kombination mit einem MPS-basierten Cluster-Solver auf reale physikalische Probleme, wie Ca_2RuO_4 angewandt werden, wo größere Cluster in Reichweite sind. Um dort endliche Temperaturen zu realisieren, sollten Zufallsvektoren hinreichend zuverlässige Ergebnisse liefern, da mit einem MPS-basierten Solver größere Systeme zugänglich sind.

Acknowledgements

Having been a member of the FMQ (Institute for Functional Matter and Quantum technologies) as it grew and new groups joined, I am sad that my time there is over. I will remember the cooperative, empathetic interchange on a personal level, giving exercise classes or lab courses on interesting topics to interested students, the down-to-earth humour of the Daghofer group and the sense of community expressed by the Loth group.

I want to express my gratitude to the following people and institutions:

- Prof. Dr. Maria Daghofer for her supervision and the interesting topic I could work on. Although most work consisted in programming, I think I learned a lot from her when expressing observations from an intuitive perspective rather than referring to keywords or technical details.
- Prof. Dr. Walter Metzner for accepting to be in my PhD examination committee.
- Prof. Dr. Sebastian Loth for accepting to be in my PhD examination committee.
- Support from the state of Baden-Württemberg through bwHPC
- All members of the FMQ for providing a pleasant working atmosphere. I especially want to thank Friedemann Aust and Pascal Strobel for proofreading the thesis and contributing suggestions to correct and improve it. Many thanks also to Johannes Roth for maintaining the IT infrastructure of the institute. Furthermore I enjoyed the company of Michael Schmid and the entire Loth group, especially Mohamad Abdo, for interesting and entertaining discussions during lunch and coffee breaks.
- Dominic Klein and Anne-Catherine Oeter for having become invaluable friends I do not want to miss.
- My family for granting me the freedom to study. My father, for relieving me of the burden to look after a house which allowed me to focus more on my work at the university. My sister for being the only person with whom I can talk about anything. And lastly my mother for listening to me when I lamented life.

Declaration

I hereby declare that this dissertation is my own work and no other than the given references have been used. All statements taken in letter or spirit from other works are marked as such. Moreover, this thesis has neither fully nor in parts been subject of another examination.

Stuttgart, May 2022 Jan Lotze

Bibliography

[Aic+06] M. Aichhorn, E. Arrigoni, M. Potthoff and W. Hanke, 'Variational cluster approach to the Hubbard model: Phase-separation tendency and finite-size effects', Phys. Rev. B **74**, 235117 (2006).

[Aic04] M. Aichhorn, 'Ordering Phenomena in Strongly-Correlated Systems: Cluster Perturbation Theory Approaches', PhD thesis (Technische Universität Graz, 2004).

[Ali+99] J. Aliaga, D. Boley, R. Freund and V. Hernández, 'A lanczos-type method for multiple starting vectors', Mathematics of Computation **69**, 1577 (1999).

[Ari+12] R. Arita, J. Kuneš, A. Kozhevnikov, A. Eguiluz and M. Imada, 'Ab initio Studies on the Interplay between Spin-Orbit Interaction and Coulomb Correlation in Sr_2IrO_4 and Ba_2IrO_4', Phys. Rev. Lett. **108**, 086403 (2012).

[AS72] M. Abramowitz and I. Stegun, *Handbook of mathematical functions* (Dover Publications, 1972).

[Bay62] G. Baym, 'Self-Consistent Approximations in Many-Body Systems', Phys. Rev. **127**, 1391 (1962).

[BF16] H. Bruus and K. Flensberg, *Many-Body Quantum Theory in Condensed Matter Physics: An Introduction* (Oxford University Press, 2016).

[BHP08] M. Balzer, W. Hanke and M. Potthoff, 'Mott transition in one dimension: Benchmarking dynamical cluster approaches', Phys. Rev. B **77**, 045133 (2008).

[BK61] G. Baym and L. Kadanoff, 'Conservation Laws and Correlation Functions', Phys. Rev. **124**, 287 (1961).

[Boe15] L. Boehnke, 'Susceptibilities in materials with multiple strongly correlated orbitals', PhD thesis (Universität Hamburg, 2015).

[Bog+15] N. Bogdanov, V. Katukuri, J. Romhányi, V. Yushankhai, V. Kataev, B. Büchner, J. van den Brink and L. Hozoi, 'Orbital reconstruction in nonpolar tetravalent transition-metal oxide layers', Nat. Comm. **6**, 7306 (2015).

[BP10] M. Balzer and M. Potthoff, 'Variational cluster approach to ferromagnetism in infinite dimensions and in one-dimensional chains', Phys. Rev. B **82**, 174441 (2010).

[BS14] A. Braun and Schmitteckert, 'Numerical evaluation of Green's functions based on the Chebyshev expansion', Phys. Rev. B **90**, 165112 (2014).

[Bur08] T. Burnus, 'Study of Charge, Spin and Orbital States in Novel Transition-Metal Oxides Using X-Ray Absorption Spectroscopy', PhD thesis (Universität zu Köln, 2008).

[Chy+11] F. Chyzak, J. Davenport, C. Koutschan and B. Salvy, 'On Kahan's Rules for Determining Branch Cuts', in 13th International Symposium on Symbolic and Numeric Algorithms for Scientific Computing (2011).

[Col15] P. Coleman, *Introduction to Many-Body Physics* (Cambridge University Press, 2015).

[Dag01] M. Daghofer, 'Berechnung thermodynamischer Suszeptibilitäten mit exakter Diagonalisierung', diploma thesis (Technische Universität Graz, 2001).

[Dag94] E. Dagotto, 'Correlated electrons in high-temperature superconductors', Rev. Mod. Phys. **66**, 763 (1994).

[Ede08] R. Eder, 'Correlated band structure of NiO, CoO, and MnO by variational cluster approximation', Phys. Rev. B **78**, 115111 (2008).

[Fel19] T. Feldmaier, 'Excitonic Antiferromagnetism in two-dimensional t_{2g}^4 Systems', PhD thesis (Universität Stuttgart, 2019).

[FNT04] Z. Fang, N. Nagaosa and K. Terakura, 'Orbital-dependent phase control in $Ca_{2-x}Sr_xRuO_4$ ($0 \leq x \leq 0.5$)', Phys. Rev. B **69**, 045116 (2004).

[Fre00] R. Freund, 'Band Lanczos Method', in *Templates for the Solution of Algebraic Eigenvalue Problems: A Practical Guide* (SIAM, 2000).

[GMM13] A. Georges, L. Medici and J. Mravlje, 'Strong Correlations from Hund's Coupling', Annu. Rev. Condens. Matter Phys. **4**, 137 (2013).

[GN01] A. Gelfert and W. Nolting, 'The absence of finite-temperature phase transitions in low-dimensional many-body models: a survey and new results', J. Phys. Condens. Matter **13**, R505 (2001).

[Gor+10] E. Gorelov, M. Karolak, T. Wehling, F. Lechermann, A. Lichtenstein and E. Pavarini, 'Nature of the Mott Transition in Ca_2RuO_4', Phys. Rev. Lett. **104**, 226401 (2010).

[Gre+19] H. Gretarsson, H. Suzuki, H. Kim, K. Ueda, M. Krautloher, B. Kim, H. Yavaş, G. Khaliullin and B. Keimer, 'Observation of spin-orbit excitations and Hund's multiplets in Ca_2RuO_4', Phys. Rev. B **100**, 045123 (2019).

[GSS08] P. Gegenwart, Q. S. and F. Steglich, 'Quantum criticality in heavy-fermion metals', Nat. Phys. **41**, 186 (2008).

[Gul+18] E. Gull, S. Iskakov, I. Krivenko, A. Rusakov and D. Zgid, 'Chebyshev polynomial representation of imaginary-time response functions', Phys. Rev. B **98**, 075127 (2018).

[GV93] C. Gros and R. Valentí, 'Cluster expansion for the self-energy: A simple many-body method for interpreting the photoemission spectra of correlated Fermi systems', Phys. Rev. B **48**, 418 (1993).

[HD01] T. Hotta and E. Dagotto, 'Prediction of Orbital Ordering in Single-Layered Ruthenates', Phys. Rev. Lett. **88**, 017201 (2001).

[Hyu+14] M. Hyuga, S. Sugiura, K. Sakai and A. Shimizu, 'Thermal pure quantum states of many-particle systems', Phys. Rev. B **90**, 121110(R) (2014).

[IE04] T. Iitaka and T. Ebisuzaki, 'Random phase vector for calculating the trace of a large matrix', Phys. Rev. E **69**, 057701 (2004).

[Jah02] W. Jahnke, 'Statistical Analysis of Simulations: Data Correlations and Error Estimation', in *Proceedings of the Euro Winter School Quantum Simulations of Complex Many-Body Systems: From Theory to Algorithms* (NIC-Directors, 2002).

[Jin+09] H. Jin, H. Jeong, T. Ozaki and J. Yu, ‘Anisotropic exchange interactions of spin-orbit-integrated states in Sr_2IrO_4’, Phys. Rev. B **80**, 075112 (2009).

[Jun+03] J. H. Jung, Z. Fang, J. He, Y. Kaneko, Y. Okimoto and Y. Tokura, ‘Change of Electronic Structure in Ca_2RuO_4 Induced by Orbital Ordering’, Phys. Rev. Lett. **91**, 056403 (2003).

[Kim+08] B. Kim, H. Jin, S. Moon, J.-Y. Kim, B.-G. Park, C. Leem, J. Yu, T. Noh, C. Kim, S.-J. Oh, J.-H. Park, V. Durairaj, G. Cao and E. Rotenberg, ‘Novel $J_{\mathrm{eff}} = 1/2$ Mott State Induced by Relativistic Spin-Orbit Coupling in Sr_2Ir_4’, Phys. Rev. Lett. **101**, 076402 (2008).

[Kim+14] J. Kim, M. Daghofer, A. H. Said, T. Gog, J. van den Brink, G. Khaliullin and B. J. Kim, ‘Excitonic quasiparticles in a spin–orbit Mott insulator’, Nat. Comm. **5**, 4453 (2014).

[Kim+18] M. Kim, J. Mravlje, M. Ferrero, O. Parcollet and A. Georges, ‘Spin-Orbit Coupling and Electronic Correlations in Sr_2RuO_4’, Phys. Rev. Lett. **120**, 126401 (2018).

[Kło+20] A. Kłosiński, D. Efremov, J. van den Brink and K. Wohlfeld, ‘Photoemission spectrum of Ca_2RuO_4: Spin polaron physics in an $S = 1$ antiferromagnet with anisotropies’, Phys. Rev. B **101**, 035115 (2020).

[LA09] X. Lu and E. Arrigoni, ‘Dispersive spectrum and orbital order of spinless p-band fermions in an optical lattice’, Phys. Rev. B **79**, 245109 (2009).

[LD21] J. Lotze and M. Daghofer, ‘Suppression of effective spin-orbit coupling by thermal fluctuations in spin-orbit coupled antiferromagnets’, Phys. Rev. B **104**, 045125 (2021).

[Len16] B. Lenz, ‘Unconventional Phases in Two-Dimensional Hubbard and Kondo-Lattice Models by Variational Cluster Approaches’, PhD thesis (Universität Göttingen, 2016).

[Li+09] G. Li, W. Hanke, A. N. Rubtsov, S. Bäse and M. Potthoff, ‘Accessing thermodynamics from dynamical cluster-embedding approaches’, Phys. Rev. B **80**, 195118 (2009).

[Li+13] Q. Li, G. Cao, S. Okamoto, J. Yi, W. Lin, B. Sales, J. Yan, R. Arita, J. Kuneš, A. Kozhevnikov, A. Eguiluz, M. Imada, Z. Gai, M. Pan and D. Mandrus, ‘Ab initio Studies on the Interplay between Spin-Orbit Interaction and Coulomb Correlation in Sr_2IrO_4 and Ba_2IrO_4’, Sci. Rep. **3**, 3073 (2013).

[Lot17] J. Lotze, ‘Mean-field extension of the variational cluster approximation to intersite interactions’, Master thesis (Universität Stuttgart, 2017).

[LW60] J. M. Luttinger and J. C. Ward, ‘Ground-State Energy of a Many-Fermion System. II’, Phys. Rev. **118**, 1417 (1960).

[Mar+11] C. Martins, M. Aichhorn, L. Vaugier and S. Biermann, ‘Reduced Effective Spin-Orbital Degeneracy and Spin-Orbital Ordering in Paramagnetic Transition-Metal Oxides: Sr_2IrO_4 versus Sr_2RhO_4’, Phys. Rev. Lett. **107**, 266404 (2011).

[Mar+18] C. Martins, B. Lenz, L. Perfetti, V. Brouet, F. Bertran and S. Biermann, ‘Nonlocal Coulomb correlations in pure and electron-doped Sr_2IrO_4: Spectral functions, Fermi surface, and pseudo-gap-like spectral weight distributions from oriented cluster dynamical mean-field theory’, Phys. Rev. Materials **2**, 032001(R) (2018).

[Min00] T. Minka, *Old and New Matrix Algebra Useful for Statistics*, Notes, 2000.

[Miz+01] T. Mizokawa, L. Tjeng, G. Sawatzky, G. Ghiringhelli, O. Tjernberg, N. Brookes, H. Fukazawa, S. Nakatsuji and Y. Maeno, 'Spin-Orbit Coupling in the Mott Insulator Ca_2RuO_4', Phys. Rev. Lett. **87**, 077202 (2001).

[MT20] K. Morita and T. Tohyama, 'Finite-temperature properties of the Kitaev-Heisenberg models on kagome and triangular lattices studied by improved finite-temperature Lanczos methods', Phys. Rev. Research **2**, 013205 (2020).

[Nie95] A. Nieto, 'Evaluating sum over the Matsubara frequencies', Computer Physics Communications **92**, 54 (1995).

[Nis+19] H. Nishida, R. Fujiuchi, K. Sugimoto and Y. Ohta, *Typicality-Based Variational Cluster Approach to Thermodynamic Properties of the Hubbard Model*, 2019, arXiv:`1909.09335 [cond-mat]`.

[Nol14] W. Nolting, *Viel-Teilchen-Theorie* (Springer, 2014).

[Ole83] A. Oleś, 'Antiferromagnetism and correlation of electrons in transition metals', Phys. Rev. B **28**, 327 (1983).

[OPV16] M. M. Odashima, B. G. Prado and E. Vernek, *Pedagogical introduction to equilibrium Green's functions: condensed matter examples with numerical implementations*, 2016, arXiv:`1604.02499v2 [cond-mat]`.

[Pae20] S. Paeckel, 'Topological and non-equilibrium superconductivity in low-dimensional strongly correlated quantum systems', PhD thesis (Universität Göttingen, 2020).

[PB11] P. Prelovšek and J. Bonča, *Ground State and Finite Temperature Lanczos Methods*, 2011, arXiv:`1111.5931v1 [ftlm]`.

[Por+18] D. Porter, V. Granata, F. Forte, S. Di Matteo, M. Cuoco, R. Fittipaldi, A. Vecchione and A. Bombardi, 'Magnetic anisotropy and orbital ordering in Ca_2RuO_4', Phys. Rev. B **98**, 125142 (2018).

[Pot03] M. Potthoff, 'Self-energy-functional approach: Analytical results and the Mott-Hubbard transition', Eur. Phys. J. B **36**, 335 (2003).

[Pot12] M. Potthoff, 'Self-Energy-Functional Theory', in *Strongly Correlated Systems – Theoretical Methods* (Springer, 2012).

[Pot14] M. Potthoff, 'Making Use of Self-Energy Functionals: The Variational Cluster Approximation', in *DMFT at 25: Infinite Dimensions* (Forschungszentrum Jülich GmbH – Institute for Advanced Simulation, 2014).

[Pot98] M. Potthoff, 'Anwendungen der Vielteilchentheorie in der Festkörperphysik', lecture notes, 1998.

[PS95] M. Peskin and D. Schroeder, *An Introduction to Quantum Field Theory* (Westview Press, 1995).

[PST00] S. Pairault, D. Sénéchal and A.-M. S. Tremblay, 'Strong-coupling perturbation theory of the Hubbard model', Eur. Phys. J. B **16**, 85 (2000).

[Sch06] F. Schwabl, *Statistical Mechanics* (Springer, 2006).

[Sch16] T. Schaller, 'Variational-cluster approximation for spin-orbit coupled correlated materials', MSc thesis (Universität Stuttgart, 2016).

[Sén08] D. Sénéchal, *An introduction to quantum cluster methods*, 2008, arXiv:`0806.2690v2 [cond-mat]`.

[Sén12] D. Sénéchal, 'Cluster Perturbation Theory', in *Strongly Correlated Systems – Theoretical Methods* (Springer, 2012).

[Sia+12] M. Siahatgar, B. Schmidt, G. Zwicknagl and P. Thalmeier, 'Moment screening in the correlated Kondo lattice model', New J. Phys. **14**, 103005 (2012).

[SL13] G. Stefanucci and R. van Leeuwen, *Nonequilibrium Many-Body Theory of Quantum Systems – A Modern Introduction* (Cambridge University Press, 2013).

[SS13] S. Sugiura and A. Shimizu, 'Canonical Thermal Pure Quantum State', Phys. Rev. Lett. **111**, 010401 (2013).

[SSY18] K. Seki, T. Shirakawa and S. Yunoki, 'Variational cluster approach to thermodynamic properties of interacting fermions at finite temperatures: A case study of the two-dimensional single-band Hubbard model at half filling ', Phys. Rev. B **98**, 205114 (2018).

[Sut+17] D. Sutter, C. Fatuzzo, S. Moser, M. Kim, R. Fittipaldi, A. Vecchione, V. Granata, Y. Sassa, F. Cossalter, G. Gatti, M. Grioni, H. Rønnow, N. Plumb, C. E. Matt, M. Shi, M. Hoesch, T. Kim, T.-R. Chang, H.-T. Jeng, C. Jozwiak, A. Bostwick, E. Rotenberg, A. Georges, T. Neupert and J. Chang, 'Hallmarks of Hunds coupling in the Mott insulator Ca_2RuO_4', Nat. Comm. **8**, 15176 (2017).

[SWY10] T. Shirakawa, H. Watanabe and S. Yunoki, 'Microscopic Study of a Spin-Orbit-Induced Mott Insulator in Ir Oxides', J. Phys. Soc. Jpn. **80**, SB010 (2010).

[SY20] K. Seki and S. Yunoki, 'Thermodynamic properties of an $S = \frac{1}{2}$ ring-exchange model on the triangular lattice', Phys. Rev. B **101**, 235115 (2020).

[Wei+06] A. Weiße, G. Wellein, A. Alvermann and H. Fehske, 'The kernel polynomial method', Rev. Mod. Phys. **78**, 275 (2006).

[Wol+14] F. Wolf, I. McCulloch, O. Parcollet and U. Schollwöck, 'Chebyshev matrix product state impurity solver for dynamical mean-field theory', Phys. Rev. B **90**, 115124 (2014).

[WSY10] H. Watanabe, T. Shirakawa and S. Yunoki, 'Microscopic Study of a Spin-Orbit-Induced Mott Insulator in Ir Oxides', Phys. Rev. Lett. **105**, 216410 (2010).

[WSY14] H. Watanabe, T. Shirakawa and S. Yunoki, 'Theoretical study of insulating mechanism in multiorbital Hubbard models with a large spin-orbit coupling: Slater versus Mott scenario in Sr_2IrO_4', Phys. Rev. B **89**, 165115 (2014).

[Zeg+05] I. Zegkinoglou, J. Strempfer, C. Nelson, J. Hill, J. Chakhalian, C. Bernhard, J. Lang, G. Srajer, H. Fukazawa, S. Nakatsuji, Y. Maeno and B. Keimer, 'Orbital Ordering Transition in Ca_2RuO_4 Observed with Resonant X-Ray Diffraction', Phys. Rev. Lett. **95**, 136401 (2005).

[ZP17] G. Zhang and E. Pavarini, 'Mott transition, spin-orbit effects, and magnetism in Ca_2RuO_4', Phys. Rev. B **95**, 075145 (2017).

[ZST06] I. Zerec, B. Schmidt and P. Thalmeier, 'Kondo lattice model studied with the finite temperature Lanczos method', Phys. Rev. B **73**, 245108 (2006).